# Chemical Processing and Characterization of Ferroelectric Tungsten Bronze Niobate Thin Films

**Wataru Sakamoto**

A Dissertation for the Degree of Doctor of Engineering at Department of Applied Chemistry, Graduate School of Engineering, Nagoya University

December, 1999

# Preface

This dissertation is submitted in fulfillment of the requirement for the Degree of Doctor of Engineering on the study of chemical processing and characterization of ferroelectric tungsten bronze niobate thin films, which has been carried out during 1995-1999 under the guidance of Professor Shin-ichi Hirano at the Department of Applied Chemistry, Graduate School of Engineering, Nagoya University.

In this work, the processing conditions and the dielectric, ferroelectric, and optical properties of tungsten bronze niobate thin films were investigated in detail in order to elucidate the basic properties of the films for the application as new electric devices.

The author is greatly indebted to Professor Shin-ichi Hirano for his pertinent guidance and encouragement throughout this study. The author thanks Associate Professor Toshinobu Yogo for his valuable suggestions and encouragement. The author also thanks Professor Kunihito Koumoto, Professor Hideaki Itoh and Associate Professor Ko-ichi Kikuta for their reviewing and comments on this dissertation. The author would like to acknowledge Mr. Ko-ji Ogiso, Mr. Tadashi Arimoto, Mr. Akihiro Kawase, Mr. Tadayuki Isaji, Miss Takae Kuroyanagi, Miss Kana Kosugi and Mr. Yu-saku Horie and all other members of laboratory for their sincere collaborations. Also, the author wishes to thank Dr. Arao Nakamura, Dr. Masao Ichida, Dr. Yu-ji Iwamoto and Dr. Satomi Ono who helped several measurements.

The author is further extended his acknowledgement to his friends, his parents and colleagues of Matsushita Electric Industrial Co., Ltd. and Matsushita Electronic Components Co., Ltd. for their continual encouragements.

Wataru Sakamoto

December, 1999

# Contents

# Chapter 1

## Introduction

## 1.1 Tungsten bronze niobate materials[1-6]

Niobate crystals, especially with perovskite or tungsten bronze structure, belong to a class of important ferroelectric materials, because they have large pyroelectric coefficients, excellent piezoelectric and electro-optic properties. Early studies of the tungsten bronze niobates, such as $PbNb_2O_6$ (lead metaniobate) were performed by Goodman in 1953, and is of special interest in high-temperature piezoelectric applications because of its large piezoelectric constant and high Curie point, 570°C. Crystallographic studies by the Francombe (1956) revealed that at room temperature there are two polymorphic forms of $PbNb_2O_6$, namely, a rhombohedral form, stable at temperatures up to 1200°C, and the ferroelectric orthorhombic form found in materials rapidly cooled from temperatures above 1250°C. $PbNb_2O_6$ and compounds of the type $PbO_x(Nb_2O_5)$, where $1 \leqq x < 3.0$, are structurally related to the tetragonal tungsten bronzes $K_{0.57}WO_3$ and $Na_{0.28}WO_3$ described by Magneli (1949). Goodman (1957) has found that the electrical properties of $PbNb_2O_6$ are considerably enhanced when Pb is partially replaced by Mg, Ca, Sr and Ba. Electrical and crystallographic studies have also been made in these laboratories for the systems $(Pb,Ba)Nb_2O_6$ (Francombe and Lewis, 1958) and $(Sr,Ba)Nb_2O_6$.

The tungsten bronze (TB) structure is constructed by the network of octahedra sharing the corners, and it could be safely said that this structure stands at intermediate positions between the perovskite-type and pyrochlore-type structures. A typical TB unit cell is composed of ten octahedra and six cages; the latters consists of two 12-coordinated (A1) sites and four 15-coordinated (A2) sites surrounded by the octahedral as shown in Fig.1-1-1. Usually, four 9-coordinated (C) sites are vacant, in which small ions such as $Li^+$ and $Mg^{2+}$, etc. can be introduced. When the octahedral sites are occupied by B ions and the remaining six sites by A ions, the compound is represented by a general formula, $A_6B_{10}O_{30}$, called a filled-tungsten bronze, where either A or B sites are to be occupied by more than two kinds of ions. Accordingly, if the binary system is composed of A-oxide and B-oxide, we could only find the $A_5B_{10}O_{30}$-type TB,

where the six A sites are occupied by five ions; thus it is called as the unfilled TB structure. Relatively large cations such as alkali ion ($K^+$, $Na^+$), alkali earth ion ($Ca^{2+}$, $Sr^{2+}$, $Ba^{2+}$), rear earth ion ($La^{3+}$, $Nd^{3+}$) and $Pb^{2+}$, $Bi^{3+}$ can occupy the A sites. On the other hand, small cations with high valency such as $Nb^{5+}$ and $Ta^{5+}$ can occupy the B sites. Therefore, ferroelectric tungsten bronze material has attracted special attention, because numerous desired properties can be designed by introducing various ions in the A sites or B sites.

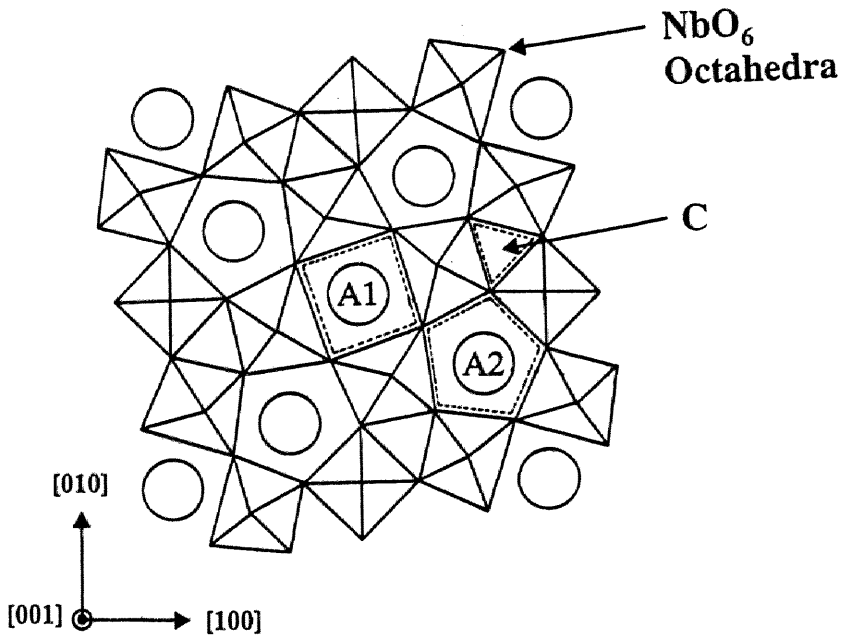


Fig.1-1-1 Structure of tungsten bronze projected onto the (001) plane.
[A1: 12-fold site, A2: 15-fold site, C: 9-fold site]

Ferroelectric tungsten bronze niobate materials are classified to the three types by the occupation of metal ions in their structure.

1) completely filled tungsten bronze

Monovalent ions occupy all sites.

ex.) $K_3Li_2Nb_5O_{15}$ (KLN)

2) filled tungsten bronze

Metal ions occupy all A sites with vacant C sites.

ex.) $Ba_2NaNb_5O_{15}$ (BNN), $Sr_2KNb_5O_{15}$ (SKN), $K_2LaNb_5O_{15}$

3) partially filled tungsten bronze

Metal ions occupy five-sixth of A sites, or one-sixth of A sites with vacant C sites.

ex.) $Pb_{1-x}Ba_xNb_2O_6$ (PBN), $Sr_{1-x}Ba_xNb_2O_6$ (SBN)

## 1.2 Ferroelectricity and structural stability of tungsten bronze structure

Tungsten bronze structure was discovered by Magneli et al. in 1949 as the $K_xWO_3$ phase. After that, many kinds of compounds with tungsten bronze structure have been synthesized. These compounds classified into three groups as shown in Table 1-2-1. In the groups listed, the third group, which has the general formula: $(A1)_2(A2)_4(C)_4(B1)_2(B2)_8O_{30}$, shows ferroelectricity.[4,7] This type of compounds, such as SBN and PBN, have excellent electrical and optical properties and have been receiving great attention.

Table 1-2-1 Some "tetragonal tungsten bronze"-type structures

| Formula | Composition range | a (Å) | b (Å) | c (Å) | Z |
|---|---|---|---|---|---|
| 1. Conducting, highly colored, nonstoichiometric bronzes | | | | | |
| $K_xWO_3$ | $x=0.9$–$1.1$ | 12.31 | ··· | 3.84 | 5 |
| $Na_xWO_3$ | $x=0.56$–$0.76$ | 12.10 | ··· | 3.75 | 5 |
| $Pb_xWO_3$ | $x=0.3$–$0.7$ | 12.20 | ··· | 3.78 | 5 |
| $Ba_xWO_3$ | $x=0.22$–$0.44$ | 12.15 | ··· | 3.84 | 5 |
| $K_xMoO_3$ | $x\simeq1.0$ | 12.32 | ··· | 3.86 | 5 |
| $BaNb_2O_6$ | | 12.60 | ··· | 3.95 | 5 |
| $BaTa_2O_6$ | | 12.60 | ··· | 3.95 | 5 |
| 2. Compounds of the type $(AO)\cdot x(B_2O_5)$ | | | | | |
| $Na_2O\cdot4Nb_2O_5$ | | 12.45 | 3×12.32 | 3.91 | c |
| $K_2O\cdot3Nb_2O_5$ | | 3×12.57 | ··· | 3.94 | c |
| $K_2O\cdot2Ta_2O_5$ | | 3×12.43 | ··· | 3.88 | c |
| $PbO\cdot xNb_2O_5$ | $x=1$–$3$ | 17.52 | 17.59 | 2×3.94 | c |
| $BaO\cdot2Nb_2O_5$ | | 12.46 | ··· | 3.97 | c |
| $SrO\cdot2\frac{1}{2}(Nb_2O_5)$ | | 12.34 | ··· | 3.94 | c |
| $BaO\cdot2Ta_2O_5$ | | 17.55 | 17.65 | 3.91 | c |
| $Nb_{16}W_{18}O_{94}$ | | 12.25 | 3×12.21 | 3.94 | c |
| 3. Ferroelectric materials $(A1)_2(A2)_4(C)_4(B1)_2(B2)_8O_{30}$ | | | | | |
| $Pb_2Nb_8O_{30}$ | | 17.65 | 17.91 | 2×3.84 | 4 |
| $Pb_2Ta_8O_{30}$ | | 17.61 | 17.91 | 2×3.87 | 4 |
| $Sr_2Ta_8O_{30}$ | | 12.45 | ··· | 2×3.85 | 2 |
| $Ba_2Ta_8O_{30}$ | | 12.59 | ··· | 2×3.92 | 2 |
| $(Pb, X)_6Nb_8O_{30}$ | X = Ca, Sr, Ba | 17.85 | 18.14 | 2×3.90 | 4 |
| $Ba_4R_2Fe_2Nb_8O_{30}$ | R = Nd, Sm, Gd | 12.47 | ··· | 3.93 | 1 |
| $Ba_xSr_{(5-x)}Nb_8O_{30}$ | $x=1.25$–$3.75$ | 12.43 | ··· | 3.91 | 1 |
| $Ba_{4.7}Nb_{8.4}Zr_{1.6}O_{30}$ | | 12.67 | 12.67 | 4.02 | 1 |
| $Ba_4Nb_8Ti_2O_{30}$ | | 12.54 | ··· | 4.01 | 1 |
| $Ba_4Na_2Nb_{10}O_{30}$ | | 17.59 | 17.63 | 4.00 | 2 |
| $K_2Li_4Nb_{10}O_{30}$ | | 12.58 | ··· | 4.01 | 1 |

The main structure of tungsten bronze is constructed from $BO_6$ octahedra affording the A1, A2 and C sites. The B ion of $BO_6$ octahedra is known to occupy two different cation sites (B(1) and B(2)), which are coordinated by four O atoms in pseudo-square planes as shown in Fig.1-2-1. O(4) and O(5) atoms can occupy two sites corresponding to the occupation of A1, A2 and C cations, and enhance the formation of the disordered structure.[7,8] Usually, Nb and Ta are well-known as B cations of ferroelectric tungsten bronze. Figure 1-2-2 shows the configuration of A sites in the unit sell of tetragonal tungsten bronze SBN. As shown in Fig.1-2-3, A1 site is surrounded by twelve O atoms (O(2) and O(5a) or O(5b)). A2 site is found to be the type of triangle prism coordination by the study of Jamieson for SBN as shown in Fig.1-2-4. When two kinds of A cation are introduced in this structure, a cation which has the smaller ionic radius dominantly occupies the A1 site since the size

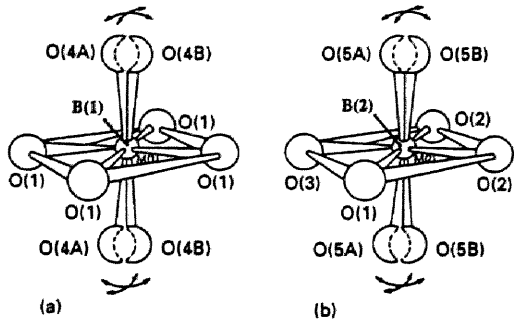


Fig.1-2-1 (a) B(1) and (b) B(2) octahedra for the tungsten bronze structure.

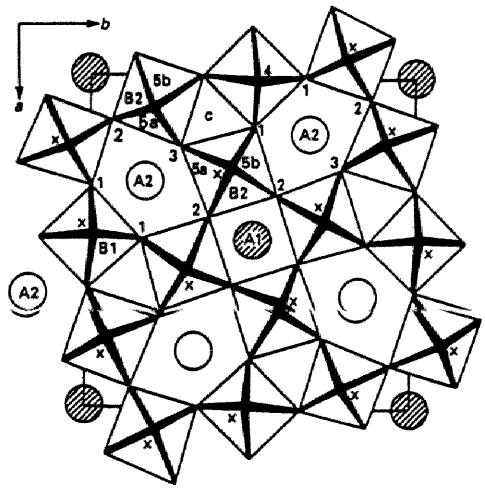


Fig.1-2-2 View of strontium barium niobate structure along the polar c axis.

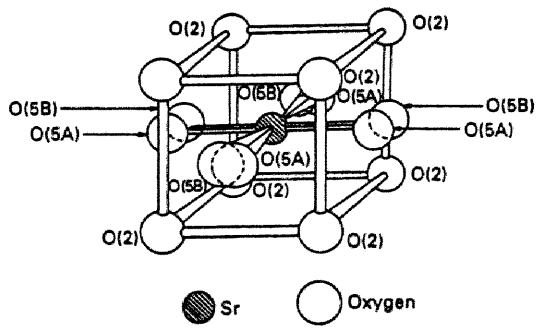


Fig.1-2-3 Cubo-octahedral coordination of the nearest neighbour oxygen atoms around strontium in the A1 site.

of A2 site is larger than A1 site. Wide variety of A cations can be introduced in A1 and A2 sites. In general, A cation is selected from Pb, Ba, Ca, Sr, K, Na and rare earth elements. C site is the smallest site and, the coordination number of nine similar to A2 site, which has triangle prism type coordination. On the other hand, C site is usually occupied with the smallest cation such as $Li^+$. There are several reasons for the complexity of tungsten bronze structure. Every $BO_6$ octahedron can tilt to several directions from c-axis, which leads to the shift of O(4) and O(5) atoms as shown in Fig.1-2-1. Jamieson et al. suggested that the diversity of distortion of $BO_6$ octahedra caused by the occupation of A1, A2 and C cations enables the transformation from tetragonal to orthorhombic symmetry.[7]

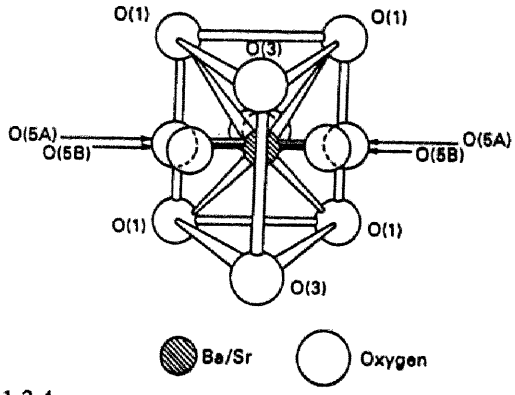


Fig.1-2-4 Tri-capped trigonal prismatic coordination of the nearest neighbour oxygen atoms around a composite Ba/Sr atom in the A2 and C sites.

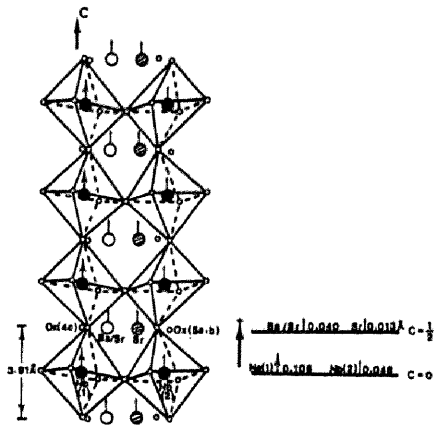


Fig.1-2-5 The nature of the cation displacements along +c, relative to the oxygen planes, which explains the macroscopic polarization [SBN]

Another reason for the complexity of the structure is that the O(4) site has only 50% occupancy. These vacancies make another atoms shift from the ideal positions, which leads to the change in symmetry of local sites. The origin of ferroelectricity is caused by the cations introduced in B, A1, A2 and C (if it is existed) sites. These cations are shifted from the O(1), O(2) and O(3) oxygen atom plane. This shift of cations results in the dipole moment oriented for specific

direction, for example, along c-axis for tetragonal SBN as shown in Fig1-2-5.[9]

The phase relationship was so far investigated for many solid solution of $A_5B_{10}O_{30}$ and $A_6B_{10}O_{30}$ systems (A=Ba, Pb, Sr, Ca, Na, K and B=Nb, Ta). Table 1-2-2 summarizes the multi-component $A_5B_{10}O_{30}$ and $A_6B_{10}O_{30}$ type compounds.[10] Cations play an important role in the stability of tungsten bronze structure for $A_5B_{10}O_{30}$ and $A_6B_{10}O_{30}$ type compounds. In the case of $A_5B_{10}O_{30}$ type niobate, only $PbNb_2O_6$ (PN) has the tungsten bronze structure. On the other hand, $BaNb_2O_6$ (BN), $SrNb_2O_6$ (SN) and $CaNb_2O_6$ (CN) [A=Ba, Sr, Ca] don't have the tungsten bronze structure. For example, the crystal structure of $SrNb_2O_6$ and $BaNb_2O_6$ is the orthorhombic structure partly constructed by edge-shared $NbO_6$ octahedra as shown in Fig1-2-6.[11] However, similar to the PN-BN, PN-SN and PN-CN systems, the tungsten bronze solid solution exists in the binary BN-SN system. Figure 1-2-7 shows the phase relation for the $A_5B_{10}O_{30}$ type ternary system, such as BN-SN-CN and BN-PN-SN systems.[10] The distributions of Curie temperature ($T_c$) and the lattice constants are shown by contour lines in the tungsten bronze type range. The lattice parameters in the orthorhombic phase are indicated by a and c instead of a, b and c, where $a_t=(a+b)/2\sqrt{2}$ is a pseudo-tetragonal constant. PN is known to have the largest ferroelectricity among unfilled-tungsten bronze compounds. Curie temperature is the "measure" for the stability of the ferroelectricity of tungsten bronze compounds.

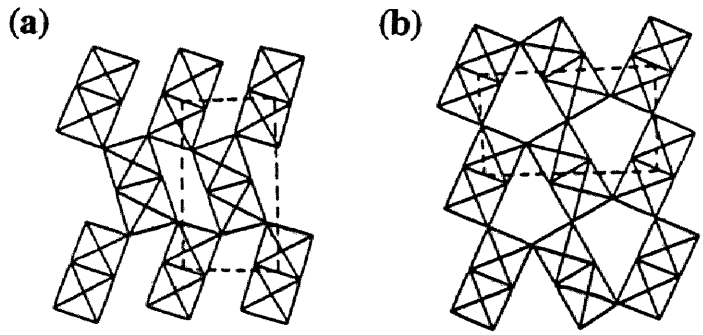


Fig.1-2-6 (a) Orthorhombic $SrNb_2O_6$ and (b) high orthorhombic $BaNb_2O_6$ structures

Table 1-2-2 Tungsten bronze niobate and tantalate compounds

| Compounds | Abbreviation | Crystal system | Lattice constant (Å) a | b | c | $T_C$(°C) |
|---|---|---|---|---|---|---|
| $PbNb_2O_6$ | PN | O | 17.51 | 17.81 | 7.73 | 560 |
| $BaNb_2O_6$ | BN | H | 12.07 | | 3.95 | |
| | | O | 12.194 | 10.268 | 7.856 | (not TB) |
| $SrNb_2O_6$ | SN | | | (Unknown) | | (not TB) |
| $CaNb_2O_6$ | CN | O | 5.764 | 15.09 | 5.232 | (not TB) |
| $PbTa_2O_6$ | PT | O | 17.68 | 17.72 | 7.754 | 265 |
| $BaTa_2O_6$ | BT | T | 17.800 | | 7.840 | — |
| $SrTa_2O_6$ | ST | T | 17.600 | | 7.703 | — |
| $Pb_2NaNb_5O_{15}$ | PNN | O | 17.606 | 17.928 | 3.856 | 531 |
| $Ba_2NaNb_5O_{15}$ | BNN | O | 17.59 | 17.61 | 7.982 | 560(300) |
| $Sr_2NaNb_5O_{15}$ | SNN | O | 17.45 | 17.49 | 3.892 | 270 |
| $Pb_2NaTa_5O_{15}$ | PNT | T | 12.45 | | 3.86 | — |
| | | | 12.473 | | 3.865 | 82 |
| $Ba_2NaTa_5O_{15}$ | BNT | T | 12.480 | | 3.915 | — |
| $Sr_2NaTa_5O_{15}$ | SNT | T | 12.395 | | 3.862 | −153 |
| $Pb_2KNb_5O_{15}$ | PKN | O | 17.78 | 17.96 | 3.928 | 374 |
| | | | 17.78 | 18.05 | 3.917 | 460 |
| $Ba_2KNb_5O_{15}$ | BKN | T | 12.55 | | 4.019 | 373 |
| $Sr_2KNb_5O_{15}$ | SKN | T | 12.47 | | 3.942 | 156 |
| $Pb_2KTa_5O_{15}$ | PKT | T | 12.585 | | 3.931 | −48 |
| | | | 12.588 | | 3.920 | −52 |
| $Ba_2KTa_5O_{15}$ | BKT | T | 12.57 | | 3.95 | — |
| | | O | 17.70 | 17.81 | 3.94 | — |
| $Sr_2KTa_5O_{15}$ | SKT | T | 12.45 | | 3.89 | |
| | | O | 17.55 | 17.66 | 3.89 | −163 |
| $Ca_2KTa_5O_{15}$ | CKT | O | 17.675 | 17.755 | 3.910 | — |

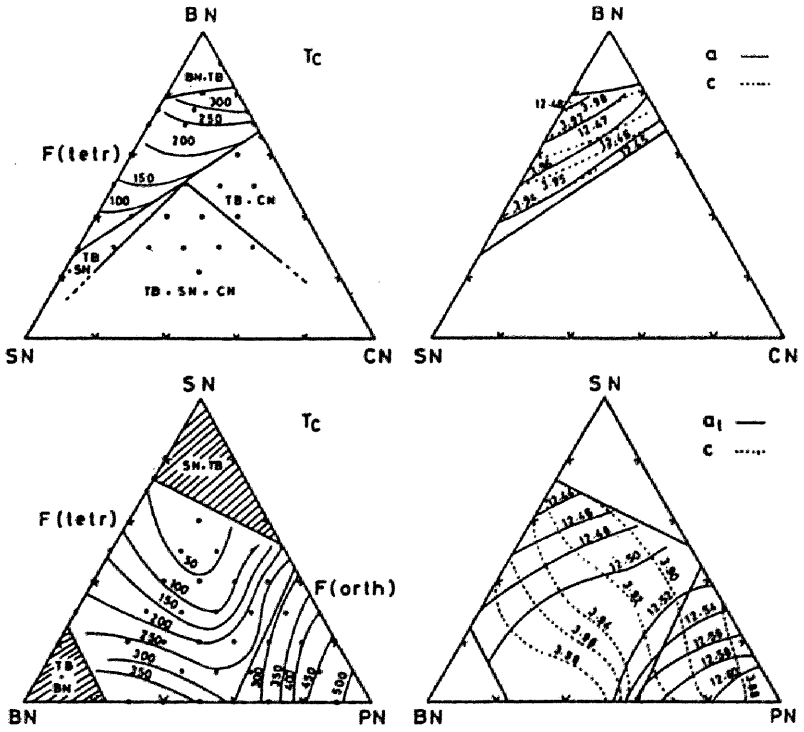


Fig.1-2-7 The $A_5B_{10}O_{30}$-type ternary systems, $(Ba, Sr, Ca)_5Nb_{10}O_{30}$ and $(Sr, Ba, Pb)_5Nb_{10}O_{30}$. The distributions of the Curie temperature ($T_C$ in °C) and the lattice constants ($a$, $c$ and $a_t$ in Å) are shown by contour lines in the TB-type range. The lattice parameters in the orthorhombic phase are indicated by $a_t$ and $c$ instead of $a$, $b$ and $c$, where $a_t=(a+b)/2\sqrt{2}$ is a pseudotetragonal constant. The components are abbreviated as BN=$Ba_5Nb_{10}O_{30}$, SN=$Sr_5Nb_{10}O_{30}$, CN=$Ca_5Nb_{10}O_{30}$ and PN=$Pb_5Nb_{10}O_{30}$, where the PN is only of the TB structure.

In addition, $A_5B_{10}O_{30}$ type tantalate [A=Pb, Ba, Sr] have the tungsten bronze structure.[10,12-14] The substitution of Ta for $A_5B_{10}O_{30}$ type niobate also stabilizes the tungsten bronze structure similar to the introduction of alkali ions for A sites. In $A_5B_{10}O_{30}$ type niobate [A=Sr, Ba], tungsten bronze crystal has been known to be formed by the substitution of Ta for Nb as shown in Table 1-2-2. Ikeda et al. investigated the effect of the substitution of B ion for $(Pb_{1-x}Ba_x)_5(Nb_{1-y}Ta_y)_{10}O_{30}$ system.[10] Figure 1-2-8 shows the change in $T_c$ and lattice constants for the tungsten bronze compounds with various chemical compositions.

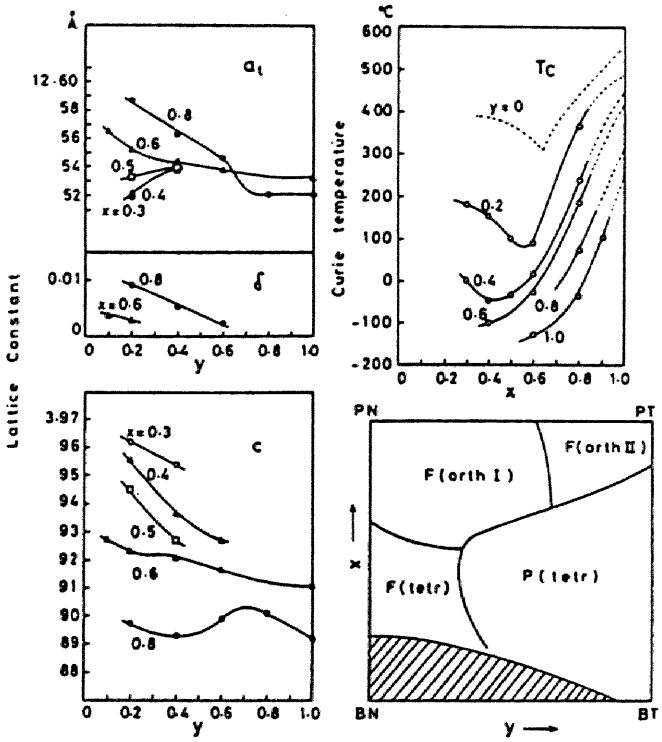


Fig.1-2-8 The $A_5B_{10}O_{30}$-type quarternary system, $(Pb_{1-x}Ba_x)_5(Nb_{1-y}Ta_y)_{10}O_{30}$. The lattice constants and the Curie temperature are shown against the composition. The lattice parameters in the orthorhombic phase are indicated by $a_t$, $\delta$ and $c$, where $a_t=(a+b)/2\sqrt{2}$ and $\delta=(b-a)/[(a+b)/2]$. The orth II phase is treated as a pseudotetragonal one. The components of the phase diagram are indicated by the abbreviation: PN=$Pb_5Nb_{10}O_{30}$, PT=$Pb_5Ta_{10}O_{30}$, BN=$Ba_5Nb_{10}O_{30}$ and BT=$Ba_5Ta_{10}O_{30}$. The hatched region is a heterogeneous region of BN+TB.

In the BT-BN binary system, the tungsten bronze range exists in the narrow area around the end member of BT. $T_c$ reached the maximum value at PN and decreased with approaching to BT side. In spite of the similarity of chemical characters between Nb and Ta, the substitution of Ta for Nb gives the great influence for ferroelectricity and greatly reduces $T_c$. Neither $SrTa_2O_6$ nor $BaTa_2O_6$ has ferroelectricity even in the low temperature region and they are paraelectric.

When A site cations are Ba and rare earth element in niobates, the tungsten bronze phase with ferroelectricity was reported for $(Ba_{1-x}R_{2x/3})Nb_2O_6$ system [R=Y,

Sm, La] when R=Sm, La is in $0.2 \leqq x \leqq 0.4$, R=Y is at x=0.25.[15]

Furthermore, change in chemical composition from $A_5B_{10}O_{30}$ to $A_6B_{10}O_{30}$ by the incorporation of alkali ions in its structure such as Na and K leads to the formation of the filled-tungsten bronze, which has high structural stability.[6,16,17] When one $A^{2+}$ ion of the $A_5B_{10}O_{30}$ type tungsten bronze is substituted for two alkali ions, the structure approaches to the $A_6B_{10}O_{30}$ type tungsten bronze. Thus, the structural stability is enhanced by the introduction of alkali ion in the A1 and A2 sites. The solid solution between $A_5B_{10}O_{30}$ and $A_6B_{10}O_{30}$ type tungsten bronze compounds completely form the tungsten bronze phase. Table 1-2-3 summarizes the well-known $A_6B_{10}O_{30}$ type filled-tungsten bronzes. These compounds are the solid solution between $A^+NbO_3$ and $A^{2+}Nb_2O_6$ type compounds.[17]

Table 1-2-3 Data for tungsten bronze-type niobates

| Composition | x* | $a_o$ | $b_o$ | $c_o$ | $T_c$ | Symmetry |
|---|---|---|---|---|---|---|
| $KNbO_3$–$PbNb_2O_6$ | 0.00 | 17.68 | 17.94 | 3.872 | 560 | Orth. |
| | .10 | 17.71 | 17.97 | 3.895 | 465 | " |
| | .20 | 17.72 | 17.97 | 3.908 | 428 | " |
| | .30 | 17.75 | 17.97 | 3.921 | 360 | " |
| | .33 | 17.78 | 17.96 | 3.928 | 374 | " |
| | .40 | 17.77 | 17.97 | 3.936 | 331 | " |
| $KSr_2Nb_5O_{15}$–$KPb_2Nb_5O_{15}$ | .30 | 17.77 | 17.88 | 3.925 | 336 | " |
| | .40 | 17.75 | 17.85 | 3.923 | 276 | " |
| | .50 | 17.67 | 17.73 | 3.911 | 206 | " |
| | .60 | 12.57 | | 3.922 | 236 | " |
| | .60 | 12.46 | | 3.924 | 132 | ? |
| | .80 | 12.53 | | 3.925 | 172 | Orth. |
| | .85 | 12.51 | | 3.931 | 133 | ? |
| | .90 | 12.51 | | 3.929 | 105 | ? |
| $K_2LaNb_5O_{15}$–$KPb_2Nb_5O_{15}$ | .20 | 12.61 | | 3.928 | 263 | Orth. |
| | .30 | 12.61 | | 3.933 | 217 | " |
| | .40 | 12.59 | | 3.936 | 177 | " |
| $KBa_2Nb_5O_{15}$–$KPb_2Nb_5O_{15}$ | .10 | 17.80 | 17.88 | 3.936 | 304 | " |
| | .20 | 17.83 | 17.83 | 3.947 | 260 | " |
| | .40 | 12.54 | | 3.998 | 285 | Tetr. |
| | .60 | 12.54 | | 4.004 | 322 | " |
| | .80 | 12.54 | | 4.015 | 357 | " |
| | .90 | 12.54 | | 4.019 | 365 | " |
| $LaNb_3O_9$–$KSr_2Nb_5O_{15}$ | .01 | 12.47 | | 3.941 | 141 | " |
| | .03 | 12.46 | | 3.940 | 107 | " |
| | .06 | 12.48 | | 3.934 | 65 | " |
| | .09 | 12.46 | | 3.919 | 35 | " |
| | .18 | 12.48 | | 3.919 | 9 | " |
| $KSr_2Nb_5O_{15}$–$KBa_2Nb_5O_{15}$ | .20 | 12.53 | | 4.010 | 325 | |
| | .40 | 12.52 | | 3.993 | 267 | |
| | .50 | 12.51 | | 3.984 | 247 | |
| | .60 | 12.51 | | 3.976 | 203 | |
| | .80 | 12.49 | | 3.955 | 171 | |

* $x$ = mole fraction of first constituent; $(1-x)$ = mole fraction of second constituent.

## 1.3 Synthesis and properties of tungsten bronze niobate materials

### 1.3.1 Synthesis of tungsten bronze niobate materials

*(1) Single Crystals*

Ferroelectric tungsten bronze niobate single crystals mainly have been grown by the Chochralski method as shown in Fig.1-3-1. Many investigations of the synthesis of tungsten bronze niobate crystals have been performed on the properties of grown crystals.[18-30] However, the basic obstacle to the practical application of this excellent material is the difficulty in growing large single crystals with a good optical homogeneity. The reproducibility in growing transparent ferroelectric tungsten bronze single crystals has been known to be poor.

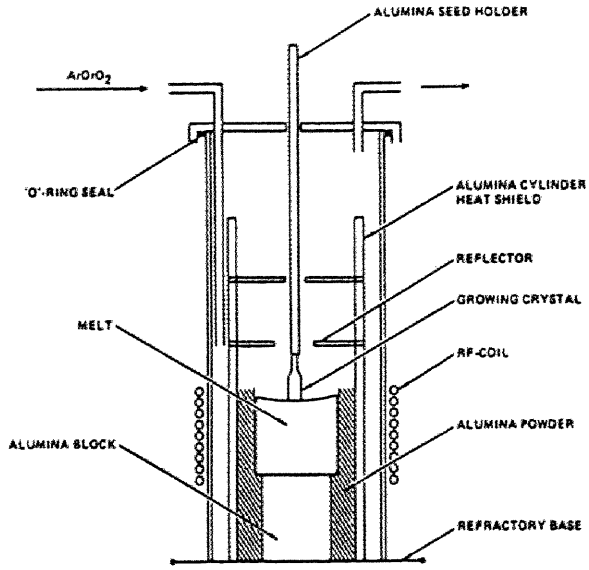


Fig.1-3-1 Schematic diagram of Czochralski single crystal growth apparatus

The main problems associated with the Czochralski growth of single crystals can be summarized as the instability of diameter and unavoidable optical inhomogeneity. The occurrence of "striation" which accounts for the inhomogeneity along the growth axis and "core" which causes the inhomogeneity along the direction normal to the growth axis, are included in the latter problem. Striation is the typical optical defect common to solid solution crystals and is quite difficult to suppress, especially in the case of strontium barium niobate. One of the significant countermeasures to this problem is to grow crystals at the composition as close to a congruent melt as possible. The determination of congruent melt composition is difficult in the fabrication of multicomponent ferroelectric niobate crystals. Furthermore, there are several problems for the fabrication of single crystals, for example, the difficulty in precise control of

composition, cracking problem caused by phase transition during cooling process, etc.

*(2) Polycrystals*

Polycrystal samples of tungsten bronze niobate material have been prepared by the conventional solid state reaction of oxide powders with a milling technique. However, the preparation of densified sample is quite difficult without hot-pressing, because its grain growth is likely to be anisotropic. Several reports of the preparation of tungsten bronze niobate polycrystals with high density, oriented grains and high transparency have been so far published.[25,26,31-41] They concern mainly with the effect of hot-pressing[31,38-41], hot isotactic pressing (HIPing)[34], sintering aids (vanadium oxide, etc.)[35] and modification of another ions for A sites (alkali or rear earth ions)[32,33,39-41].

For example, the dielectric, piezoelectric and optical properties of SBN polycrystals prepared by the hot-pressing or HIPing were examined by several researchers.[31,34] From one of these results, it is confirmed that the anisotropies of about 1.5 times were found in both the permittivity and the electromechanical coupling factor for the directions perpendicular and parallel to that of hot-pressing.[31] The anisotropy of properties is due to the grain orientation of sintered samples. From this results, grain oriented samples with high density are found to be important to reach the better properties of tungsten bronze niobate even if it is polycrystalline. Similarly, the properties of other tungsten bronze niobates (SKN[37] and PBN[39-41]) with oriented grains are investigated. The effect of various dopants on several properties of tungsten bronze niobate as well as the densification and microstructure control of polycrystalline ceramics are also studied.

### 1.3.2 Properties of tungsten bronze niobate single crystals and polycrystals

Tungsten bronze niobate crystals, such as SBN and PBN, are known to exhibit excellent ferroelectric and optical properties. Fig.1-3-2 shows the classification of various types of tungsten bronze crystals based on their crystal structure and ferroelectric and optical properties.[42] Several tungsten bronzes, such

as SBN, BSKNN ($(K_xNa_{1-x})_{0.4}(Sr_yBa_{1-y})_{0.8}Nb_2O_6$), KLN, SKN, morphotropic PBN, SNN ($Sr_2NaNb_5O_{15}$), have potential utility in several optical applications, although the growth of high-quality crystal has proven to be difficult as described in the previous section. This section focuses on several properties of ferroelectric tungsten bronze niobate materials.

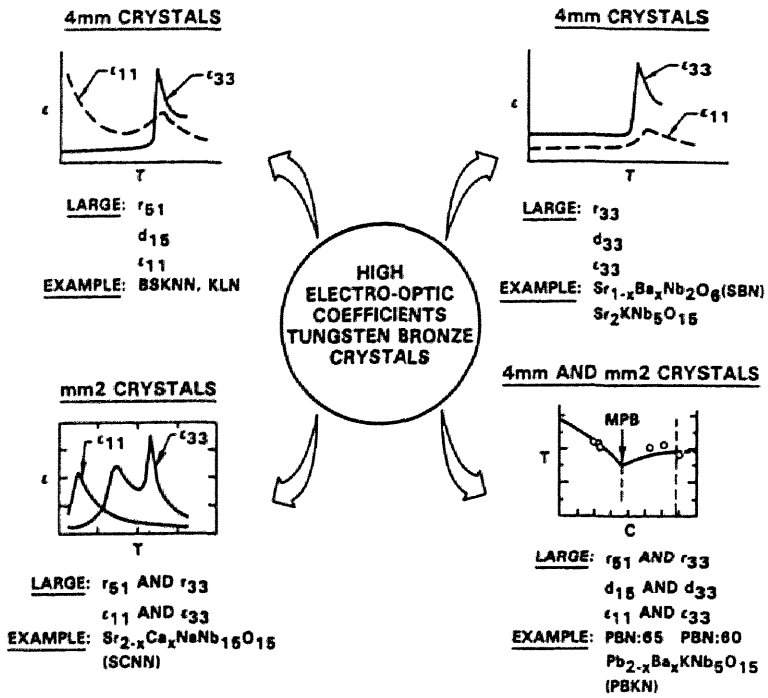


Fig.1-3-2 Classification of tungsten bronze ferroelectric crystals

### *(1)Dielectric properties*[6,9,34,42-52]

#### *(a) Characteristic behavior of tungsten bronze niobates as a relaxor ferroelectrics*

In oxygen-octahedron type ferroelectric compositions which exhibit diffuse phase transitions and weak field dielectric permittivity with strong low frequency ($10^5$ Hz) dispersion, it has become evident that the polarization mechanisms operating in the vicinity of the dielectric maximum are qualitatively different from the expected "soft mode" behavior of normal displacive ferroelectrics. It had been noticed that all relaxors had the possibility of more than one type of ions at identical crystallographic positions. Therefore, a model of composition

fluctuations was proposed for explaining the ferroelectric relaxor behavior by a random distribution of ions occupying the same lattice site. This compositional fluctuation model has been further described by an energy model which relates the ferroelectric stability to the scale of polar regions by energy argument. Though the cation ordering being responsible for the phase transition behavior of relaxor is well accepted, it would be ambiguous if the changes in the cation ordering were accompanied by a change in the chemical composition, since this by itself may affect the phase transition behavior.

There have been several studies reported about quenching/annealing related to the ordering changes in relaxor materials. Compositional fluctuation plays a key role in the perovskite relaxor of $Pb(Sc_{1/2}Ta_{1/2})O_3$, which has been demonstrated by Setter and Cross using the B site (Sc:Ta) ordering control.[44] It was shown that the fully ordered material gave a sharp first order phase transition while the disordered one gave a classic relaxor behavior. A decrease in $T_c$ of about 10°C was observed for disordered material by quenching.

As regards the tungsten bronze niobate, the ferroelectric $Sr_{1-x}Ba_xNb_2O_6$ (SBN) has been chosen as a representative because it is probably one of the most extensively studied solid solution systems of tungsten bronze relaxor. The tetragonal tungsten bronze prototype structure is projected onto the (001) plane as shown in Figure 1-1-1. The chemical formula of tungsten bronze SBN can be represented by $(A1)_2^{XII}(A2)_4^{XV}(C)_4^{IX}(B1)_2^{VI}(B2)_8^{VI}O_{30}^{VI}$ in which A1, A2 and C are the 12-, 15- and 9-fold coordinated sites in the crystal structure. B is 6-fold coordinated site surrounded by an oxygen octahedron. For SBN composition, the C site is always vacant. $Sr^{2+}$ and $Ba^{2+}$ are distributed in A1 and A2 sites with one-sixth of the A sites being vacant. Dielectric properties of SBN with different Sr/Ba ratios have been investigated by Glass.[56] When the Sr/Ba ratio is 34/66, the structure entropy is expected to be the lowest while only Sr cations occupy the A1 site and only Ba cations occupy the A2 site. The phase transition becomes more diffuse when the Sr/Ba ratio becomes larger.

It is now evident that the phase transition broadening is a very general

phenomenon in solid solutions and other disordered structures. The frequency-dependent maximum of dielectric constant generally neither coincides with the peak of dielectric loss, nor with the peak of pyroelectric coefficient. When the ferroelectric–paraelectric transition is gradual, and diffused over a temperature range, it is usually referred to the Curie range. Within this range the ferroelectric exhibits unusual properties. The spontaneous polarization and other properties, such as the specific heat, the optical absorption edge, the refractive index and the electrooptic properties, vary gradually throughout the Curie range. The behavior may be due to several reasons, compositional fluctuations, thermal fluctuation in the Curie region, structural defects, etc. In the case of single crystals of strontium barium niobate (SBN), the effect is very pronounced and strongly depends on the Sr/Ba ratio as described above.

The dielectric constants of the (001) direction as functions of temperature and measurement frequency are shown in Fig.1-3-3 for $Sr_{0.5}Ba_{0.5}Nb_2O_6$ (SBN50/50), $Sr_{0.6}Ba_{0.4}Nb_2O_6$ (SBN60/40) and $Sr_{0.75}Ba_{0.25}Nb_2O_6$ (SBN75/25), respectively. With increasing Sr content, the value of dielectric constant is suppressed, the peak broaden (with enhanced dispersion), and the temperature of the maximum decreased. The stronger relaxor characteristics with increasing Sr content, undoubtedly, reflects enhanced disorder.

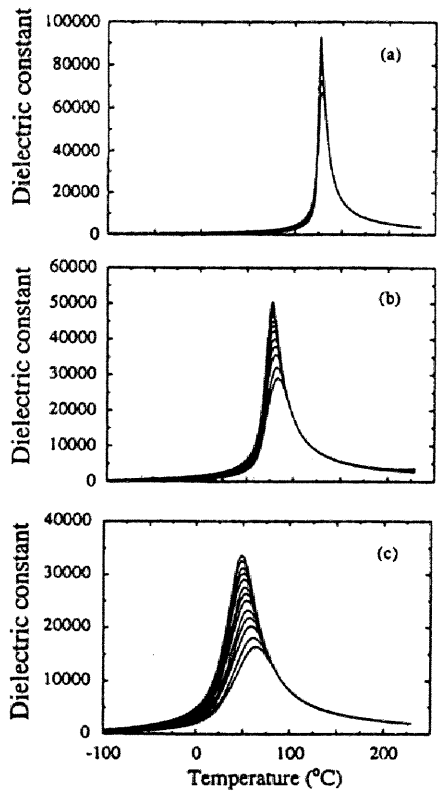


Fig.1-3-3 Dielectric constant as a function of temperature for various SBN compositions at various frequencies. (a) 50/50, (b) 60/40 and (c) 75/25.

The top curve is the lowest frequency and the bottom the highest.

The disorder in the SBN family of relaxors may be related to the random distributions of A1 and A2 sites cations in its structure. The existence of needlelike nanopolar domains which are characteristic for SBN relaxor ferroelectrics were also confirmed by TEM observation.[46,47]

The orientational dependence of dielectric constant as a function of temperature is shown in Fig.1-3-4 for (001)- and (100)-aligned SBN75/25 crystals, respectively. A strong orientational dependence can clearly be observed. The maximum dielectric constant along the (001) was ~100 times that along the (100). In addition, no relaxational behavior was observed in the (100) response and no remanence could be sustained. In contrast, the orientational dependences of the dielectric response for the well-known relaxor dielectrics of PMN are shown in Fig.1-3-5 for (100) and (111) crystals, respectively. The dielectric responses are nearly independent of crystallographic orientation. In addition, an equivalent remnant polarization is observed for either orientation. These results clearly illustrate that the relaxor behavior of SBN is strongly anisotropic, which is distinctly different from the near-isotropic behavior of the PMN type.[46,47]

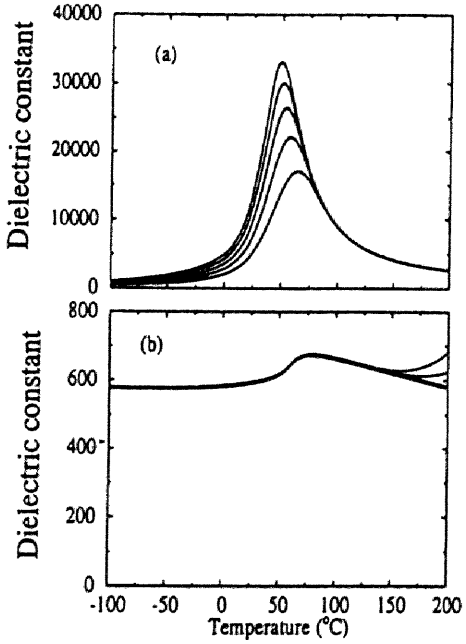


Fig.1-3-4 Dielectric constant for SBN75/25 as a function of temperature for various crystallographic orientations. (a) (001) and (b) (100).

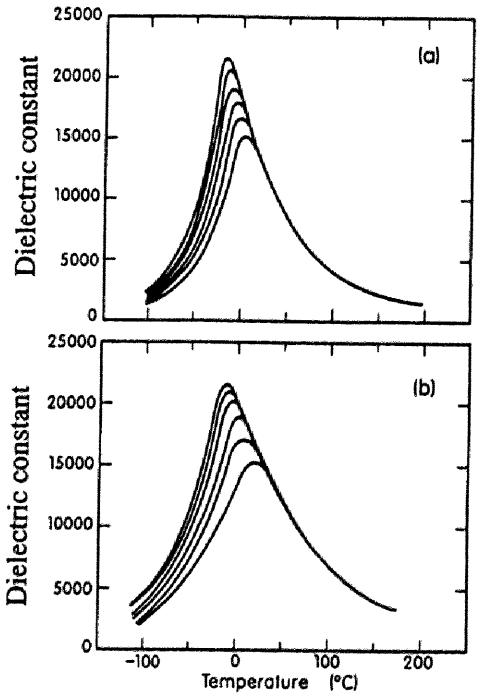


Fig.1-3-5 Dielectric constant of PMN as a function of temperature and frequency for various orientations: (a) (100) and (b) (111).

Huang et al. studied the effect of cation ordering on the phase transition behavior in tungsten bronze ferroelectric relaxor material by the thermal quenching and annealing to change the cation distribution without changing the chemical compositions (Fig.1-3-6). It was assumed that there was some disorder in the cation distribution which can be quenched in at a lower temperature.[43,48] Quenching was found to decrease the degree of relaxor characteristics. TEM observation revealed a decrease in the size of nanoelastic domains and an increase in the size of nanopolar domains.[48]

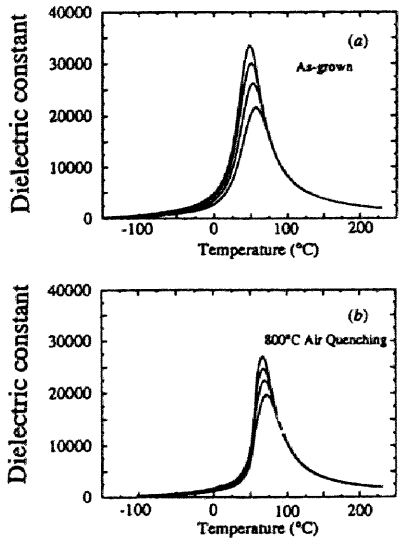


Fig.1-3-6 Dielectric susceptibility as a function of temperature and frequency for SBN75/25 at several thermal histories.
(a) As-grown and (b) 800°C air quenched.
The measurement frequencies used were $10^2$, $10^3$, $10^4$ and $10^5$ Hz (from top to bottom in the figure).

Similar to this investigation, the dielectric properties of ordered and disordered PBN ceramics with various compositions, which prepared by controlling the cooling process were reported by Xiao et al.[51,52]

*(b) Morphotropic phase boundary system*

The search for increased electrooptic, pyroelectric and piezoelectric effects in the tungsten bronze ferroelectric niobate family has stimulated interest in a number of potential morphotropic phase boundary (MPB) systems. On a binary phase diagram, an MPB appears as a nearly vertical line separating two distinct ferroelectric phases. This phase boundary generally occurs at a nearly constant composition over a wide temperature range of $T_c$. An example is shown in Fig.1-3-7 for the bronze MPB system, $Pb_{1-x}Ba_xNb_2O_6$ (PBN), which possesses both orthorhombic and tetragonal structures near x=0.37. The MPB system is also

well-known for the perovskite $Pb(Zr_{1-x}Ti_x)O_3$ solid solution [x=0.47]. Poled ceramics or single crystals of such MPB ferroelectrics can show an enhancement of numerous physical properties. For example, piezoelectric coefficients at room temperature are shown in Fig.1-3-8. The MPB behavior was also described by Jaffe et al.[1] The lead barium niobate (PBN) solid solution is arguably the most studied and developed MPB system in the tungsten bronze family. In addition to sintered ceramics, PBN has also been developed in the form of hot-pressed, grain oriented ceramics and as bulk single crystals using the Czochralski growth method. The latter has been especially useful for determining the directionally dependent ferroelectric properties in this system, revealing the unusual behavior which can occur at compositions near the morphtropic boundary. Another systems such as PKN ($Pb_2KNb_5O_{15}$)-SNN, BNN-SNN, BNN-SKN are also investigated about the MPB behavior.[6]

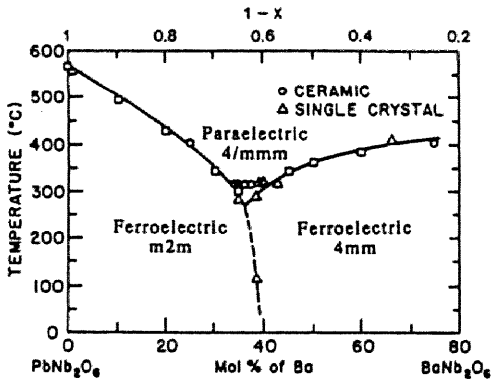


Fig.1-3-7 Phase diagram of the tungsten bronze solid solution $Pb_{1-x}Ba_xNb_2O_6$ over the range $0.2 \leqq 1\text{-}x \leqq 1.0$

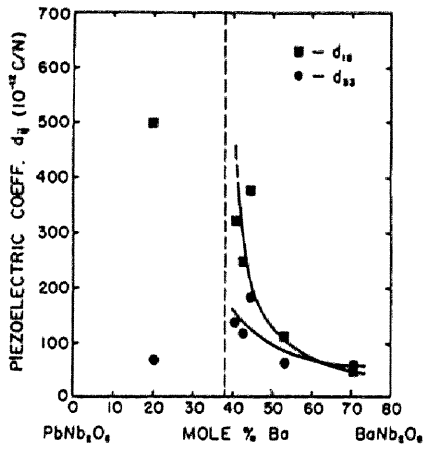


Fig.1-3-8 Piezoelectric coefficients (R.T.) as a function of the various $Pb_{1-x}Ba_xNb_2O_6$ compositions

### *(2) Piezoelectric properties*[20,55]

All materials undergo a small change in dimensions when subjected to an electric field. If the resultant strain is proportional to the square of the field, it is known as the electrostrictive effect. Some materials show the reverse phenomenon to the applied stress. The phenomenon is called the piezoelectric effect. Piezoelectric crystals are electrically polarized or undergo a change in polarization

when subjected to a stress. The application of a compressive stress in a direction results in a tensile stress for the opposite direction. Conversely, the application of an electric field will stretch or compress the crystal depending on the orientation of the applied field to the polarization in the crystal.

Among the electronic devices using piezoelectricity of tungsten bronze niobates, surface acoustic wave (SAW) devices have been receiving great attention. Until today, SAW devices are almost exclusively fabricated using $LiNbO_3$, $LiTaO_3$, or α-quartz ($SiO_2$), and it has become increasingly clear that these materials have serious disadvantages for many applications. For example, the relatively poor SAW electromechanical coupling constant ($k^2$) of α-quartz ($10\times10^{-4}$) and $LiTaO_3$ ($60\times10^{-4}$) render these materials unacceptable for devices that require large bandwidth. While the poor temperature coefficient of SAW velocity of $LiNbO_3$ (90 ppm/°C) renders this material unsuitable where the frequency stability is important. A large amount of work has gone into improving existing materials such as $LiNbO_3$ and into investigating new piezoelectric materials in an effort to find one which either combines high coupling with sufficiently low temperature coefficient of SAW velocity or shows significantly higher SAW velocity than existing materials. The research work on the tungsten bronze family compositions such as $Pb_2KNb_5O_{15}$, $Ba_2NaNb_5O_{15}$ and $Sr_{1-x}Ba_xNb_2O_6$ is found to be promising and opens new prospects for developing piezoelectric materials for SAW applications.

The design of temperature-stable SAW devices having low insertion loss and broad bandwidth will require piezoelectric substrate materials which are temperature-compensated and have larger piezoelectric coupling constants than that of ST-cut quartz or Y-Z cut $LiNbO_3$. The orthorhombic tungsten bronze $Pb_2KNb_5O_{15}$ (PKN) crystal appears to be the most interesting candidate, since it exhibits excellent piezoelectric characteristics and shows an anomalous elastic constant temperature coefficient which leads to the existence of zero-temperature-coefficient-direction (ZTCD) cuts for SAW device application. Unfortunately, this material did not find commercial application due to extreme difficulty in obtaining suitable size single crystals. Nevertheless, the materials is

attractive and the tungsten bronze family in general provides one of the more promising groups for locating high coupling, temperature-compensated SAW materials.

Table 1-3-1 Important piezoelectric tungsten bronze compositions for Surface Acoustic Wave (SAW) Applications

| PROPERTY | $Pb_2KNb_5O_{15}$ (PKN) | $Ba_2NaNb_5O_{15}$ (BNN) | $Sr_{.6}Ba_{.4}Nb_2O_6$ (SBN) | $K_3Li_2Nb_5O_{15}$ (KLN) | $Sr_2KNb_5O_{15}$ (SKN) |
|---|---|---|---|---|---|
| Electromechanical Coupling Constant $k_{33}$<br>$k_{15}$<br>$k_{24}$ | ----<br>0.69<br>0.73 | 0.45<br>0.12<br>0.25 | 0.45<br>0.24<br>---- | 0.52<br>0.34<br>---- | 0.54<br>0.30<br>---- |
| Piezoelectric Constant ($10^{-12}$C/N) | $d_{33}$ = 62<br>$d_{15}$ = 470<br>$d_{24}$ = 470 | $d_{15}$ = 32<br>$d_{24}$ = 45 | $d_{33}$ = 130<br>$d_{15}$ = 31 | $d_{33}$ = 57<br>$d_{15}$ = 68 | |
| SAW-Electromechanical Coupling Constant ($K^2$) | 188 x $10^{-4}$ | ---- | 180 x $10^{-4}$ | ---- | ---- |
| Temperature Coefficient of SAW Velocity | Y-cut,+24 ppm<br>Z-cut,-30 ppm | Close to $\alpha$-quartz | Z-cut,-50 ppm<br>(110),-18 ppm | ---- | ---- |
| Curie Temperature (°C) | 460 | 560 | 72 | 405 | 156 |
| Crystal Symmetry | Ortho T.B.* | Ortho T.B. | Tetra T.B. | Tetra T.B. | Tetra T.B. |

*T. B. = Tungsten Bronze Structure

The tungsten bronze family embraces some 100 or more known compounds and several solid solutions; hence, the possibility of developing a suitable candidate within this family is encouraging. Table 1-3-1 summarizes the piezoelectric characteristics for several orthorhombic and tetragonal tungsten bronze composition crystals. Based on this information, it is possible to trade-off some of the properties for crystals which can easily be grown and modified according to device requirements. In the case of tetragonal tungsten bronze solid solution $Sr_{1-x}Ba_xNb_2O_6$, $[0.25 \leqq x \leqq 0.75]$, its piezoelectric properties and Curie temperature can be changed in the desired range. Although the values of $k_{15}$ (coupling constant) and $d_{15}$ (piezoelectric coefficient) for SBN are smaller to those attainable in the best bronze composition (PKN), SBN provides a model system for studying the composition dependence of key quantities. It is interesting to note that SBN solid solution crystals, specifically $Sr_{0.75}Ba_{0.25}Nb_2O_6$, exhibit the highest electrooptic and piezoelectric coefficients of any well behaved ferroelectric

materials. The SBN solid solution crystals possess temperature-compensated orientations, and high SAW electromechanical coupling has been reported for the (001)–plate propagating along the (100) direction; its value is measured to be 180 $\times 10^{-4}$. This value is similar to the coupling found in other important orthorhombic tungsten bronze crystals such as PKN indicating that crystals in this family are potentially important for future SAW device applications.[55]

*(3) Pyroelectric properties*[28,54,56-59]

Pyroelectricity is the phenomena that materials generate electrical charge by the change in polarization according with the change of temperature. Pyroelectric material can be applied as an infrared sensor, because the surface charge is induced by temperature change caused by the quite small amount of irradiated infrared beam, which can be detected. Pyroelectric coefficient ($\gamma$) is the very important parameter. True pyroelectricity results from the temperature dependence of the spontaneous polarization $P_s$ of polar materials and is therefore exhibited by ferroelectric materials whether they are single domain single crystals or poled ceramics. Because a change in polarization in a solid is accompanied by a change in surface charges, it can be detected by an induced current in an external circuit.

Among the tungsten bronze niobates, ferroelectric $Sr_{1-x}Ba_xNb_2O_6$ (SBN) was found to be successfully used at room temperature as a pyroelectric detector of both infrared radiation and ultraviolet (even vacuum ultraviolet) radiation with nanosecond response time. The improvement of this detector over other pyroelectric detectors is mainly due to the very large pyroelectric coefficients of SBN and to the apparent absence of any oscillatory piezoelectric signal due to mechanical oscillations of the ferroelectric block, at high frequencies. A detector with SBN shows a faster response than any other room temperature operating thermal detector. The response can be made flat over a wide spectral range, and detectors can be used without any window materials. Thus in situation where detector sensitivity is less important than high frequency response, room temperature operation, or broad special response, SBN is a very useful material for the application in a pyroelectric detector. And further, the effect of the doping of

rare earth ions on the pyroelectric properties of SBN was investigated by S.T.Liu et al.[57] On the other hand, lead based tungsten bronze niobate, PBN solid solution also has large pyroelectric coefficients. R.Guo et al. studied the pyroelectric properties of $PbNb_2O_6$-$BaNb_2O_6$ system near the MPB composition as shown in Table 1-3-2.[59]

Table 1-3-2 Pyroelectric coefficients of PBN compositions measured using Byer-Roundy method

| $Pb_{1-x}Ba_xNb_2O_6$ Composition 1-x | Symmetry | Pyro. Coefficient (at 20°C) ($\mu C/m^2$-K) | Pyro. Coefficient MaximumValue Obtained ($\mu C/m^2$-K) |
|---|---|---|---|
| 0.34 | Tetragonal | $p_3$=82 | $p_3$=224 at 213°C |
| 0.57 | Tetragonal | $p_3$=134 | $p_3$=1250 at 240°C |
| 0.615 | Orthorhombic/Tetragonal | $p_2$=196<br>$p_3$=142 | $p_2$=5432 at 149.8°C<br>$p_3$=4468 at 240°C |
| 0.684 | orthorhombic | $p_2$=336 | $p_2$=3004 at 218.4°C |
| *$Pb_{0.86}Ba_{0.19}Nb_{1.98}O_6$ | Orthorhombic | 210 | |

***(4) Electro-optic properties***[5,23,34,60-68]

Optoelectronics is the area that optics and electronics were united into one. Technology using light as an energy source immediately developed for the area of multi optical communication with laser beam, management of information, display, instrumental measurement, processing, medical, illuminations and so on. The system constructed by optoelectronics is applied in several devices such as illumination device, optical fibers, modulators, optical shutters and optical waveguides.

Electro optic effect is the phenomenon of the change of refractive indices generated by the applied voltage. Linear electrooptic (Pockels) effect is that the values of refractive indices are in proportion linearly with applied voltage and quadratic electrooptic (Kerr) effect is that the values of refractive indices are in proportion in squarely with applied voltage, respectively.

Crystals that are noncentrosymmetric, i.e., that lack a center of symmetry, may exhibit both linear and quadratic electrooptic and elastooptic effects. In all the crystals discussed in this chapter, the linear effects are dominant. Thus, a linear change in optical index of refraction can be induced by an electric field (electrooptic effect), or by strain (elastooptic effect), or under illumination by a laser (photorefractive effect). Strain can be induced by an electric (or piezoelectric) field by a stress (elasticity).

Several experimental results were reported concerning the light beam deflection using the electrooptic effect in a single crystal prism of ferroelectrics such as $KTa_xNb_{1-x}O_3$ and $BaTiO_3$. The main objective of those experiments seems to determine the linear or quadratic electrooptic coefficients of the materials. It is very interesting also from the practical viewpoint of light beam deflector that, in those experiments, a large angle of deflection of order of 1 mrad. could be obtained with a simple isosceles prism. It was reported that ferroelectric tungsten bronze SBN has a transverse linear electrooptic coefficient an order or two orders of magnitude larger than that any other well-behaved crystals. Electrooptic figure of merit for several ferroelectric crystals is summarized in Table 1-3-3.

Table 1-3-3 Electro-optic figure of merit for leading ferroelectric crystals

| Crystal | Dielectric Constant | | Electro-Optic Coefficient $10^{-12}$ m/V | | | |
|---|---|---|---|---|---|---|
| | $\varepsilon_{11}$ | $\varepsilon_{33}$ | $r_{33}$ | $r_{51}$ | $r_{13}/\varepsilon$ | $n^3 r_{13}/\varepsilon$ |
| $Sr_{0.75}Ba_{0.25}Nb_2O_6$ (SBN:75) | 500 | 3000 | 1400 | 42 | 0.467 | 5.60 |
| $Sr_{0.6}Ba_{0.4}Nb_2O_6$ (SBN:60) | 450 | 900 | 420 | 42 | 0.522 | 6.26 |
| $Sr_{2-x}Ca_xNaNb_5O_{15}$ (SCNN) | 1700 | 1700 | ≥ 1800 | - | 0.470 | 5.65 |
| $Pb_{0.6}Ba_{0.4}Nb_2O_6$ (PBN:60) | 1900 | 500 | - | ≥ 1600 | 0.840 | 10.10 |
| BSKNN-1 | 360 | 120 | 150 | ≥ 200 | 0.550 | 6.67 |
| BSKNN-2 | 700 | 170 | 170 | 350 | 0.500 | 6.00 |
| BSKNN-3 | 780 | 270 | - 270 | - 400 | 0.510 | 6.15 |
| $BaTiO_3$ | 4100 | 1500 | 80 | 1600 | 0.390 | 4.01 |
| $KNbO_3$ | 950 | 201 | 67 | 380 | 0.4 | 4.20 |

One can, therefore, expect to build an SBN light beam deflector which has a simpler prism configuration and lower operating voltage than conventional $KD_2PO_4$ iterated-prism deflectors. Also, $Sr_{1-x}Ba_xNb_2O_6$ series of niobate solid solution crystals can be used to make modulators, frequency multipliers, and other electro-optical devices. Furthermore, R.Guo et al. investigated the electrical and optical properties of PBN system.[67,68] Figure 1-3-9 shows several properties of tetragonal PBN as a function of composition. From Fig.1-3-9(c), it turns out that the quite large electrooptic coefficient was considered to be achieved by controlling the composition near the MPB.

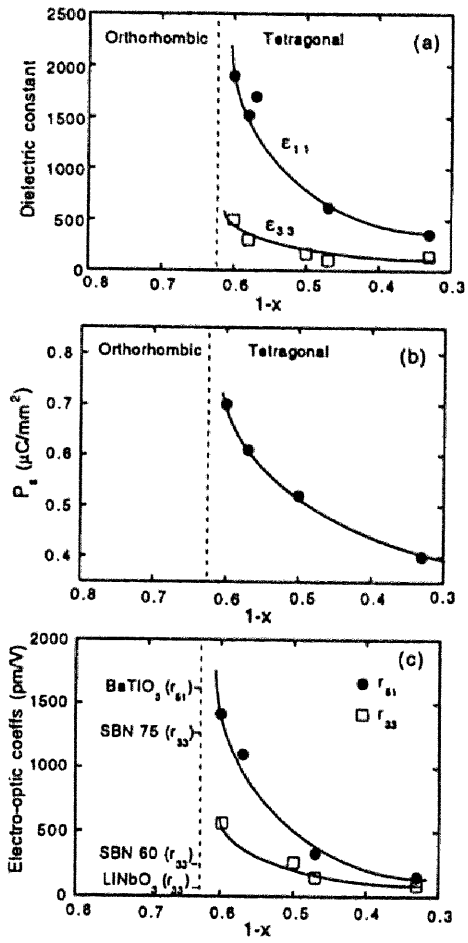


Fig.1-3-9 (a) Dielectric constants, (b) spontaneous polarization, and (c) estimated electro-optic coefficients of tetragonal PBN as a function of composition

Regarding with these materials, the electrooptic coefficient is one of the most important parameters for device applications. Although there has been remarkable recent progress in growing single crystals of high quality, there are still some restrictions in their application because of their size, complex shape, and stress resistance. Next section describes further the special optical properties of tungsten bronze niobate crystals.

*(a) Photorefractive Effect*[5,62-68]

Photorefractive effect is the local changes in refractive index produced by illumination. The issues connected with photorefractive effect include the sensitivity of the material to illumination and the speed which the index can be made to change. In spontaneously polarized ferroelectric crystals, light-induced free carriers exited in an illuminated region of the crystal are displaced along the polar axis to be retrapped. The resulting space charge generates an electric field, which gives rise to a refractive index change through the linear electrooptic effect.

Since ferroelectric tungsten bronze crystals have a large linear electro-optic coefficient ($r_{33}$), they have been receiving a great attention as a excellent photorefractive material according with $BaTiO_3$. Recent years, great deals of effort were paid for the investigation of the application using the photorefractive properties of ferroelectric tungsten bronze such as SBN and $(K_xNa_{1-x})_{0.4}(Sr_yBa_{1-y})_{0.8}Nb_2O_6$ (BSKNN). Photorefractive properties of tungsten bronze niobate, such as sensitivity and response time, etc. were found to be improved by the Ce ion doping as shown in Table 1-3-4. Megumi et al. reported that the addition of Ce produces a broad absorption in SBN60 crystals, which increases the sensitivity considerably.[66] Undoped SBN60 is transparent in the visible range, with its fundamental absorption edge at about 0.37 μm. The addition of Ce develops a distinct but wide absorption band around 0.50 μm, which differs markedly from the electronic absorption edge. The Ce ion photoionizes by means of the reaction

$Ce^{3+} + h\nu \rightarrow Ce^{4+} + e^-$ (reduction).

Both the $Ce^{3+}$ and the $Ce^{4+}$ valence states appear to be present, since the sensitivity improves from $10^{-5}$ to $10^{-3}$ $cm^2/J$. This improvements is 2 orders of magnitude higher than to $Fe^{3+}$, $U^{6+}$ and $Rh^{3+}$-doped $LiNbO_3$.[5]

The applications of electrooptic materials in such items as optical integrated circuits, optical resonators, and power and image transmitters have been extensively studied and have recently attracted much attention. In particular, the potential applications of real-time holography, optical data storage and optical

phase conjugators for adaptive optics are important for high-power laser or microwave systems. Optical phase conjugation has been demonstrated using low- to average -power lasers and ferroelectric single crystals such as barium titanate ($BaTiO_3$) and strontium barium niobate (SBN).

Table 1-3-4 Goals for photorefractive studies and current status of Ce-doped tungsten bronze crystals

| Desired Properties | Observed Properties* | | |
|---|---|---|---|
| | Ce-Doped SBN:60 | Ce-Doped SBN:75 | Ce-Doped BSKNN |
| 1) Sensitivity - $10^{-4}$-$10^{-5}$ $cm^2/J$ | - $10^{-3}$ $cm^2/J$ | - $10^{-3}$ $cm^2/J$ | - $10^{-3}$ $cm^2/J$ |
| 2) Large Coupling Coefficient ≥ 1 $cm^{-1}$ | ≥ 13 $cm^{-1}$ | ≥ 11 $cm^{-1}$ | ≥ 10 $cm^{-1}$ |
| 3) Large Size and Optical Quality | ≥ 2.5 cm dia. | - 2.0 cm dia. | - 1.5 cm dia. |
| 4) Large Electro-Optic Coefficient | $r_{33}$ = 420 - $10^{-12}$ m/V | $r_{33}$ = 1400 - $10^{-12}$ m/V | $r_{51}$ ≥ 400 - $10^{-12}$ m/V |
| 5) 2- and 4-Wave Mixing Response Time - 1 ms | ≥ 50 ms at 6 W/cm² | ≥ 120 ms at 6 W/cm² | ≥ 100 ms at 6 W/cm² |
| 6) Fast Self-Pumped Response Time | ----- | 1.6 s at 2 W/$cm^2$ | 8.8 s at 2 W/$cm^2$ |
| 7) Fast Beam Fanning Response Time | 0.05 s at 2 W/$cm^2$ | 0.25 s at 2 W/$cm^2$ | 0.6 s at 2 W/$cm^2$ |
| 8) Spectral Response (0.4 to 2.0 μm) | 0.48 to 1.0 μm | 0.48 to 1.0 μm | 0.48 to 1.0 μm |

*Photorefractive properties may improve further with optimized Ce concentration.

*(b) Second Harmonic Generation (SHG)*[29,69-72]

Recently, according to the development of laser materials and techniques, there have come to be required optical elements which suffer no optical damage even for particularly powerful laser beam and also have powers for efficient modulation and multiplication. There are tungsten bronze type oxides having oxygen octahedron structure which meet the requirements. Tungsten bronze type transparent ferroelectric oxide has excellent properties for a high electro-optical effect and high non-linear optical effect such as Second Harmonic Generation (SHG), but, in general, the reproducibility in growing crystals is poor. The detailed description of SHG is shown in Fig.1-3-10.

From many efforts, it was found that some alkali and alkaline earth metal niobates having tungsten bronze structure possess fairly good nonlinear optical properties. Among them, $Ba_2NaNb_5O_{15}$ is especially good in the application of

frequency multiplication in nonlinear optics, and has no laser damage at room temperature. The compound $Ba_2NaNb_5O_{15}$ has been the subject of much interest for second harmonic generation and parametric oscillation experiments, because BNN crystal has a large nonlinear optical coefficient compared with that of well-known $LiNbO_3$ crystal. A new very useful ferroelectric crystal BSKNN was developed in 1981, and is especially suitable to make medium power laser modulators and self-pumped phase conjugators. Potassium lithium niobate ($K_3Li_2Nb_5O_{15}$, KLN) crystals are also well known as useful materials for electrooptic and nonlinear-optic applications because of its high stability to intense laser irradiation, and large linear and nonlinear optical coefficients.

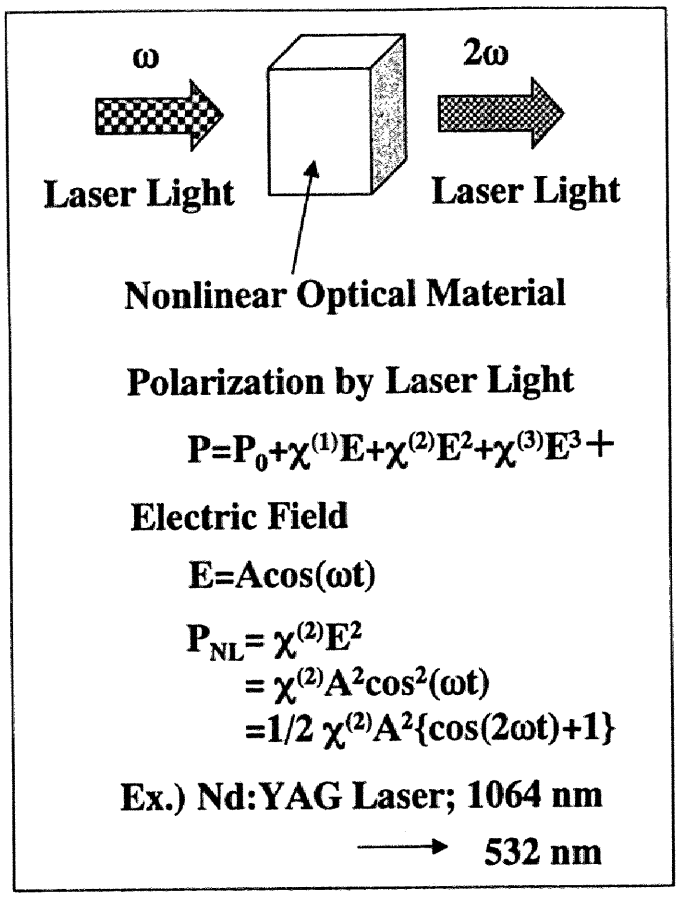


Fig.1-3-10 Description of Second Harmonic Generation (SHG)

## 1.4 Thin film processing and application[73-76]

Thin film processing is quite important for the development of device miniaturization, hybridization and lower working voltage. Several properties of functional materials are required for applications at a sub-micron level. Thin film processing techniques also have been receiving great attention for applications in semiconductor memories, opto-electronics, electronic components, optics, display devices, sensors and emerging area. The low temperature thin film processing also requires the precise control of chemical composition, the desired direction of crystal growth, and high crystallinity. In order to achieve these requirements, several fabrication methods of thin films, such as vacuum evaporation, sputtering, laser ablation, chemical vapor deposition and chemical solution deposition process, were studied. In this area, epitaxial single-crystal thin films with epitaxy are usually expected.

### 1.4.1 Ferroelectric tungsten bronze niobate thin films[76]

The tungsten-bronze materials consist more than 190 individual end member compounds and numerous possible solid solutions with simple or complex compounds. The end members offer one of the most versatile, extensive and potentially useful families of ferroelectrics based on oxygen octahedra. Among those ferroelectrics, a number of niobates having a tetragonal or orthorhombic tungsten-bronze structure such as SBN, SKN, BSKNN, PBN, PKN, BNN and KLN have attracted a great deal of attention due to their potential applications in electrooptic, nonlinear optic, photorefractive, pyroelectric and SAW devices. However, the growth of these crystals with sufficient sizes and quality is generally difficult because of complex structures and high melting points. The preparation of dense polycrystals is also very difficult because of the anisotropic grain growth as describe in 1.3.1. Thus, the investigations about tungsten bronze niobate materials were limited to the growth of single crystals from melt and to the preparation of polycrystals by solid state reaction. One approach for the solution of this serious problem is the film synthesis with highly preferred orientation (or epitaxy) on easily available non-crystalline and single crystal substrates.

Recently, with the progress of thin film technology, intensive efforts have been focused on the preparation of epitaxial thin films of perovskite PZT and La doped PZT (PLZT) on single crystal MgO, $SrTiO_3$ and sapphire for applications in pyroelectric, piezoelectric and optical devices. Although the number of reports for the preparation and characterization of tungsten bronze niobate thin films were much less than those of ferroelectric perovskite thin films, such as $PbTiO_3$, $(Pb,La)TiO_3$, PZT, $BaTiO_3$, several researches have performed recently on the film synthesis of SBN[77-94], PBN[6,76,95] and BNN[96-99] as summarized in Table 1-4-1.

Table 1-4-1 Studies for the fabrication and characterization of ferroelectric tungsten bronze niobate thin films

| Compounds | Fabrication method | Reference |
|---|---|---|
| $(Sr,Ba)Nb_2O_6$ [SBN] | Sputtering | 77 |
| | Laser ablation including PLD*1 | 78-82 |
| | MOCVD*2 | 83-86 |
| | CSD*3 including sol-gel | 87-93 |
| | Other method | 94 |
| $(Pb,Ba)Nb_2O_6$ [PBN] | Sputtering | 6,76,95 |
| $Ba_2NaNb_5O_{15}$ [BNN] | CSD, PLD, etc | 96-99 |

*1 PLD: Pulsed Laser Deposition
*2 MOCVD: Metallo-Organic Chemical Vapor Deposition
*3 CSD: Chemical Solution Deposition

### 1.4.2 Fabrication methods of ferroelectric thin films[75]

Various techniques available today for the fabrication of thin films are noticeably more varied in type and in sophistication than a couples of decades ago. Better equipment and more advanced techniques has, undoubtedly, led to higher quality films, and indeed, may be a primary factor in the now routine achievement of ferroelectricity in thin films (50 nm or greater) prepared by a selection of

different methods. The major methods presently used to produce thin films are listed in Table 1-4-2.

Table 1-4-2 Thin film deposition techniques

| | Fabrication method |
|---|---|
| **I. Vapor phase** | **Thermal evaporation**<br>**RF magnetron sputtering**<br>**Ion beam/ Ion beam assisted sputtering**<br>**Laser ablation including PLD**<br>**CVD, MOCVD** |
| **II. Liquid phase** | **CSD including sol-gel (spin, cast, dip)**<br>**Liquid phase epitaxy** |
| **III. Solid phase** | **Reduction/Reoxidation (in situ)** |

The methods utilized in successfully fabricating ferroelectric thin films can generally be classified into two categories;

(1) vapor phase depositions and

(2) liquid phase chemical processing techniques.

In both cases, the films which are usually produced are of a polycrystalline nature, however, in many instances it is desirable to produce epitaxial film growth which is more readily achieved with sputtering techniques. On the other hand, wet chemical processing (CSD including sol-gel) methods have proven to be more popular for most applications because of their lower capital equipment costs and ease of preparing the films. Chemical vapor deposition (CVD, MOCVD) techniques are now undergoing rapid development because recent results are very promising regarding high deposition rates, pinhole-free films, good step coverage and stoichiometry control. Laser ablation including PLD has also recently been reported to be a variable technique for producing excellent films.

### 1-4-3 Chemical solution deposition process[100,101]

*(1) Chemical solution process*

The chemical solution process is one of the most common processes as the fabrication method of thin film. This process is widely applied for optical, electrical, magnetical, mechanical catalysis, etc. The most important advantages of chemical solution process are high purity, good homogeneity, lower processing temperature, ease of composition control, versatile shaping and preparing by simple and cheap apparatus compared with other method. As the fabrication method of thin film, this process receives great attention because of the precise composition control for the preparation of multicomponent compounds. However, the more the number of elements, the more complicated the solution chemistry, leading to difficult problems for the desired crystalline phase. Therefore, it is required to investigate the solution of multicomponent system in detail. Also, the crystallization behavior is complicated, so the investigation of crystallization process is a key for film synthesis.

The first report of a wet chemical processing of ferroelectric thin film was the synthesis of $BaTiO_3$ film by Fukushima et al. in 1975. They used a mixed alkoxide and organic salt precursors for the fabrication of $BaTiO_3$ film. Application of sol-gel processing for the PZT thin films started in 1984 with the reports by Wu et al. and Fukushima et al. and followed by Budd et al. in 1985. Meanwhile, chemical processing of thin films of other ferroelectric oxides have made remarkable progresses. Ferroelectric thin films ranging from polycrystalline, texture-oriented polycrystalline and epitaxial in nature have been synthesized for 15 years.

Similar to other thin-film deposition techniques, chemical solution processing including sol-gel process is essentially a mass transport process. The transformation of a liquid solution to a solid crystalline film is accomplished through three steps:

1. Precursor materials are dissolved in a homogeneous solution, thus assuring molecular-level mixing of different precursor compounds.

2. Mass transport is completed upon spin or dip coating of a thin layer of the solution onto the substrate surface. A thin layer of amorphous gel film is formed on the substrate.
3. The as-deposited thin film together with the substrate is then heated to cause densification and crystallization of the film.

The chemical modification of metallo-organic compounds leads to the development of new molecular engineering. The chemical design of these new precursors allows the chemical solution synthesis of several materials in the form of fine powders, fibers, or films. Figure 1-4-1 illustrates the general flow diagram for the fabrication of thin films by the chemical solution processing through metallo-organics. The formation of the intermediate compound, e.g. complex alkoxide, is usually described as a homogeneous solution.

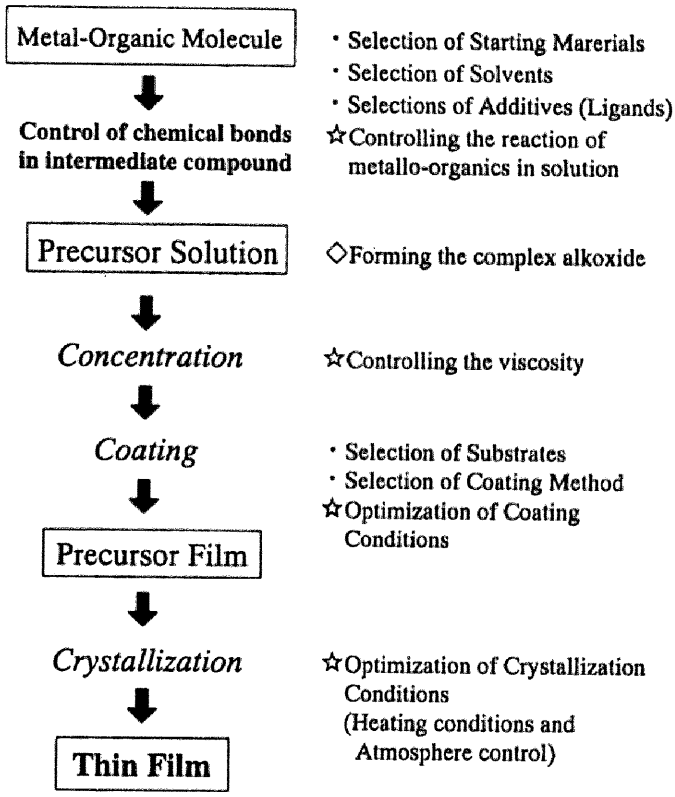


Fig.1-4-1 Process flow for the fabrication of thin films by the chemical solution deposition

### *(2) Coating techniques*

The common techniques used for applying films from the chemical solution are dipping, draining, spinning, and spraying. They have several advantages and disadvantages, taking into the consideration of fabricating devices. Dipping has been used to produce uniform coatings about 100 nm in thickness on nonporous surfaces. The coating thickness (H) is described by the equation [L.D.Landau and V.G.Levich, *Acta Phys.Chem. URSS*, **17**, 42 (1942)].

$$H=K(v\eta_{sol}/D_{sol})^{0.5}$$

where K is a constant, which depends on the angle of the surface, $\eta_{sol}$ and $D_{sol}$, are viscosity and density of the sol, and $v$ is the withdrawal velocity. Note that the coating thickness on the nonporous substrate varies directly with the pulling-up rate. Drain coating is a variation in which the substrate is fixed and the vessel containing the sol is raised and lowered. Spin coating is used to coat one side of a substrate rotated at about 3-4 Hz. The solution is also sprayed onto the surface of the rotating substrate. The thickness of film every coating always ranged 0.1-0.3 μm, because the films which have the more thickness per coating are likely to crack during drying and heating process. To increase the film thickness, the coating-heating process is repeated. In order to obtain dense and carbon-free films, the optimization of heating process such as temperature, heating rate and atmosphere is also very important.

### 1.4.4 Application of ferroelectric thin films[75]

A number of application areas for ferroelectric thin and thick films are indicated in Fig.1-4-2. These are (1) capacitors, dielectric buffer layers, (2) non-volatile memories, (3) piezoelectric resonators, actuators, ultrasonic sensors and high-frequency surface acoustic wave devices, (4) pyroelectric infrared (IR) detectors and imagers, (5) integrated optic switches, couplers and modulators, electrooptic displays and electrooptic, transverse non-waveguide mode shutters. Although specific examples of these applications can be cited as devices in development, it should be pointed out that relatively few of them have reached the market. Thin-film devices based upon a wide variety of ferroelectrics with perovskite and tungsten bronze structures have been explored. The representative applications of ferroelectric (or dielectric) thin films are as follows;

*(1) Semiconductor memories*

Ferroelectrics used in the nonvolatile and dynamic random access memory applications reveal potentially large markets. An illustration of FERAM cell cross-section, a schematic diagram of the electric circuit and a typical hysteresis loop of a ferroelectric thin film element are shown in Fig.1-4-3.

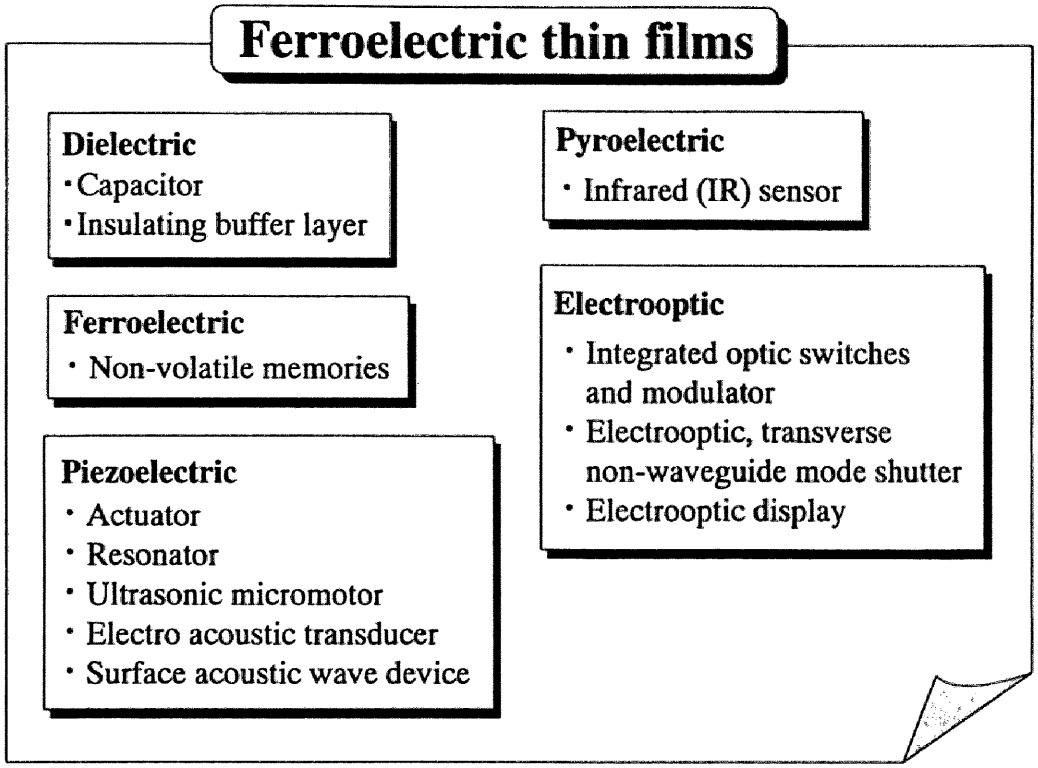


Fig.1-4-2 Application areas of ferroelectric thin films

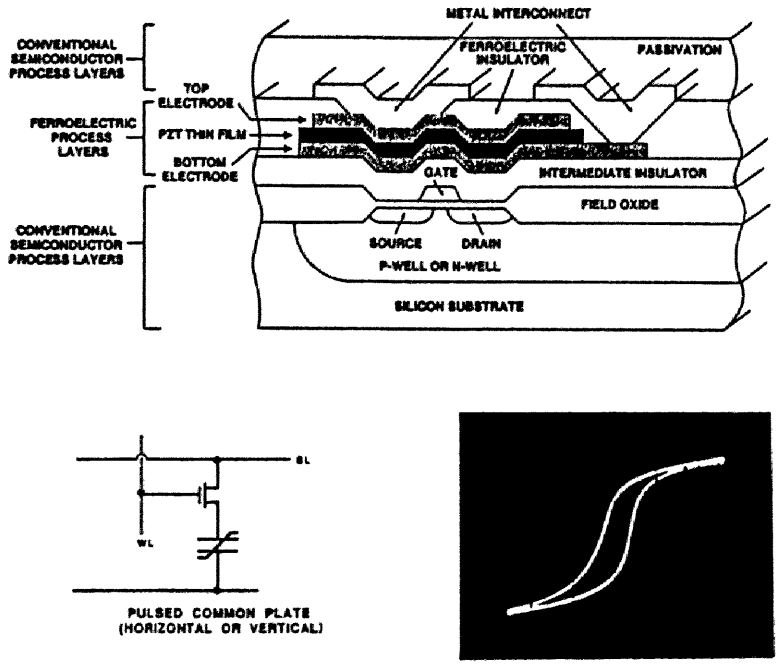


Fig.1-4-3 Cross-sectional view of Si CMOS device with superimposed ferroelectric thin film [PZT film] switching memory (top), schematic circuit of memory structure (bottom left) and typical hysteresis loop of ferroelectric thin film (bottom light).

As can be seen from the figure, the film serves as a memory switching capacitor in series with a transistor whose source is connected to the bit line, the gate to the word line and the drain to the pulsed 5 volt common. The polarization of the ferroelectric film switches to the opposite polarity when the transistor is turned on by the appropriate voltage on the gate. In order to interrogate the memory (i.e., detect the polarization state of the ferroelectrics), it is pulsed and monitored for a given current/time waveform envelope which is indicative of its polarization state. Since the polarization state is destructively read out, that state must also be read back into the cell again in order to preserve the original memory information.

An alternative memory scheme, whereby the ferroelectric film is placed in the gate area of the transistor, is also under development and has shown promising results. The memory is known as a FEMFET, which has an advantage that it does not destructively read the memory during integration, hence this type is referred to a non-destructive read out device.

In yet another memory device, a conventional DRAM, the capacitor consists of dielectric $SiO_2$ layer. The ferroelectric film can replace $SiO_2$ in DRAM, because it has a much higher dielectric constant ($\varepsilon_r$=1000) than $SiO_2$ ($\varepsilon_r$=4), leading to the much less area than $SiO_2$.

*(2) Display devices*

The dielectric thin films are used as the insulating layer of electro luminescence (EL) devices as shown in Fig.1-4-4. The requirements of insulating layer are high transparency over wide wavelength region, high dielectric breakdown voltage and high dielectric constant. The latter two requirements allow to apply a high voltage to the luminescent layer.

*(3) Electrical components*

As electrical components related with dielectric thin film, the piezoelectric effect and pyroelectric effect are mainly used for several applications such as SAW filters (Fig.1-4-5) and pyroelectric sensors[102] (Fig.1-4-6), etc. In both cases, the synthesis of highly oriented (direction of polarization) thin film is very important for the fabrication of devices. Infrared sensor also needs to reduce the

thermal capacity by the configuration of thin film and substrate in the device as shown in Fig.1-4-6.

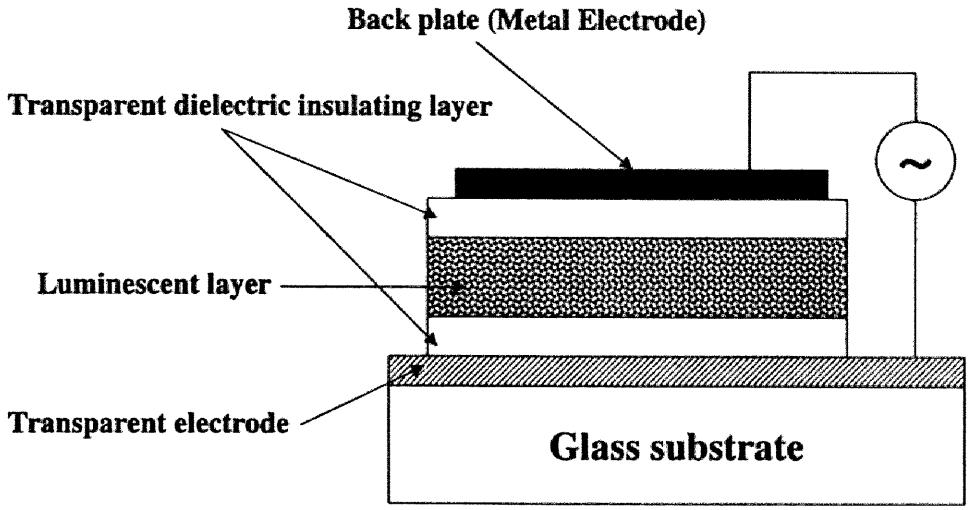


Fig.1-4-4 Schematic drawing of Electro Luminescent (EL) Device

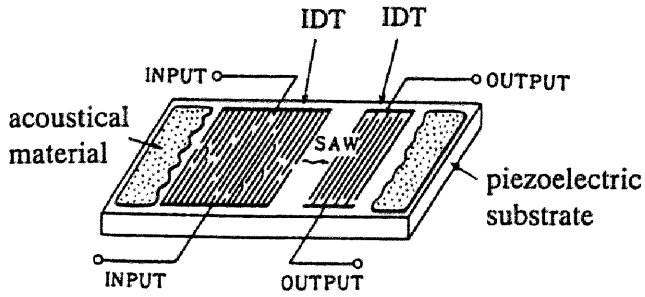


Fig.1-4-5 Schematic drawing of surface acoustic wave (SAW) filter device

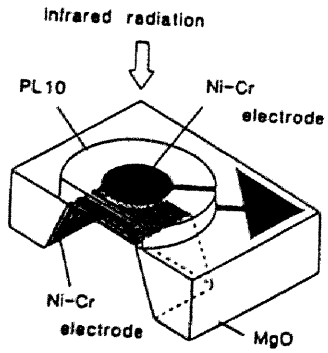


Fig.1-4-6 Schematic drawing of pyroelectric infrared sensor [Point-type].

*(4) Optolelctronics*

When ferroelectric thin films with high preferred orientation along polar axis, high transparency and high refractive index are fabricated, these films are expected to be applied in various electrooptic devices.

The modes of operation which are presently in use for electrooptic films are shown in Fig. 1-4-7. In device (A), surface electrodes provide the electrical address to the film and the optical address can be made from one of three different directions; i.e., along the ①, ② or ③ axes. When the direction along the ① axis is used in the film plane, this mode is referred to the longitudinal waveguide mode; along the ② axis, it is the transverse waveguide mode; and along ③ axis, it is the transverse non-waveguide mode. In device (B), electrodes perpendicular to the major surfaces provide the electrical address and again the optical address can be made from one of three different directions. When the optical address along the ① or ② axes is used, it is referred to a transverse waveguide mode; and along the ③ axis, it is a longitudinal non-waveguide mode. These devices obviously reveal that integrated optical waveguiding in ferroelectric films is important for future applications.

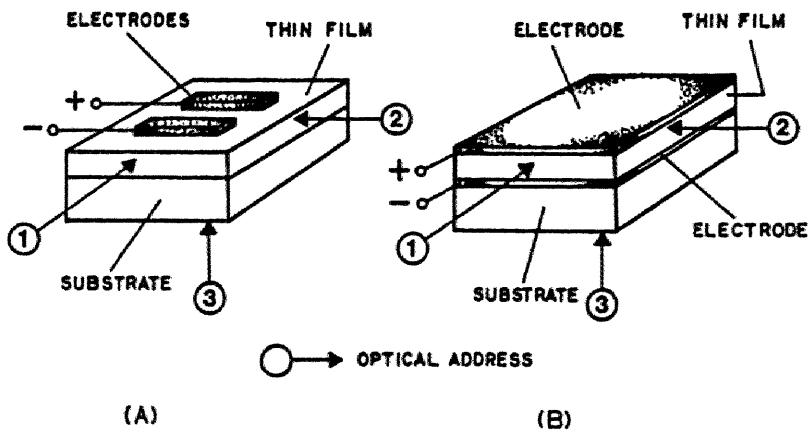


Fig.1-4-7 Modes of operation for electrooptic ferroelectric films utilizing (A) single-surface electrodes and (B) double-surface electrodes.

Various techniques, which are used to address ferroelectric thin film devices electrically and optically are shown in Fig.1-4-8. Both waveguide and non-waveguide modes are illustrated. In the non-waveguide mode, it should be remembered that quite high electric fields must be applied due to the optical retardation for effective modulation. As shown in Fig.1-4-8, the strain/optical effect is induced in the film when an electric field is applied to the device. Figure 1-4-9 illustrates the typical configuration of electrooptic switch utilizing the total internal reflection waveguide-mode of PLZT ferroelectric film. Optical waveguiding is confined to the stepped channel of 50 nm high which is ion-milled into the PLZT film.

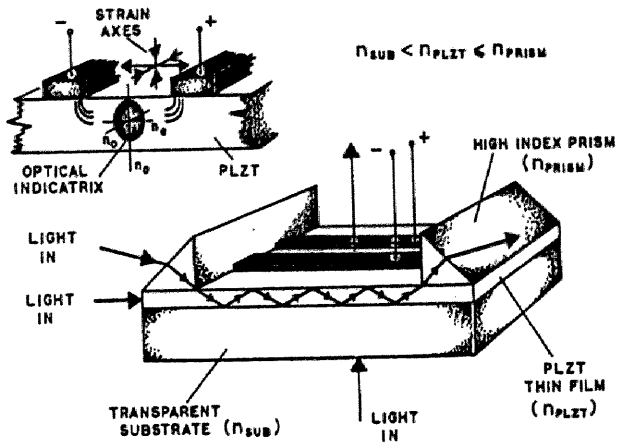


Fig.1-4-8 Waveguide and non-waveguide addressing schemes for ferroelectric thin film [PLZT* film].
*PLZT: $(Pb,La)(Zr,Ti)O_3$

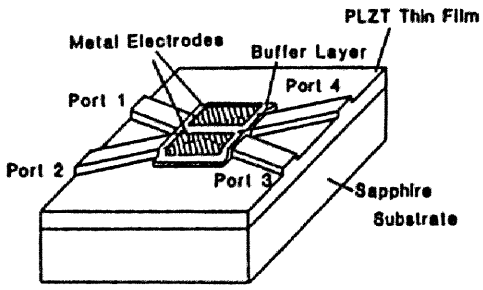


Fig.1-4-9 Configuration of total internal reflection switch using a PLZT/sapphire structure.

## 1.5 Objectives of present study

In view of the search on the tungsten bronze structure as mentioned above, ferroelectric tungsten bronze niobate thin films with preferred orientation along polar axis can be proposed for various applications. Therefore, the control of the film orientation associated with the direction of polarization is a key factor because ferroelectric tungsten bronze niobates show the anisotropy of their properties for each direction of crystals. On the other hand, the composition control is the significant factor for reaching the optimal properties of resultant films. Dielectric thin films with high transparency and high refractive index are also used for application in optical devices, including optical waveguides. If the fabrication of films at higher temperatures is carried out, the film quality might degrade due to the exaggerated grain growth and reaction between the substrates and films. The crystallization of ferroelectric tungsten bronze films at lower temperatures is indispensable for the fabrication of high-quality films. The structural stability of tungsten bronze niobate is enhanced by the introduction of alkali ion, such as $K^+$ or $Na^+$, in the 15-fold and 12-fold sites because the structure approaches the filled-tungsten bronze with increase in the amount of alkali ion. A chemical solution deposition (CSD) process is considered to be the most suitable process for the fabrication of multicomponent thin films such as ferroelectric tungsten bronze niobate.

This study has been carried out for the synthesis and characterization of ferroelectric tungsten bronze thin films by the chemical solution process using metallo-organic compounds. For the establishment of thin film processing, it is required to optimize the processing conditions, such as the structure of metallo-organic precursors, the selection of substrate, coating process, crystallization process. In these materials, several properties can be optimized by controlling the chemical composition and orientation of resultant films. Furthermore, the synthesized films are expected to show the new properties different from the conventional bulk materials.

The main objectives of this study are summarized as follows:

1. Establishment of synthesis route of tungsten bronze niobate thin films by the chemical solution deposition process.
2. Investigation of the structure of metallo-organic precursor in coating solution to control the chemical composition and homogeneity of resultant films.
3. Study of crystallization behavior of synthesized precursor powders and thin films to obtain the crystallographic phase which shows the desired properties.
4. Control of orientation with desired direction and investigation of three dimensional relation between oriented film and substrate.
5. Characterization of electrical and optical properties of fabricated films to examine the potential for applications.

## References


1. B.Jaffe, W.R.Cook Jr and H.Jaffe, "Chapter 9 Non-Perovskite oxide piezoelectrics and ferroelectrics", Chap. 9, pp. 213-235 in Piezoelectric ceramics, Academic Press, New York (1971).

2. F.Jona and G.Shirane, "CHAPTER VI MISCELLANEOUS COMPLEX OXIDES", Chap. VI, pp. 262-279 in FERROELECTRIC CRYSTALS, Dover Publications, Inc., New York (1993).

3. G.Goodman, "Ferroelectric Properties of Lead Metaniobate", *J. Am. Ceram. Soc.*, **36** [11] 368-372 (1953).

4. M.H.Francombe, "The Relation between Structure and Ferroelectricity in Lead Barium and Barium Strontium Niobates", *Acta Cryst.*, **13** 131-140 (1960).

5. R.R.Neurgaonkar and W.K.Cory, "Progress in Photorefractive Tungsten Bronze Crystals", *J. Opt. Soc. Am. B*, **3** [2] 274-282 (1986).

6. J.R.Oliver, R.R.Neurgaonkar and L.E.Cross, "Ferroelectric Properties of Tungsten Bronze Morphotropic Phase Boundary Systems", *J. Am. Ceram. Soc.*, **72** [2] 201-211 (1989).

7. P.B.Jamieson, S.C.Abrahams, and J.L.Bernstein "Ferroelectric Tungusten Bronze-Type Crystal Structures. Ⅰ. Barium Strontium Niobate $Ba_{0.27}Sr_{0.75}Nb_2O_{5.78}$", *J. Chem. Phys.*, **48** 5048-5057 (1968)

8. M.P.Trubelja, E.Ryba, D.K.Smith "A Study of positional disorder in strontium barium niobate", *J. Mater. Sci.*, **31** 1435-1443 (1996).

9. L.A.Bursill and P.J.Lin, "Chaotic states observed in strontium barium niobate", *Philosophical Magazine B*, **54** [2] 157-170 (1986).

10. T.Ikeda, K.Uno, K.Oyamada, A.Sagara, J.Kato, S.Takano, and H.Sato, "Some Solid Solution of the $A_5B_{10}O_{30}$-and $A_6B_{10}O_{30}$-Type Tungsten-Bronze Ferroelectrics", *Jap. J. App. Phys.*, **17** 341-348 (1978).

11. Y.Repelin, E.Husson et H.Brusset, "Etude par spectroscopies d'absorption i.r. et de diffusion Raman des composes $A^{II}B_2{}^{V}O_6$ de structure de type "blocs 1×2" -I. Etude du niobate de baryum $BaNb_2O_6$", *Spectrochimica Acta*, **35A** 937-948 (1979).

12. F.Galasso, L.Katz and R.Ward "Tantalum Analogs of the Tetragonal Tungsten Bronzes", *J. Am. Chem. Soc.*, **81** 5898-5899 (1959).

13. F.Galasso, G.Layden and G.Ganung "$ANb_2O_6$ AND $ATa_2O_6$ PHESES", *Mater. Res. Bull.*, **3** 397-407 (1968).

14. C.D.Whiston and A.J.Smith "Double Oxides containing Niobium or Tantalum. Ⅱ. Systems Involving Strontium or Barium", *Acta. Cryst.*, **23** 82-84 (1967).

15. K.Masuno "X-Ray and Dielectric Studies of the Systems $(Ba_{1-x}R_{2x/3})Nb_2O_6$, Where R is Y, Sm or La", *J. Phys. Soc. Jap.*, **19**, 323-328 (1964).

16. L.G.Van Uitert, H.J.Levinstein, J.J.Rubin, C.D.Capio, E.F.Dearborn and W.A.Bonner "SOME CHARACTERISTICS OF NIOBATES HAVING "FILLED" TETRAGONAL TUNGSTEN BRONZE-LIKE STRUCTURES", *Mater. Res. Bull.*, **4** 63-74 (1969).

17. E.A.Giess, B.A.Scott, G.Burns, D.F.O'kane and A.Segmuller, "Alkali Strontium-Barium-Lead Niobate Systems with a Tungsten Bronze Structure : Crystallographic Properties and Curie Points", *J. Am. Ceram. Soc.*, **52** [5] 276-281 (1969).

18. A.A.Ballman and H.Brown, "The Growth and Properties of Strontium Barium Methaniobate, $Sr_{1-x}Ba_xNb_2O_6$, a Tungsten Bronze Ferroelectric", *J. Cryst. Growth*, **1** 311-314 (1967).

19. K.Megumi, N.Nagatsuma, Y.Kashiwada, Y.Furuhata, "The Congruent Melting Composition of Strontium Barium Niobate", *J. Mater. Sci.*, **11** 1583-1592 (1976).

20. R.R.Neurgaonkar, M.H.Kalisher, T.C.Lim, E.J.Staples and K.L.Keester, "Czochralski Single Crystal Growth of $Sr_{0.61}Ba_{0.39}Nb_2O_6$ for Surface Acoustic Wave Applications", *Mater. Res. Bull.*, **15** 1235-1240 (1980).

21. R.R.Neurgaonkar, W.K.Cory and J.R.Oliver, "Growth and Applications of Ferroelectric Tungsten Bronze Family Crystals", *Ferroelectrics*, **51** 3-8 (1983).

22. R.R.Neurgaonkar, W.W.Ho, W.K.Cory and W.F.Hall, "Low and High Frequency Dielectric Properties of Ferroelectric Tungsten Bronze $Sr_2KNb_5O_{15}$ Crystals", *Ferroelectrics*, **51** 185-191 (1984).

23. R.R.Neurgaonkar, W.K.Cory and J.R.Oliver, "Growth and Optical Properties of Ferroelectric Tungsten Bronze Crystals", *Ferroelectrics*, **142** 167-188 (1993).

24. T.R.Shrout and L.E.Cross, "Ferroelectric Properties of Tungsten Bronze Lead Barium Niobate (PBN) Single Crystals", *Ferroelectrics Lett.*, **44** 325-330 (1983).

25. R.Guo, A.S.Bhalla, C.A.Randall, Z.P.Chang and L.E.Cross, "Properties of Morphotropic Phase Boundary Lead Barium Niobate (PBN) Compositions", *Ferroelectrics*, **93** 193-201 (1989).

26. R.Guo, A.S.Bhalla, C.A.Randall, Z.P.Chang and L.E.Cross, "Polarization Mechanisms of Morphotropic Phase Boundary Lead Barium Niobate (PBN) Compositions", *J. Appl. Phys.*, **67** [3] 1453-1460 (1990).

27. G.Burns, F.H.Dacol, R.Guo and A.S.Bhalla, "Ferroelectric $(Pb,Ba)Nb_2O_6$ near the Morphotropic Phase Boundary", *Appl. Phys. Lett.*, **57** [6] 543-544 (1990).

28. R.Guo, A.S.Bhalla, C.A.Randall and L.E.Cross, "Dielectric and Pyroelectric Properties of the Morphotropic Phase Boundary Lead Barium Niobate (PBN) Single Crystals at Low Temperature (10-300K)", *J. Appl. Phys.*, **67** [10] 6405-6410 (1990).

29. L.G.Van Uitert, J.J.Rubin and W.A.Bonner, "Growth of $Ba_2NaNb_5O_{15}$ Single Crystals for Optical Applications", *IEEE J. Quantum Electronics*, **4** [10] 622-667 (1968).

30. A.A.Ballman, J.R.Carruthers and H.M.O'bryan, Jr.,"Growth of Uncracked Barium-Sodium Niobate Crystals", *J. Cryst. Growth*, **6** [2] 184-186 (1970).

31, K.Nagata, Y.Yamamoto, H.Igarashi and K.Okazaki, "Properties of the Hot-Pressed Strontium Barium Niobate Ceramics", *Ferroelectrics*, **38** 853-856 (1981).

32. K.Umakantham, S.N.Murty, K.S.Rao and A.Bhanumathi, "Effect of Rare-Earth Ions on the Properties of Modified (Sr,Ba)$Nb_2O_6$ Ceramics", *J. Mater. Sci. Lett.*, **6** 565-567 (1987).

33. A.Bhanumathi, S.N.Murty, K.Umakantham, K.C.Mouli, G.Padmavathi, K.T.Rao and V.Syamalamba, "Ferroelectric Properties of Tungsten Bronze Ceramics", *Ferroelectrics*, **102** 173-181 (1990).

34. N.S.VanDamme, A.E.Sutherland, L.Jones, K.Bridger and S.R.Winzer, "Fabrication of Optically Transparent and Electrooptic Strontium Barium Niobate Ceramics", *J. Am. Ceram. Soc.*, **74** [8] 1785-1792 (1991).

35, S.Nishiwaki, J.Takahashi and K.Kodaira, "Effect of Additives on Microstructure Development and Ferroelectric Properties of $Sr_{0.3}Ba_{0.7}Nb_2O_6$ Ceramics", *Jpn. J. Appl. Phys.*, **33** [9B] 5477-5481 (1994).

36. T.Kimura, S.Miyamoto and T.Yamaguchi, "Microstructure Development and Dielectric Properties of Potassium Strontium Niobate Ceramics", *J. Am. Ceram. Soc.*, **73** [1] 127-130 (1990).

37. B.Boufrou, G.Desgardin and B.Raveau, "Tetragonal Tungsten bronze Niobate, $K_{0.2}Sr_{0.4}NbO_3$ : A New Material for Capacitors with Flat Dielectric Curves", *J. Am. Ceram. Soc.*, **74** [11] 2809-2814 (1991).

38. T.Kimura, S.Saibol and K.Nagata, "Effect of Grain Orientation on Curie Temperature of $KSr_2Nb_5O_{15}$ Solid Solutions", *J. Ceram. Soc. Japan*, **103** [2] 132-137 (1995).

39. K.Nagata, Y.Kawabata, K.Okazaki, "Anisotropies of Hot-Pressed (Pb,Ba,La)$Nb_2O_6$ Ceramics," *Jpn. J. Appl. Phys.*, **22** [9] 1353-1356 (1983).

40. M.Yasuoka and M.Marutake, "Optical and Electrical Properties of La-Modified (Pb-Ba)$Nb_2O_6$ Ferroelectric Ceramics", *Jpn. J. Appl. Phys.*, **30** [9B] 2322-2325 (1991).

41. R.R.Neurgaonkar, J.R.Oliver, J.G.Nelson and L.E.Cross, "Piezoelectric and Ferroelectric Properties of La-Modified and Unmodified Tungsten Bronze $Pb_{0.6}Ba_{0.4}Nb_2O_6$ Dense Ceramics", *Mater. Res. Bull.*, **26** 771-777 (1991).

42. R.R.Neurgaonkar, J.R.Oliver, W.K.Cory and L.E.Cross, "Ferroelectric Properties of Lanthanum-Modified $Sr_{0.6}Ba_{0.4}Nb_2O_6$ Single Crystals", *J. Cryst. Growth*, **89** 463-470 (1988).

43. R.Guo, A.S.Bhalla, G.Burns and F.H.Dacol, "Studies on Annealing and Quenching of Strontium Barium Niobate (SBN) Single Crystals: A-Site Cation Ordering-Disordering Effect", *Ferroelectrics*, **93** 397-405 (1989).

44. N.Setter, L.E.Cross, "The Role of B-site Cation Disorder in Diffuse Phase Transition Behavior of Perovskite Ferroelectrics", *J. Appl. Phys.*, **51** [8] 4356-4360 (1980).

45. R.R.Neurgaonkar, W.F.Hall, J.R.Oliver, W.W.Ho and W.K.Cory, "Tungsten Bronze $Sr_{1-x}Ba_xNb_2O_6$ : A Case History of Versatility", *Ferroelectrics*, **87** 167-179 (1988).

46. W-H.Huang, D.Viehland and R.R.Neurgaonkar, "Anisotropic GlassLike Characteristics of Strontium Barium Niobate Relaxors", *J. Appl. Phys.*, **76** [1] 490-496 (1994).

47. D.Viehland, Z.Xu and W-H.Huang, "Structure-property relationships in strontium barium niobate I. Needle-like nanopolar domains and the metastably-locked incommensurate structure", *Philosophical Magazine A*, **71** [2] 205-217 (1995).

48. W-H.Huang, Z.Xu and D.Viehland, "Structure-property relationships in strontium barium niobate II. Quenching and annealing effects", *Philosophical Magazine A*, **71** [2] 219-229 (1995).

49. B.Jimenez, C.Alemany, J.Mendiola and E.Maurer, "Phase Transitions in Ferroelectric Ceramics of the Type $Sr_{0.5}Ba_{0.5}Nb_2O_6$", *J. Phys. Chem. Solids*, **46** [12] 1383-1386 (1985).

50. R.R.Neugaonkar, J.R.Oliver, L.E.Cross, "Ferroelectric Properties of Tetragonal Tungsten Bronze Single Crystals", *Ferroelectrics*, **56** 31-36 (1984).

51. X.Xiao, Z.Zeng, Z.Gui, L.Li, X.Zhang, "The Role of $A_1$-site Vacancies in Belt Nano-domains of $Pb_{1-x}Ba_xNb_2O_6$ (PBN) Solid Solution", *J. Mater. Res.*, **11** [3] 650-656 (1996).

52. X.Xiao, Y.Xu, Z.Zeng, Z.Gui, L.Li, X.Zhang, "Effect of A-site Vacancy Order-Disorder States on Diffuse Phase Transition of the Morphotropic phase Boundary $Pb_{1-x}Ba_xNb_2O_6$ Ferroelectrics", *J. Mater. Res.*, **11** [9] 2302-2308 (1996).

53. C.A.Randall, R.Guo, A.S.Bhalla, L.E.Cross, "Microstructure-Property Relations in Tungsten Bronze Lead Barium Niobate, $Pb_{1-x}Ba_xNb_2O_6$", *J. Mater. Res.*, **6** 1720-1728 (1991).

54. R.Lane, D.L.Mack, K.R.Brown, "Dielectric, Piezoelectric and Pyroelectric Properties of the $PbNb_2O_6$-$BaNb_2O_6$ System", *Trans. J. Brit. Ceramic. Soc.*, **71** 11-22 (1972).

55. R.R.Neurgaonkar and L.E.Cross, "Piezoelectric Tungsten bronze Crystals for SAW Device Applications", *Mater. Res. Bull.*, **21** 893-899 (1986).

56. A.M.Glass, "Investigation of the Electrical Properties of $Sr_{1-x}Ba_xNb_2O_6$ with Special Reference to Pyroelectric Detection", *J. Appl. Phys.*, **40** [12] 4699-4713 (1969).

57. S.T.Liu and R.B.Maciolek, "Rare-Earth-Modified $Sr_{0.5}Ba_{0.5}Nb_2O_6$ Ferroelectric Crystals and their Applications as Infrared Detectors", *J. Electronic Mater.* **4** [1] 91-100 (1975).

58. T.R.Shrout, H.Chen and L.E.Cross, "Dielectric and Piezoelectric Properties of $Pb_{1-x}Ba_xNb_2O_6$ Ferroelectric Tungsten Bronze Crystals", *Ferroelectrics*, **74** 317-324 (1987).

59. R.Guo, A.S.Bhalla and L.E.Cross, "Pyroelectric Properties of Lead Barium Niobate Single Crystals", *Ferroelectrics*, **118** 77-83 (1991).

60. P.V.Lenzo, E.G.Spencer and A.A.Ballman, "Electro-optic coefficients of Ferroelectric Strontium Barium Niobate", *Appl. Phys. Lett.*, **11** [1] 23-24 (1967).

61. M.Lee, H.Lee, R.K.Route and R.S.Feigelson, "Optical Properties of Lead Barium Niobate ($Pb_{1-x}Ba_xNb_2O_6$) Crystals", *J. Appl. Phys.* **81** [2] 917-923 (1997).

62. M.D.Ewbank, R.R.Neurgaonkar, W.K.Cory and J.Feinberg, "Photorefractive properties of Strontium-Barium Niobate", *J. Appl. Phys.*, **62** [2] 374-380 (1987).

63. R.R.Neurgaonkar, W.K.Cory, J.R.Oliver, M.D.Ewbank and W.F.Hall, "Development and Modification of Photorefractive Properties in the Tungsten Bronze Family Crystals", *Optical Engineering*, **26** [5] 392-405 (1987).

64. D.Rytz, B.A.Wechsler, R.N.Schwartz, C.C.Nelson, C.D.Brandle, A.J.Valentino and G.W.Berkstresser, "Temperature Dependence of Photorefractive Properties of Strontium-Barium Niobate ($Sr_{0.6}Ba_{0.4}Nb_2O_6$)", *J. Appl. Phys.*, **66** [5] 1920-1924 (1989).

65. R.R.Neurgaonkar, W.K.Cory, J.R.Oliver, M.Khoshnevisan and E.J.Sharp, "Ferroelectric Tungsten Bronze Crystals and Their Photorefractive Applications", *Ferroelectrics*, **102** 3-14 (1990).

66. K.Megumi, H.Kozuka, M.Kobayashi and Y.Furuhata, "High-Sensitive Holographic Strage in Ce-doped SBN", *Appl. Phys. Lett.*, **30** [12] 631-633 (1977).

67. A.Liu, L.Hesselink, M.Lee and R.S.Feigelson, "Electro-Optic and Photorefractive Two-Beam Coupling Properties of Lead Barium Niobate Crystals", *J. Appl. Phys.*, **83** [5] 2826-2830 (1998).

68. M.Lee, R.S.Feigelson A.Liu and L.Hesselink, "Photorefractive Properties of tungsten Bronze Ferroelectric Lead barium Niobate ($Pb_{1-x}Ba_xNb_2O_6$) Crystals", *J. Appl. Phys.*, **83** [11] 5967-5972 (1998).

69. J.E.Geusic, H.L.Levinstein, J.J.Rubin, S.Singh and L.G.Van Uitert, "The Non-Linear Optical Properties of $Ba_2NaNb_5O_{15}$", *Appl. Phys. Lett.*, **11** [9] 269-271 (1967).

70. S.Singh, D.A.Draegert and J.E.Geusic, "Optical and Ferroelectric Properties of Barium Sodium Niobate", *Phys. Rev. B*, **2** [7] 2709-2724 (1970).

71. D.F.Eaton, "Nonlinear Optical Materials", *Science*, **253** [5017] 281-287 (1991).

72. S.K.Kurz and T.T.Perry, "A Powder Technique for the Evaluation of Nonlinear Optical Materials", *J. Appl. Phys.*, **39** [8] 3798-3813 (1968).

73. M.H.Francombe, "Ferroelectric Films and Their Device Applications", *Thin Solid Films*, **13** 413-433 (1972).

74. L.M.Sheppard, "Advances in Processing of Ferroelectric Thin films", *Am. Ceram. Soc. Bull.*, **71** [1] 85-95 (1992).

75. G.H.Haertling, "Current Status of Thin/Thick Film of Ferroelectrics", *Ceram. Trans.*, **25** 1-18 (1991).

76. M.Adachi and A.Kawabata, "Ferroelectric Thin Films of Tungsten-Bronzes", *Ceram. Trans.*, **25** 303-313 (1991).

77. R.R.Neurgaonkar, I.S.Santha and J.R.Oliver, "Growth of Grain-Oriented Tungsten Bronze SBN Films on Si", *Mater. Res. Bull.*, **26** 983-988 (1991).

78. S.S.Thony, K.E.Youden, J.S.Harris, Jr., and L.Hesselink, "Growth of Epitaxial Strontium Barium Niobate Thin Films by Pulsed Laser Deposition", *Appl. Phys. Lett.*, **65** [16] 2018-2020 (1994).

79. W.Lin, T.Tseng, S.Lin, S.Tu, S,Yang, J.Harn, K.Liu and I.Lin " Growth of epitaxial like $(Sr_{0.5}Ba_{0.5})Nb_2O_6$ Ferroelectric Films", *Jpn. J. Appl. Phys.*, **34** L625-L627 (1995).

80. D.Trivedi, P.Tayebati, and M.Tabat "Mesurement of large electro-optic coefficients in thin films strontium barium niobate ($Sr_{0.6}Ba_{0.4}Nb_2O_6$)", *Appl. Phys. Lett.*, **68** 3227-3229 (1996).

81. Y.Y.Zhu, R.F.Xiao, and G.K.L.Wong "Pulsed laser deposition of optical waveguiding strontium barium niobate films", *J. Appl. Phys.*, **82** 4908-4911(1997).

82. M.Nakano, H.Tabata, K.Tanaka, Y.Katayama and T.Kawai, "Fabrication and Characterization of (Sr,Ba)$Nb_2O_6$ Thin Films by Pulsed Laser Deposition", *Jpn. J. Appl. Phys.*, **36** [10A] L1331-L1332 (1997).

83. Z.Lu, R.S.Feigelson, R.K.Route, S.A. DiCarolis, R.Hiskes and R.D.Jacowitz, "Solid source MOCVD for the epitaxial growth of thin oxide films", *J. Cryst. Growth*, **128** 788-792 (1993).

84. M.J.Nyatrom, B.W.Wessels, W.P.Lin, G.K.Wong, D.A.Neumayer and T.J.Marks "Nonliner optical properties of textured strontium barium niobate thin films prepared by metalorganic chemical vapor deposition", *Appl. Phys. Lett.*, **66** 1726-1728 (1995).

85. L.D.Zhu, J.Zhao, F.Wang, P.E.Norris, G.D.Fogarty, B.Steiner, P.Lu, B.Kear, S.B.Kang, B.Gallois, M.Sinclair, D.Dimos and M.Cronin-Golomb "Epitaxitial electro-optical $Sr_xBa_{1-x}Nb_2O_6$ films by single-source plasma-enhanced metalorganic chemical vapor deposition", *Appl. Phys. Lett.*, **67** 1836-1838 (1995).

86. M.Lee and R.S.Feigelson "Growth of epitaxial strontium barium niobate thin films by solid source metal-organic chemical vapor deposition", *J. Cryst. Growth*, **180** 220-228 (1997).

87. Y.Xu, C.J.Chen, R.Xu and J.D.Mackenzie, "Ferroelectric $Sr_{0.6}Ba_{0.4}Nb_2O_6$ Thin Films by the Sol-Gel Process: Electrical and Optical Properties", *Phys. Rev. B*, **44** [1] 35-41 (1991).

88. C.J.Chen, Y.Xu, R.Xu and J.D.Mackenzie, "Ferroelectric and Pyroelectric Properties of Strontium Barium Niobate Films Prepared by the Sol-Gel Method", *J. Appl. Phys.*, **69** [3] 1763-1765 (1991).

89. S.Hirano, T.Yogo, K.Kikuta, H.Urahata, Y.Isobe, T.Morishita, K.Ogiso and Y.Ito, "Chemical Processing of Ferroelectric Niobates Epitaxial Films", *Mater. Res. Soc. Symp. Proc.*, **271** 331-338 (1992).

90. S.Hirano, T.Yogo, K.Kikuta and K.Ogiso, "Preparation of Strontium Barium Niobate by Sol-Gel Method", *J. Am. Ceram. Soc.*, **75** [6] 1697-1700 (1992).

91. J.D.Mackenzie, "Nonlinear Optical Materials by Sol-Gel Method", *J. Sol-Gel Sci. Tech.*, **1** 7-19 (1993).

92. L.A.Momoda, M.C.Gust and M.L.Mecartney "PROCESSING EFFECTS ON THE MICROSTRUCTURE OF SOL-GEL DERIVED SBN THIN FILMS", *Mater. Res. Soc. Symp. Proc.*, **346** 297-302 (1994).

93. C.H.Luk, C.L.Mak, K.H.Wong "Characterization of strontium barium niobate films prepared by sol-gel process using 2-methoxyethanol", *Thin Solid Films*, **298** 57-61 (1997).

94, R.R.Neurgaonkar and E.T.Wu, "Epitaxial Growth of Ferroelectric T.B. $Sr_{1-x}Ba_xNb_2O_6$ Films for Optoelectronic Applications", *Mater. Res. Bull.*, **22** 1095-1102 (1987).

95. M.Adachi, A.Kawabata and F.Takeda, "Preparation of Tungsten-Bronze Thin Films", *Jpn. J. Appl. Phys.*, **30** [9B] 2208-2211 (1991).

96. M.Tsukioka, T.Mashio, M.Shimazu and T.Nakamura, "Preferable Orientation of Crystalline Thin Film of Modified BNN System", *Modern Phys. Lett. B*, **3** [6] 465-470 (1989).

97. J.M.Boulton, G.Teowee, W.M.Bommersbach and D.R.Uhlmann, "Sol-Gel Derived Sodium Barium Niobate and Bismuth Titanate Films", pp.303-308, in *Ferroelectric Thin Films II* (*Mater. Res. Soc. Proc.*) **243** Edited by A.I.Kingon, E.R.Myers and B.Tuttle, Mater. Res. Soc., Pittsburgh (1992).

98. J.M.Liu, F.Zhang, Z.G.Liu, S.N.Zhu, L.J.Shi, Z.C.Wu and N.B.Ming, "Epitaxial Growth of Optical $Ba_2NaNb_5O_{15}$ Waveguide Film by Pulsed Laser Deposition", *Appl. Phys. Lett.*, **65** [16] 1995-1997 (1994).

99. S.N.Zhu, Y.Y.Zhu, J.M.Liu, Z.Y.Zhang, H.Shu, J.F.Hong, C.Z.Ge and Z.S.Lin, "Epitaxial $Ba_2NaNb_5O_{15}$ Thin Film by Pulsed Laser Deposition and its Waveguide Properties", *Optics Lett.*, **20** [3] 291-293 (1995).

100. B.I.Lee and E.J.A.Pope, "VI-21 Crystalline and Amorphous Thin Films of Ferroelectric Oxides", VI-21, pp. 481-500 in Chemical Processing of Ceramics, Marcel Dekker, Inc., New York (1971).

101. S.Hirano, T.Yogo, K.Kikuta, K.Kato, W.Sakamoto and S.Ogasawara, "Sol-Gel Processing and Characterization of Ferroelectric Films", *Ceram. Trans.*, **25** 19-32 (1991).

102. K.Iijima, R.Takayama, Y.Tomita and I.Ueda, "Epitaxial Growth and Pyroelectric Properties of Lanthanum-Modified Lead Titanate Thin Films", *J. Appl. Phys.*, **60** [8] 2914-2919 (1986).

# Chapter 2

## Synthesis and Properties of Strontium Barium Niobate (SBN) and Potassium Substituted SBN (KSBN) Thin Films

## 2.1 Introduction

Strontium barium niobate ($Sr_{1-x}Ba_xNb_2O_6$, SBN) is a ferroelectric solid solution between $BaNb_2O_6$ and $SrNb_2O_6$ and has a tetragonal tungsten bronze structure.[1,2] Phase diagram of $SrNb_2O_6$-$BaNb_2O_6$ system is illustrated in Fig.2-1-1. The solid solution is reported to have compositions from x=0.25 to 0.75 as shown in Fig.2-1-2.[3] SBN has been receiving great attention for various applications (summarized in Table 2-1-1) because of its large pyroelectric coefficient, excellent piezoelectric, electrooptic properties and photorefractive sensitivity.[4-8] Representative properties of SBN are shown in Table 2-1-2. SBN is also an important material because of lead-free composition. Alkali or rare-earth ion have been doped in SBN crystal in order to improve its properties.[9-12]

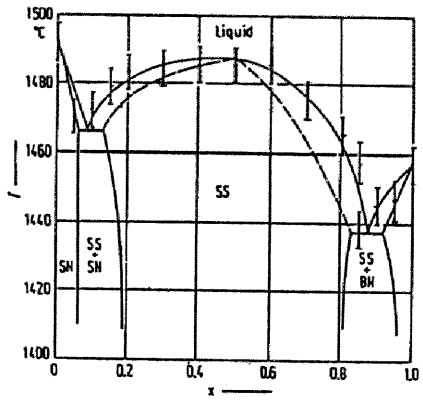


Fig.2-1-1 Phase diagram of $(1-x)SrNb_2O_6$-$xBaNb_2O_6$ binary system.
[SS: tungsten bronze type ss, SN: $SrNb_2O_6$ type ss, BN: $BaNb_2O_6$ type ss. Dashed line is solidus line.]
<J.R.Carruthers et al., J. Electron. Soc.: SOLID STATE SCIENCE, 117 [11] 1426-30 (1970).>

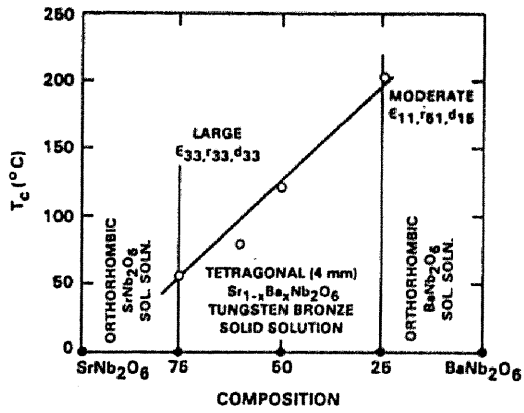


Fig.2-1-2 Curie temperature versus composition for the $SrNb_2O_6$-$BaNb_2O_6$ binary system. (Ref. 10)

SBN ceramics have been prepared by the solid state reaction of oxide powders via conventional firing and milling techniques.[13-15] Hot-pressing is found to be necessary for the improvement of optical properties by reducing porosity of sintered SBN ceramics.[15] SBN single crystals have been grown mainly by the Czochralski method.[6,16,17] However, the growth of single crystals is usually difficult (see Chapter 1, section 1.3.1), except for the congruent melt composition at x=0.6.[16] On the other hand, SBN thin films on substrates have been prepared by

liquid-phase epitaxy, RF sputtering, etc.[17,18] Control of the Sr/Ba ratio without impurity is one of the key factors to optimize the properties of SBN. However, the precise control of composition is usually difficult both in the flux growth technique and the sputtering technique. And further, the control of film orientation associated with the direction of polarization is required for pyroelectric, piezoelectric and electrooptic applications. Dielectric thin films with high transparency and high refractive index are also expected for application in optical devices, especially optical waveguides. A chemical solution deposition (CSD) process is considered to be the most suitable process for the fabrication of multicomponent thin films such as SBN.[20-23] The crystallization temperature of tungsten bronze SBN is required to be lower as possible in order to fabricate high quality thin films. The tungsten bronze structure can be stabilized by the formation of filled-tungsten bronze.[11] Neither $BaNb_2O_6$ (BN) nor $SrNb_2O_6$ (SN) is ferroelectric material and has tungsten bronze structure. However, BN and SN constitute the solid solution with alkali ions, yielding ferroelectric tungsten bronzes, such as $Ba_2NaNb_5O_{15}$ (BNN), $Ba_2KNb_5O_{15}$ (BKN), $Sr_2NaNb_5O_{15}$ (SNN) and $Sr_2KNb_5O_{15}$ (SKN). Strontium barium niobate (SBN) also could be stabilized as a ferroelectric tungsten bronze phase by substitution with alkali ion.

Table 2-1-1 Applications for SBN single crystals (Ref. 30)

| Applications | Important characteristics | | Remarks |
|---|---|---|---|
| Surface Acoustic Wave (SAW) | Mechanical coupling coefficient, $k^2$: | $180 \times 10^{-4}$ | * *Filters and Resonators* |
| | Temperature Compensation: | −50 to −100 ppm for (001) | * *Delay Lines* (SBN:60 and SBN:50) |
| | | −60 ppm for (100) | |
| Electro-Optics | Large $r_{ij}/\varepsilon$, $r_{33} = 1400 \times 10^{-12}$ m/V (SBN:75), | | * Optical Wave Guide |
| | $= 420 \times 10^{-12}$ m/V (SBN:60) | | * Optical Switches |
| | Excellent optical quality | | * Optical modulators (SB:60 and SBN:75) |
| Pyroelectric | Moderate $p/\varepsilon$, large pyroelectric coeffient (>0.05 μC/cm²-°C) | | * Uncooled IR Detector (SBN:50, SBN:60 and $La^{3+}$ modified SBN) |
| Millimeter Wave | Large $dn/dE$: $2.6 \times 10^{-6}$ m/V | | * Phase Modulation for Beam Steering |
| | | | * Optical Modulators (SBN:60, SBN:75) |
| Photorefractive | Large $n^3r^{eff}/\varepsilon$ or $n^3r_{ij}$ | | * Optical Computing |
| | Response time: | 10–40 ms | * Laser Hardening |
| | Coupling coefficient: | 20–45 $cm^{-1}$ | * Phase Conjugation |
| | Special response: | 0.4 to 1.0 μm | * Image Processing |
| | Optical quality crystals | | * 3-D Storage |
| | | | ($Ce^{3+}$, $Fe^{3+}$ and $Cr^{3+}$-doped SBN:60 and SBN:75) |

This chapter focuses on the synthesis and characterization of highly oriented SBN and potassium substituted SBN (KSBN) thin films through metallo-organics.

The effects of the substitution with $K^+$ for $Sr^{2+}$ or $Ba^{2+}$ site in the SBN structure and the pre-crystallization of tungsten bronze seed layer on substrate were investigated for the low temperature synthesis of tungsten bronze films. The structure of SBN and KSBN precursor in solution and the three dimensional relation between synthesized film and substrate were analyzed. The electrical and optical properties of tungsten bronze SBN and KSBN films were also evaluated.

**Table 2-1-2 Ferroelectric and optical properties of SBN crystals (Ref.30)**

| Property | SNB:75 | SBN:60 | SBN:50 |
|---|---|---|---|
| Lattice Constants(Å) | a = 12.458 | a= 12.467 | a=12.481 |
| | c = 3.928 | c= 3.938 | c= 3.954 |
| Tc(℃) | 56° | 75° | 118° |
| Dielectric Constant | $\varepsilon_{33}$ = 3000 | $\varepsilon_{33}$ = 900 | $\varepsilon_{33}$ = 580 |
| | $\varepsilon_{11}$ = 500 | $\varepsilon_{11}$ = 470 | $\varepsilon_{11}$ = 450 |
| Polarization ($\mu C/cm^2$) | 27 | 28-30 | 32 |
| Pyroelastic Coeff. ($\mu C/cm^2$ -℃) | $1.25 \times 10^{-1}$ | $9.7 \times 10^{-2}$ | $5.4 \times 10^{-2}$ |
| Electro-optic Coeff. | $r_{33}$ = 1400 | $r_{33}$ = 420 | $r_{33}$ = 180 |
| ($10^{-12}$ m/V) | $r_{40}$ = 40 | $r_{51}$ = 60 | $r_{51}$ = 80 |
| Piezoelectric Coeff. | — | $d_{33}$ = 165 | $d_{33}$ = 90 |
| ($10^{-12}$ C/N) | — | $d_{15}$ = 31 | $d_{15}$ = 35 |
| Photorefractive Characteristics: | | | |
| 1. Response time | 100 ms | 10-40 ms | — |
| 2. Coupling coeff. | 15 $cm^{-1}$ | 20-45 $cm^{-1}$ | — |
| 3. Spectral response | 0.4 to 0.6 μm | 0.4 to 1.0 μm | — |

## 2.2 Experimental

Figure 2-2-1 shows an experimental procedure for fabrication of strontium barium niobate (SBN) and potassium substituted strontium barium niobate (KSBN) powders and thin films.

*(1) Synthesis of SBN and KSBN precursor solutions*

Strontium metal [Raremetallic, Japan], Barium metal [Furu-uchi Chemical, Japan], $KOCH_2CH_3$ (potassium ethoxide, KOEt) [Ko-jundo Chemical, Japan] and $Nb(OCH_2CH_3)_5$ (niobium pentaethoxide, $Nb(OEt)_5$) [Trichemical and Ko-jundo

Chemical, Japan] were selected as starting materials. Ethanol was dried over magnesium ethoxide and distilled prior to use as absolute ethanol. 2-Ethoxyethanol (ethylene glycol monoethyl ether, EGMEE) was also dried over molecular sieve and distilled before use. All procedures were conducted in a dry nitrogen-gas ($N_2$) atmosphere, because starting materials are extremely sensitive to moisture. Sr, Ba metal and KOEt corresponding to the $K_y(Sr_{1-x}Ba_x)_{1-y/2}Nb_2O_6$ [x=0, 0.25, 0.5, 0.75, 1.0, y=0, 0.2, 0.4 summarized in Table 2-2-1] composition were dissolved in absolute ethanol.

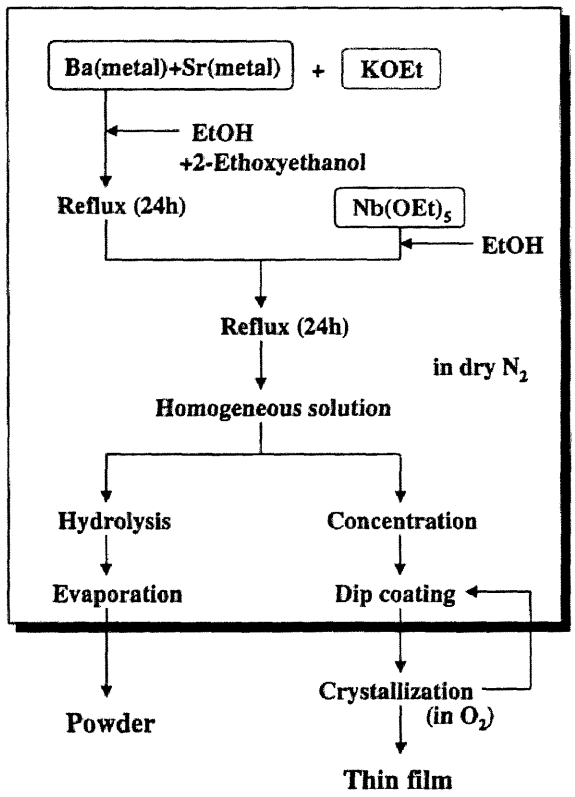


Fig.2-2-1 Experimental procedure for preparation of strontium barium niobate (SBN) and potassium substituted SBN (KSBN) powders and thin films.

Table 2-2-1 Chemical composition of SBN and potassium substituted SBN (KSBN)

| Sr/Ba | K (mol%)* | General formula | Abbreviation |
|---|---|---|---|
| 50/50 | 0 | $(Sr_{0.5}Ba_{0.5})Nb_2O_6$ | SBN50 |
| 75/25 | 0 | $(Sr_{0.75}Ba_{0.25})Nb_2O_6$ | SBN75 |
| 25/75 | 40 | $K_{0.4}(Sr_{0.25}Ba_{0.75})_{0.8}Nb_2O_6$ | KSBN25 |
| 50/50 | 20 | $K_{0.2}(Sr_{0.5}Ba_{0.5})_{0.9}Nb_2O_6$ | $K_{0.2}$SBN50 |
| 50/50 | 40 | $K_{0.4}(Sr_{0.5}Ba_{0.5})_{0.8}Nb_2O_6$ | $K_{0.4}$SBN50 |
| 75/25 | 40 | $K_{0.4}(Sr_{0.75}Ba_{0.25})_{0.8}Nb_2O_6$ | KSBN75 |

*** 40 mol%; Composition of filled tungsten bronze**

2-Ethoxyethanol (EGMEE) was added to the solution as a stabilizing agent. The molar ratio of EGMEE to SBN or KSBN precursor was from 6 to 12. The solution was refluxed for 18 h and then mixed with $Nb(OEt)_5$ solution. The mixed solution was reacted again at a reflux temperature for 18 h. Then, the solution was condensed to about 0.2 mol/l by removal of solvent by vacuum evaporation.

*(2) Fabrication of SBN and KSBN thin films*

Films were fabricated using the precursor solution by dip-coating on fused silica, MgO(100) and Pt(100)/MgO(100) substrates. The dip-coating apparatus is shown in Fig.2-2-2. A Pt(100) layer was deposited on MgO(100) by radio-frequency (RF) magnetron sputtering [Anelva, SPF-322H] at 650°C in an argon and oxygen gas (1/1) mixture (pressure of 0.5 Pa) in accordance with the literature.[24]

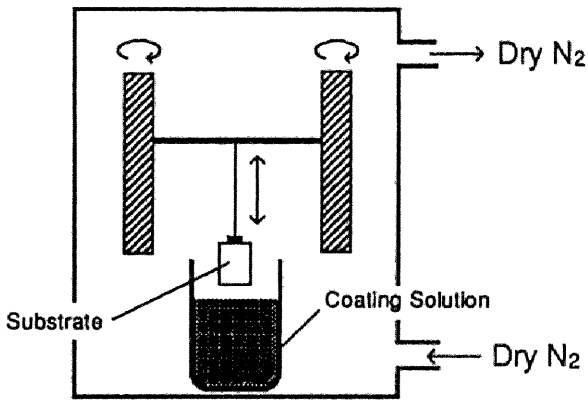


Fig.2-2-2 The apparatus for dip-coating.

The thickness of the Pt electrode was about 100-200 nm. The withdrawal rate of substrate from the precursor solution was 0.6 mm/s. Prior to dip-coating, fused silica and MgO(100) substrates were cleaned with absolute ethanol by ultrasonication and substrates were soaked in absolute ethanol at 60°C to clean the surface. The deposited films were dried in flowing dry $N_2$. After the precursor film on substrates was calcined at 350°C for 1 h at a rate of 5°C/min, the film was heated to a crystallization temperature for 1 h, followed by cooling in an $O_2$ flow at a rate of 5°C/min. The coating-crystallization process was repeated several times to increase the film thickness. The heating schedule is shown in Fig.2-2-3. The thickness of crystallized film per dip coating was about 0.03 μm, when the precursor film was withdrawn at a rate of 0.6 mm/s.

An underlayer was prepared on substrates using 0.02 mol/l precursor solution at a withdrawal rate of 0.6 mm/s. The thin layer of the precursor on a

substrate was heat-treated at 700°C for 1 h under the same conditions described above. Then, the precursor film was coated on the precrystallized underlayer using 0.2 mol/l solution at a withdrawal rate of 0.6 mm/s.

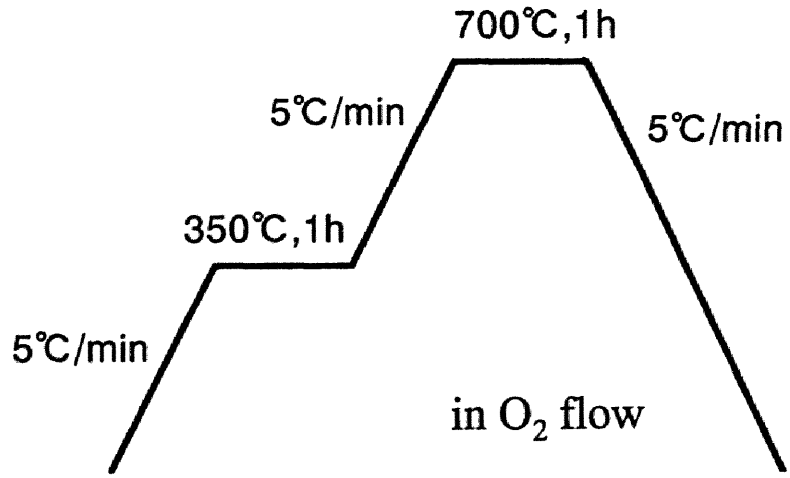


Fig.2-2-3 Heating schedule of SBN and KSBN precursor films.

*(3) Preparation of SBN and KSBN powder samples*

Powder samples were also prepared from the precursor solution in order to study the crystallization behavior. The solution was hydrolyzed with deionized water which was diluted with absolute ethanol. The precipitate was dried at 100°C to yield a white solid, which was then heat-treated at temperatures between 500°C and 1400°C in an oxygen flow for 1 h.

*(4) Characterization of precursors in solutions*

Nuclear magnetic resonance (NMR) spectroscopy was employed to investigate the structure of synthesized metallo-organic precursors. $^{1}H$ and $^{13}C$ NMR spectra were recorded by a Gemini 200 spectrometer [Varian] in $CDCl_3$ solution using tetramethylsilane (TMS) as the internal standard. $^{93}Nb$ NMR spectra of precursors were recorded at 61.14 MHz [Bruker Instruments, AC250] in ethanol

solutions. Chemical shifts of $^{93}Nb$ spectrum were calibrated with tetramethylammonium hexachloroniobate $(CH_3)_4N[NbCl_6]$ in $CD_3CN$ as the standard.

*(5) Characterization methods of prepared powders and thin films*

The prepared powders and films were characterized by X-ray diffraction (XRD) analysis using Cu Kα radiation with a monochromator and a pole figure attachment [Rigaku, RAD 2X and B-8]. The crystallographic phases of SBN and KSBN powders and films were characterized by Raman microprobe spectroscopy using 488 nm Ar laser beam [JASCO, NR1100]. The films on substrates were observed by scanning electron microscopy (SEM) [JEOL, JSM-6100] and field-emitted scanning electron microscopy (FE-SEM) [Hitachi, S-4500]. The transmittance of the films on transparent substrates was measured with a UV-visible spectrometer [Hitachi, U-3410]. The propagation modes in the films were measured via the prism coupling method, using a He-Ne (632.8 nm) laser beam [Metricon, Model PC-2010 Prism Coupler]. The electrical properties of films were measured using an Au top electrode deposited on the SBN or KSBN films and a sputtered Pt(100) layer on MgO(100) as a bottom electrode shown in Fig.2-2-4.

The thickness of top electrode was about 100 nm. The area of the electrode was $3.88 \times 10^{-4}$ $cm^2$. The measurement of dielectric properties was conducted on thin films in a wafer cryostat [Sanwa Musen, WM-363-1] using an LCR meter

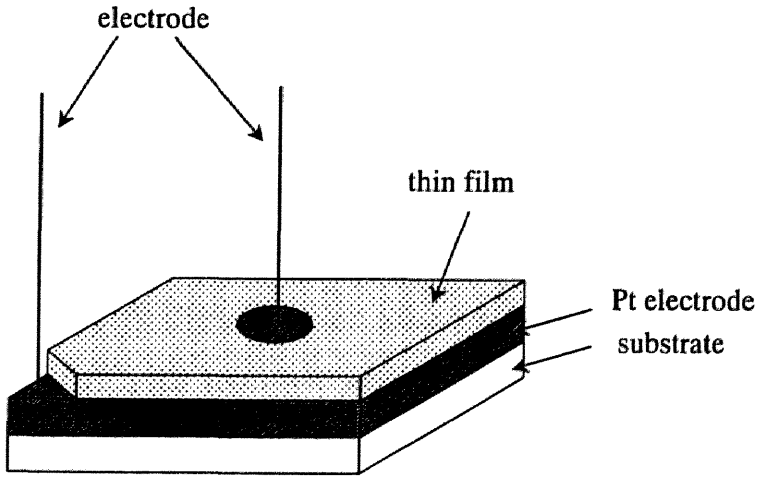


Fig.2-2-4 Measurement system of electrical properties.

[Hewlett-Packard, 4194A] from 30°C to 200°C in an air atmosphere or from –190°C to 200°C under vacuum (1.0 Pa). The P-E hysteresis loops of films were also evaluated with a ferroelectric test system [Radiant Technology, RT66A] at 60 Hz at various temperatures in the wafer cryostat under vacuum (1.0 Pa).

## 2.3 Results and discussion

### 2.3.1 Synthesis of precursor solutions

*(1) Effect of the stabilizing agent for precursor solution*

A $Sr_{1-x}Ba_xNb_2O_6$ (SBN) precursor solution was prepared from Ba, Sr and $Nb(OEt)_5$ in ethanol. However, the solid powder precipitated from the SBN precursor solution within several days. So, the precursor solution was stabilized by the modification of ligands. The homogeneity and stability of the coating solution were found to be greatly improved by the addition of EGMEE. The long-term stability of the SBN precursor added with 12 equiv. EGMEE (EGMEE/SBN precursor=12) was found to be better than that including 6 equiv. EGMEE. The effect of ligand to SBN precursor on treating with EGMEE was analyzed by $^1H$ and $^{13}C$ NMR spectroscopy.

Figure 2-3-1 shows $^1H$ NMR spectra of 2-ethoxyethanol and the $Sr_{0.5}Ba_{0.5}Nb_2O_6$ (SBN50) precursor including 6 equiv. EGMEE. The signal due to hydroxy group (-OH) at 2.9 ppm (Fig.2-3-1(a)) disappears in Fig.2-3-1(b). The signals of 2-ethoxyethoxy groups ($CH_3CH_2OCH_2CH_2O$) are observed at 1.2 ppm ($C\underline{H}_3CH_2OCH_2CH_2O$-), 3.5 ppm ($CH_3C\underline{H}_2OCH_2CH_2O$-, $CH_3CH_2OC\underline{H}_2CH_2O$-) and 3.7 ppm ($CH_3CH_2OCH_2C\underline{H}_2O$-) in Fig.2-3-1(a). However, the peak at 3.7 ppm ($CH_3CH_2OCH_2C\underline{H}_2O$-) shifts to a downfield of 4.3 ppm in Fig.2-3-1(b). The downfield shift suggests the formation of $CH_3CH_2OCH_2CH_2O$-M bond (M; metal). Figure 2-3-2 illustrates $^{13}C$ NMR spectra of the SBN50 precursors including two different amounts of EGMEE. The signals of 2-ethoxyethoxy groups ($CH_3CH_2OCH_2CH_2O$) are observed at 15 ppm ($\underline{C}H_3CH_2OCH_2CH_2O$-), 67 ppm ($CH_3\underline{C}H_2OCH_2CH_2O$-), 72 ppm ($CH_3CH_2O\underline{C}H_2CH_2O$-) and 70 ppm ($CH_3CH_2OCH_2\underline{C}H_2O$-) in Fig.2-3-2(a). The peak at 62 ppm

($CH_3CH_2OCH_2\underline{C}H_2O$-H) of free EGMEE also shifts to a downfield of 70 ppm ($CH_3CH_2OCH_2\underline{C}H_2O$-M) in Fig.2-3-2(a). Ethoxy group bonded to metal atoms is also observed at 68 ppm ($CH_3\underline{C}H_2O$-) and 19 ppm ($\underline{C}H_3CH_2O$-). When the amount of EGMEE increases from 6 equiv. to 12 equiv., the signals of ethoxy groups decrease in intensity as shown in Fig.2-3-2(b). The ethoxide ligands on metals are almost substituted for ethoxyethoxy group as shown in Fig.2-3-2(b). 12 equivalents of EGMEE to SBN were required to stabilize fully the SBN precursor solution. The results of $^{13}C$ NMR indicate that the SBN precursor is stabilized by the coordination of 2-ethoxyethoxy group to metals.

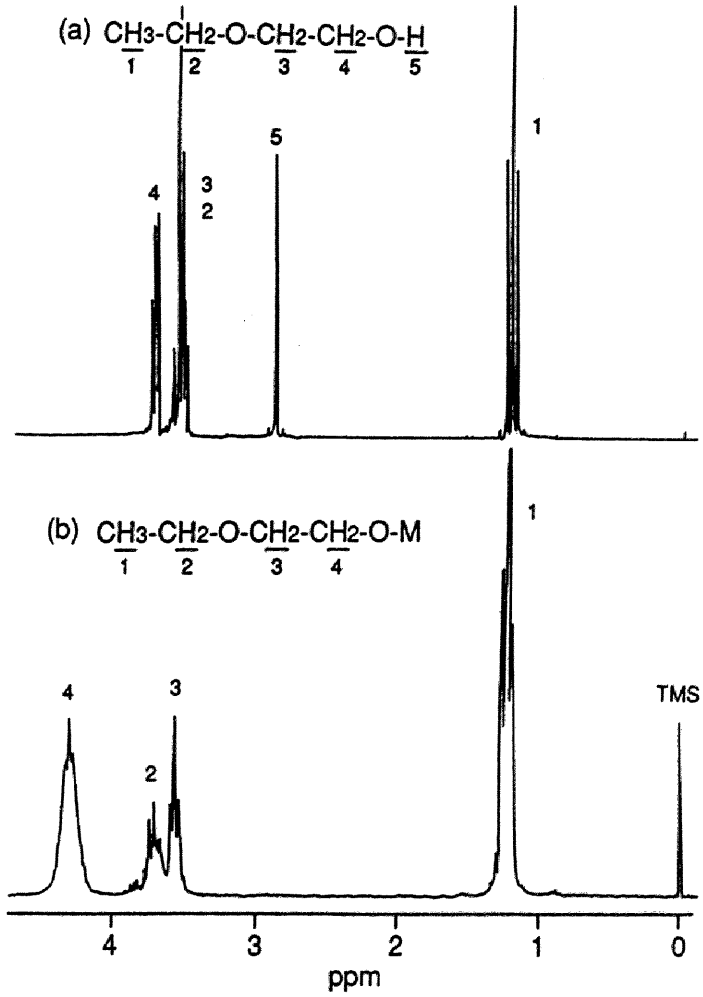


Fig.2-3-1 $^1H$ NMR spectra of (a) 2-ethoxyethanol (EGMEE) and (b) $Sr_{0.5}Ba_{0.5}Nb_2O_6$ (SBN50) precursor [6 equiv. EGMEE added].

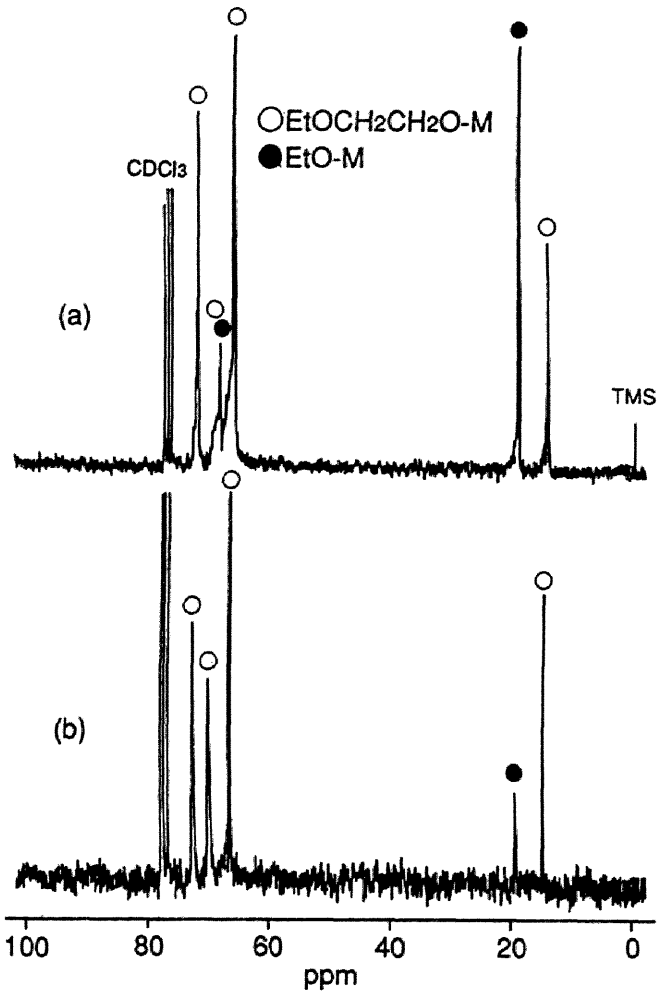


Fig.2-3-2 $^{13}C$ NMR spectra of $Sr_{0.5}Ba_{0.5}Nb_2O_6$ (SBN50) precursors
(a) 6 equiv. EGMEE added (b) 12 equiv. EGMEE added.

Figure 2-3-3 shows the $^{93}Nb$ NMR spectra of the SBN50 precursors. Starting niobium ethoxide exhibits two or three broad signals due to association and ligand exchange. Two moles of niobium ethoxide were reacted with 1 mole of Ba and Sr metal (Ba:Sr=50:50) in ethanol forming the SBN precursor. $^{93}Nb$ NMR of the SBN precursor in ethanol solution shows a single signal at $-1180$ ppm with a half-value width of 1570 Hz as shown in Fig.2-3-3(a). This result indicates the formation of a complex alkoxide with highly symmetric niobium-oxygen octahedron of $[Nb(OR)_6]$. The single signal is in good agreement with the structure of $Ba[Nb(O^iP_r)_6]_2$ or $Sr[Nb(O^iP_r)_6]_2$ proposed by Govil et al.[25] The SBN precursor stabilized by 2-ethoxyethanol (6 equiv.) in ethanol solution shows a

similar single resonance at −1180 ppm with a larger half-value width of 2740 Hz (Fig.2-3-3(b)). The SBN precursor including 12 equiv. EGMEE showed a signal with a half-value width of 3910 Hz at −1180 ppm. The signal increased in half-value width with increasing EGMEE amount from 0 to 12 equiv.. The increase in half-value width suggests the presence of coordination between metals and 2-ethoxyethoxy groups in ethanol solution.

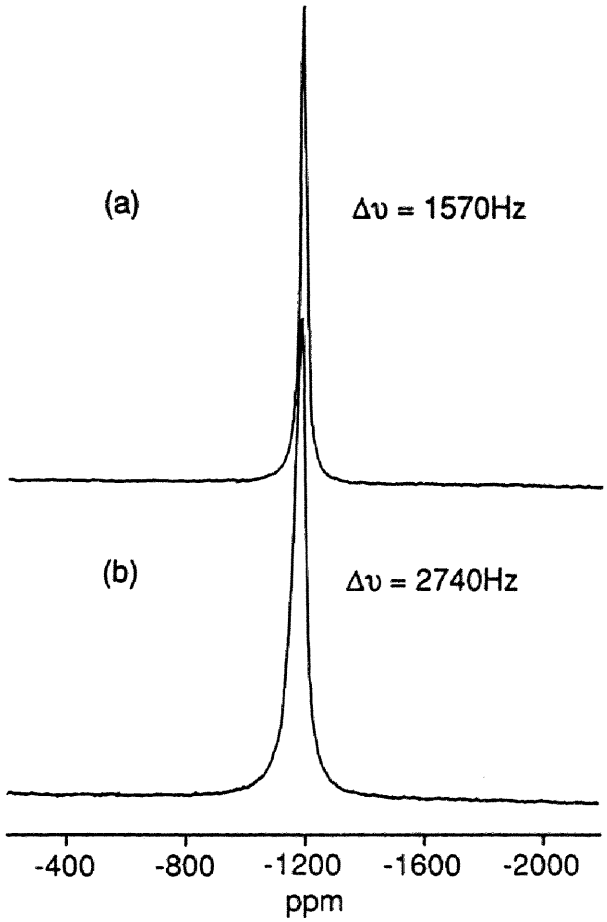


Fig.2-3-3 $^{93}$Nb NMR spectra of SBN50 precursor solutions (a) in ethanol and (b) in ethanol +6 equiv. EGMEE.

*(2) Structure of SBN and KSBN precursors*

Potassium substituted SBN (KSBN) precursor solutions were also prepared by controlling the reaction of Ba, Sr, KOEt and $Nb(OEt)_5$ in ethanol as in the case of SBN precursor solution. A KSBN precursor including 12 equiv. EGMEE (EGMEE/KSBN=12) was found to have a sufficient long-term stability. The structure of KSBN precursor was also analyzed by $^{1}H$, $^{13}C$ and $^{93}Nb$ NMR spectroscopy. The results of $^{1}H$ and $^{13}C$ NMR indicate that the KSBN precursor is stabilized by the coordination of 2-ethoxyethoxy group to metals similar to the SBN precursor. $^{93}Nb$ NMR of the $K_{0.4}SBN50$ precursor in ethanol solution including 12 equiv. amount of EGMEE shows a single signal at $-1180$ ppm with a half-value width of 3910 Hz. The single signal of $K_{0.4}SBN50$ precursor solution indicates the formation of a complex alkoxide with highly symmetric niobium-oxygen octahedron of $[Nb(OR)_6]$, which is consistent with the structure of $Sr[Nb(O^iPr)_6]_2$, $Ba[Nb(O^iPr)_6]_2$ and $K[Nb(OEt)_6]$ reported by Mehrotra and co-workers.[25,26] The SBN50 precursor without any potassium including 12 equiv. EGMEE in ethanol shows a similar single resonance at $-1180$ ppm with a half-value width of 3910 Hz (described above). The signal of $K[Nb(OEt)_6]$ appeared at -1150 ppm. Since $^{93}Nb$ has a quadrupole moment (I=9/2), the broadening of signals is usually observed. Hence, the signal derived from $K[Nb(OR)_6]$ is considered to be superimposed in the broad signal of $M[Nb(OR)_6]_2$ (M=Ba, Sr).

Based upon the spectroscopic data, the SBN precursor consists of $M[Nb(OR)_6]_2$ (M=Sr, Ba, $R=OCH_2CH_2OCH_2CH_3$ or $OCH_2CH_3$) units. The distribution of Sr and Ba in the complex alkoxide is uniform at a molecular level in solution. And further, the composition of $K_{0.4}SBN50$ ($K_{0.4}(Sr_{0.5}Ba_{0.5})_{0.8}Nb_2O_6$) corresponds to a mixture of $0.4K[Nb(OR)_6]$, $0.4Sr[Nb(OR)_6]_2$ and $0.4Ba[Nb(OR)_6]_2$. The KSBN precursor consists of $M[Nb(OR)_6]_2$, and $M'Nb(OR)_6$ (M=Sr, Ba, M'=K, $R=OCH_2CH_2OCH_2CH_3$ or $OCH_2CH_3$) units as shown in Fig.2-3-4, which are mixed at a molecular level in solution.

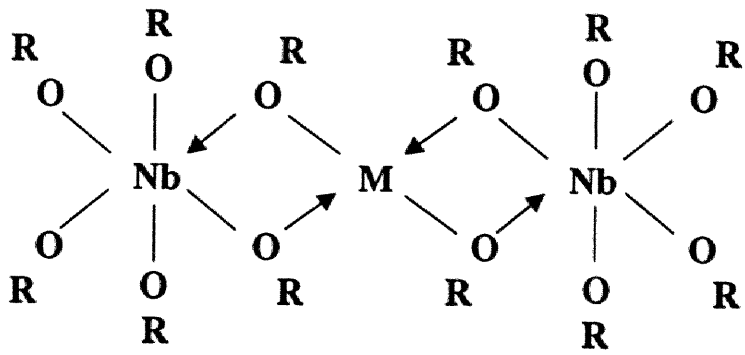


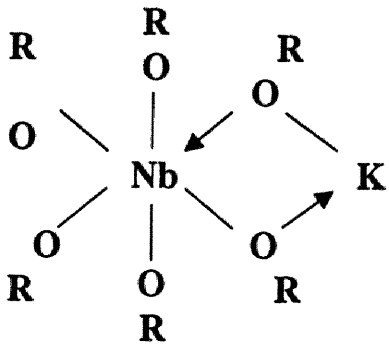


R : $-CH_2CH_3$ or $-CH_2CH_2OCH_2CH_3$

Fig.2-3-4 Proposed structure of SBN and KSBN precursor.

### 2.3.2 Crystallization behavior of SBN precursor

*(1) Crystallization of SBN precursor*

SBN precursor powders were synthesized from the precursor solution in order to investigate the crystallization behavior. Figure 2-3-5 shows XRD profiles of $Sr_{0.5}Ba_{0.5}Nb_2O_6$ (SBN50) powders heat-treated at various temperatures. It turns out from Fig.2-3-5 that SBN precursor powder was in X-ray amorphous state below 500°C and crystallized in the low temperature (not tungsten bronze) phase at 700°C. At 1000°C, tetragonal tungsten bronze SBN began to form, and completely transformed to the tetragonal tungsten bronze SBN at 1200°C. Figure

2-3-6 illustrates XRD profiles of $(Sr_{1-x}Ba_x)Nb_2O_6$ powders with various compositions (x=0, 0.3, 0.5, 0.6, 0.7, 1.0) heat-treated at 700°C. The end members of $BaNb_2O_6$ (BN) and $SrNb_2O_6$ (SN) were hexagonal and orthorhombic single phase, respectively. From Figs.2-3-5 and 2-3-6, the phase of SBN crystallized at 700°C was determined to be the SBN low temperature phase because the diffraction patterns were quite different from that of tetragonal tungsten bronze SBN. The SBN powder crystallized in the tetragonal tungsten bronze phase could not be transformed to the low temperature phase even after the aging at 700°C for 24 h. This result indicates that the SBN low temperature phase is a meta-stable phase. Once SBN powder crystallized to the tungsten bronze phase, this structure is found to be stable.

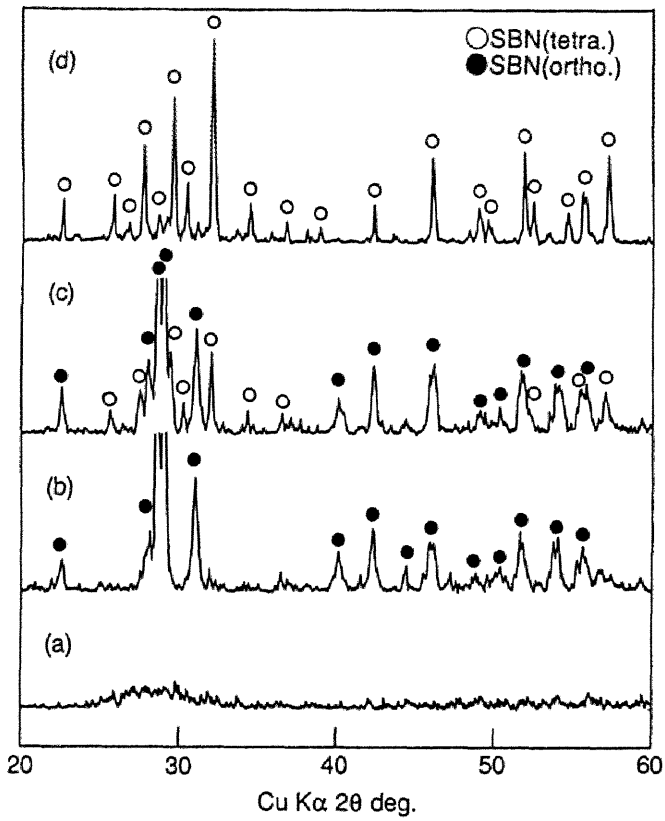


Fig.2-3-5 XRD profiles of SBN50 precursor powders heat-treated at various temperatures (a) 550°C, (b) 700°C, (c) 1000°C and (d) 1200°C. [tetra.: tetragonal tungsten bronze phase] [ortho.: orthorhombic low temperature phase]

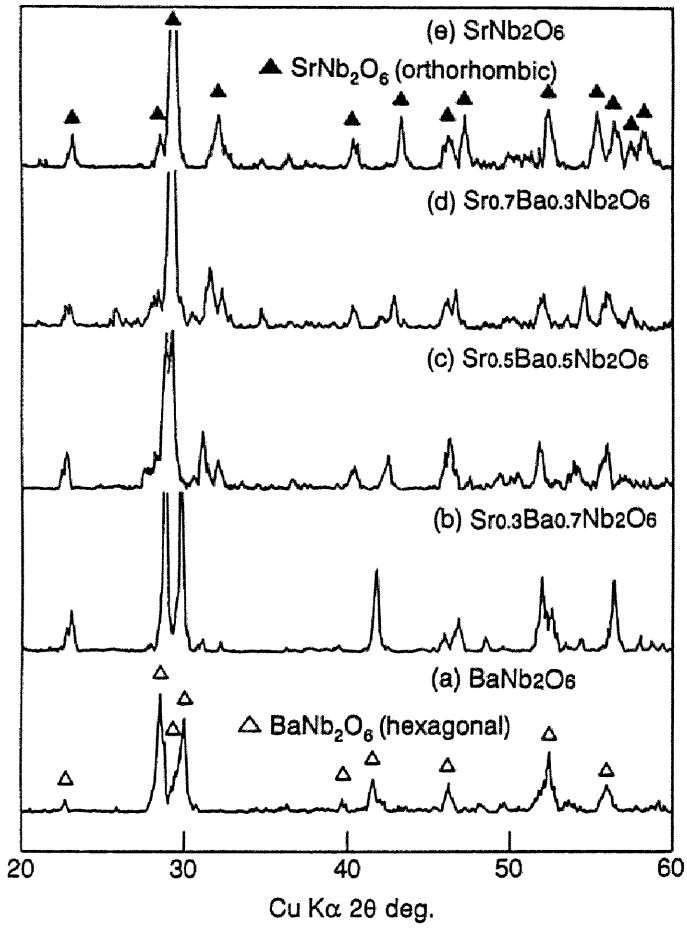


Fig.2-3-6 XRD profiles of $Sr_{1-x}Ba_xNb_2O_6$ powders with various compositions heat-treated at 700°C [(a) x=1.0, (b) x=0.7, (c) x=0.5, (d) x=0.3 and (e) x=0].

### *(2) Structure of SBN low temperature phase*

Raman spectroscopic analysis was employed to examine the crystallographic phase of the SBN low temperature phase. Figure 2-3-7 shows Raman spectra of $SrNb_2O_6$ and SBN50 powders crystallized at 700°C. $SrNb_2O_6$ powder was prepared by the same route as SBN50. The profile of SBN50 (Fig.2-3-7(b)) was consistent with that of $SrNb_2O_6$ (Fig.2-3-7(a)), although these profiles were slightly different to each other. The profile of $SrNb_2O_6$ was in good agreement with the spectrum reported by Repelin et al.[27] SBN precursor powder with Sr rich composition

($Sr_{1-x}Ba_xNb_2O_6$, $x \leqq 0.5$) crystallized at 700°C also showed similar profiles. Since SBN50 has an unfilled tungsten bronze structure described in Chap.1 (section 1.1), the Nb-O octahedra easily construct the edge-shared structure like $SrNb_2O_6$ as shown in Fig.2-3-7(a). From these spectra, it turns out that the SBN50 low temperature phase has the orthorhombic $SrNb_2O_6$ like structure studied by Repelin et al.[27]

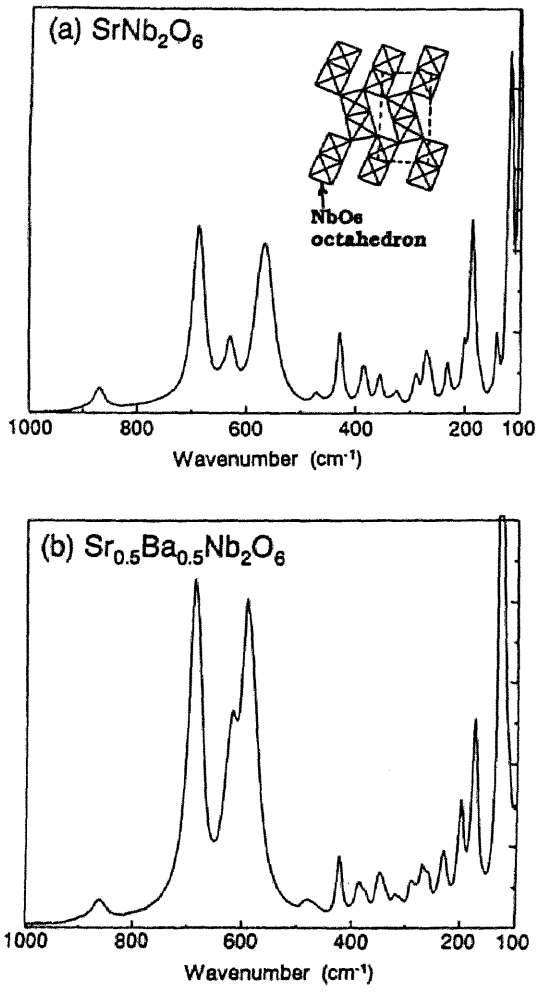


Fig.2-3-7 Raman spectra of (a) $SrNb_2O_6$ and (b) $(Sr_{0.5}Ba_{0.5})Nb_2O_6$ powders heat-treated at 700°C.

### 2.3.3 The substitution for strontium and barium site by potassium in SBN structure

In order to investigate the effect of the substitution for Sr or Ba sites with potassium ions, the $K_{0.4}(Sr_{0.5}Ba_{0.5})_{0.8}Nb_2O_6$ ($K_{0.4}$SBN50) and $K_{0.2}(Sr_{0.5}Ba_{0.5})_{0.9}Nb_2O_6$ ($K_{0.2}$SBN50) powders were prepared by the hydrolysis of the $K_x(Sr_{0.5}Ba_{0.5})_{1-x/2}Nb_2O_6$ [x=0.2, 0.4] precursor solution. In this case, potassium ion was selected as the alkali ion because the radius of $K^+$ was close to that of $Sr^{2+}$ and $Ba^{2+}$. Figure 2-3-8 shows XRD profiles of $K_{0.4}$SBN50 and $K_{0.2}$SBN50 powders heat-treated at 700°C. These powders were X-ray amorphous below 550°C, and directly crystallized to the tetragonal tungsten bronze phase above 600°C. The crystallization temperature of tungsten bronze was not affected by the amount of potassium. The Raman spectrum patterns of these powders shown in Fig.2-3-9 are in good agreement with that of the tetragonal tungsten bronze SBN50 ($Sr_{0.5}Ba_{0.5}Nb_2O_6$) powder, although the scattering positions are slightly shifted to each other.[28]

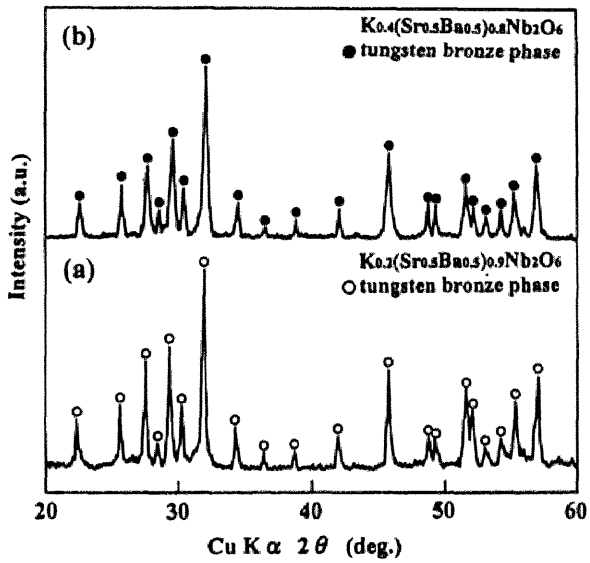


Fig.2-3-8 XRD profiles of (a) $K_{0.2}Sr_{0.45}Ba_{0.45}Nb_2O_6$ ($K_{0.2}$SBN50) and (b) $K_{0.4}Sr_{0.4}Ba_{0.4}Nb_2O_6$ ($K_{0.4}$SBN50) powders heat-treated at 700°C.

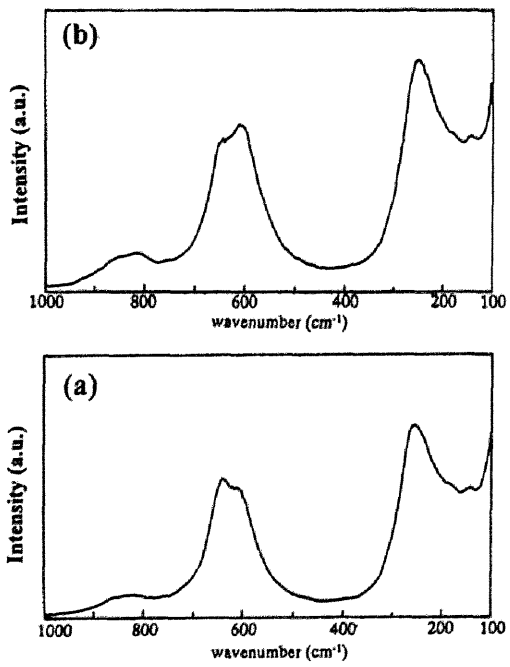


Fig.2-3-9 Raman spectra of (a) $K_{0.2}Sr_{0.45}Ba_{0.45}Nb_2O_6$ ($K_{0.2}$SBN50) and (b) $K_{0.4}Sr_{0.4}Ba_{0.4}Nb_2O_6$ ($K_{0.4}$SBN50) powders heat-treated at 700°C.

The SBN50 precursor without any potassium substitution crystallized in the orthorhombic low temperature phase at 700°C prior to the formation of tetragonal tungsten bronze phase. Then, the orthorhombic SBN powder was completely transformed to the tetragonal phase at 1200°C as described in previous section. It turns out from Fig.2-3-8 that the substitution of K for Sr or Ba was found to be very effective to form the tungsten bronze phase at lower temperatures without any formation of the orthorhombic low temperature phase.

The lattice parameters of alkoxy-derived $K_x(Sr_{0.5}Ba_{0.5})_{1-x/2}Nb_2O_6$ [x=0, 0.2, 0.4] powders are summarized in Table 2-3-1. The values of lattice parameters slightly increase with increasing potassium in amount, and are slightly larger than that of SBN50 tetragonal tungsten bronze powder. The values of SBN50 are comparable with those reported in JCPDS 39-265 (a=12.4652Å, c=3.9521Å). This difference comes from the substitution of $Sr^{2+}$ or $Ba^{2+}$ sites by $K^+$ ions in the SBN50 structure. The radius of $K^+$ is larger than that of $Ba^{2+}$ and $Sr^{2+}$.

**Table2-3-1 Lattice constant changes of alkoxy-derived powders***

| Composition | a (Å) | c (Å) |
|---|---|---|
| SBN50 [1)] | 12.467 | 3.946 |
| $K_{0.2}$SBN50 [2)] | 12.494 | 3.964 |
| $K_{0.4}$SBN50 [2)] | 12.528 | 3.974 |

**(*) Tetragonal tungsten bronze phase**
**powders crystallized at 1) 1200°C and 2) 1000°C**

Therefore, the lattice parameter becomes slightly larger with an increase of potassium. The stabilization mechanism of SBN tungsten bronze is explained by the configuration of Nb-O octahedron. The SBN50 low temperature phase has a

$SrNb_2O_6$ like structure confirmed by Raman spectroscopy (Fig.2-3-7).[27] One $Sr^{2+}$ or $Ba^{2+}$ ion is substituted for two $K^+$ ions in the SBN structure. The structure of SBN approaches to the filled-tungsten bronze with an increase of potassium amount. Thus, the tungsten bronze structure can be stabilized, and KSBN precursors prepared by the chemical process crystallize easily to the tungsten bronze phase in the low temperature region compared with SBN50 precursors.

In the case of different Sr/Ba ratio composition, similar results were obtained using the $K^+$ addition. Figure 2-3-10 shows XRD profiles of $K_{0.4}(Sr_{0.75}Ba_{0.25})_{0.8}Nb_2O_6$ (KSBN75) powders heat-treated at 550°C and 650°C. The KSBN75 powder is X-ray amorphous below 550°C (Fig.2-3-10(a)) and directly crystallizes to the tetragonal tungsten bronze phase at 650°C (Fig.2-3-10(b)).

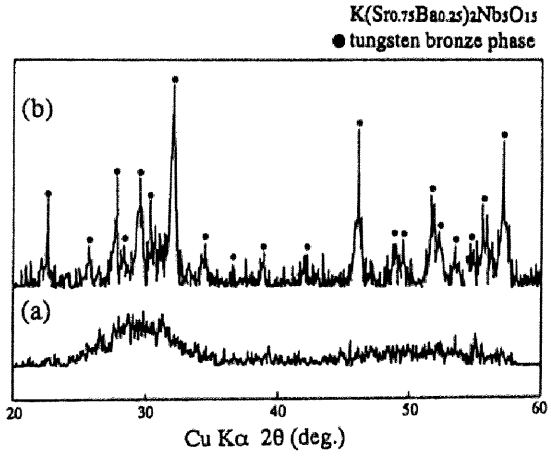


Fig.2-3-10 XRD profiles of $K(Sr_{0.75}Ba_{0.25})_2Nb_5O_{15}$ (KSBN75) powders heat-treated at (a) 550°C and (b) 650°C.

When $Sr_{0.75}Ba_{0.25}Nb_2O_6$ (SBN75) was synthesized by the same process, the SBN75 powder crystallized to the orthorhombic low temperature phase ($SrNb_2O_6$ like structure) at 700°C prior to the formation of tetragonal tungsten bronze similarly to the case of SBN50. The transformation of the orthorhombic SBN75 powder to the tetragonal tungsten bronze phase is found to be quite difficult even after heat treatment at 1400°C. Further investigation for Ba rich composition such as $K_{0.4}(Sr_{0.25}Ba_{0.75})_{0.8}Nb_2O_6$ (KSBN25) revealed that KSBN25 powder was also found to crystallize directly in the tetragonal tungsten bronze phase above 600°C.

### 2.3.4 Preparation of tungsten bronze SBN and KSBN thin films

#### *(1) Synthesis of SBN thin films*

Figure 2-3-11 shows XRD profiles of $Sr_{0.5}Ba_{0.5}Nb_2O_6$ (SBN50) films

crystallized at 700°C and 1000°C on MgO(100) substrates. SBN films on MgO(100) show strong 001 and 002 reflections as shown in Fig.2-3-11. From the XRD patterns, it was impossible to judge whether SBN50 thin film on MgO(100) crystallized to tetragonal of tungsten bronze or orthorhombic metastable phase, because SBN thin films crystallized at 700°C and 1000°C had almost the same XRD profiles.

SBN thin films on MgO(100) substrates were characterized further by Raman microprobe spectroscopy. At first, crystallized SBN powder samples were examined. Two remarkably different patterns of crystalline powders were obtained. The crystallographic phases of these powders were confirmed by the XRD analysis in Fig.2-3-5. The SBN powder crystallized at 700°C can be judged to be the low-temperature metastable phase and has the orthorhombic $SrNb_2O_6$ like structure described in section 2.3.2.

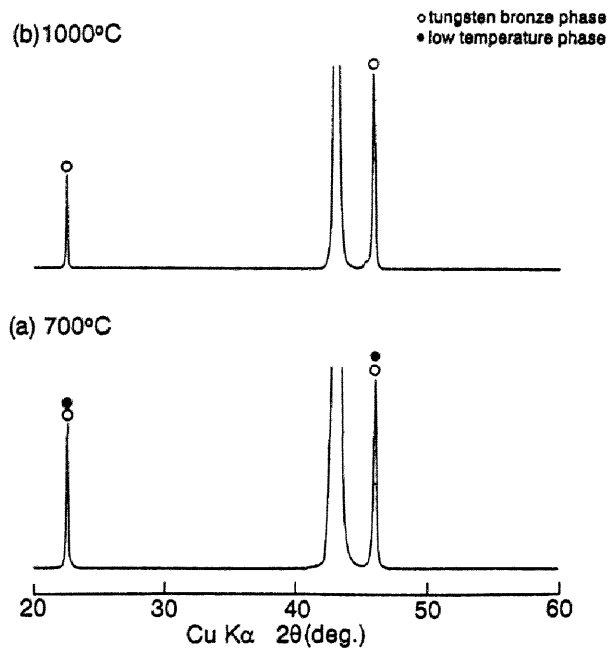


Fig.2-3-11 XRD profiles of SBN50 thin films on MgO(100) substrates crystallized at (a) 700°C and (b) 1000°C.

On the other hand, the spectrum of SBN50 crystallized at 1200°C is in good agreement with that of tetragonal SBN of tungsten bronze as reported by Burns et al.[28]

Figure 2-3-12 shows the Raman microprobe spectra of SBN thin films on MgO(100) substrates. The SBN thin film crystallized at 700°C is composed of two crystalline phases (orthorhombic low-temperature phase and tetragonal tungsten bronze phase) as shown in Fig.2-3-12(a). On the other hand, SBN thin films heat-treated at 1000°C is the tetragonal tungsten bronze (Fig.2-3-12(b)). On the

basis of XRD analysis, the powder crystallized in the orthorhombic phase at 700°C, and began to be transformed to the tetragonal phase at 1000°C.[20] Single-phase tetragonal SBN powder was formed at 1200°C (section 2.3.3). Fig.2-3-12 shows that the film on a substrate does crystallize in the tetragonal phase more easily compared with powders.

The low temperature formation of the tetragonal phase is attributed to the roles of the orientation of the substrate, the expansion mismatch and stress between the films and the substrates. However, the heat-treatment at 1000°C is found to be required to transform completely to the tetragonal SBN of tungsten bronze even on MgO(100) substrates. The quality of SBN film crystallized at 1000°C was not so good because exaggrated grain growth was observed on the surface image of SEM.

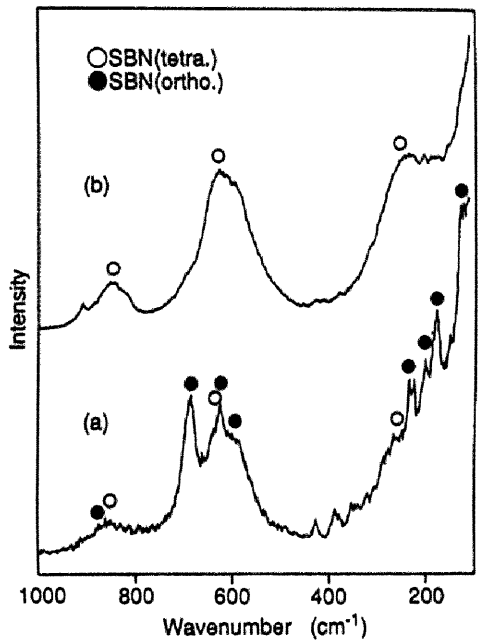


Fig.2-3-12 Raman spectra of SBN50 films on MgO(100) substrates heat-treated at (a) 700°C and (b) 1000°C.
[tetra.: tetragonal tungsten bronze phase]
[ortho.: orthorhombic low temperature phase]

The crystallographic alignment of oriented tungsten bronze SBN thin films on MgO(100) was investigated by the X-ray pole figure measurement. The result of measurement for SBN50 film crystallized at 1000°C is consistent with that of potassium substituted SBN (KSBN) thin film on MgO(100) and Pt(100)/MgO(100) substrates, which is discussed in section 2.3.4(3) in more detail. This result agrees with that of SBN film on MgO(100) substrate prepared by pulsed laser deposition.[29]

*(2) Synthesis of KSBN thin films*

For SBN film synthesis, the crystallization of ferroelectric tungsten bronze phase on substrates encounters the problem of the formation of a low temperature

phase. In order to prepare tungsten bronze thin films on substrates at lower temperature, the substitution of $K^+$ for $Sr^{2+}$ or $Ba^{2+}$ site was investigated as in the case of powder samples.

Figure 2-3-13 shows the XRD profile of $K_{0.4}(Sr_{0.5}Ba_{0.5})_{0.8}Nb_2O_6$ (KSBN50) and $K_{0.4}(Sr_{0.75}Ba_{0.25})_{0.8}Nb_2O_6$ (KSBN75) thin films on fused silica substrates crystallized at 700°C. Similar to the potassium-substituted SBN (KSBN) powders, thin films on substrates directly crystallized to the tetragonal tungsten bronze phase above 650°C with c-axis (direction of polarization) preferred orientation. The c-axis preferred orientation is easy to occur since the c-plane of SBN is the closest packed plane of tungsten bronze structure.

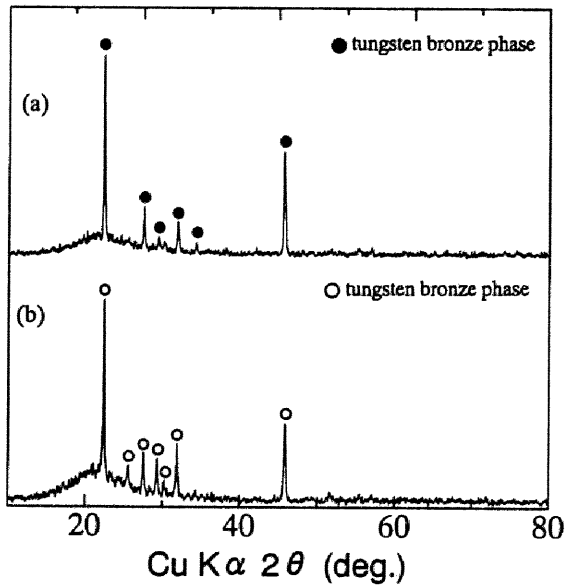


Fig.2-3-13 XRD profiles of (a) $K_{0.4}$SBN50 and (b) KSBN75 thin films on fused silica substrates heat-treated at 700°C.

However, when the underlayer was not precrystallized on substrates, these films were polycrystalline and had no preferred orientation. The quite thin underlayer was found to be the key for the synthesis of oriented KSBN thin films even if on the non-crystalline substrates.

MgO(100) and Pt(100)/MgO(100) were selected as substrates to fabricate highly oriented KSBN thin films. Figure 2-3-14 shows the XRD profiles of $K_{0.4}$SBN50 and $K_{0.2}$SBN50 thin films on MgO(100) substrates crystallized at 700°C. The $K_{0.4}$SBN50 and $K_{0.2}$SBN50 films on MgO(100) have strong 001 and 002 reflections as shown in Figs.2-3-14(a) and (b). The $K_{0.4}$SBN50 and $K_{0.2}$SBN50 films on Pt(100)/MgO(100) crystallized above 600°C also show an excellent c-axis preferred orientation. In the case of SBN50 thin films prepared on MgO(100), XRD profiles of the SBN50 thin films crystallized at 700°C were almost the same

as those at 1000°C.

However, Raman spectra of these films were quite different depending upon the crystallographic phase (section 2.3.4(1)). This means that XRD analysis is not a sufficient method to determine the phase of $K_{0.4}$SBN50 and $K_{0.2}$SBN50 thin films on MgO(100) substrates. Figure 2-3-15 shows Raman spectra of $K_{0.4}$SBN50 and $K_{0.2}$SBN50 thin films on MgO(100) substrates heat-treated at 700°C, which reveal that the thin films are confirmed to be single-phase tungsten bronze, because the profiles are consistent with those of $K_{0.4}$SBN50 and $K_{0.2}$SBN50 powder shown in Figs.2-3-9(a) and (b). The KSBN film showed the characteristic Raman scatterings of the tungsten bronze niobate, such as the Nb-O-Nb bending modes (220-300 $cm^{-1}$) and the symmetric stretching mode of the $NbO_6$ octahedron (580-700 $cm^{-1}$). The formation of the tetragonal tungsten bronze phase is attributed to the substitution of potassium as in the case for the powders.

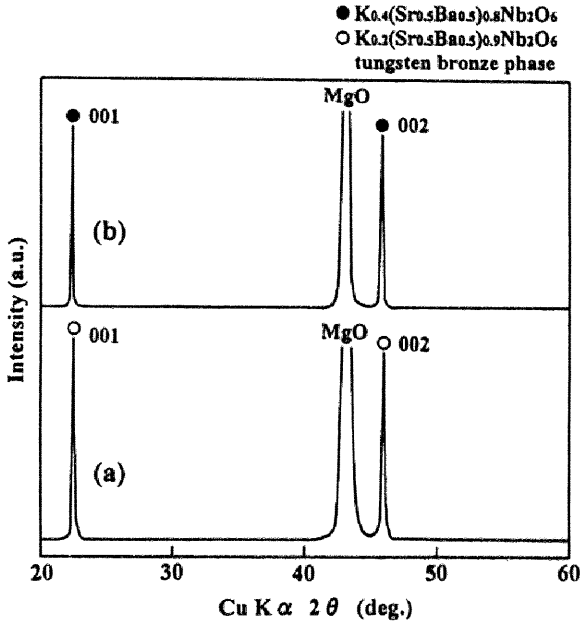


Fig.2-3-14 XRD profiles of (a) $K_{0.2}$SBN50 and (b) $K_{0.4}$SBN50 thin films on MgO(100) substrates heat-treated at 700°C.

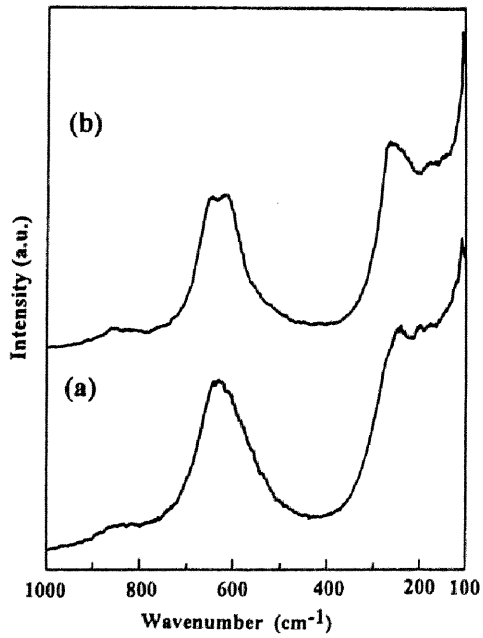


Fig.2-3-15 Raman spectra of (a) $K_{0.2}$SBN50 and (b) $K_{0.4}$SBN50 thin films on MgO(100) substrates heat-treated at 700°C.

The potassium substituted SBN thin films of tetragonal tungsten bronze do crystallize completely at much lower temperatures compared with the SBN thin films.

KSBN thin films with various compositions were also investigated. Figure 2-3-16 shows XRD profiles of $K_{0.4}(Sr_{0.75}Ba_{0.25})_{0.8}Nb_2O_6$ (KSBN75) thin films crystallized at 700°C on MgO(100) and Pt(100)/MgO(100) substrates. The KSBN75 films on MgO(100) also have strong 001 and 002 reflections as shown in Fig.2-3-16(a). Although the (002) reflection of KSBN75 is superimposed with Pt(200), KSBN75 films on Pt(100)/MgO(100) also show (001) plane preferred orientation (Fig.2-3-16(b)). $K_{0.4}(Sr_{0.25}Ba_{0.75})_{0.8}Nb_2O_6$ (KSBN25) thin films on MgO(100) and Pt(100)/MgO(100) also showed a prominent c-axis preferred orientation. The KSBN75 thin films on MgO(100) substrates were also characterized further by Raman microprobe spectroscopy as in the case of SBN50 and KSBN50 films. Figure 2-3-17 shows the Raman spectra of the KSBN75 powder and thin film on MgO(100) crystallized at

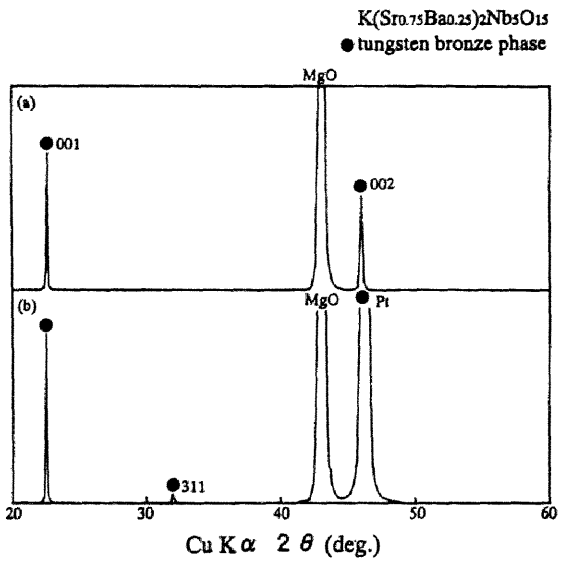


Fig,2-3-16 XRD profiles of KSBN75 thin films heat-treated at 700°C on (a) MgO(100) and (b) Pt(100)/MgO(100) substrates.

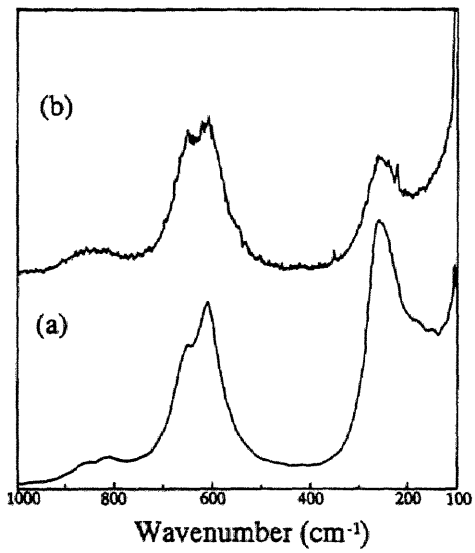


Fig.2-3-17 Raman spectra of (a) KSBN75 powder and (b) KSBN75 thin film on MgO(100) heat-treated at 700°C.

700°C. The spectral pattern of the KSBN75 powder shown in Fig.2-3-17(a) is in good agreement with that of the tetragonal tungsten bronze powder in Fig.2-3-9. The KSBN75 thin film crystallized at 700°C is a single-phase tungsten bronze (Fig.2-3-17(b)), because the profile is consistent with that of KSBN75 powder shown in Fig.2-3-17(a). The direct formation of the tetragonal tungsten bronze phase for various Sr/Ba ratio compositions is attributed to the substitution of potassium for strontium or barium of SBN.

*(3) Three dimensional relation between film and substrate*

The X-ray pole figure measurement was employed in order to investigate the crystallographic alignment of the KSBN thin films on MgO(100) and Pt(100)/Mg0(100) substrates. Figures 2-3-18(a) and (b) show (311) X-ray pole figure and β scan of the $K_{0.4}$SBN50 films on Pt(100)/MgO(100) substrates. The term β is the rotation axis perpendicular to the film plane, and α is the rotation axis perpendicular to β and θ. The X-ray pole figure of the Pt layer on MgO(100) shows spots at every 90° along β at α=45°, which confirms the three dimensional relation between Pt(100) and MgO(100) with the four-fold symmetry. The a-axis of MgO agrees perfectly with the a-axis of Pt. The {311} planes intersect the <001> direction of the film at 45°. Also, The {311} planes show eight equivalent planes around the <001> direction as illustrated in Fig.2-3-19. The pole figure of a single crystal $K_{0.4}$SBN50 film on MgO(100) or Pt(100)/MgO(100) is calculated to show eight spots at α=45° (β interval=52.5° and 37.5°) as shown in Fig.2-3-20. However, the pole figure shown in Fig.2-3-18(a) exhibits additional spots than that of $K_{0.4}$SBN50 single crystal. Also, the pole figure of the $K_{0.4}$SBN50 film on MgO(100) is the same as that shown in Fig.2-3-18(a). From β scan of the (311) plane of KSBN in Fig.2-3-18(b), 12 peaks with two different intensities were obtained. This result suggests that the c-plane due to the additional KSBN lattice should be considered to intersect the a-plane of MgO or Pt. Supposed that the angle between the a-axis of MgO or Pt and the a-axis of the other KSBN grain is 18.5°, the pole figures theoretically constructed for the $K_{0.4}$SBN50/MgO(100) is shown in Fig.2-3-21. Figure 2-3-21 consists of two sets of eight spots, one is

marked as ○, the other as ▲. Figure 2-3-21 is in good agreement with Fig.2-3-18(a). The intensity ratio of four strong peaks to eight weak peaks is about 2 in Fig.2-3-18(b), because 4 spots of ○ are superimposed on four spots of ▲ in Fig.2-3-21. Two crystal lattice planes of $K_{0.4}$SBN50 are, therefore, intergrown at an orientation of 18.5° on MgO(100) and Pt(100)/MgO(100) substrates. Tungsten bronze KSBN thin films with other chemical compositions also showed the same pole figure patterns. These results are consistent with that of SBN films on MgO(100) prepared via both the chemical solution deposition (in section 2.3.4(1)) and the pulsed laser deposition reported by Thony et al.[29] The reason for two orientations mechanism was attributed to the atomic alignment matching between c-plane of tetragonal KSBN and MgO(100). The analysis for the (211) plane of the present KSBN films supports the same intergrowth feature as that for the (311) plane.

The formation of tetragonal tungsten bronze phase on MgO(100) and Pt(100)/MgO(100) is attributed to the assistance of nucleation sites with atomic alignment of substrates. The calculated lattice mismatch between KSBN50(001) and MgO(100) is 6.1 % on the basis of the pole-figure measurement. The crystal lattice in terms of atomic alignment and electrostatic interaction is best for this configuration, even though the epitaxal relationship of SBN(100)//(310)MgO implies a 6-7 % lattice mismatch. Deposited Pt layers on MgO(100) had a (100) orientation with a three dimensional alignment. Platinum has a fcc atomic packing with a lattice parameter of 3.923Å. The lattice mismatch between KSBN(001) and Pt(100) is calculated to be 0.9 % on the basis of the pole-figure measurement. The crystallization of KSBN films with c-axis preferred orientation results from the crystallographic matching of KSBN(001) to Pt(100)/MgO(100). The similar analysis was carried out for $K_{0.2}$SBN50 films on MgO(100) and Pt(100)/MgO(100). The results for $K_{0.2}$SBN50 also support the intergrowth of two crystal lattice of KSBN. The results of measurement for KSBN75 films indicate that tungsten bronze KSBN films show the same orientation regardless of composition.

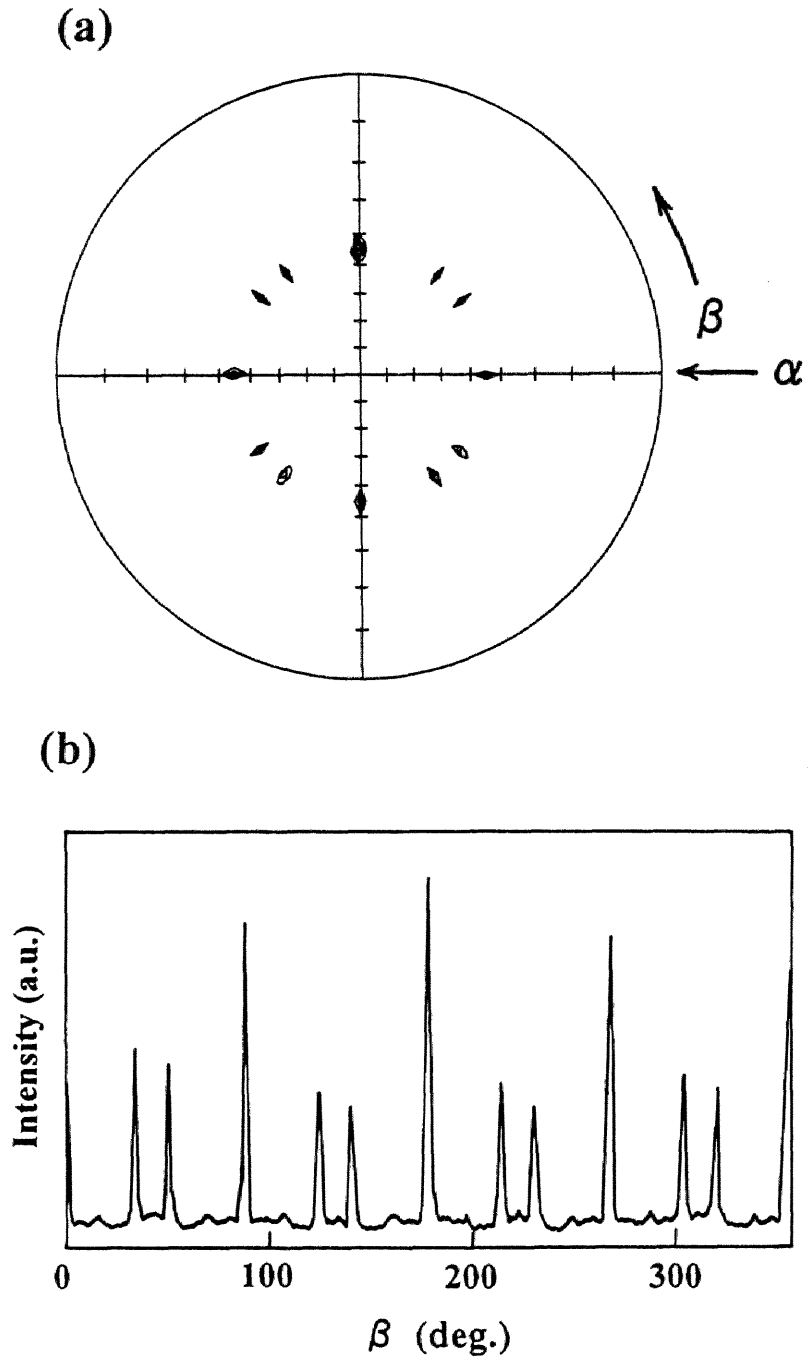


Fig.2-3-18 (a) X-ray pole figure and (b) $\beta$ scan of $K_{0.4}$SBN50 films on Pt(100)/MgO(100) heat-treated at 700°C [$2\theta$ =31.8°, for (311)].

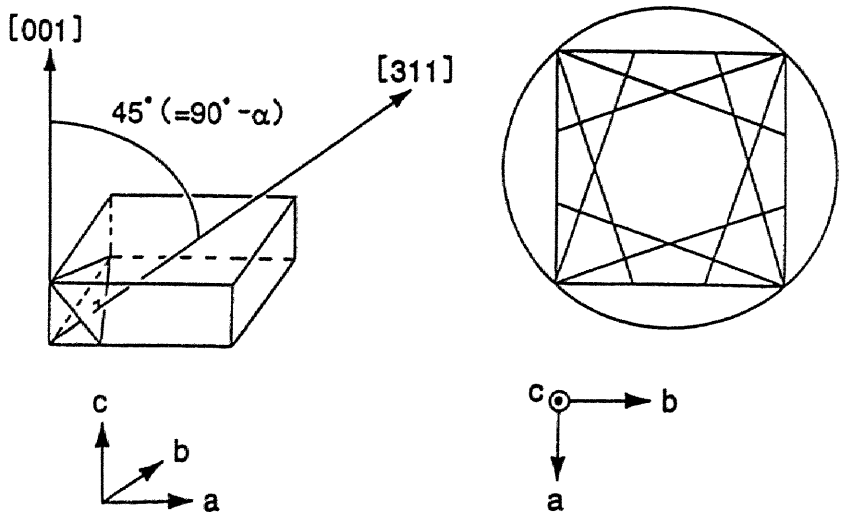


Fig.2-3-19 Relationship between the (311) plane and tetragonal unit.

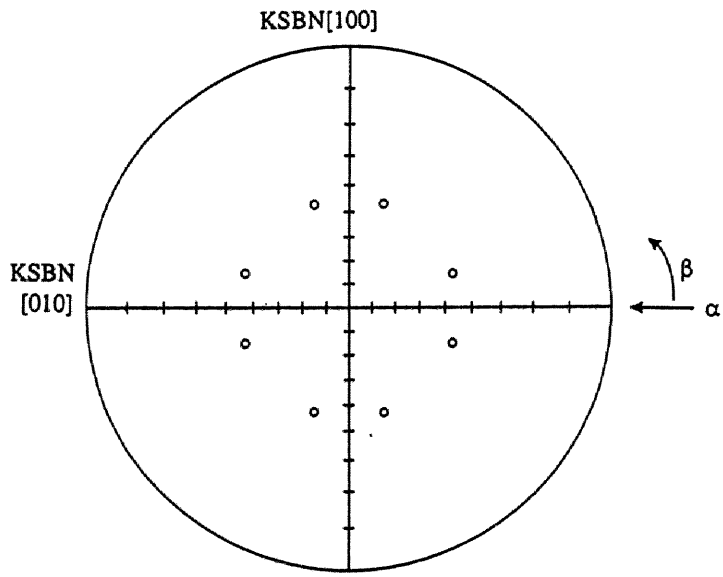


Fig.2-3-20 Caluculated pole figure pattern of $K_{0.4}$SBN50 single crystal constructed for tetragonal (311).

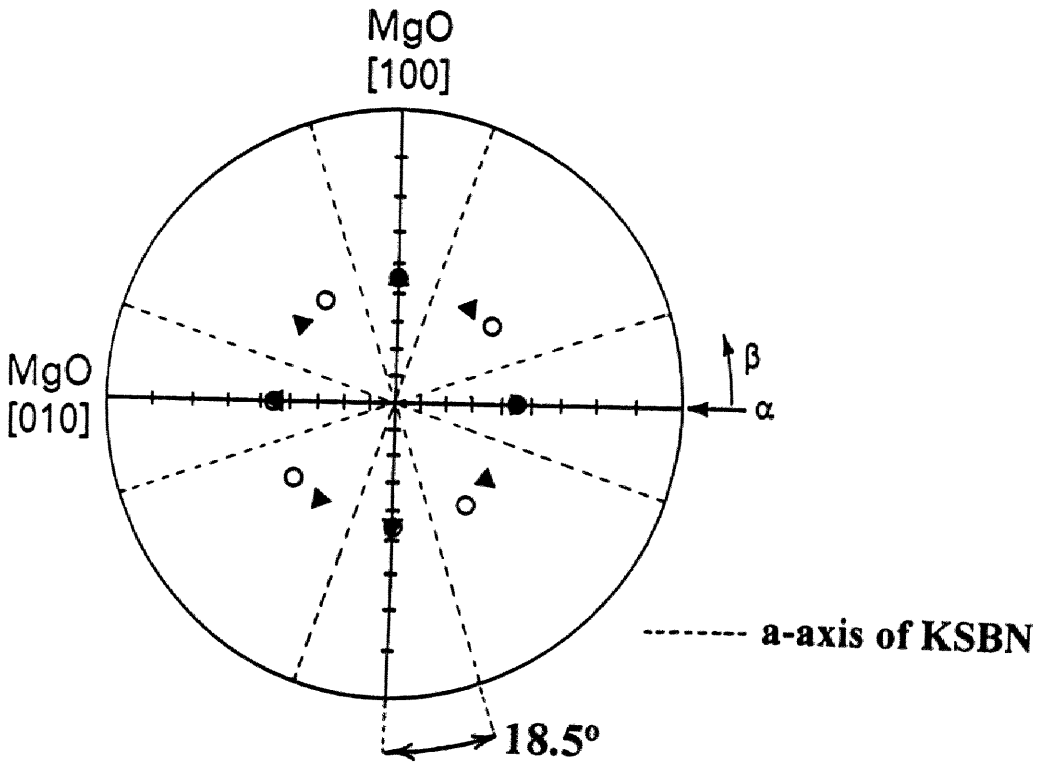


Fig.2-3-21 Calculated X-ray pole figure of KSBN films on Pt(100)/MgO(100) and MgO(100) intergrown at 18.5° (two KSBN lattices are shown by ○ and ▲).

KSBN thin films prepared on fused silica also showed c-axis preferred orientation. The three dimensional relation between KSBN thin film and fused silica substrate was also investigated by X-ray pole figure measurement. The result indicates that the crystal lattice of KSBN had no three-dimensional regularity on fused silica substrate. The reason for the c-axis orientation was attributed to the atomic alignment of the most closed packing plane of tetragonal tungsten bronze KSBN.

*(4) Synthesis of SBN thin films on KSBN seed layer*

It was found to be difficult to crystallize tungsten bronze SBN films directly on substrates at lower temperature (in section 2.3.4(1)). KSBN75 thin film is used as a seed layer for the preparation of SBN50 thin film. A KSBN75 seed layer was fabricated on substrates, and then pre-crystallized under the same conditions of SBN film synthesis. The reasons for the selection of KSBN75 seed layer are as follows ;

(a) KSBN75 has the tetragonal tungsten bronze structure.

(b) Synthesized KSBN75 precursor easily crystallizes to the tungsten bronze phase on substrates.

(c) Lattice mismatch between SBN50 and KSBN75 is small.

The value of lattice parameter of SBN50 is close to that of KSBN75. The lattice mismatch between SBN50 and KSBN75 is about 0.3 %.

Figure 2-3-22 shows XRD profiles of $(Sr_{0.5}Ba_{0.5})Nb_2O_6$ (SBN50) films crystallized at 700°C on MgO(100) and KSBN75/MgO(100) substrates. SBN50 thin films on MgO(100) and KSBN75/MgO(100) show strong two reflections as shown in Fig.2-3-22. From the XRD patterns, it was impossible to judge whether SBN50 thin films on MgO(100) and KSBN75/MgO(100) crystallized to tetragonal tungsten bronze or orthorhombic metastable phase, because SBN thin films crystallized on MgO(100) and KSBN75/MgO(100) had almost the same XRD profiles. SBN thin films on MgO(100) and KSBN75/MgO(100) substrates had to be characterized

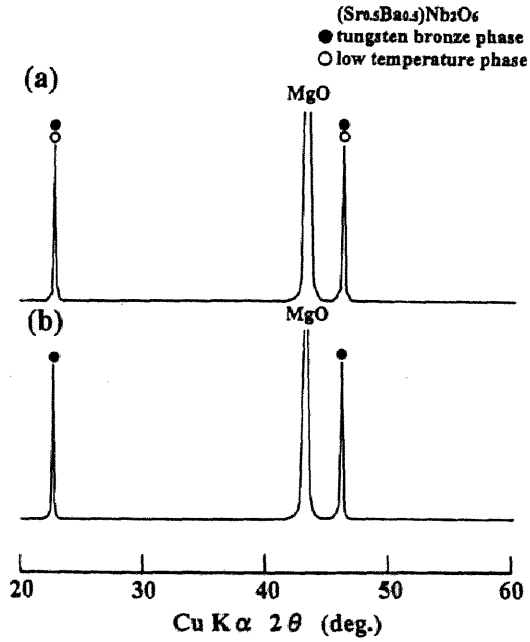


Fig.2-3-22 XRD profiles of SBN50 thin films (a) on MgO(100) and (b) on MgO(100) using KSBN75 seed layer heat-treated at 700°C.

further by Raman spectroscopy.

Figure 2-3-23 shows the Raman spectrum of SBN50 thin film on KSBN75/MgO(100) crystallized at 700°C. Different patterns of crystalline films were obtained as shown in Fig.2-3-13(a) and Fig.2-3-23. The spectrum pattern of SBN50 on MgO(100) in Fig.2-3-13(a) is composed of the tetragonal tungsten bronze and the orthorhombic low temperature phase.

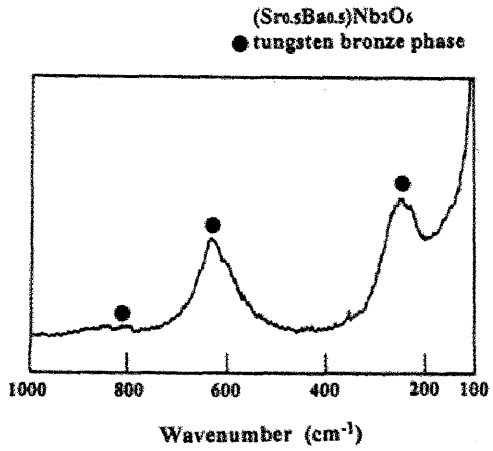


Fig.2-3-23 Raman spectrum of SBN50 thin film on MgO(100) using KSBN75 seed layer heat-treated at 700°C.

Heat-treatment at 1000°C was required to crystallize the single-phase tungsten bronze SBN50 film on MgO(100) (in section 2.3.4(1)). On the other hand, the spectrum of SBN50 thin films on KSBN75/MgO(100) shown in Fig.2-3-23 is in good accordance with that of tetragonal tungsten bronze SBN reported.[28] This results indicate that the crystallization temperature of tungsten bronze single phase can be decreased greatly by using the KSBN75 seed layer compared with SBN50 film prepared directly on MgO(100) and that the nucleation and growth of tungsten bronze SBN depend upon the KSBN75 seed layer. In addition, the formation of c-axis highly oriented film is attributed to the assistance of nucleation sites derived from the atomic alignment of substrates with a small mismatch.

In order to investigate the three dimensional crystallographic relation between SBN thin film and substrate, the X-ray pole figure measurement was employed. According to the X-ray pole figure, the c-plane of the additional SBN lattice should be considered to intersect a-plane of MgO, and the angle between a-axis of MgO and a-axis of the other SBN grain is 18.5°. The orientation for SBN50 thin films on KSBN75/MgO(100) was consistent with that for tungsten bronze SBN50 on MgO(100) crystallized at 1000°C and KSBN thin film on

MgO(100) crystallized at 700°C as described in section 2.3.4(3).

### 2.3.5 Electrical Properties of SBN and KSBN films

*(1) Dielectric properties of SBN50 Films*

The quality of the tungsten bronze SBN50 film crystallized at 1000°C was not good for the measurement of electrical properties, while SBN50 film crystallized at 700°C had a uniform thickness, no voids and cracks, which enable to characterize dielectric properties. The dielectric constant and loss tangent for SBN50 films on Pt(100)/MgO(100) substrates crystallized at 700°C are summarized in Table 2-3-2. Although the permittivity increases with increasing film thickness from 0.5 to 1.2 μm, the value of SBN thin film is much lower than that for SBN single crystals ($\varepsilon_{33}$=380, at 1 kHz).[30] Also the grain size of SBN films was confirmed to be about 50 nm by TEM micrographs. The presence of orthorhombic low temperature phase is considered to be the main reason for the lower $\varepsilon_r$ compared with single crystals. And so-called size effects, such as small grain sizes and stress from substrates are also responsible for the properties of synthesized film.

Table 2-3-2 Dielectric properties of SBN50 thin films crystallized at 700°C

| Substrate | Film Thickness (μm) | Dielectric Const. / Loss Tangent 10 kHz | 100 kHz | 1 MHz |
|---|---|---|---|---|
| Pt(100)/MgO(100) | 0.5 | 32 | 33 | 33 |
| | | 0.01 | 0.01 | 0.01 |
| | 1.2 | 79 | 73 | 72 |
| | | 0.07 | 0.03 | 0.02 |

*(2) Dielectric properties of SBN50 on KSBN75 films*

Tungsten bronze SBN50 thin films on KSBN75/Pt(100)/MgO(100) with prominent c-axis preferred orientation are confirmed by XRD and Raman spectroscopic analysis in section 2.3.4(4). The temperature dependence of dielectric constant and loss tangent for SBN50 film on KSBN75/Pt(100)/MgO(100) crystallized at 700°C are shown in Fig.2-3-24. The Curie temperature of the film was found to be about 70°C at 1 kHz, which depended on the measured frequency. The Curie temperature of the SBN50 film shifted to the low temperature region and the peaks of ε-T curve were broadened in comparison with the reported SBN single crystals.[31]

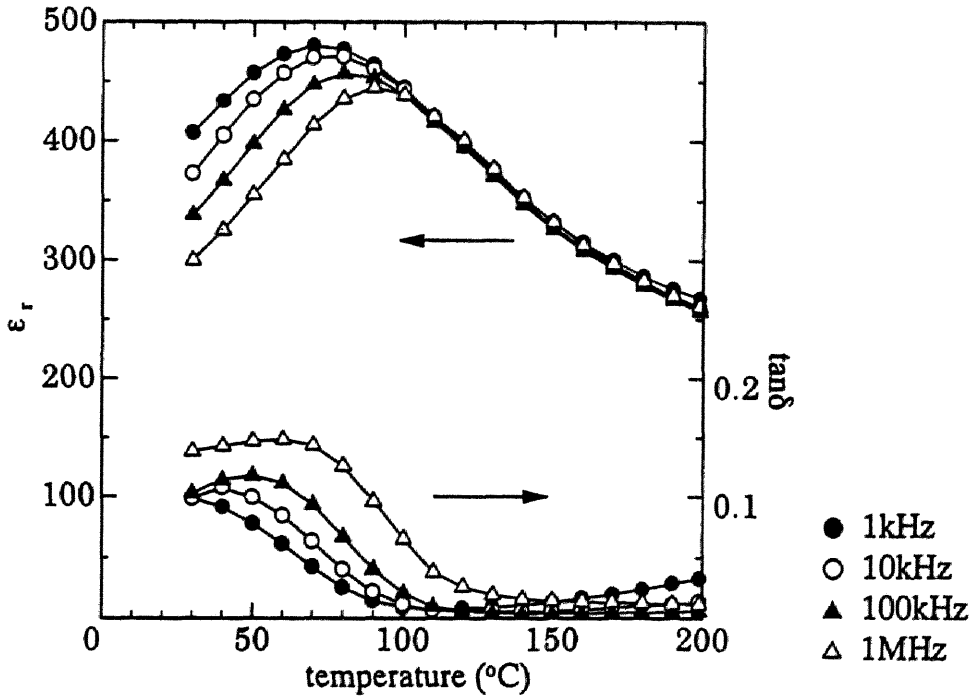


Fig.2-3-24 Temperature dependence of dielectric constant and loss tangent of SBN50 thin film on KSBN75/Pt(100)/MgO(100) substrate heat-treated at 700°C.

These results reveal that the films seem to behave as relaxor type character. This behavior is characteristic for the property along the c-axis of SBN single crystal, especially that has Sr rich compositions. The dielectric constant of the SBN50 thin film at $T_c$ is much lower than that of SBN50 single crystal.[31] Several factors such as small grain size, mechanical stress imposed on the films by the substrates may be responsible for the lower dielectric constant and diffuse phase transition.

*(3) Dielectric and ferroelectric properties of KSBN films*

Figure 2-3-25 shows SEM photographs of $K_{0.4}$SBN50 and KSBN75 thin films on Pt(100)/MgO(100) substrate crystallized at 700°C. The film thickness is about 0.5 μm after 20 cycles dipping (including 2 cycles dipping for underlayer). The surface smoothness of the tungsten bronze $K_{0.4}$SBN50 and KSBN75 films crystallized at 700°C was found to be good enough from the SEM surface images. In addition, those films have a uniform thickness, no voids and cracks, which enable to characterize dielectric and ferroelectric properties.

Figure 2-3-26 shows the temperature dependence of the dielectric constant and loss tangent for the $K_{0.4}(Sr_{0.5}Ba_{0.5})_{0.8}Nb_2O_6$ ($K_{0.4}$SBN50) film crystallized at 700°C on a Pt(100)/MgO(100) substrate. The dielectric maximum of the $K_{0.4}$SBN50 film was observed at around 140°C at 1 kHz. The Curie point ($T_c$) of the $K_{0.4}$SBN50 thin film is a much lower than that for potassium substituted SBN bulk ceramics.[9] The value of dielectric constant at the Curie point is much lower than that of SBN50 single crystals.[31] The peaks of ε-T curves are broadened compared with SBN single crystals. Also, the temperatures of the dielectric constant maxima depend slightly upon the frequency of measurement. Ferroelectric tungsten bronze niobate crystals are known to show the difference in several properties for each direction of the crystal. Especially, the dielectric properties of SBN single crystal for along a-axis and c-axis are significantly different as shown in Fig.1-3-4 (Chap.1). The present KSBN films have highly preferred orientation for c-axis. The films showed the characteristic properties along the c-axis of SBN crystal. This behavior is considered to be the relaxor type. The cations of $K^+$, $Sr^{2+}$ and $Ba^{2+}$ may occupy more randomly the sites constructed

by the Nb-O octahedron in the tungsten bronze structure compared with single crystals. In addition, the grain size of the $K_{0.4}$SBN50 thin film ranged from 50 to 100 nm observed by atomic force microscope (AFM) images. These features might reflect the diffuse phase transition of the $K_{0.4}$SBN50 thin film on Pt(100)/MgO(100). Figure 2-3-27 shows the temperature dependence of the dielectric constant and loss tangent measured at 10 kHz for KSBN75 film crystallized at 700°C on a Pt(100)/MgO(100) substrate. The dielectric maximum of the KSBN75 film is observed at around 50-70°C. The Curie point of the KSBN75 thin film is a little higher than that for SBN75 single crystals reported by Huang et al.[31] The value of the dielectric constant is also much lower than that of SBN75 single crystals as in the case of $K_{0.4}$SBN50 film. The grain size of the KSBN75 thin film was also confirmed to be approximately 100 nm. The substitution with potassium is one of the reasons for the shift of the Curie point, because, in general, the Curie temperature of SBN shifts to higher temperature side by substitution with alkali ion.[11,12] Additional factors, such as mechanical stress imposed on the films by the substrates, may be responsible for the shift and smearing of the Curie point.

The P-E hysteresis loop was measured so as to study the ferroelectric behavior of the KSBN films. In this case, the measurement at low temperatures was carried out, since the ferroelectric phase was supposed to be stable to exhibit nearly saturated P-E hysteresis loops. Figure 2-3-28 shows a typical P-E hysteresis loop (Fig.2-3-28(a)) and temperature dependence of remnant polarization (Fig.2-3-28(b)) for a $K_{0.4}$SBN50 thin film crystallized at 700°C on a Pt(100)/MgO(100) substrate measured under vacuum. The hysteresis measured at −190°C shows the remnant polarization ($P_r$) of 22 μC/cm$^2$ and the coercive field ($E_c$) of 99 kV/cm (Fig.2-3-28(a)). The typical ferroelectric P-E hysteresis loops were also observed at 20°C. The values of remnant polarization were gradually decreased with raising measurement temperature as shown in Fig.2-3-28(b). The change in $P_r$ is strongly related to the diffuse phase transition of the ε-T curves in Fig.2-3-26. The shape of hysteresis loop changed from typical ferroelectric one to

paraelectric one. This behavior is in accordance with the result for non-substituted SBN.[19] Also, the remnant polarization of $K_{0.4}$SBN50 thin film is lower than that of SBN single crystal (32 $\mu C/cm^2$).[30] Figure 2-3-29 shows the P-E hysteresis loops for a KSBN75 thin film crystallized at 700°C on a Pt(100)/MgO(100) substrate. The P-E hysteresis loops were measured at −190°C and 20°C. The remnant polarization ($P_r$) is 12 $\mu C/cm^2$, and the coercive field ($E_c$) is 100 kV/cm at −190°C. Similar to the results of $K_{0.4}$SBN50 film on Pt(100)/MgO(100) described above, the value of remnant polarization gradually decreased as the temperature of measurement is raised. There is a strong relation between the change in the hysteresis loop and the diffuse phase transition of the ε-T curve in Fig.2-3-27. The remnant polarization of KSBN75 thin film also showed a lower value than that of SBN75 single crystal (27 $\mu C/cm^2$).[30] SBN films are reported to show small polarization.[19] Effects of the substitution with potassium, small grain size and stress from substrates are responsible not only for the lower $P_r$ value but also for the higher $E_c$ compared with single crystals. Further studies on the effect of substitution with potassium, the Sr/Ba ratio and the lattice mismatch with substrates on the properties of KSBN films are required to clarify the dielectric behavior of KSBN film in more detail.

(a)

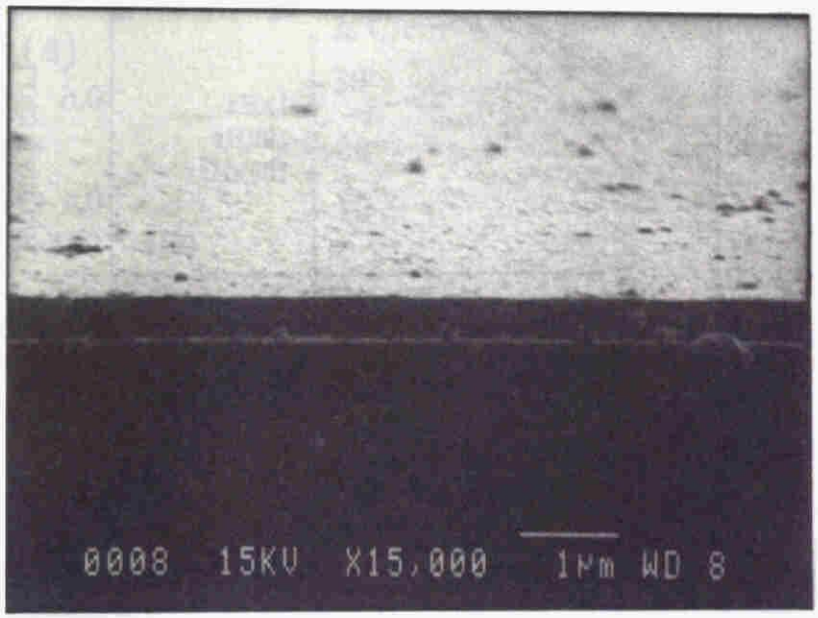


(b)

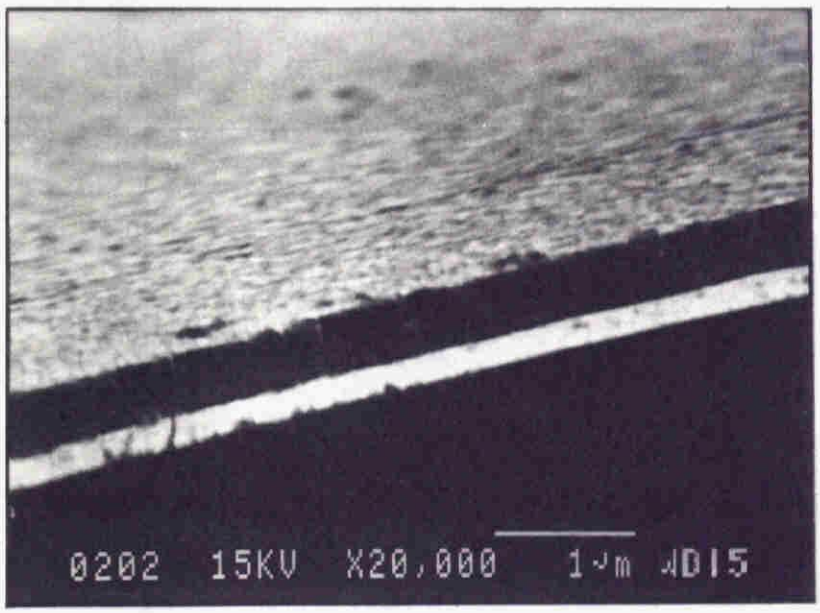


Fig.2-3-25 SEM photographs of (a) $K_{0.4}$SBN50 and (b) KSBN75 thin films on Pt(100)/MgO(100) substrates crystallized at 700°C.

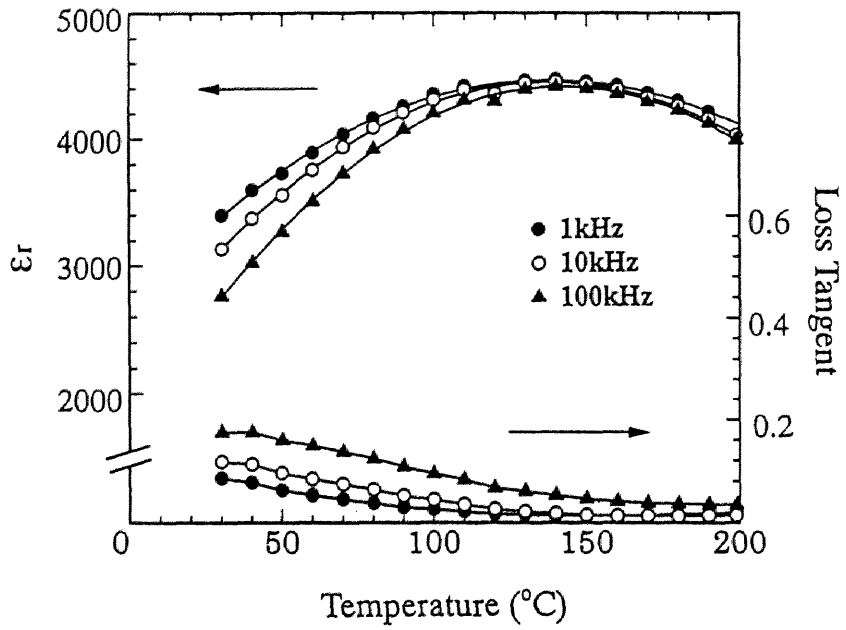


Fig. 2-3-26 Temperature dependence of dielectric constant and loss tangent of $K_{0.4}$SBN50 thin film on Pt(100)/MgO(100) substrate crystallized at 700°C.

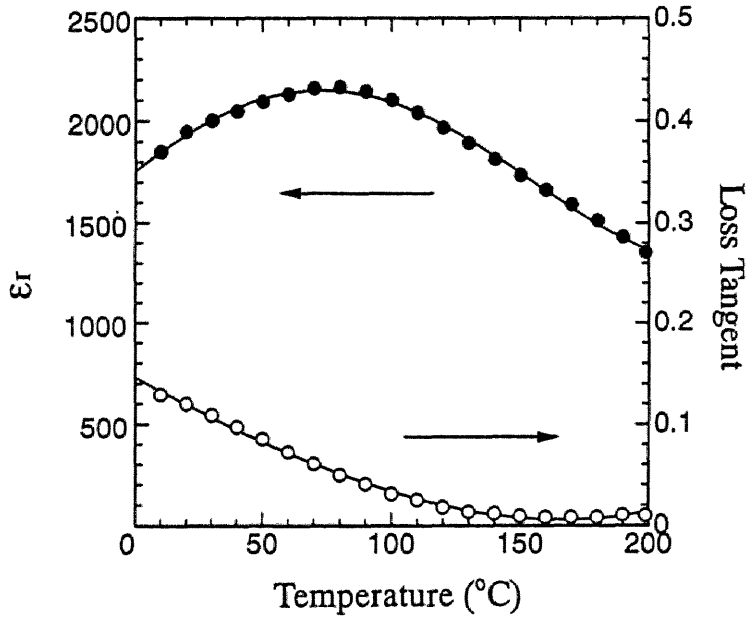


Fig.2-3-27 Temperature dependence of dielectric constant and loss tangent of KSBN75 thin film on a Pt(100)/MgO(100) substrate heat-treated at 700°C measured at 10 kHz.

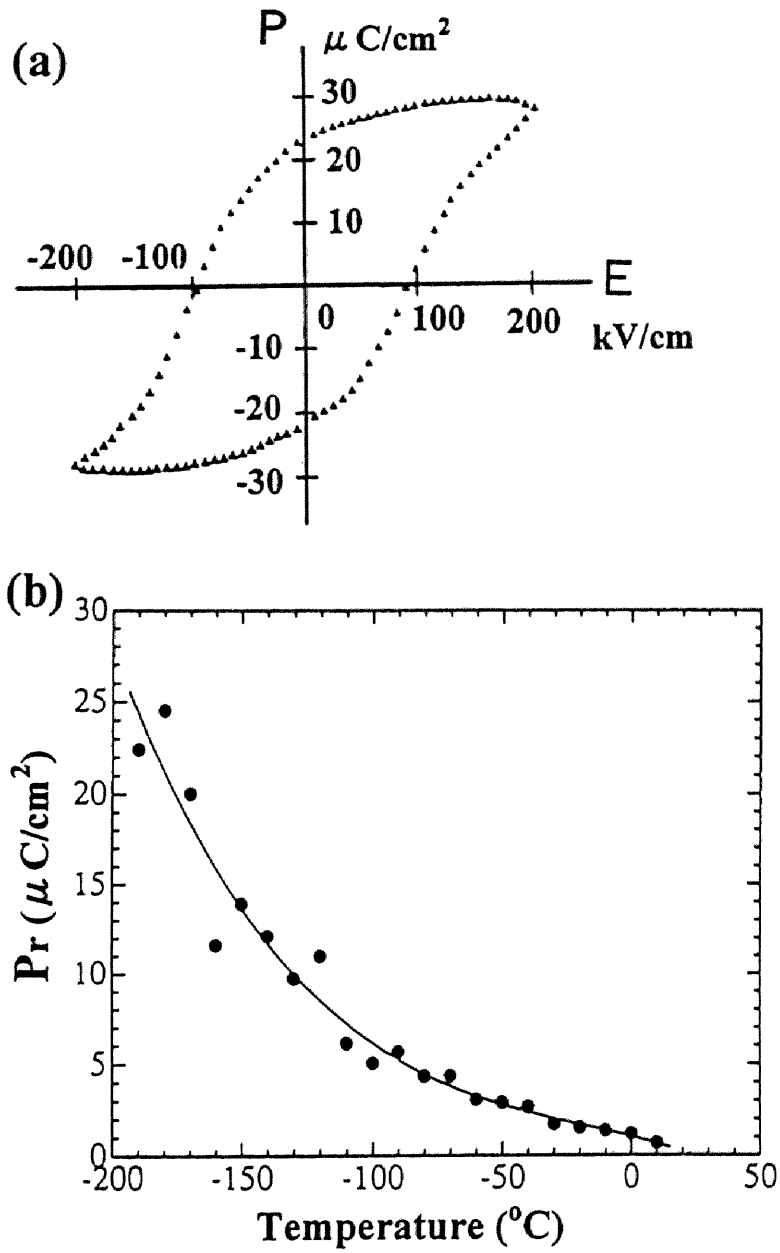


Fig. 2-3-28 (a) P-E hysteresis loop and (b) temperature dependence of remnant polarization change for $K_{0.4}$SBN50 thin film on Pt(100)/MgO(100) substrate crystallized at 700°C.

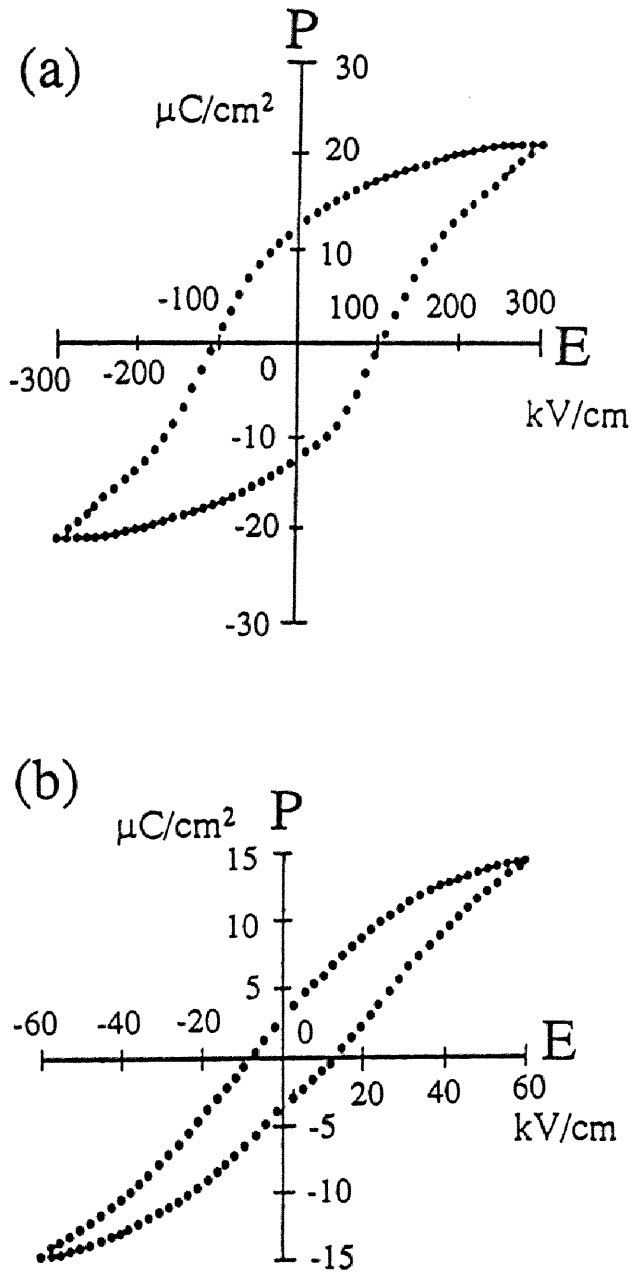


Fig.2-3-29 P-E hysteresis loops of KSBN75 thin film on a Pt(100)/MgO(100) substrate crystallized at 700°C measured at (a) −190°C and (b) 20°C.

### 2.3.6 Optical properties of KSBN thin films

The KSBN film prepared by the chemical solution process has a smooth surface and quite small grain sizes confirmed by AFM images. Optical properties of KSBN films crystallized at 700°C on fused silica and MgO(100) substrates were characterized. Since the laser light propagation and propagation loss depend also upon the transparency of the film, the preparation of transparent KSBN films is required to achieve the optimal properties of KSBN. The KSBN films formed on fused silica and MgO(100) substrates were highly transparent. SEM photographs are shown in Fig.2-3-30. These films have a quite smooth surface topology with no cracks and voids. Optical transmittance measured in the wavelength from 190 to 2600 nm is shown in Fig.2-3-31. The absorption edge is 340 nm, which is consistent with the reported value. The interference pattern indicates that the film has a uniform thickness. The film thickness estimated from the interference was in good agreement with that observed by SEM. The transparency of the KSBN film degrades with increasing processing temperature above 800°C. The low processing temperature is also desired to synthesize the highly transparent KSBN films for laser beam propagation measurement.

In order to investigate the qualities of the KSBN films for application in the optical wave guide devices, the optical propagation and the refractive indices of synthesized films were examined by a prism coupler waveguide method, illustrated in Fig.2-3-32. The beam entered into the high-refractive-index prism made of $TiO_2$ (rutile) normally undergoes total internal reflection at the prism/film interface. At a certain incidence angle, the light disobeys the total reflection conditions, and enters into the film. Thus, the beam by the total reflection causes a sharp drop in intensity. The refractive index of each mode can be determined by recording these angles with known refractive index and base angle of the prism. According to Snell's law, this mode index is the ratio of the velocity of light in vacuum to the velocity of the mode in the waveguide. The incident light is generally polarized either parallel or perpendicular to the waveguide plane. For a uniform, isotropic slab waveguide, the corresponding characteristic propagating

modes are referred to as "TE" (transverse electric) and "TM" (transverse magnetic) modes, respectively. If the crystal axes are appropriately oriented, the same designation can be suitable for anisotropic guides or guides on anisotropic substrates. Both the refractive indices and the film thickness are calculated from the observed modes. Ferroelectric tungsten bronze niobate crystals are well-known to have high refractive index (above 2.28) compared with $SiO_2$ glass (1.46) and MgO(1.60). Figure 2-3-33 shows the TE-mode observation via the prism coupling method for the $K_{0.4}$SBN50 thin films prepared on MgO(100) substrates. Three modes, numbers (m) 0, 1 and 2, appear in both the TE and TM modes. The calculated refractive index and film thickness from the three mode angles in TE mode were about 2.27 and 0.5 μm, respectively. The values of refractive indices for TE- and TM-observation were about 2.27 and 2.23, respectively which indicates the birefringence of the KSBN films. The refractive indices of synthesized KSBN thin films on substrates were summarized in Table 2-3-3. Although KSBN films on fused silica substrates also showed c-axis preferred orientation, the birefringence becomes smaller because the degree of c-axis orientation, which is also the optic axis, is low compared with the film prepared on MgO(100). The values of refractive index are consistent with those of tungsten bronze niobate single crystals [for example, SBN60 (2.29)]. The good agreement of the refractive index with that of single crystal reveals that the KSBN film is almost fully dense. This film was dense enough to show the high refractive index and found to have a potential for application in optical wave-guide by combining with the micro-patterning process.

(a)

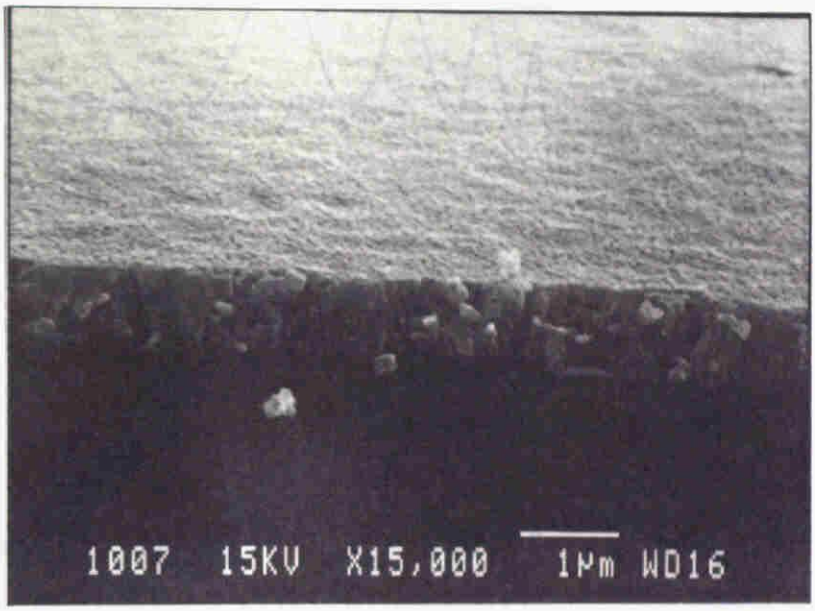


(b)

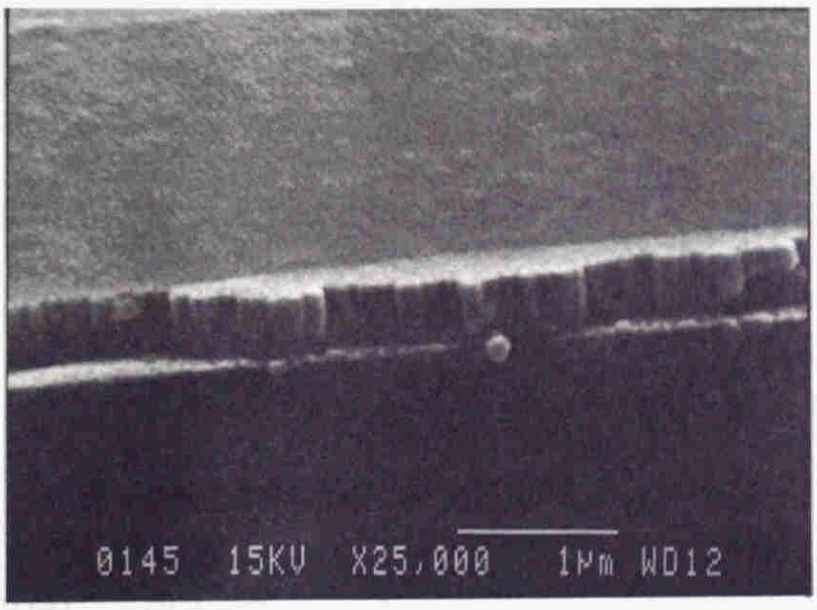


Fig.2-3-30 SEM photographs of $K_{0.4}$SBN50 thin films on (a) fused silica and (b) MgO(100) substrates.

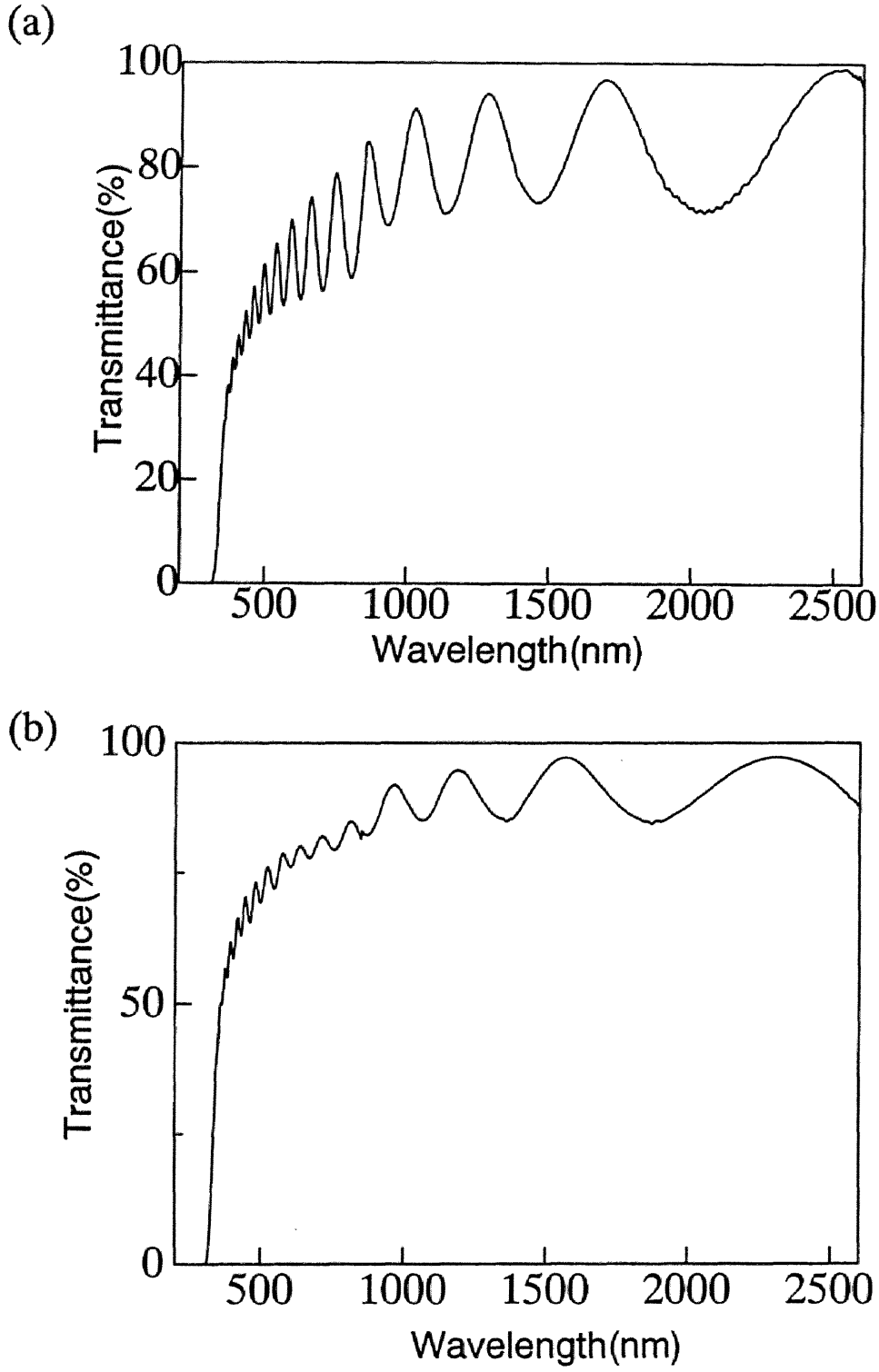


Fig.2-3-31 Optical transmittance of $K_{0.4}$SBN50 thin films on (a) fused silica and (b) MgO(100) substrates crystallized at 700°C.

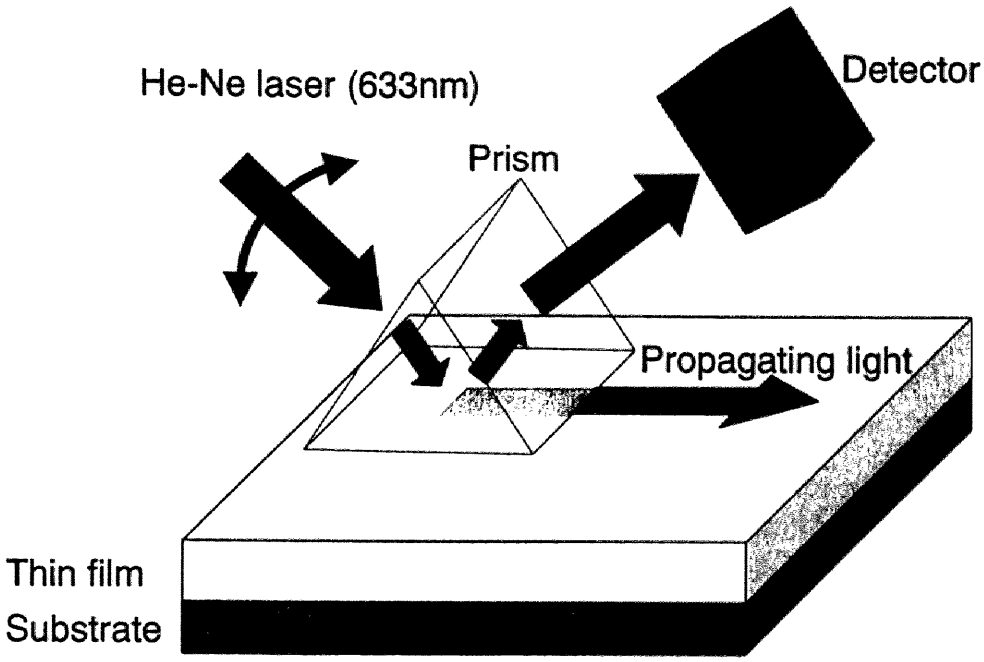


Fig.2-3-32 Setup for the optical propagation measurement in the KSBN thin films on fused silica and MgO(100) substrates (mode measurement).

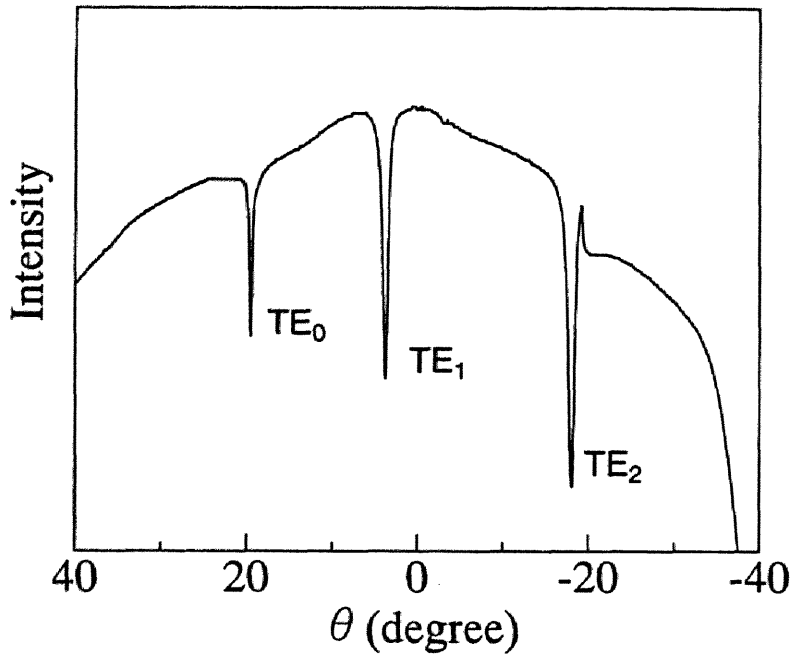


Fig.2-3-33 Optical-propagation for the $K_{0.4}$SBN50 thin film on MgO(100) substrate crystallized at 700°C (TE-mode observation).

Table 2-3-3 Refractive indices of synthesized KSBN thin films

| | refractive Index | |
|---|---|---|
| | **TE mode** | **TM mode** |
| **KSBN50/fused silica** | 2.25 | 2.24 |
| **KSBN50/MgO(100)** | 2.27 | 2.23 |
| **KSBN75/fused silica** | 2.25 | 2.25 |

## 2.4 Conclusions

Crack-free SBN ($Sr_{1-x}Ba_xNb_2O_6$) and potassium substituted SBN ($K_y(Sr_{1-x}Ba_x)_{1-y/2}Nb_2O_6$ [KSBN]) films with highly preferred orientation were successfully synthesized on MgO(100) and Pt(100)/MgO(100) substrates through metallo-organics. The results shown in chapter 2 are summarized as follows :

1. A homogeneous, stable SBN and KSBN precursor solutions were prepared by controlling the reaction of strontium metal, barium metal, potassium ethoxide and niobium ethoxide in a mixture solvent of absolute ethanol and 2-ethoxyethanol. $^{1}H$, $^{13}C$ and $^{93}Nb$ NMR showed that the SBN and KSBN precursors were stabilized by the coordination of 2-ethoxyethoxy group to metals. The structure of SBN and KSBN precursors were found to consist of complex alkoxides, such as $Sr[Nb(OR)_6]_2$, $Ba[Nb(OR)_6]_2$ and $K[Nb(OR)_6]$ with highly symmetric Nb-O octahedron.
2. Synthesized SBN precursor powders are found to crystallize in the SBN low temperature phase prior to form the tetragonal tungsten bronze SBN. The structure of the SBN low temperature phase was also found to be the orthorhombic $SrNb_2O_6$ like structure in Sr rich composition range. For the SBN film synthesis, a mixture of orthorhombic SBN (not tungsten bronze) phase and tetragonal SBN (tungsten bronze) phase crystallized at 700°C on MgO(100) substrates, which was completely transformed to the single-phase tetragonal SBN at 1000°C. The incorporation of potassium promoted the direct crystallization of KSBN precursor powders and thin films in the tetragonal tungsten bronze phase without any intermediate formation of the low-temperature phase.
3. SBN and KSBN films on MgO(100) and Pt(100)/MgO(100) showed a prominent c-axis preferred orientation. Two crystal lattice planes of tungsten bronze SBN and KSBN were intrergrown at an orientation of 18.5° on MgO(100) and Pt(100)/MgO(100). Tungsten bronze KSBN thin films on fused silica substrates with c-axis preferred orientation also fabricated using a KSBN underlayer.

4. By using KSBN75 thin film as a seed layer, SBN50 thin films on MgO(100) substrates directly crystallized to the tetragonal tungsten bronze phase at 700°C, which is about 300°C lower than that of SBN50 film without seed layer.
5. The Curie temperature of the KSBN film on Pt(100)/MgO(100) was found to depend on the chemical composition. The ferroelectric KSBN phase was stable enough around the room temperature and underwent the gradual phase transition with increasing temperature. The change in remnant polarization with temperature is strongly related to the diffuse phase transition of the ε-T curves. SBN50 thin films on KSBN75/Pt(100)/MgO(100) showed diffuse phase transition as a relaxor dielectrics.
6. Synthesized tungsten bronze KSBN thin films on fused silica and MgO(100) substrates showed high transparency with wide wavelength region and were found to propagate the He-Ne laser light. The refractive indices of the KSBN50 films were calculated to be 2.27 and 2.23 from the angles of observed TE and TM modes, respectively, which showed the birefringence.

## References


1. M.H.Francombe, "The Relation between Structure and Ferroelectricity in Lead Barium and Barium Strontium Niobates", *Acta Cryst.*, **13** 131-140 (1960).

2. B.Jaffe, W.R.Cook Jr and H.Jaffe, "Chapter 9 Non-Perovskite oxide piezoelectrics and ferroelectrics", Chap. 9, pp. 213-235 in Piezoelectric ceramics, Academic Press, New York (1971).

3. A.A.Ballman and H.Brown, "The Growth and Properties of Strontium Barium Methaniobate, $Sr_{1-x}Ba_xNb_2O_6$, a Tungsten Bronze Ferroelectric", *J. Cryst. Growth*, **1** 311-314 (1967).

4. A.M.Glass, "Investigation of the Electrical Properties of $Sr_{1-x}Ba_xNb_2O_6$ with Special Reference to Pyroelectric Detection", *J. Appl. Phys.*, **40** [12] 4699-4713 (1969).

5. P.V.Lenzo, E.G.Spencer and A.A.Ballman, "Electro-optic coefficients of Ferroelectric Strontium Barium Niobate", *Appl. Phys. Lett.*, **11** [1] 23- (1967).

6. R.R.Neurgaonkar and W.K.Cory, "Progress in Photorefractive Tungsten Bronze Crystals", *J. Opt. Soc. Am. B*, **3** [2] 274-282 (1986)

7. M.D.Ewbank, R.R.Neurgaonkar, W.K.Cory and J.Feinberg, "Photorefractive properties of Strontium-Barium Niobate", *J. Appl. Phys.*, **62** [2] 374-380 (1987).

8. D.Rytz, B.A.Wechsler, R.N.Schwartz, C.C.Nelson, C.D.Brandle, A.J.Valentino and G.W.Berkstresser, "Temperature Dependence of Photorefractive Properties of Strontium-Barium Niobate ($Sr_{0.6}Ba_{0.4}Nb_2O_6$)", *J. Appl. Phys.*, **66** [5] 1920-1924 (1989).

9. E.A.Giess, B.A.Scott, G.Burns, D.F.O'kane and A.Segmuller, "Alkali Strontium-Barium-Lead Niobate Systems with a Tungsten Bronze Structure : Crystallographic Properties and Curie Points", *J. Am. Ceram. Soc.*, **52** [5] 276-281 (1969).

10. R.R.Neurgaonkar, W.K.Cory, J.R.Oliver, M.D.Ewbank and W.F.Hall, "Development and Modification of Photorefractive Properties in the Tungsten Bronze Family Crystals", *Optical Engineering*, **26** [5] 392-405 (1987).

11. K.Umakantham, S.N.Murty, K.S.Rao and A.Bhanumathi, "Effect of Rare-Earth Ions on the Properties of Modified (Sr,Ba)$Nb_2O_6$ Ceramics", *J. Mat. Sci. Lett.*, **6** 565-567 (1987).

12. A.Bhanumathi, S.N.Murty, K.Umakantham, K.C.Mouli, G.Padmavathi, K.T.Rao and V.Syamalamba, "Ferroelectric Properties of Tungsten Bronze Ceramics", *Ferroelectrics* **102** 173-181 (1990).

13. N.S.VanDamme, A.E.Sutherland, L.Jones, K.Bridger and S.R.Winzer, "Fabrication of Optically Transparent and Electrooptic Strontium Barium Niobate Ceramics", *J. Am. Ceram. Soc.*, **74** [8] 1785-1792 (1991).

14, S.Nishiwaki, J.Takahashi and K.Kodaira, "Effect of Additives on Microstructure Development and Ferroelectric Properties of $Sr_{0.3}Ba_{0.7}Nb_2O_6$ Ceramics", *Jpn. J. Appl. Phys.*, **33** [9B] 5477-5481 (1994).

15, K.Nagata, Y.Yamamoto, H.Igarashi and K.Okazaki, "Properties of the Hot-Pressed Strontium Barium Niobate Ceramics", *Ferroelectrics*, **38** 853-856 (1981).

16. K.Megumi, N.Nagatsuma, Y.Kashiwada, Y.Furuhata, "The Congruent Melting Composition of Strontium Barium Niobate", *J. Mater. Sci.*, **11** 1583-1592 (1976).

17. R.R.Neurgaonkar, M.H.Kalisher, T.C.Lim, E.J.Staples and K.L.Keester, "Czochralski Single Crystal Growth of $Sr_{0.61}Ba_{0.39}Nb_2O_6$ for Surface Acoustic Wave Applications", *Mater. Res. Bull.*, **15** 1235-1240 (1980).

18, R.R.Neurgaonkar and E.T.Wu, "Epitaxial Growth of Ferroelectric T.B. $Sr_{1-x}Ba_xNb_2O_6$ Films for Optoelectronic Applications", *Mater. Res. Bull.*, **22** 1095-1102 (1987).

19. R.R.Neurgaonkar, I.S.Santha and J.R.Oliver, "Growth of Grain-Oriented Tungsten Bronze SBN Films on Si", *Mater. Res. Bull.*, **26** 983-988 (1991).

20. S.Hirano, T.Yogo, K.Kikuta and K.Ogiso, "Preparation of Strontium Barium Niobate by Sol-Gel Method", *J. Am. Ceram. Soc.*, **75** [6] 1697-1700 (1992).

21. J.D.Mackenzie, "Nonlinear Optical Materials by Sol-Gel Method", *J. Sol-Gel Sci. Tech.*, **1** 7-19 (1993).

22. Y.Xu, C.J.Chen, R.Xu and J.D.Mackenzie, "Ferroelectric $Sr_{0.6}Ba_{0.4}Nb_2O_6$ Thin Films by the Sol-Gel Process: Electrical and Optical Properties", *Phys. Rev. B*, **44** [1] 35-41 (1991).

23. C.J.Chen, Y.Xu, R.Xu and J.D.Mackenzie, "Ferroelectric and Pyroelectric Properties of Strontium Barium Niobate Films Prepared by the Sol-Gel Method", *J. Appl. Phys.*, **69** [3] 1763-1765 (1991).

24. K.Iijima, R.Takayama, Y.Tomita and I.Ueda, "Epitaxial Growth and Pyroelectric Properties of Lanthanum-Modified Lead Titanate Thin Films", *J. Appl. Phys.*, **60** [8] 2914-2919 (1986).

25. S.Govil, P.N.Kapoor and R.C.Mehrotra, "Double Isopropoxides of Niobium and Tantalum with Alkaline Earth Metals", *J. Inorg. Nucl. Chem.*, **38** [1] 172-173 (1976).

26. R.C.Mehrotra, M.M.Agrawal and P.N.Kapoor, "Alkali-Metal Hexaalkoxides of Niobium and Tantalum", *J. Chem. Soc.* (A), 2673-2676 (1968).

27. Y.Repelin, E.Husson et H.Brusset, "Etude par spectroscopies d'absorption i.r. et de diffusion Raman des composes $A^{II}B_2{}^{V}O_6$ de structure de type "blocs 1×2" -I. Etude du niobate de baryum $BaNb_2O_6$", *Spectrochimica Acta*, **35A** 937-948 (1979).

28. G.Burns, F.H.Dacol, R.R.Neurgaonkar, A.S.Bhalla and R.Guo, "Raman Measurements of the Ferroelectric $Ba_{0.4}Sr_{0.6}Nb_2O_6$", *Ferroelectrics*, **108** 189-193 (1990).

29. S.S.Thony, K.E.Youden, J.S.Harris, Jr., and L.Hesselink, "Growth of Epitaxial Strontium Barium Niobate Thin Films by Pulsed Laser Deposition", *Appl. Phys. Lett.* **65** [16] 2018-2020 (1994).

30. R.R.Neurgaonkar, W.F.Hall, J.R.Oliver, W.W.Ho and W.K.Cory, "Tungsten Bronze $Sr_{1-x}Ba_xNb_2O_6$ : A Case History of Versatility", *Ferroelectrics*, **87** 167-179 (1988).

31. W-H.Huang, D. Viehland and R.R.Neurgaonkar, "Anisotropic GlassLike Characteristics of Strontium Barium Niobate Relaxors", *J. Appl. Phys.*, **76** [1] 490-496 (1994).

# Chapter 3

## Synthesis and Properties of Strontium Potassium Niobate (SKN) Thin Films

## 3.1 Introduction

Strontium potassium niobate ($Sr_2KNb_5O_{15}$, SKN) is a ferroelectric material and has a tetragonal tungsten bronze structure, and constitutes filled tungsten bronze.[1-4] The electrical properties of SKN are comparable with those of $Sr_{1-x}Ba_xNb_2O_6$ (SBN) solid solution and summarized in Table 3-1-1.[5-7] Therefore, SKN has been expected for applications in infrared detectors, SAW filters and several electro-optic devices because of its excellent pyroelectric, piezoelectric, electro-optic properties.[5-9]

Table 3-1-1 Properties of $Sr_{0.6}Ba_{0.4}Nb_2O_6$ and $Sr_2KNb_5O_{15}$ (Ref. 6)

| Property | $Sr_{0.6}Ba_{0.4}Nb_2O_6$ | $Sr_2KNb_5O_{15}$ |
|---|---|---|
| Lattice Constants(Å) | a =12.462 | a =12.470 |
| | c = 3.938 | c = 3.942 |
| Curie Temp. $T_c$ (℃) | 72 | 150 |
| Dielectric Constant, after poling, at 23℃ | $\varepsilon_{33}$ = 470 | $\varepsilon_{33}$ = 760 |
| | $\varepsilon_{11}$ = 204 | $\varepsilon_{11}$ = 750 |
| Piezoelectric Coeff. ($10^{-12}$ C/N) | $d_{33}$ = 130 | - |
| | $d_{15}$ = 31 | - |
| SAW Electromechanical Coupling Constant | 180 ×$10^{-4}$ | 90 ×$10^{-4}$ |
| Pyroelectric Coeff. ($\mu C/m^2$-°C) | 850 | 650 |
| Electro-Optic Coeff. $r_{33}$ (m/V) | 420 × $10^{-12}$ | 160 × $10^{-12}$ |
| Electro-Mechamical Coupling Coeff. | $k_{33}$ = 0.47 | $k_{33}$ = 0.44 |
| | $k_{15}$ = 0.24 | $k_{15}$ = 0.26 |
| Spontaneous Polarization, $P_s$, ($C/m^2$) | 0.65 | - |

SKN ceramics have been prepared by the solid state reaction of oxide powders at 1300-1350°C via the conventional firing and milling techniques.[10-12] Hot-pressing is very effective to improve both the density and the degree of grain orientation of sintered SKN ceramics.[12] SKN single crystals have been grown mainly by the Czochralski method.[5-7,13,14] However, the growth of single crystals is usually difficult to control the composition. Recently, the demand for thin film

processing has increased for integrated-device development.[15,16] Highly c-axis (direction of polarization of SKN crystal) oriented tungsten bronze SKN thin films are proposed for pyroelectric, piezoelectric and electro-optic applications. However, synthesis of SKN films has not been reported yet.

This chapter describes the synthesis of highly oriented tungsten bronze SKN thin films by controlling the reaction of metal alkoxides. The structure of SKN precursor was characterized by $^{1}H$, $^{13}C$ and $^{93}Nb$ nuclear magnetic resonance (NMR) spectroscopy. The crystallization process and orientation of SKN films on substrates were investigated. Dielectric properties of oriented SKN films on Pt(100)/MgO(100) substrates were also evaluated.

## 3.2 Experimental

Figure 3-2-1 shows an experimental procedure for fabrication of $Sr_2KNb_5O_{15}$ (SKN) powders and thin films. Sr metal [Raremetallic, Japan], $KOCH_2CH_3$, (KOEt) [Ko-jundo Chemical, Japan] and $Nb(OCH_2CH_3)_5$, ($Nb(OEt)_5$) [Trichemical and Ko-jundo Chemical, Japan] were selected as starting materials. Ethanol was dried over magnesium ethoxide and distilled prior to use as absolute ethanol. All procedures were conducted in a dry $N_2$ atmosphere, because starting materials are extremely sensitive to moisture. Metallic Sr was dissolved in absolute ethanol. The solution was refluxed for 2 h and then KOEt corresponding to the $Sr_2KNb_5O_{15}$ composition was added. After dissolving KOEt at room temperature, the solution was mixed with $Nb(OEt)_5$ solution. The mixed solution was refluxed again for 18 h to react the metal alkoxides. Then, the solution was condensed to approximately 0.1 mol/l by removal of solvent by vacuum evaporation.

Films were fabricated using the precursor solution by dip-coating on fused silica, MgO(100) and Pt(100)/MgO(100) substrates. A Pt(100) layer was deposited on MgO(100) by the same process described in Chapter 2. The withdrawal rate of substrate from the precursor solution, the treatment of substrates prior to dip-coating and drying process after coating were carried out by the same way as

for the SBN and KSBN films (in Chap.2). After the film was calcined at 350°C for 1 h at a heating rate of 5°C/min, the film was heated at a crystallization temperature for 1 h, and then cooled down in dry $O_2$ flow at a rate of 5°C/min. The coating-crystallization process was repeated several times to increase the thickness of the film. The thickness of crystallized film per dip coating was 0.05 μm, when the precursor film was withdrawn at a rate of 0.6 mm/s with 0.1 mol/l solution. For the preparation of SKN films on MgO(100) and Pt(100)/MgO(100) substrates, an underlayer was precoated using 0.01 mol/l SKN precursor solution at a withdrawal rate of 0.6 mm/s. The thin layer of SKN precursor on MgO(100) and Pt(100)/MgO(100) was heat-treated at 750°C under the same conditions described above. Then the precursor film was coated on the precrystallized SKN underlayer using 0.1 mol/l solution.

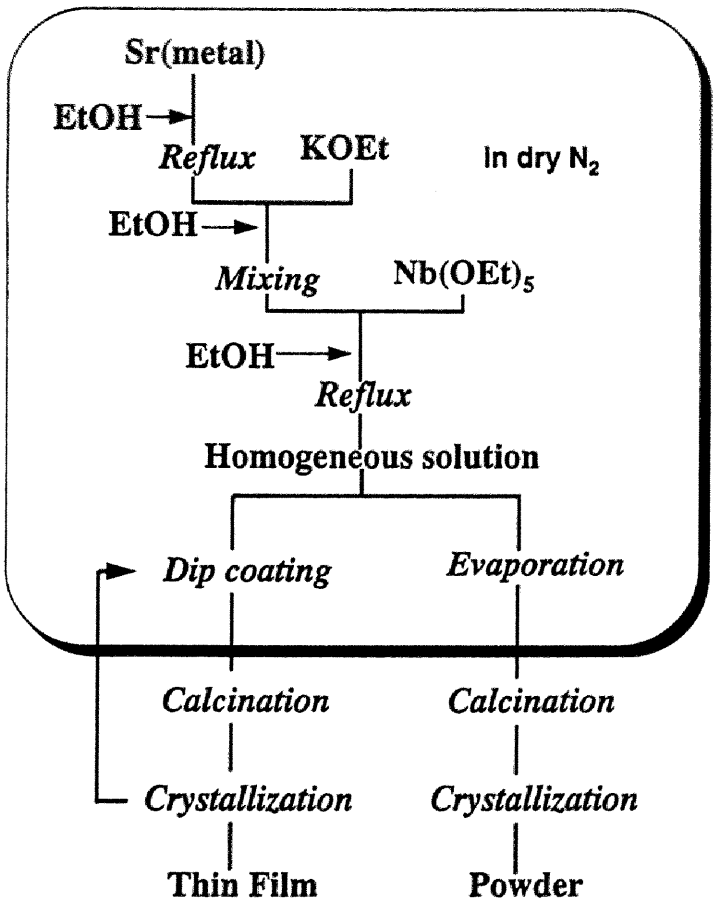


Fig.3-2-1 Experimental procedure for preparation of $Sr_2KNb_5O_{15}$ (SKN) powders and thin films.

Powders were also prepared from the precursor solution to investigate the crystallization behavior. The solvent was removed from the SKN solution by vacuum evaporation. The SKN precursor was calcined at 300°C to yield a brown solid, which was then heat-treated at temperatures between 550°C and 700°C in an oxygen flow for 1 h at a rate of 10°C/min.

The characterization methods of SKN precursor in solution, crystallographic phases of powder and thin film samples, the transmittance of synthesized film on substrate, microstructures and electrical properties are the same as in Chap.2.

## 3.3 Results and discussion

### 3.3.1 Synthesis of precursor solutions

A stable and homogeneous $Sr_2KNb_5O_{15}$ (SKN) precursor solution was prepared by the reaction of Sr, KOEt and $Nb(OEt)_5$ in ethanol. The structure of SKN precursor in solution was analyzed by $^1H$, $^{13}C$ and $^{93}Nb$ NMR spectroscopy as in the case of SBN and KSBN (Chap.2, section 2.3.1).

Figure 3-3-1 shows $^1H$ NMR spectra of the SN ($SrNb_2O_6$), the KN ($KNbO_3$) and the $Sr_2KNb_5O_{15}$ (SKN) precursor. The signals of ethoxy groups ($CH_3CH_2O$) of the SN precursor are observed at 1.23, 1.31 ppm ($C\underline{H}_3CH_2O$-) and 4.25, 4.36 ppm ($CH_3C\underline{H}_2O$-) in Fig.3-3-1(a). The SN precursor comprises two kinds of ethoxy groups, which correspond to

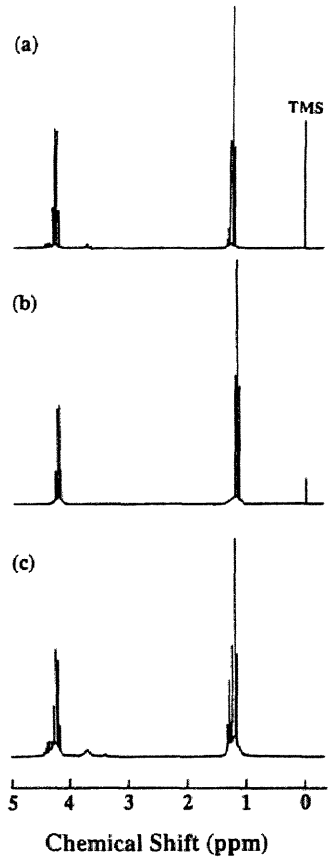


Fig.3-3-1 $^1H$ NMR spectra of (a) $SrNb_2O_6$ (SN) precursor, (b) $KNbO_3$ (KN) precursor and (c) $Sr_2KNb_5O_{15}$ (SKN) precursor.

the bridged and terminal confirmed by the integration ratio. The KN precursor shows the signals of ethoxy groups ($CH_3CH_2O$) at 1.18 ppm ($C\underline{H}_3CH_2O$-) and 4.24 ppm ($CH_3C\underline{H}_2O$-) in Fig.3-3-1(b). The ethoxide ligands on metals of the KN precursor almost are equivalent. Figure 3-3-1(c) shows $^1H$ NMR spectrum of the SKN precursor. The signals of ethoxy groups bonded to metal atoms ($CH_3CH_2O$) are observed at 1.21, 1.30 ppm ($C\underline{H}_3CH_2O$-) and 4.24, 4.37 ppm ($CH_3C\underline{H}_2O$-) in Fig.3-3-1(c). In Fig.3-3-1(c), the signals at 1.21, 1.30 and 4.24, 4.37 ppm are assigned to the SN precursor, and the signals at 1.21 and 4.24 ppm to the KN precursor. The signals of the KN precursor at 1.21 and 4.24 ppm are superimposed on the signals of the SN precursor. The integration ratio of SN ethoxy to KN ethoxy is 2, which satisfies the composition of $Sr_2KNb_5O_{15}$. It turns out from the results of $^1H$ NMR that the SKN precursor consists of the complex alkoxides, $Sr[Nb(OEt)_6]_2$ and $KNb(OEt)_6$. The slight changes in chemical shift indicate the formation of the SKN precursor through the reaction of starting alkoxides. In addition, the data of $^{13}C$ NMR spectra of SN, KN and SKN precursors supported the result by $^1H$ NMR.

Figure 3-3-2 illustrates the $^{93}Nb$ NMR spectra of the SN ($SrNb_2O_6$), the KN ($KNbO_3$) and the SKN precursors in ethanol. Starting niobium ethoxide exhibits two or three broad signals due to association and ligand exchange. Two moles of niobium ethoxide were reacted with 1 mole of Sr metal in ethanol forming the SN precursor. The SN precursor shows a signal at $-1184$ ppm with a half-value width of 1470 Hz (Fig.3-3-2(a)). On the other hand, one mole of niobium ethoxide was reacted with 1 mole of KOEt in ethanol forming the KN precursor. The KN precursor shows a signal at $-1150$ ppm with a half-value width of 3990 Hz (Fig.3-3-2(b)). $^{93}Nb$ NMR of the SKN precursor in ethanol solution shows a single signal at $-1184$ ppm with a half-value width of 2450 Hz as shown in Fig.3-3-2(c). This result indicates the formation of a complex alkoxide with highly symmetric niobium-oxygen octahedron of $[Nb(OR)_6]$. The single signal is in good agreement with the structure of $KNb(OEt)_6$ and $Sr[Nb(O^iPr)_6]_2$ proposed by Mehrotra and co-workers.[17,18]

The spectrum of the SKN precursor is composed of a single signal at a different chemical shift of − 1184 ppm. The SKN precursor also contains $[Nb(OEt)_6]$ units. Three kinds of ethoxy groups of the SKN precursor observed in $^1H$ NMR correspond to $KNb(OEt)_6$ and $Sr[Nb(OEt)_6]_2$ in the SKN precursor. However, in $^{93}Nb$ NMR spectra, the difference appears as only a different chemical shift of the SKN precursor. This is due to the broad signal of $^{93}Nb$ nucleus, which is one of the quardrupole nuclei (I=9/2). The line width of a quardrupole nucleus is strongly related to its quardrupole moment and the value of the electric field gradient along the bond.

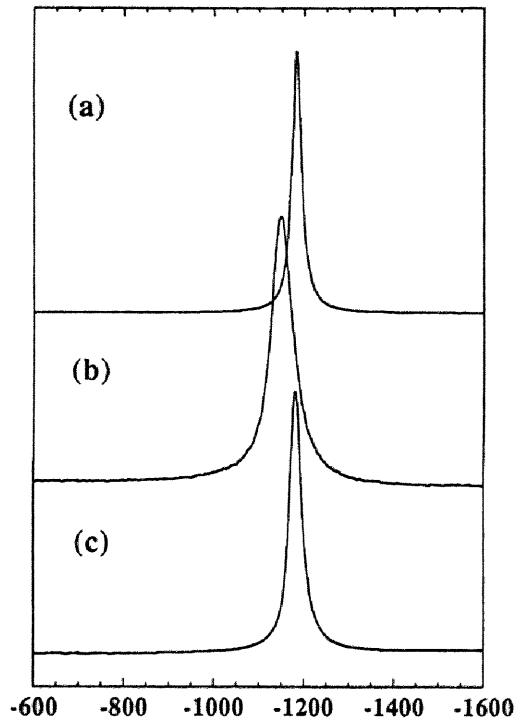


Fig.3-3-2 $^{93}Nb$ NMR spectra of (a) $SrNb_2O_6$ (SN) precursor, (b) $KNbO_3$ (KN) precursor and (c) $Sr_2KNb_5O_{15}$ (SKN) precursor solutions.

Thus, the broadening of the signal is attributable to both the large quardrupole moment and the increase in imbalance around octahedrally coordinated niobium.[19]

Based upon the NMR spectroscopic data, the SKN precursor is considered to consist of a uniform mixture of $Sr[Nb(OEt)_6]_2$ and $KNb(OEt)_6$ units with interaction at a molecular level in solution.

### 3.3.2 Synthesis of highly oriented SKN thin films

Powders were prepared from the precursor solution to study the crystallization behavior. Figure 3-3-3 shows XRD profiles of $Sr_2KNb_5O_{15}$ (SKN) powders heat-treated at various temperatures. The powders were crystallized after calcination of the SKN precursor at 300°C. The SKN powder is X-ray amorphous

below 550°C, and directly crystallizes to the tetragonal tungsten bronze phase above 600°C. In the case of $Sr_{0.5}Ba_{0.5}Nb_2O_6$ (SBN50) and $Pb_{0.6}Ba_{0.4}Nb_2O_6$ (PBN60) powders, the low temperature phase was formed prior to the formation of tungsten bronze phase as described in Chap.2 and Chap.4. Heat treatment above 1200°C was required for the complete transformation to the tungsten bronze SBN and PBN.

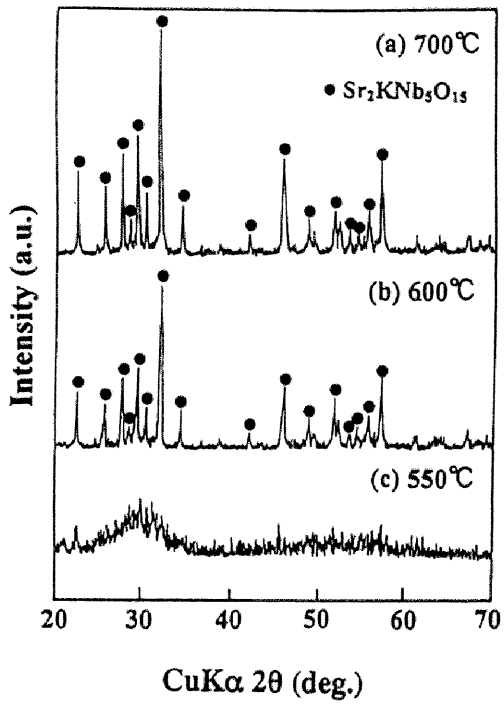


Fig.3-3-3 XRD profiles of SKN powders heat-treated at (a) 700°C, (b) 600°C and (c) 550°C.

The structure of these compounds (SBN, PBN) is the unfilled tungsten bronze.

The stabilization mechanism of the tungsten bronze structure can be explained by the configuration of Nb-O octahedron. In the SKN structure, all of 15-fold and 12-fold coordinated sites distributed in the apex-shared Nb-O octahedra are occupied by $Sr^{2+}$ and $K^+$ ions. The SKN precursor crystallizes readily to the tungsten bronze phase, because SKN has the filled tungsten bronze structure with high structural stability.

Similar to the SKN powder, SKN films prepared on fused silica substrates are found to crystallize directly to the tetragonal tungsten bronze phase above 600°C on silica substrates. However, those films are polycrystalline with no preferred orientation.

In order to synthesize c-axis highly oriented SKN thin films, MgO(100) single crystal substrates were selected because the oxygen alignment of a-plane of MgO can match to that of c-plane of tungsten bronze SKN. Figure 3-3-4 shows the XRD profiles of SKN films crystallized at 700°C on MgO(100) and

Pt(100)/MgO(100) substrates.

The SKN films on MgO(100) have strong 001 and 002 reflections as in Fig.3-3-4(a), indicating that the SKN thin films were crystallized at 700°C with c-axis preferred orientation by selecting MgO(100) substrates. Although the 002 reflection of SKN is superimposed on Pt(200), SKN thin films on Pt(100)/MgO(100) also show (001) plane orientation (Fig.3-3-4(b)). The degree of orientation was greatly improved by precoating a underlayer on MgO(100) and Pt(100)/MgO(100) substrates, using a dilute SKN precursor solution.

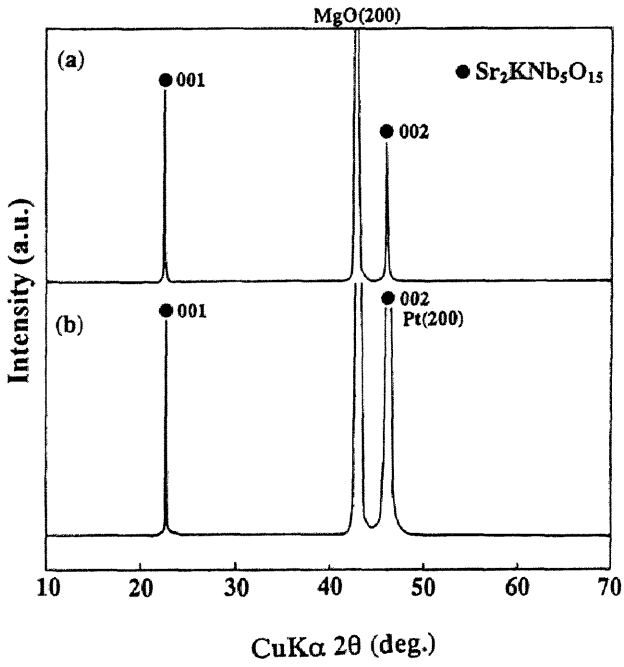


Fig.3-3-4 XRD profiles of SKN thin films heat-treated at 700°C on (a) MgO(100) and (b) Pt(100)/MgO(100) substrates.

The effect of precrystallized underlayer has described in Chap.5 (section 5.3.2).

XRD analysis is not a sufficient method for the determination of crystalline phase of tungsten bronze thin films on substrates. In the case of SBN50 thin films on MgO(100), the XRD profile of tungsten bronze SBN50 thin film was almost the same as that of SBN50 thin film including the low temperature phase as described in Chap.2 (section 2.3.4). Therefore, the SKN thin films on MgO(100) substrates were characterized further by Raman spectroscopy. Figure 3-3-5 shows the Raman microprobe spectra of SKN powder and thin film on MgO(100) substrate crystallized at 700°C. The SKN powder crystallized at 700°C was identified to be the tetragonal tungsten bronze phase by XRD analysis (Fig.3-3-3(a)). The spectrum of SKN powder shown in Fig.3-3-5(a) is in good agreement with that of tetragonal SKN of tungsten bronze as reported by Burns et al.[20] Figure 3-3-5(b)

shows the Raman microprobe spectrum of the SKN thin film on MgO(100) substrate. The SKN thin film crystallized at 700°C is also confirmed to be the tetragonal tungsten bronze phase, because the profile is consistent with that of SKN powder shown in Fig.3-3-5 (a).

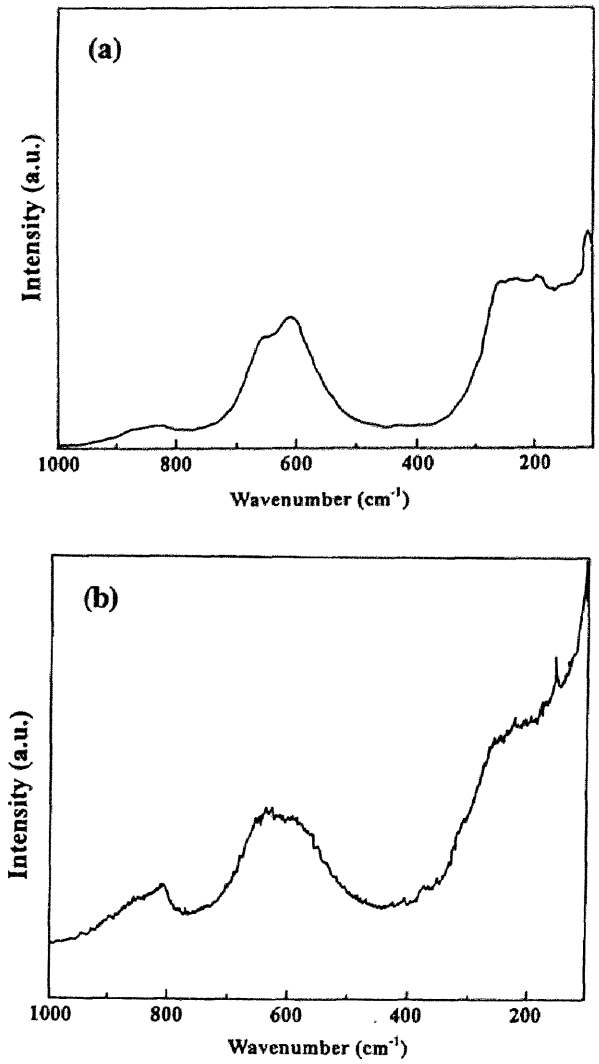


Fig.3-3-5 Raman microprobe spectra of (a) tungsten bronze SKN powder and (b) SKN thin film on MgO(100)
[after heat treatment at 700°C].

Figure 3-3-6 shows the edge-on profile of the SKN film on a MgO(100) substrate crystallized at 700°C. The film has a smooth surface topology with no cracks and voids. Figure 3-3-7 shows the UV-visible spectrum of SKN film on MgO(100) crystallized at 700°C. This spectrum showed interference fringes, supporting the uniform thickness of the film on substrate. The absorption edge was 340 nm. The c-axis oriented SKN thin films on MgO(100) were highly transparent from 340 to 2600 nm and has a potential for several optical applications.

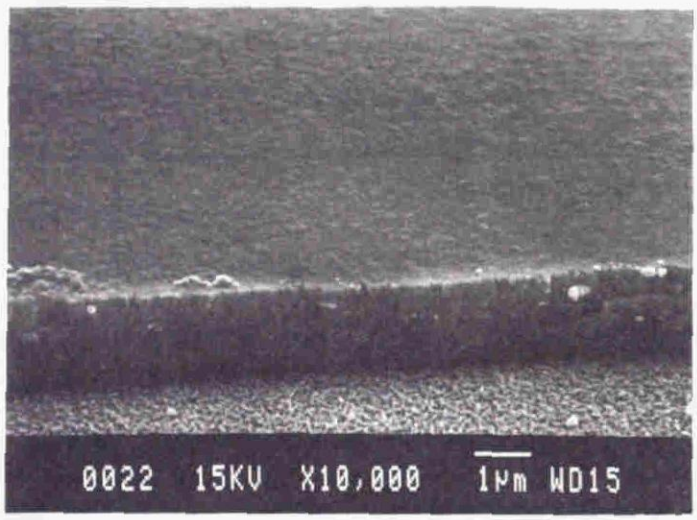


Fig.3-3-6 SEM photograph of SKN thin film on a MgO(100) substrate heat-treated at 700°C.

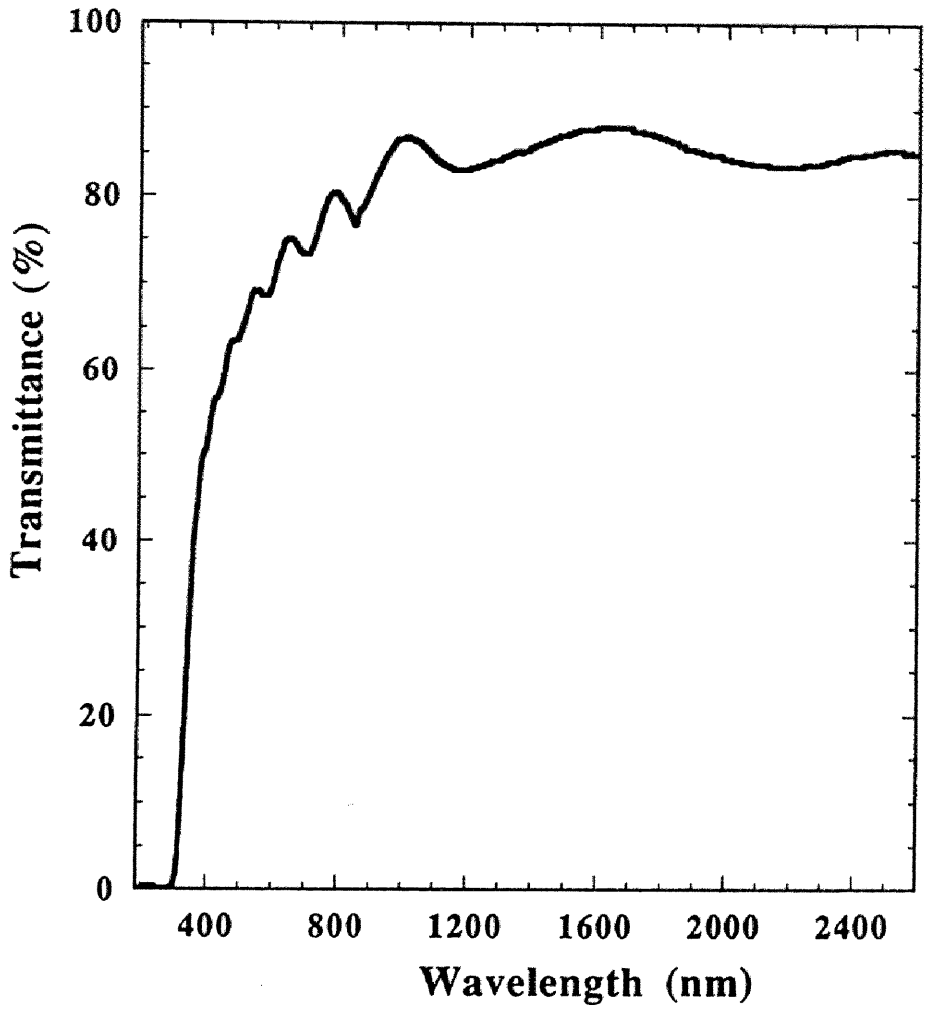


Fig.3-3-7 UV-visible spectrum of SKN film on a MgO(100) substrate crystallized at 700°C.

### 3.3.3 Mechanism of orientation

X-ray pole figure measurements were employed to investigate the crystallographic alignment of $Sr_2KNb_5O_{15}$ (SKN) thin films on MgO(100) substrates as in the case of SBN and KSBN thin films in Chap.2 (section 2.3.4). Figure 3-3-8 indicates the result of measurement for (211) plane of SKN crystallized at 700°C. The term β and α are the rotation axes as described in section 2.3.4(3). Figure 3-3-9(a) shows the calculated pattern for single crystal of SKN which shows eight spots at α= 55 degrees. The {211} planes intersect the <001> direction of the film at 55°. Also, the {211} planes show eight equivalent planes around the <001> direction. However, the pole figure shown in Fig.3-3-8 exhibits more spots than that of Fig.3-3-9(a). This result suggests that the c-plane of the additional SKN lattice intersects the a-plane of MgO. Assuming that the angle between the a-axis of MgO and the a-axis of the other SKN grains is 18.5°, the pole figure is theoretically constructed as shown in Fig.3-3-9(b), which is in good agreement with the measured one in Fig.3-3-8. This result reveals that two crystal lattice planes of SKN are intergrown at an orientation of 18.5° on the MgO(100) substrate. This result is consistent with that of SBN and KSBN films on the MgO(100) substrates prepared by the chemical solution process describe in Chap.2 (section 2.3.4), because SKN and SBN or KSBN have the same crystal structure and the lattice constant of SKN is close to that of SBN or KSBN. The analysis for the (311) plane of the these SKN thin films was consistent with that for the (211) plane. The formation of SKN tetragonal phase on MgO(100) is attributed to the assistance of nucleation sites with appropriate atomic alignment on substrates. Figure 3-3-10 illustrates the relation between the atomic alignment of MgO(100) and c-plane of SKN. These two planes are well-matched to each other. The calculated lattice mismatch of oxygen-atom alignment between SKN(001) and MgO(100) is 6.6 %, on the basis of the pole figure measurement. The nucleation site with the angle of 18.5° has the same probability of growth as that of − 18.5°. Therefore, the two/in-growth structure was observed on MgO(100) substrates.

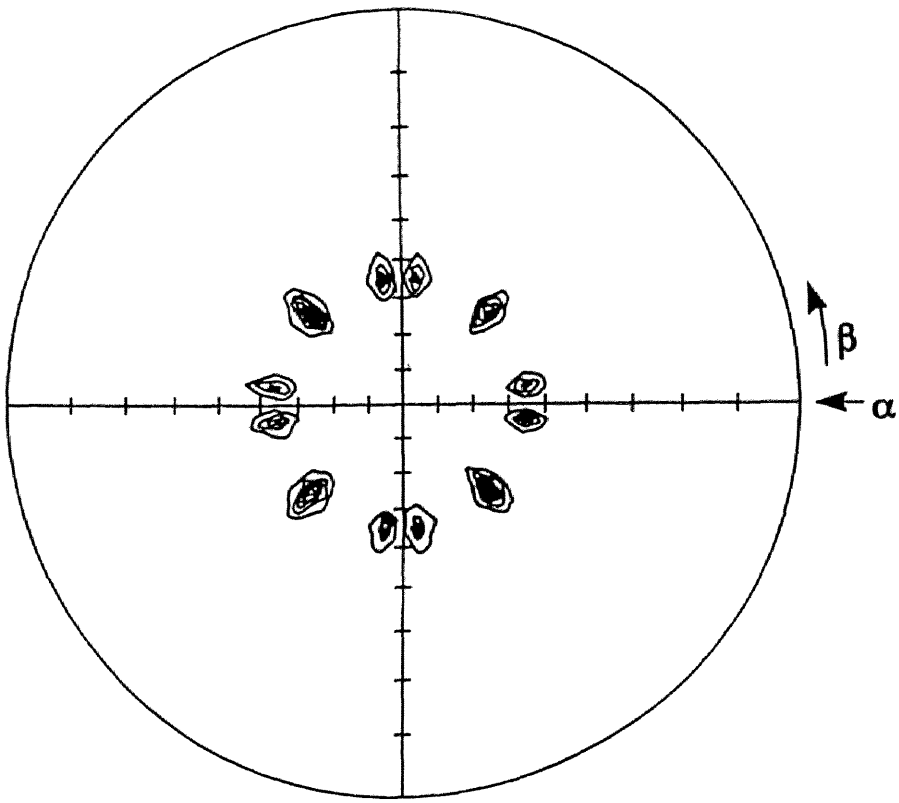


Fig.3-3-8 X-ray pole figure of SKN thin film on a MgO(100) substrate heat-treated at 700°C [2 $\theta$ =27.7°, for the (211) plane].

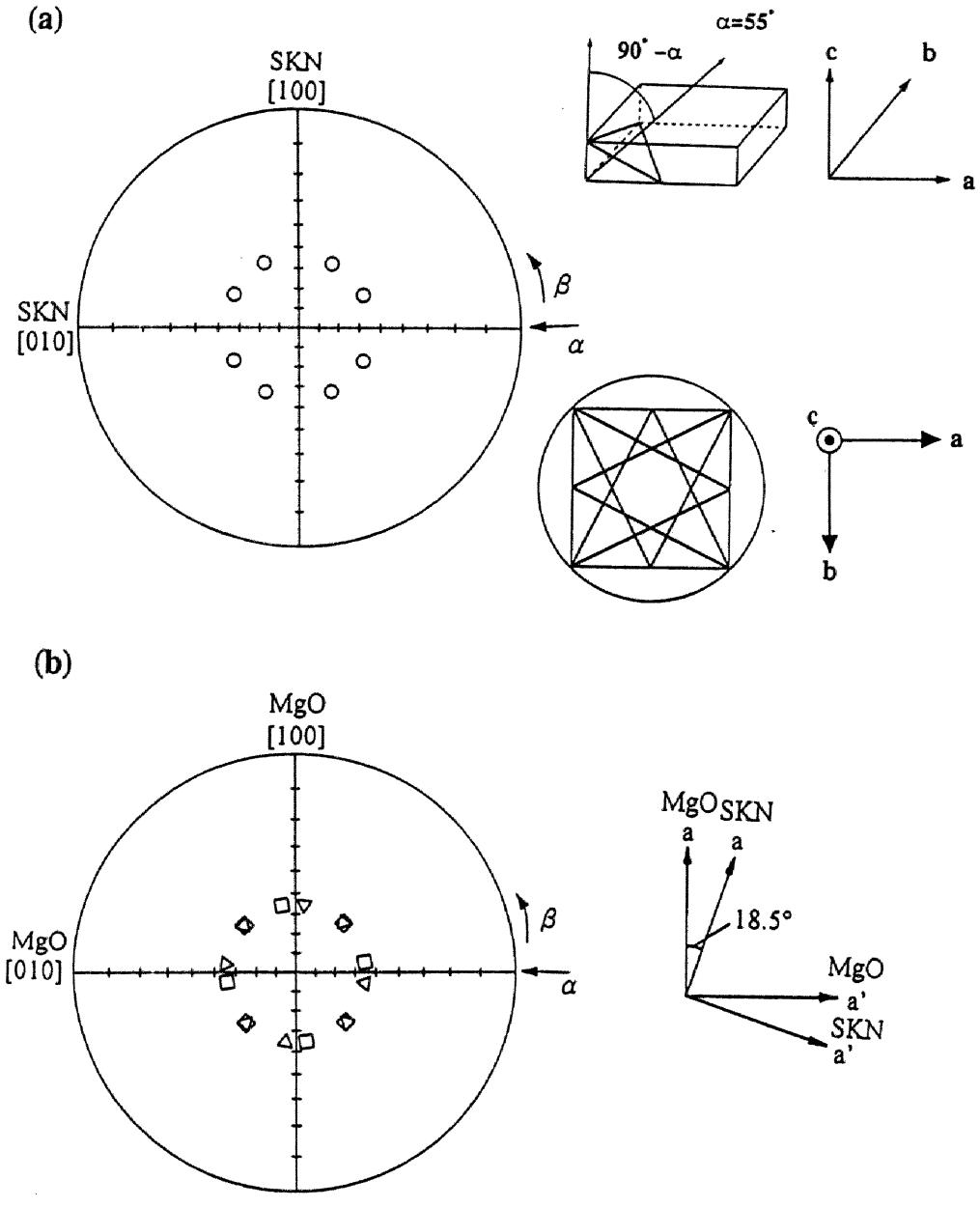


Fig.3-3-9 (a) Calculated pole figure of SKN single crystal constructed for tetragonal (211) and (b) result of analysis of SKN thin film on MgO(100).

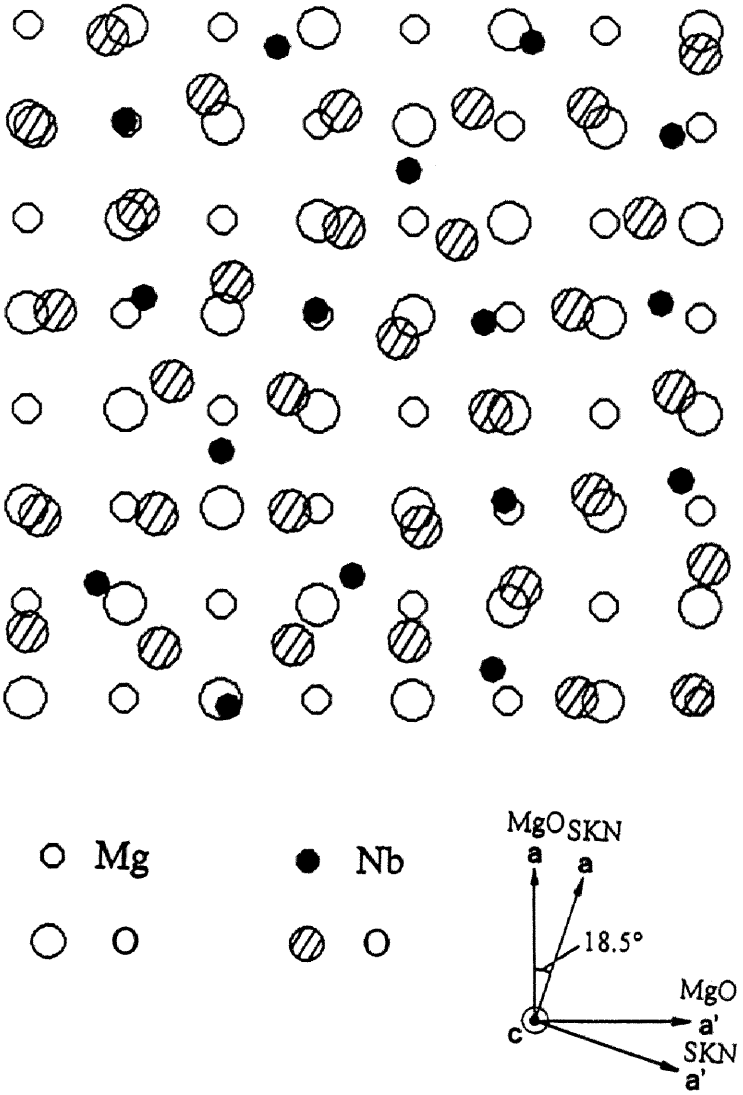


Fig.3-3-10 Relation of Atomic alignment between MgO(100) and c-plane of SKN proposed on the basis of the pole figure.

### 3.3.4 Dielectric properties of SKN films

The temperature dependence of the dielectric constant and loss tangent for SKN film crystallized at 700°C on a Pt(100)/MgO(100) substrate is shown in Figure 3-3-11. The Curie temperature ($T_c$) of the SKN film was about 70°C at 1 kHz, which depended on the measured frequency. The reported $T_c$ is around

155°C.[1,3-8,13,14] The Curie temperature of the SKN film shifted to the low temperature region and the peaks of ε-T curves were broadened compared with reported SKN single crystals.[8,13] The dielectric constant of the SKN film was about 590 at 20°C at 1 kHz, which is much lower than that for SKN single crystals ($\varepsilon_{33}$= above 20000, at 1 kHz at $T_c$).[13] The grain size of the SKN thin film was confirmed to be 100-150 nm, using atomic force microscope (AFM) images. The broadening of the ε-T curves may be due to several factors such as small grain size, interfacial effects and mechanical stress imposed on the films by the substrates.

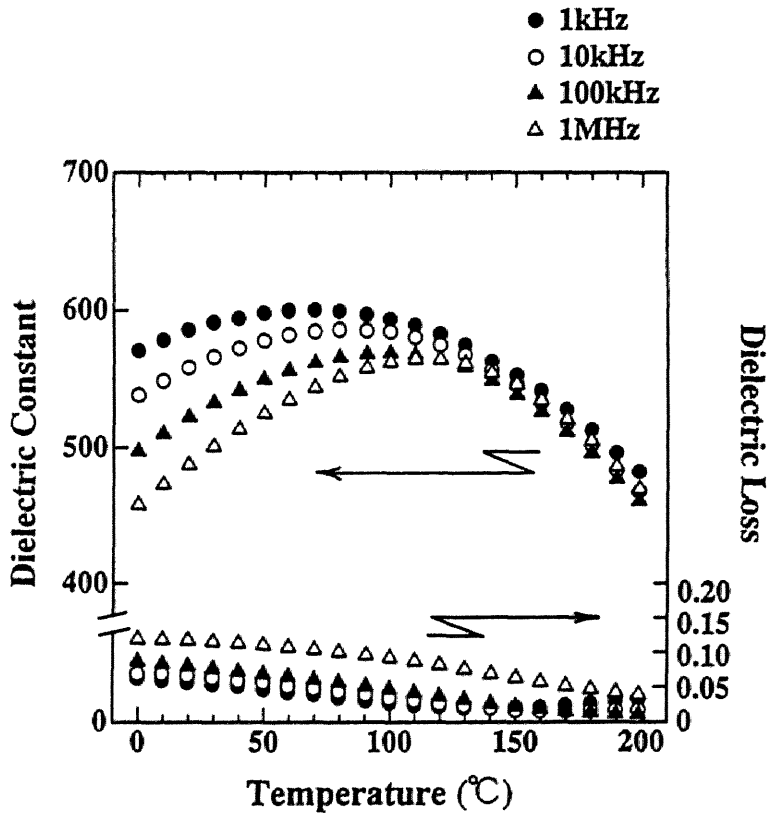


Fig.3-3-11 Temperature dependence of dielectric constant and loss tangent of SKN thin film on a Pt(100)/MgO(100) substrate crystallized at 700°C.

## 3.4 Conclusions

Crack-free $Sr_2KNb_5O_{15}$ (SKN) films with c-axis preferred orientation were successfully synthesized on MgO(100) and Pt(100)/MgO(100) substrates from metallo-organics. A homogeneous and stable SKN precursor solution was prepared from strontium metal, potassium ethoxide and niobium ethoxide in ethanol. The SKN precursor was the complex alkoxide between $Sr[Nb(OEt)_6]_2$ and $KNb(OEt)_6$ with highly symmetric niobium-oxigen octahedron. SKN precursor powders and thin films on substrates directly crystallized to the tetragonal tungsten bronze phase above 600°C. The SKN films on MgO(100) and Pt(100)/MgO(100) showed a c-axis preferred orientation. Two crystal lattice planes of SKN were intrergrown at an orientation of 18.5° on MgO(100). The dielectric constant of SKN thin films on Pt(100)/MgO(100) was approximately 600 at 70°C of the Curie temperature ($T_c$) at 1 kHz.

## References

1. E.A.Giess, B.A.Scott, G.Burns, D.F.O'Kane and A.Segmuller, "Alkali Strontium-Barium-Lead Niobate Systems with Tungsten Bronze Structure : Crystallographic Properties and Curie Points", *J. Am. Ceram. Soc.*, **52** [5] 276-281 (1969).

2. B.A.Scott, E.A.Giess, D.F.O'Kane and G.Burns, "Phase Equilibria in the $KNbO_3$-$SrNb_2O_6$ and $KNbO_3$-$BaNb_2O_6$ System", *J. Am. Ceram. Soc.*, **53** [2] 106-109 (1970).

3. M.Pouchard, J-P.Chaminade, A.Perron, J.Ravez et P.Hagenmuller, "Influence de Divers Types de Substitutions Cationiques Sur Les Proprietes Dielectriques de Niobates de Structure "Bronzes Oxygenes de Tungstene Quadratiques"", *J. Solid State Chem.*, **14** 274-282 (1975).

4. T.Ikeda, K.Uno, K.Oyamada, A.Sagara, J.Kato, S.Takano and H.Sato, "Some Solid Solution of the $A_5B_{10}O_{30}$- and $A_6B_{10}O_{30}$-Type Tungsten-Bronze Ferroelectrics", *Jpn. J. Appl. Phys.*, **17** [2] 341-348 (1978).

5. R.R.Neurgaonkar, W.K.Cory and J.R.Oliver, "Growth and Applications of Ferroelectric Tungsten Bronze Family Crystals", *Ferroelectrics*, **51** 3-8 (1983).
6. R.R.Neugaonkar, J.R.Oliver, L.E.Cross, "Ferroelectric Properties of Tetragonal Tungsten Bronze Single Crystals", *Ferroelectrics*, **56** 31-36 (1984).
7. R.R.Neurgaonkar and W.K.Cory, "Progress in Photorefractive Tungsten Bronze Crystals", *J. Opt. Soc. Am. B*, **3** [2] 274-282 (1986).
8. E.A.Giess, G.Burns, D.F.O'Kane and A.W.Smith, "Ferroelectric and Optical Properties of $KSr_2Nb_5O_{15}$", *Appl. Phys .Lett.*, **11** [7] 233-234 (1967).
9. R.Clarke and F.W.Ainger, "The Electro-Optic Properties of Ferroelectric KSN Crystals", *Ferroelectrics*, 7 101-102 (1974).
10. T.Kimura, S.Miyamoto and T.Yamaguchi, "Microstructure Development and Dielectric Properties of Potassium Strontium Niobate Ceramics", *J. Am. Ceram. Soc.*, **73** [1] 127-130 (1990).
11. B.Boufrou, G.Desgardin and B.Raveau, "Tetragonal Tungsten bronze Niobate, $K_{0.2}Sr_{0.4}NbO_3$ : A New Material for Capacitors with Flat Dielectric Curves", *J. Am. Ceram. Soc.*, **74** [11] 2809-2814 (1991).
12. T.Kimura, S.Saibol and K.Nagata, "Effect of Grain Orientation on Curie Temperature of $KSr_2Nb_5O_{15}$ Solid Solutions", *J. Ceram. Soc. Japan*, **103** [2] 132-137 (1995).
13. R.R.Neurgaonkar, W.W.Ho, W.K.Cory and W.F.Hall, "Low and High Frequency Dielectric Properties of Ferroelectric Tungsten Bronze $Sr_2KNb_5O_{15}$ Crystals", *Ferroelectrics*, **51** 185-191 (1984).
14. R.R.Neurgaonkar, W.K.Cory and J.R.Oliver, "Growth and Optical Properties of Ferroelectric Tungsten Bronze Crystals", *Ferroelectrics*, **142** 167-188 (1993).
15. M.H.Francombe, "Ferroelectric Films and Their Device Applications", *Thin Solid Films*, **13** 413-433 (1972).
16. L.M.Sheppard, "Advances in Processing of Ferroelectric Thin films", *Am. Ceram. Soc. Bull.*, **71** [1] 85-95 (1992).
17. R.C.Mehrotra, M.M.Agrawal and P.N.Kapoor, "Alkali-Metal Hexaalkoxides of Niobium and Tantalum", *J. Chem. Soc.* (A), 2673-2676 (1968).

18. S.Govil, P.N.Kapoor and R.C.Mehrotra, "Double Isopropoxides of Niobium and Tantalum with Alkaline Earth Metals", *J. Inorg. Nucl. Chem.*, **38** [1] 172-173 (1976).

19. D.Rehder, "Early Transition Metals, Lantanides and Actinides", in Multinuclear NMR, Edited by J.Mason, Plenum Press, New York, 1987.

20. G.Burns, J.D.Axe and D.F.O'Kane, "Raman Measurements of $NaBa_2Nb_5O_{15}$ and Related Ferroelectrics", *Solid State communications*, **7** 933-936 (1969).

# Chapter 4

## Synthesis and Properties of Lead Barium Niobate (PBN) and Potassium Substituted PBN (KPBN) Thin Films

## 4.1 Introduction

Lead barium niobate [$(Pb,Ba)Nb_2O_6$, PBN] is a solid solution between $PbNb_2O_6$ and hypothetical $BaNb_2O_6$ and has a tungsten bronze structure.[1,2] PBN is known to have a morphotropic phase boundary (MPB) near the $(Pb_{0.6}Ba_{0.4})Nb_2O_6$ (PBN60) composition, which separates a tetragonal ferroelectric phase (4mm) and an orthorhombic ferroelectric phase (m2m) as shown in Fig.4-1-1. Similar to the well-known perovskite PZT [$Pb(Zr,Ti)O_3$] ceramics, the extraordinary large dielectric, piezoelectric and electro-optic coefficients are reported for PBN at around MPB composition.[3-7] PBN has been expected for applications in pyroelectric sensors, SAW filters and several electro-optic devices. Alkali or rare earth ion modified PBN was reported for the improvement of its properties.[8,9]

PBN single crystals have been grown mainly by the Czochralski method.[3-6,10] However, the growth of PBN single crystal with high quality encounters several problems due to the evaporation of Pb and the difficulties in determination of congruent melt composition and its control. Cracking caused by the paraelectric to ferroelectric phase transition during cooling process is also a serious problem. Although PBN ceramics have been prepared by the solid state reaction of oxide powders at high temperatures via a conventional firing and milling techniques, the high temperature process causes the problem of PbO loss.[3,4,7]

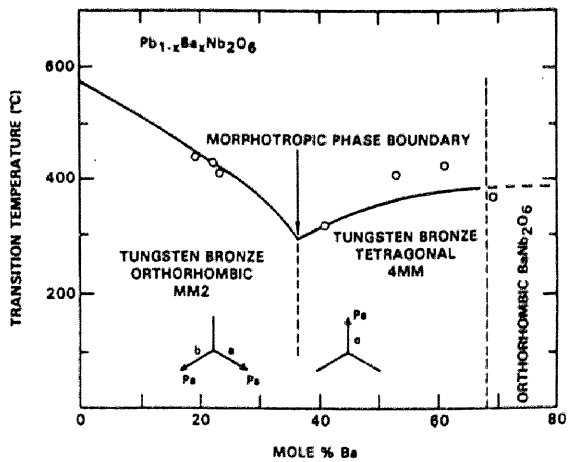


Fig.4-1-1 Phase diagram for the binary $PbNb_2O_6$-$BaNb_2O_6$ ($(Pb,Ba)Nb_2O_6$, PBN) morphotropic system.
Points indicate several bulk crystal compositions (Ref. 7).

Recently, the demand for thin film processing has increased for the

development of integrated devices.[11,12] Highly oriented PBN films so far prepared on sapphire substrates were fabricated by the sputtering technique.[13,14] PBN thin films with preferred orientation along polar axis can be proposed for pyroelectric, piezoelectric and electro-optic applications. However, the precise control of composition is usually difficult by this method. The composition control is the significant factor for obtaining the optimal properties of lead based ferroelectrics such as PBN. Dielectric thin films with high transparency and high refractive index are also used for application to optical devices, including optical waveguides. When high temperature heat treatment is required for the film fabrication, the film quality usually degrades due to the exaggerated grain growth and reaction between the substrates and films. The crystallization of ferroelectric tungsten bronze films at lower temperatures is indispensable for the fabrication of high-quality films. The substitution for Pb or Ba site with alkali ion is expected to decrease the crystallization temperature of the tungsten bronze phase, because the structure of PBN approaches that of filled-tungsten bronze with increase of alkali ion substitution in amount.[7,15] Thus, the structural stability is enhanced by the introduction of alkali ion, such as $K^+$ or $Na^+$, in the 15-fold and 12-fold sites.[7] On the other hand, alkali rare earth niobate, such as $K_{0.8}La_{0.4}Nb_2O_6$, is reported to have the tungsten bronze structure, especially the filled-tungsten bronze structure, and its tungsten bronze phase is considered to exhibit high structural stability.[16] Further increase in the stability of the tungsten bronze phase is expected by the formation of a solid solution with $K_{0.8}La_{0.4}Nb_2O_6$ (La doping).

This chapter describes the synthesis of highly oriented lead barium niobate (PBN) and potassium substituted lead barium niobate (KPBN) thin films through metallo-organic substances. The structure of PBN and KPBN precursor in solution were studied by using NMR spectroscopy. The structure of the low temperature phase and the effect of the substitution with potassium and the lanthanum doping for lead or barium sites on the crystallization of tungsten bronze phase were also investigated. The mechanism of orientation, and the electrical and optical properties of synthesized films were also characterized.

## 4.2 Experimental

Figure 4-2-1 shows the process flow for preparing lead barium niobate (PBN) and potassium (and lanthanum) substituted lead barium niobate (KPBN (and KPBLN)) powders and thin films.

*(1) Synthesis of precursor solutions*

Ba metal [Furu-uchi Chemical, Japan], anhydrous $Pb(CH_3COO)_2$, $KOCH_2CH_3$ (KOEt), $La(OCH(CH_3)_2)_3$ (lanthanum tri-iso-propoxide, $La(O^iPr)_3$) and $Nb(OCH_2CH_3)_5$ ($Nb(OEt)_5$) [Ko-jundo Chemical, Japan] were selected as starting materials. 2-Methoxyethanol (ethylene glycol monomethyl ether, EGMME) was dried over molecular sieve and distilled before use. Since starting materials are extremely sensitive to moisture, the entire procedure was carried out in dry nitrogen. $Pb(CH_3COO)_2$, KOEt and $Nb(OEt)_5$ corresponding to the composition of $K_x(Pb_{0.6}Ba_{0.4})_{1-x/2}Nb_2O_6$ [x=0, 0.1, 0.2, 0.3, 0.4] and $K_{0.45}(Pb_{0.6}Ba_{0.4})_{0.7}La_{0.05}Nb_2O_6$ were dissolved in absolute 2-methoxyethanol. After reflux for 24 h, Ba metal was added to the solution. The mixture solution was refluxed for 24 h yielding a homogeneous solution. In the case of La modified KPBN (KPBLN) synthesis, $La(O^iPr)_3$ was added to the solution followed by reflux 18 h to obtain a KPBLN solution. The precursor solution was condensed to approximately 0.1 mol/l and 0.3 mol/l by removal of the solvent under vacuum.

*(2) Fabrication of thin film samples*

Films were fabricated using the precursor solution by dip coating on fused silica, MgO(100) and Pt(100)/MgO(100) substrates. Pt(100) layer was deposited on MgO(100) by RF magnetron sputtering described in Chapter 2. Prior to dip-coating, fused silica, MgO(100) and Pt(100)/MgO(100) substrates were cleaned with absolute 2-methoxyethanol in the same way as in Chap.2. Precursor films were prepared on MgO(100) or Pt(100)/MgO(100) substrates using a 0.1 mol/l PBN, KPBN and KPBLN precursor solution to synthesize highly oriented films by controlling the nucleation. On a fused silica substrate however, a 0.3 mol/l precursor solution was used to increase the thickness of the film per coating. The deposited films were dried in dry $N_2$. After the precursor film on MgO(100) or

Pt(100)/MgO(100) substrate was calcined at 400°C for 1 h at a rate of 2°C/min, the film was heated at the crystallization temperature for 1 h, followed by cooling under $O_2$ flow at a rate of 10°C/min. The coating-crystallization process was repeated several times to increase the film thickness. On the other hand, a rapid heating and cooling treatment (400°C/min) for 0.5 h was employed for the precursor films on fused silica substrates after 10 cycles of a coating-calcination process at 400°C for 1 h at a rate of 2°C/min. Crystallization by the rapid heating process was also repeated a few times to increase the film thickness.

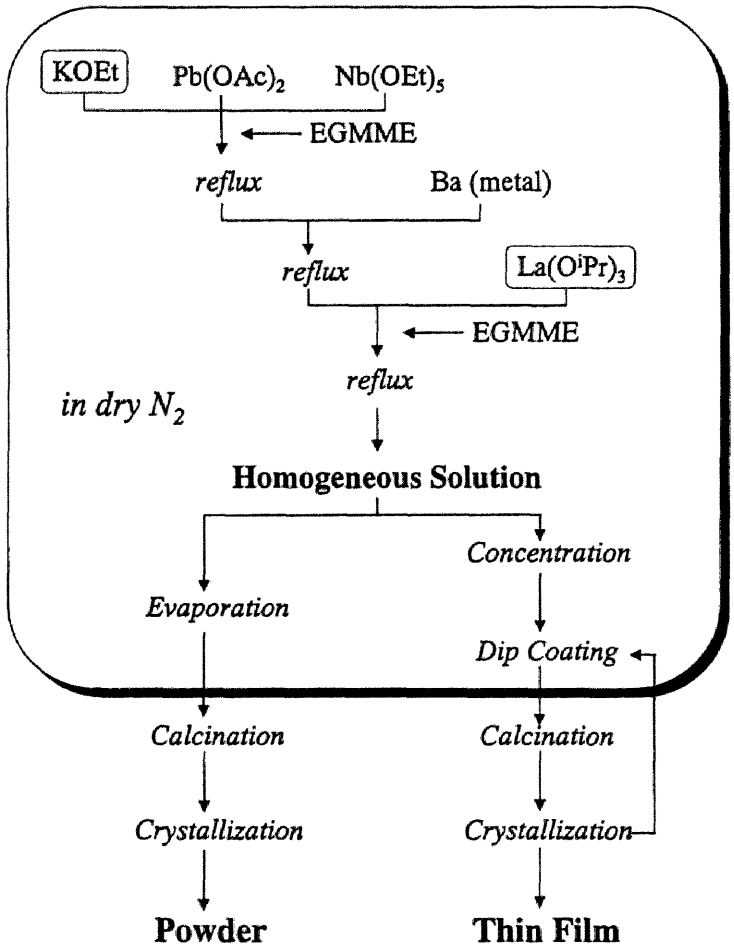


Fig.4-2-1 Process flow for preparing lead barium niobate (PBN), potassium and lanthanum substituted PBN (KPBN and KPBLN) powders and thin films.

A thin layer was prepared as an underlayer on MgO(100) and Pt(100)/MgO(100) substrates using 0.02 mol/l precursor solution at a withdrawal rate of 0.6 mm/s. The thin layer of precursor on a substrate was heat-treated at 800°C under the gradual heating-cooling process. Then, the precursor film was coated on the precrystallized PBN or KPBN or KPBLN underlayer using 0.1 mol/l solution at a withdrawal rate of 0.6 mm/s. And then, two types of crystallization processes described above were performed.

***(3) Preparation of precursor powders***

Powder samples were also prepared from the precursor solution to investigate the crystallization behavior. The solvent was removed by vacuum evaporation to obtain PBN or KPBN or KPBLN precursor. The precursor was calcined at 400°C, which was then heat-treated at temperatures between 700°C and 1250°C in an oxygen flow for 1 h as described in the film synthesis.

***(4) Characterization of precursor solutions***

The precursor solution was analyzed by IR spectroscopy with a FT-IR instrument [NICOLET, 50DBX] using the KBr method. $^{1}H$ and $^{13}C$ NMR spectra were recorded by a Gemini 200 spectrometer [Varian] in $CDCl_3$ solution using tetramethylsilane as internal standard. $^{93}Nb$ and $^{207}Pb$ NMR spectra of precursors in 2-methoxyethanol solutions were recorded at 61.14 and 52.26 MHz, respectively [Bruker Instruments, AC250]. The standards of chemical shifts of $^{93}Nb$ and $^{207}Pb$ spectra were tetramethylammonium hexachloroniobate $(CH_3)_4N[NbCl_6]$ in $CD_3CN$ and $Pb(NO_3)_2$ in $D_2O$, respectively.

***(5) Characterization methods of powder and thin film samples***

The prepared powders and films were characterized by X-ray diffraction (XRD) using Cu Kα radiation with a monochromator and a ψ scan attachment [Rigaku, RAD 2X and B-6]. The crystallographic phases of powders and films, the microstructures of synthesized films, the transmittance of the films on transparent substrates and the propagation modes in the films were characterized by the same methods described in Chap.2. The electrical properties of the films were measured using Au vacuum-deposited onto the surface of the synthesized films as the top

electrode and a sputtered Pt(100) layer on MgO(100) as the bottom electrode (Chap.2, Fig.2-2-4). The measurement of dielectric properties was conducted on the thin films using a hot stage [SIGNATONE, MODEL S-1060], from 30°C to 300°C in air. The P-E hysteresis loops of the films were also evaluated as in Chap.2.

## 4.3 Results and discussion

### 4.3.1 Synthesis of precursor solutions

In the case of PBN synthesis, a homogeneous solution was obtained by the reaction among barium metal, niobium alkoxide and anhydrous lead acetate in 2-methoxyethanol (EGMME). The reaction of $Nb(OEt)_5$ with $Pb(CH_3COO)_2$ in 2-methoxyethanol at a reflux temperature of 125°C yielded a homogeneous solution. After Ba metal was reacted with the solution, a stable PBN precursor solution was obtained. However, when Ba metal dissolved in EGMME was added to an EGMME solution of $Pb(CH_3COO)_2$, a solid precipitated immediately from the solution. This precipitate is considered to be $Ba(CH_3COO)_2$, because this compound has a poor solubility in organic solvents. No homogeneous solution was obtained even after the refluxing of the precipitate with $Nb(OEt)_5$. The key point of the preparing PBN coating solution is the pre-reaction of $Nb(OEt)_5$ and $Pb(CH_3COO)_2$ in order to suppress the formation of $Ba(CH_3COO)_2$.

Figure 4-3-1 shows $^1H$ NMR spectra of 2-methoxyethanol and the PBN60 ($Pb_{0.6}Ba_{0.4}Nb_2O_6$) precursor. The signal due to hydroxy group (-O<u>H</u>) at 3.1 ppm (Fig.4-3-1(a)) disappears in Fig.4-3-1(b). The signals of 2-methoxyethoxy groups ($CH_3OCH_2CH_2O$) are observed at 3.4 ppm ($C\underline{H}_3OCH_2CH_2O$-), 3.5 ppm ($CH_3OC\underline{H}_2CH_2O$-) and 3.7 ppm ($CH_3OCH_2C\underline{H}_2O$-) in Fig.4-3-1(a). However, the peak at 3.7 ppm ($CH_3OCH_2C\underline{H}_2O$-) shifted to a downfield of 4.4 ppm in Fig.4-3-1(b). Figure 4-3-2 shows $^{13}C$ NMR spectra of 2-methoxyethanol and the PBN60 precursor. The signals of 2-methoxyethoxy groups ($CH_3OCH_2CH_2O$) are observed at 59 ppm ($\underline{C}H_3OCH_2CH_2O$-), 74 ppm ($CH_3O\underline{C}H_2CH_2O$-) and 62 ppm ($CH_3OCH_2\underline{C}H_2O$-) in Fig.4-3-2(a). However, the peak at 62 ppm

($CH_3OCH_2\underline{C}H_2O$-) shifts to a low field of 70 ppm as shown in Fig.4-3-2(b). The downfield shift suggests the formation of $CH_3OCH_2CH_2O$-M bond. No ethoxy group is observed at 60 and 20 ppm. Also, no carbonyl carbon of acetate group is detected at 180 ppm. These changes indicate that both the ethoxy group of $Nb(OEt)_5$ and the acetate group of $Pb(CH_3COO)_2$ were completely substituted for 2-methoxyethoxy groups yielding $CH_3OCH_2CH_2O$-M bonds in the PBN precursor.

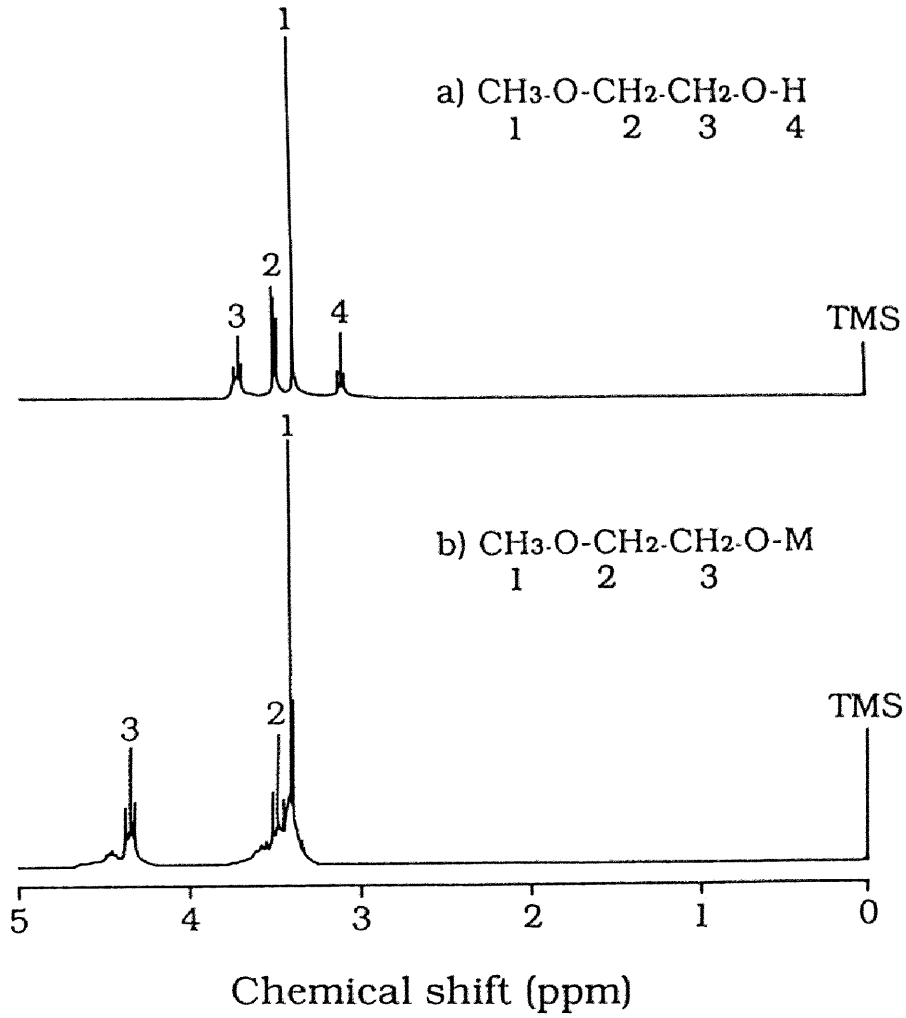


Fig.4-3-1 $^1H$ NMR spectra of (a) 2-methoxyethanol and (b) PBN60 ($Pb_{0.6}Ba_{0.4}Nb_2O_6$) precursor

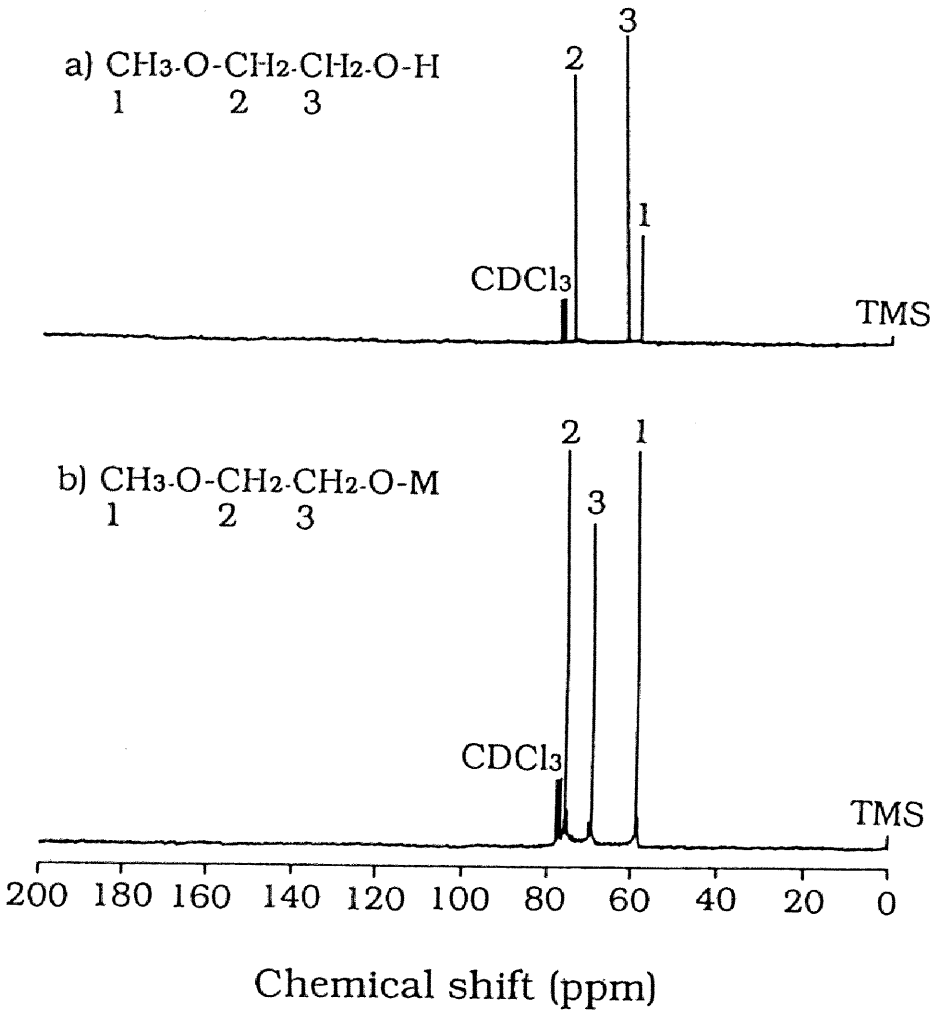


Fig.4-3-2 $^{13}C$ NMR spectra of (a) 2-methoxyethanol and (b) PBN60 ($Pb_{0.6}Ba_{0.4}Nb_2O_6$) precursor

Figure 4-3-3 shows the $^{93}Nb$ NMR spectra of the BN ($BaNb_2O_6$) precursor and the PBN60 ($Pb_{0.6}Ba_{0.4}Nb_2O_6$) precursor. Although monomeric niobium ethoxide itself is 5-coordinated, niobium ethoxide undergoes the association and the ligand exchange reaction in ethanol producing two or three broad signals.[17] Two moles of niobium ethoxide were reacted with 1 mole of Ba metal in 2-methoxyethanol forming the BN precursor. $^{93}Nb$ NMR of the BN precursor shows a single signal at -1174 ppm with a half-value width of 3300 Hz. The single signal is in good agreement with the structure of $Ba[Nb(O^iPr)_6]_2$ proposed by

Govil et al.[18]

The PBN precursor shows a similar single resonance at -1168 ppm with a larger half-value width of 7340 Hz (Fig.4-3-3(b)) compared with the BN precursor. This result indicates the formation of a complex alkoxide with highly symmetric niobium-oxygen octahedron of $[Nb(OR)_6]$. The increase in half-value width suggests the presence of interaction between Pb atom and $[Nb(OR)_6]^{-1}$ of $Ba[Nb(OR)_6]_2$ in solution. $^{207}Pb$ NMR spectrum of $Pb(CH_3COO)_2$ in $CD_3OD$ showed a signal at 1973 ppm. After the reaction was completed, however, the signal at 1973 ppm disappeared. This result also suggests the formation of PBN precursor.

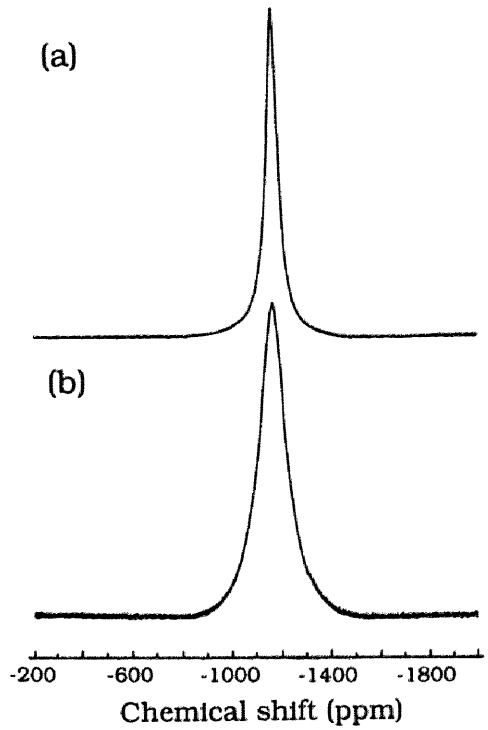


Fig.4-3-3 $^{93}Nb$ NMR spectra of (a) BN ($BaNb_2O_6$) precursor and (b) PBN60 precursor solutions

FT-IR analysis showed the distillate from the reaction mixture contained ester (ethyl acetate or 2-methoxyethyl acetate), which was detected based upon the characteristic absorption of 1740 $cm^{-1}$. The ester was a reaction product between eliminated acetate and ethanol or 2-methoxyethanol.

Based upon the spectroscopic data, the PBN precursor consists of $M[Nb(OR)_6]_2$ (M=Pb, Ba, $R=OCH_2CH_2OCH_3$) units as shown in Fig.4-3-4. The distribution of Pb and Ba in the complex alkoxide is uniform at a molecular level in solution.

On the other hand, a homogeneous KPBN precursor solution was prepared

by controlling the reaction of starting materials in 2-methoxyethanol (EGMME). The key point in preparing KPBN coating solution is the pre-reaction of $Pb(CH_3COO)_2$, KOEt and $Nb(OEt)_5$ to suppress the formation of $Ba(CH_3COO)_2$ as in the preparation of PBN precursor solution. From the data of $^{1}H$, $^{13}C$ and $^{93}Nb$ NMR, it turns out that the KPBN precursor is composed of complex alkoxide precursors, such as $Pb[Nb(OCH_2CH_2OCH_3)_6]_2$, $Ba[Nb(OCH_2CH_2OCH_3)_6]_2$ and $K[Nb(OCH_2CH_2OCH_3)_6]$, with highly symmetric niobium-oxygen octahedron. Similar to the PBN precursor, the KPBN precursor consists of a uniform mixture of these complex alkoxide units with interaction at a molecular level in solution.

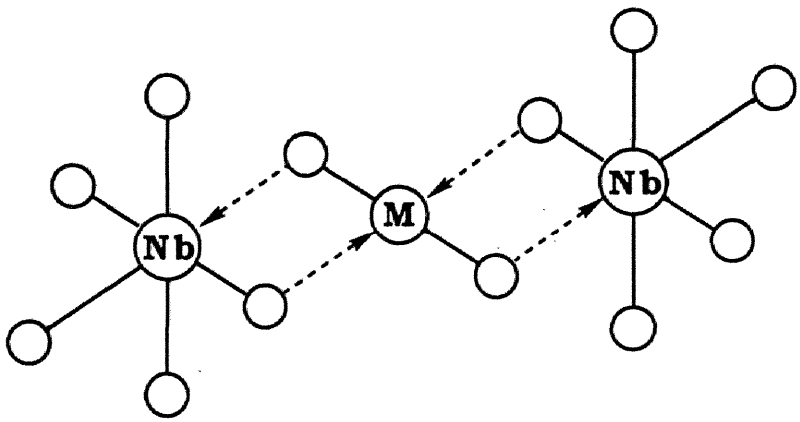


**M: Pb, Ba**
**O: OR (R= $-CH_2CH_2OCH_3$)**

Fig.4-3-4 Proposed structure of PBN precursor

### 4.3.2 Crystallization behavior of PBN precursor

*(1) Crystallization of PBN precursor*

PBN precursor powders were prepared to investigate the crystallization behavior. Figure 4-3-5 illustrates XRD profiles of PBN60 powders heat-treated at various temperatures between 400°C and 1250°C for 1 h. The PBN60 powder is in a non-crystalline state below 500°C, and crystallized at 600°C as shown in Fig.4-3-5(a). Since the XRD pattern is similar to that of hexagonal $PbNb_2O_6$ (Francombite),[2,19] the crystalline phase is considered to be the hexagonal PBN low temperature phase, and is not the tungsten bronze.

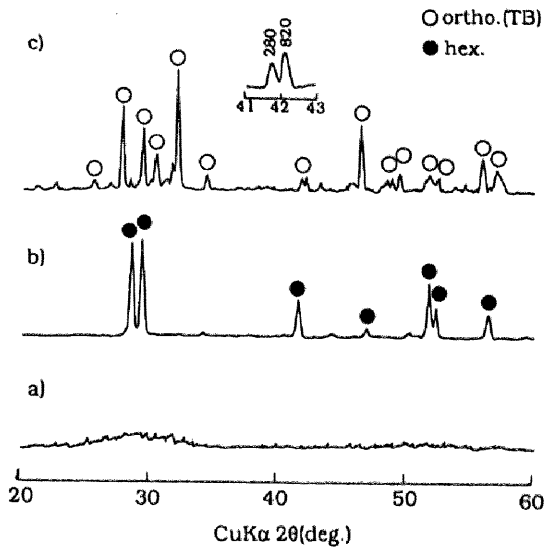


Fig.4-3-5 XRD profiles of PBN60 powders heat-treated at (a) 400°C, (b) 600°C and (c) 1250°C.
[ortho.(TB): orthorhombic tungsten bronze phase]
[hex.: hexagonal low temperature phase]

The hexagonal PBN is completely transformed to the orthorhombic tungsten bronze PBN at 1250°C as shown in Fig.4-3-5(c). The orthorhombic structure is confirmed by the splitting of 280 and 820 reflections at around $2\theta=42^\circ$. According to Bhalla et al.'s report that the MPB composition was near $Pb_{0.63}Ba_{0.37}Nb_2O_6$, PBN60 was in the range of the tetragonal tungsten bronze phase.[3,4] However, the crystallization of PBN60 (close to MPB composition) is also known to be greatly influenced by processing method and conditions. The current PBN60 powder crystallizes to the hexagonal phase and then is transformed to the orthorhombic tungsten bronze phase on heating. The hexagonal low temperature phase is considered to be a metastable phase similar to the SBN low-temperature phase in Chap.2 (section 2.3.2). The present alkoxy-derived PBN55 ($Pb_{0.55}Ba_{0.45}Nb_2O_6$) and PBN30 ($Pb_{0.3}Ba_{0.7}Nb_2O_6$) powders were found to crystallize to the tetragonal

phase at 1250°C. In this method, therefore, the MPB composition probably exists between PBN55 ($Pb_{0.55}Ba_{0.45}Nb_2O_6$) and PBN60 ($Pb_{0.6}Ba_{0.4}Nb_2O_6$).

*(2) Structure of PBN low temperature phase*

In the case of $(Pb_{0.6}Ba_{0.4})Nb_2O_6$ (PBN60) synthesis, PBN60 low temperature phase crystallized at 600°C prior to the formation of tungsten bronze PBN, then the PBN powder was completely transformed to the tungsten bronze phase at 1250°C as described above.[17] In order to investigate the structure of the low temperature phase in more detail, XRD and Raman spectroscopic analyses were used. Figure 4-3-6 shows XRD profiles and Raman spectra of $PbNb_2O_6$ and PBN60 powders heat-treated at 700°C. $PbNb_2O_6$ powder was prepared by the similar chemical solution process. Since the XRD pattern of PBN60 shown in Fig.4-3-6(a) is quite similar to that of hexagonal $PbNb_2O_6$[19] (Fig.4-3-6(b)) identified by JCPDS 29-779, the crystalline phase of PBN60 in Fig.4-3-6(a) is considered to be the hexagonal PBN, which does not have the tungsten bronze structure.

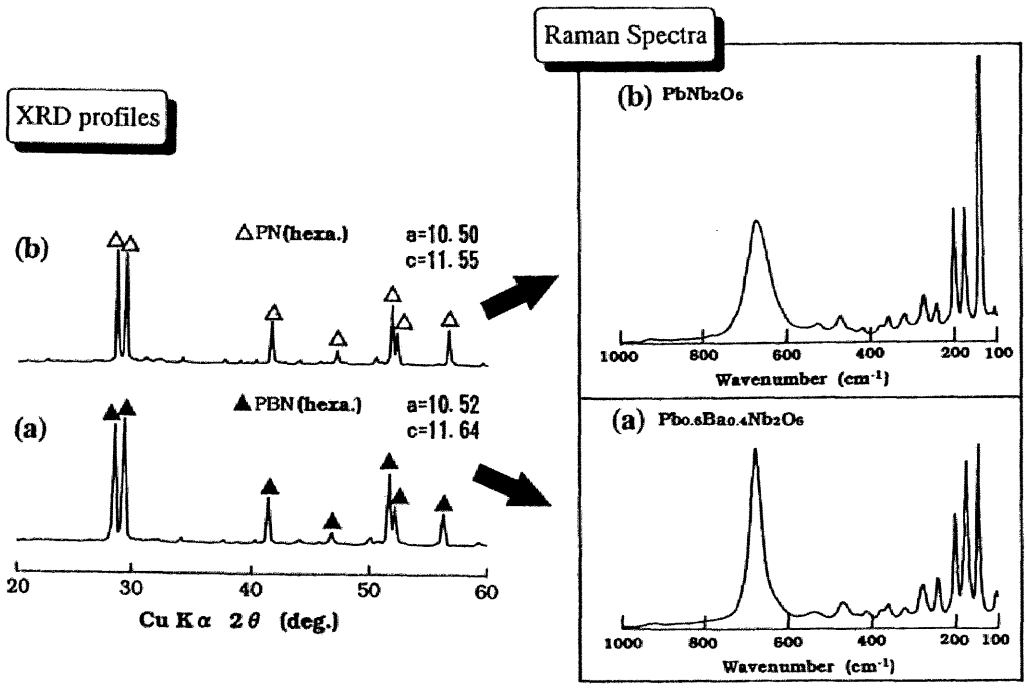


Fig.4-3-6 XRD profiles and Raman spectra of (a) PBN60 and (b) $PbNb_2O_6$ powders heat-treated at 700°C.
[hexa: hexagonal phase]

The measured lattice parameters of the PBN hexagonal low temperature phase (a=10.524Å, c=11.641Å) are slightly bigger than the values of the $PbNb_2O_6$ hexagonal phase (a=10.501Å, c=11.555Å). This change is due to the substitution of $Pb^{2+}$ sites by $Ba^{2+}$ ions in the $PbNb_2O_6$ structure. This difference is due to the incorporation of $Ba^{2+}$ ions for $Pb^{2+}$ sites in the hexagonal $PbNb_2O_6$ structure, because the radius of $Ba^{2+}$ is larger than that of $Pb^{2+}$. Raman spectrum of PBN60 powder is also consistent with that of hexagonal $PbNb_2O_6$ powder, although the scattering positions are slightly different to each other.

In addition, Raman spectrum of $PbNb_2O_6$ powder shown in Fig.4-3-6(b) is in good agreement with that of hexagonal $PbNb_2O_6$ reported by Repelin et al.[20] Figure 4-3-7 illustrates the proposed structure of the low temperature phase of PBN derived from the chemical process. Hexagonal PBN60 low temperature phase was judged to have the hexagonal $PbNb_2O_6$ like structure as shown in Fig.4-3-7.

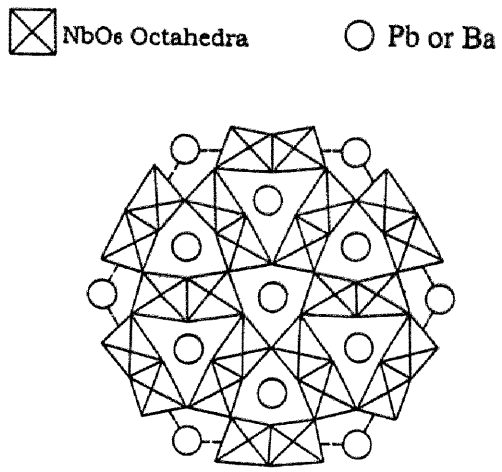


Fig.4-3-7 Proposed structure of the PBN low temperature phase projected onto the (001) plane (hexagonal $PbNb_2O_6$ like structure).

### 4.3.3 Effect of the formation of filled-tungsten bronze

The $K_x(Pb_{0.6}Ba_{0.4})_{1-x/2}Nb_2O_6$ [x=0 (PBN60), 0.1 ($K_{0.1}$PBN60), 0.2 ($K_{0.2}$PBN60), 0.3 ($K_{0.3}$PBN60), 0.4 ($K_{0.4}$PBN60)] powders were prepared from the KPBN precursor solution. In this case, potassium ion is selected as an alkali ion for substitution, because the radius of $K^+$ is close to that of $Pb^{2+}$ or $Ba^{2+}$. Figure 4-3-8 shows XRD profiles of $K_x(Pb_{0.6}Ba_{0.4})_{1-x/2}Nb_2O_6$ [x=0-0.4] powders heat-treated at 700°C. The amount of potassium greatly influenced the formation temperature of tungsten bronze phase.

Figure 4-3-9 shows the relation between the amount of substituted potassium and the crystallization temperature of single-phase tungsten bronze. The formation temperature of tungsten bronze phase greatly decreases from 1250°C (x=0, PBN60) to 700°C (x=0.4, $K_{0.4}$PBN60) with increasing potassium as shown in Fig.4-3-9. The formation of solid solution with potassium was found to be very effective to form the tungsten bronze phase at lower temperatures. The stabilization mechanism of PBN tungsten bronze is explained by the configuration of Nb-O octahedron as in the case of strontium barium niobate (SBN). PBN60 has the unfilled tungsten bronze structure, in which 1/6 of 15-fold and 12-fold coordinated sites distributed in the apex-shared Nb-O octahedron are vacant. Thus, the Nb-O octahedra prefer to construct the edge-shared structure like $PbNb_2O_6$ or $BaNb_2O_6$ as reported.[20] The PBN60 low temperature phase is found to have the $PbNb_2O_6$ (hexagonal) like structure as shown in Fig.4-3-7. When one $Pb^{2+}$ or $Ba^{2+}$

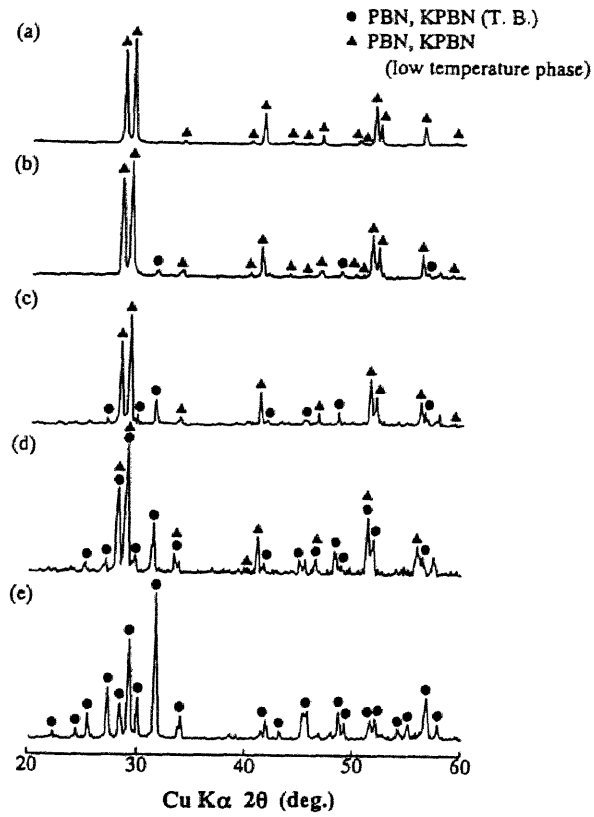


Fig.4-3-8 XRD profiles of $K_x(Pb_{0.6}Ba_{0.4})_{1-x/2}Nb_2O_6$ powders heat-treated at 700°C (a) x=0 (PBN60), (b) x=0.1 ($K_{0.1}$PBN60), (c) x=0.2 ($K_{0.2}$PBN60), (d) x=0.3 ($K_{0.3}$PBN60) and (e) x=0.4 ($K_{0.4}$PBN60) compositions. [T.B.: tungsten bronze phase]

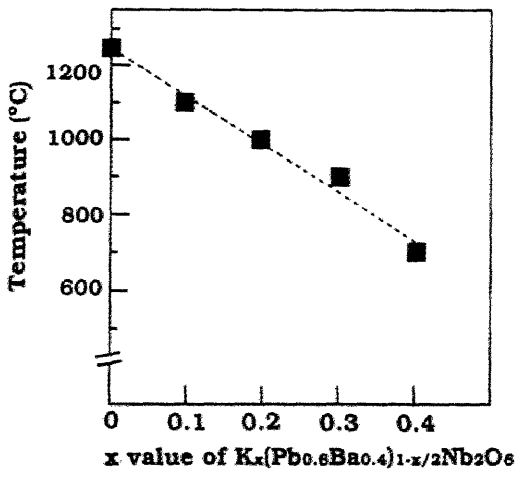


Fig.4-3-9 Relation between amount of substituted potassium and crystallization temperature of single-phase tungsten bronze.

ion is substituted by $K^+$, two $K^+$ ions must be introduced in the 15-fold or 12-fold coordinated site of the PBN structure to keep the charge neutrality of crystal. As the amount of potassium increases, the structure of PBN approaches to the filled-tungsten bronze. Therefore, the structural stability of tungsten bronze phase is enhanced, and the current KPBN powders crystallize in tungsten bronze at lower temperatures compared with PBN60 precursor powders.

### 4.3.4 Preparation of highly oriented tungsten bronze KPBN thin films

Based upon the results of KPBN powder synthesis, $K_{0.4}(Pb_{0.6}Ba_{0.4})_{0.8}Nb_2O_6$ ($K_{0.4}$PBN60) composition was selected for the preparation of thin films. MgO(100) and Pt(100)/MgO(100) were also selected as substrates in order to synthesize c-axis (polar axis) highly oriented KPBN thin films. Figure 4-3-10 shows XRD profiles of $K_{0.4}$PBN60 thin films on MgO(100) substrates heat-treated at various temperatures. Highly oriented $K_{0.4}$PBN60 thin films were synthesized by using MgO(100) substrates, because the $K_{0.4}$PBN60 films on MgO(100) crystallized at 700°C and 750°C show only strong 001 and 002 reflections as shown in Fig.4-3-10. Figure 4-3-11 illustrates the XRD profiles of the $K_{0.4}$PBN60 thin films on Pt(100)/MgO(100) substrates crystallized at various temperatures. The KPBN60 films heat-treated above 600°C on Pt(100)/MgO(100) crystallized with (001) plane preferred orientation as shown in Fig.4-3-11, which included small amount of pyrochlore phase. Only by XRD, however, it is quite

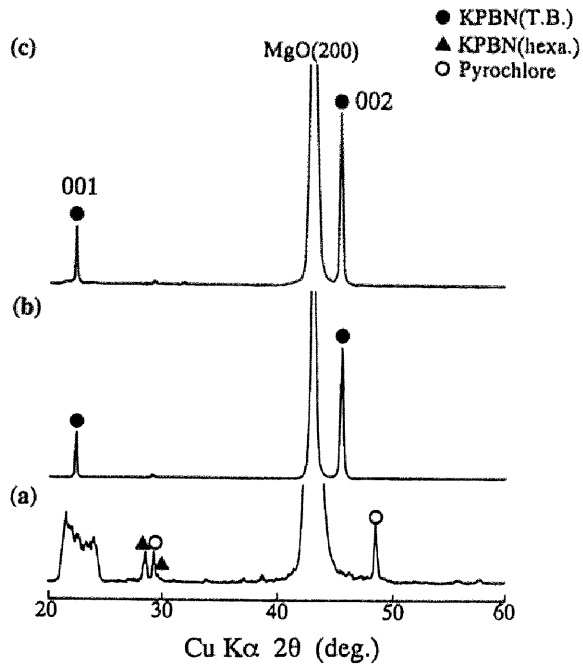


Fig.4-3-10 XRD profiles of $K_{0.4}(Pb_{0.6}Ba_{0.4})_{0.8}Nb_2O_6$ ($K_{0.4}$PBN60) thin films on MgO(100) substrates heat-treated at (a) 600°C, (b) 700°C and (c) 750°C. [T.B.: tungsten bronze phase] [hexa: hexagonal low temperature phase]

difficult to judge whether the $K_{0.4}$PBN60 thin films on MgO(100) crystallized in the tungsten bronze phase or the another phase, because XRD shows only a few reflections due to the preferred orientation.

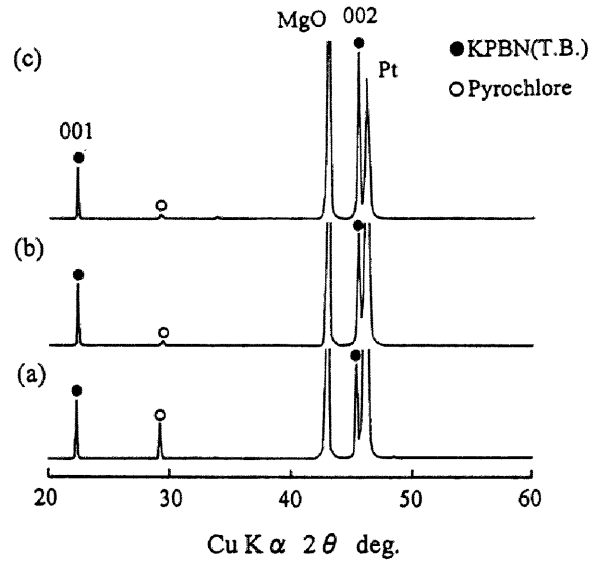


Fig.4-3-11 XRD profiles of $K_{0.4}$PBN60 thin films on Pt(100)/MgO(100) substrates crystallized at (a) 600°C, (b) 700°C and (c) 750°C.

Figure 4-3-12 shows XRD profiles and Raman spectra of PBN60 thin films on MgO(100) substrates heat-treated at 700°C and 900°C. In the case of PBN60 films prepared on MgO(100), the d values of diffractions for the PBN60 thin films crystallized at 700°C and 900°C are slightly different to each other. Furthermore, Raman spectra of these films are obviously different as shown in Fig.4-3-12. These spectra are consistent with those of the hexagonal PBN60 and the tungsten bronze PBN60 powder, respectively. From these results, the PBN60 thin film on MgO(100) crystallizes to the $PbNb_2O_6$ (hexagonal) like low temperature phase at 700°C, which is completely transformed to the tungsten bronze phase at 900°C.

KPBN thin films on MgO(100) substrates were also characterized further by Raman microprobe spectroscopy as in the case of PBN60 films. Figure 4-3-13 shows Raman spectra of the tungsten bronze $K_{0.4}$PBN60 powder and the $K_{0.4}$PBN60 thin film on MgO(100) substrate. Characteristic Raman shifts corresponding to the Nb-O-Nb bending modes (220-300 $cm^{-1}$) and the symmetric stretching mode of the $NbO_6$ octahedron (580-700 $cm^{-1}$) for the tungsten bronze niobate are observed in Fig.4-3-13(a) and 4-3-13(b). The $K_{0.4}$PBN60 thin films crystallized on MgO(100) are confirmed to be a single-phase of tungsten bronze, since the profile (Fig.4-3-13(b)) is consistent with that of $K_{0.4}$PBN60 powder

shown in Fig.4-3-13(a).

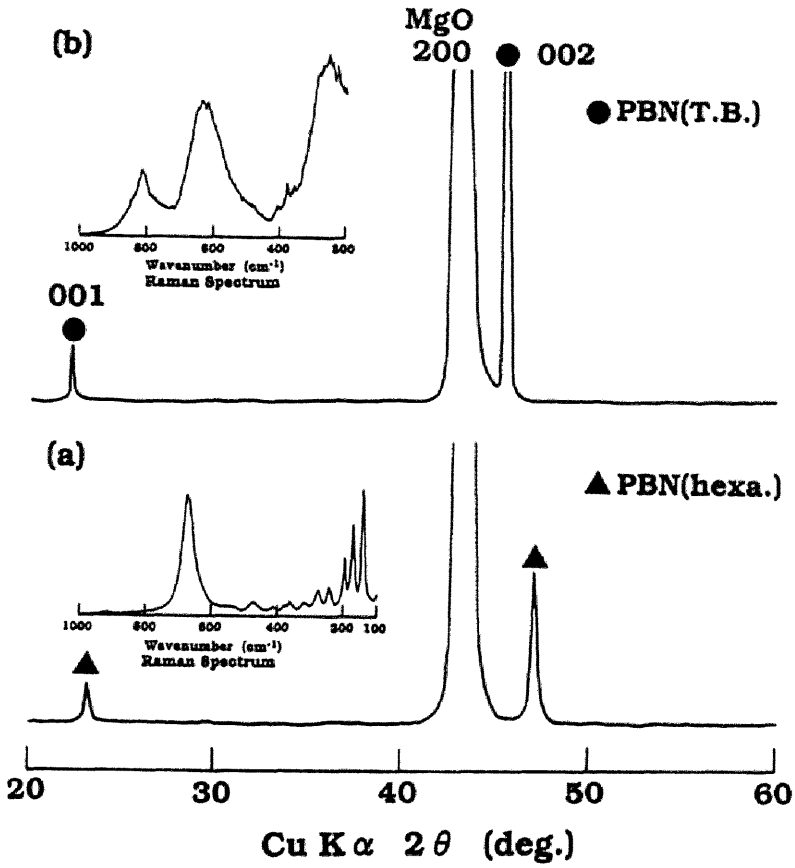


Fig.4-3-12 XRD profiles and Raman spectra of PBN60 thin films heat-treated at (a) 700°C and (b) 900°C.

[T.B.: tungsten bronze phase]

[hexa: hexagonal low temperature phase]

The formation of the tungsten bronze phase is assisted by the formation of a solid solution with potassium. By substitution with potassium, the tungsten bronze structure can be stabilized through the formation of filled-tungsten bronze structure. In the case of PBN60 films on MgO(100) substrates, a heat treatment above 900°C is required to transform PBN60 completely to the tungsten bronze phase. On the other hand, the KPBN60 thin films of tetragonal tungsten bronze were crystallized at lower temperatures as compared with PBN60 thin film on MgO(100).

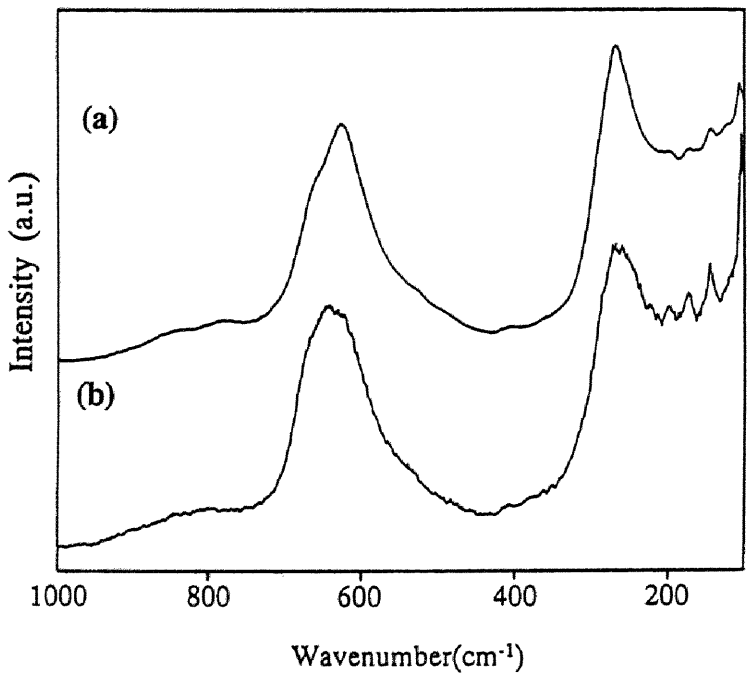


Fig.4-3-13 Raman spectra of (a) tungsten bronze $K_{0.4}$PBN60 powder and (b) $K_{0.4}$PBN60 thin film on a MgO(100) substrate heat-treated at 750°C.

### 4.3.5 Orientation mechanism of KPBN thin films with c-axis preferred orientation

The ψ scan of X-ray diffraction was employed to examine the orientational relationship between the KPBN film and MgO(100) or Pt(100)/MgO(100) substrates. Figure 4-3-14 shows the results of ψ scan for the (211) plane of the $K_{0.4}$PBN60 film crystallized at 750°C on Pt(100)/MgO(100). Figure 4-3-14 also shows the ψ scans for the (220) plane of Pt on MgO(100) and the (220) plane of MgO substrate. The term ψ indicates the rotation axis perpendicular to the film plane. The θ-2θ scan was performed on the MgO(220) plane and the Pt(220) plane.

A 220 peak of MgO and a 220 peak of Pt were detected at $2\theta=60.30^\circ$ and $2\theta=65.41^\circ$, respectively. Thus, the Pt(220) planes are almost parallel to the MgO(220) planes. The $\theta$-$2\theta$ scan on the KPBN(211) plane on Pt(100)/MgO(100) gave a 211 peak of KPBN at $2\theta=27.28^\circ$. 12 peaks with two different intensities were observed as shown in Fig.4-3-14(a). The same profile was observed for the $K_{0.4}$PBN60 thin films on MgO(100). The substrate peak appeared nearly at the same azimuthal $\psi$ angles separated 90° from each other as shown in Figs.4-3-14(b) and 4-3-14(c). The three-dimensional relationship between Pt(100) and MgO(100) was confirmed by the four-fold symmetry of the $\psi$ scans. The a-axis of MgO was consistent with that of Pt as reported by Yogo et al.[17] Since the {211} planes of KPBN show eight equivalent planes around the <001> direction, theoretically 8 peaks should be observed every $\psi=53^\circ$ and 37° as shown in Fig.4-3-15(a). However, the profile shown in Fig.4-3-14(a) exhibits more peaks than those calculated for KPBN single crystal. The intensity ratio of four strong peaks to eight weak peaks is about 2, because the former increase in intensity by superimposition. This result suggests that the other c-plane of KPBN lattice intersects the a-plane of MgO or Pt. Assuming that the angle between the a-axis of MgO or Pt and the a-axis of the other KPBN grain is 18.5°, the calculated pattern is obtained as shown in Fig.4-3-15(b), which is in good agreement with the measured one shown in Fig.4-3-14(a). Therefore, two crystal lattice planes of KPBN are intergrown at an orientation of 18.5° on the MgO(100) and Pt(100)/MgO(100) substrates. This result agrees with that of the $Sr_{1-x}Ba_xNb_2O_6$ or $K_{0.4}(Sr_{0.75}Ba_{0.25})_{0.8}Nb_2O_6$ film on the MgO(100) substrate prepared by the chemical solution process in Chap.2 and pulsed laser deposition.[21] The analysis for the (311) plane of the present KPBN thin films [$2\theta=31.63^\circ$] supports a similar intergrowth behavior as that for the (211) plane.

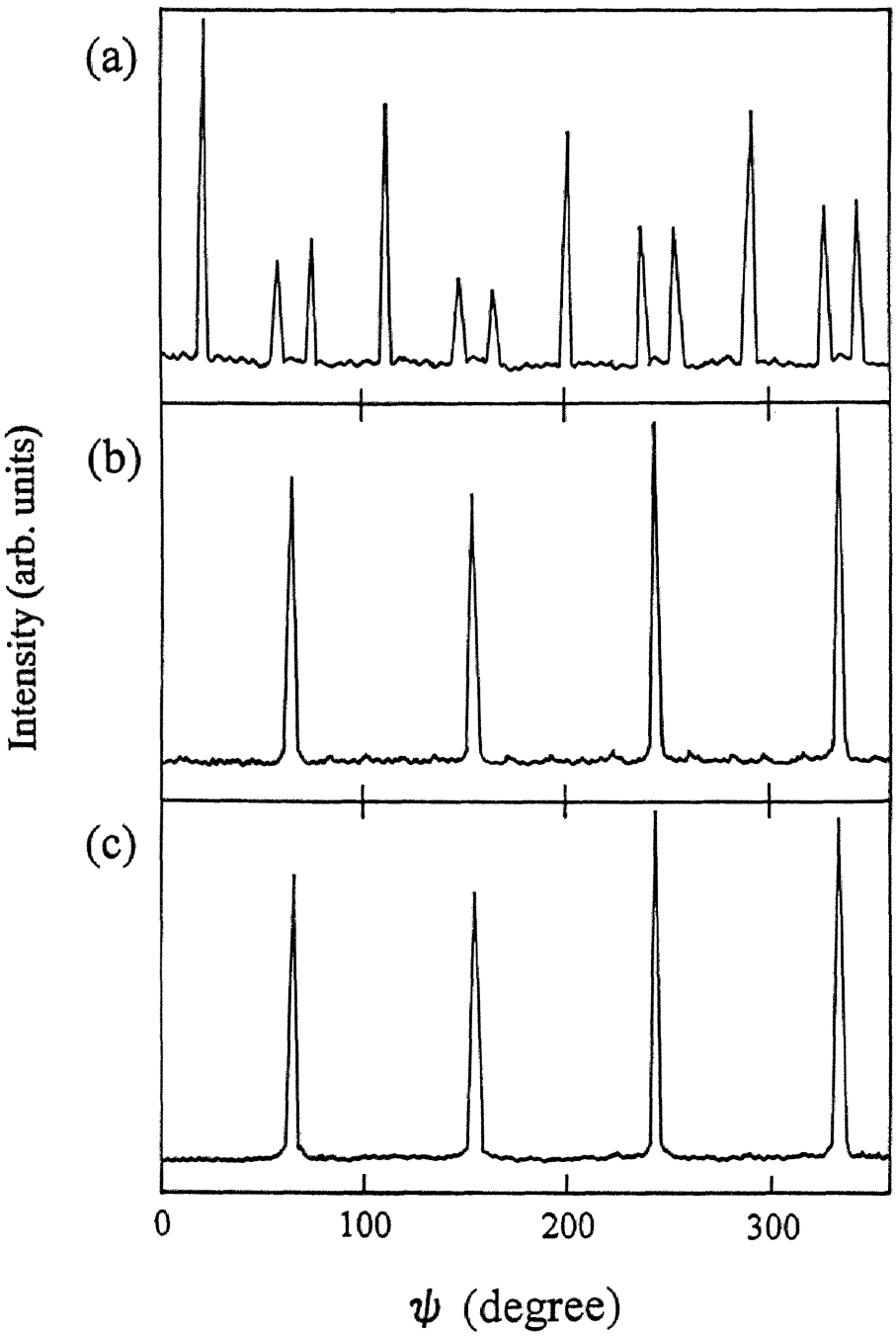


Fig.4-3-14 $\psi$ scans of X-ray diffraction of (a) $K_{0.4}$PBN60 film on Pt(100)/MgO(100) crystallized at 750°C measured for the (211) plane, (b) Pt on MgO(100) for the (220) plane and (c) MgO substrate for the (220) plane.

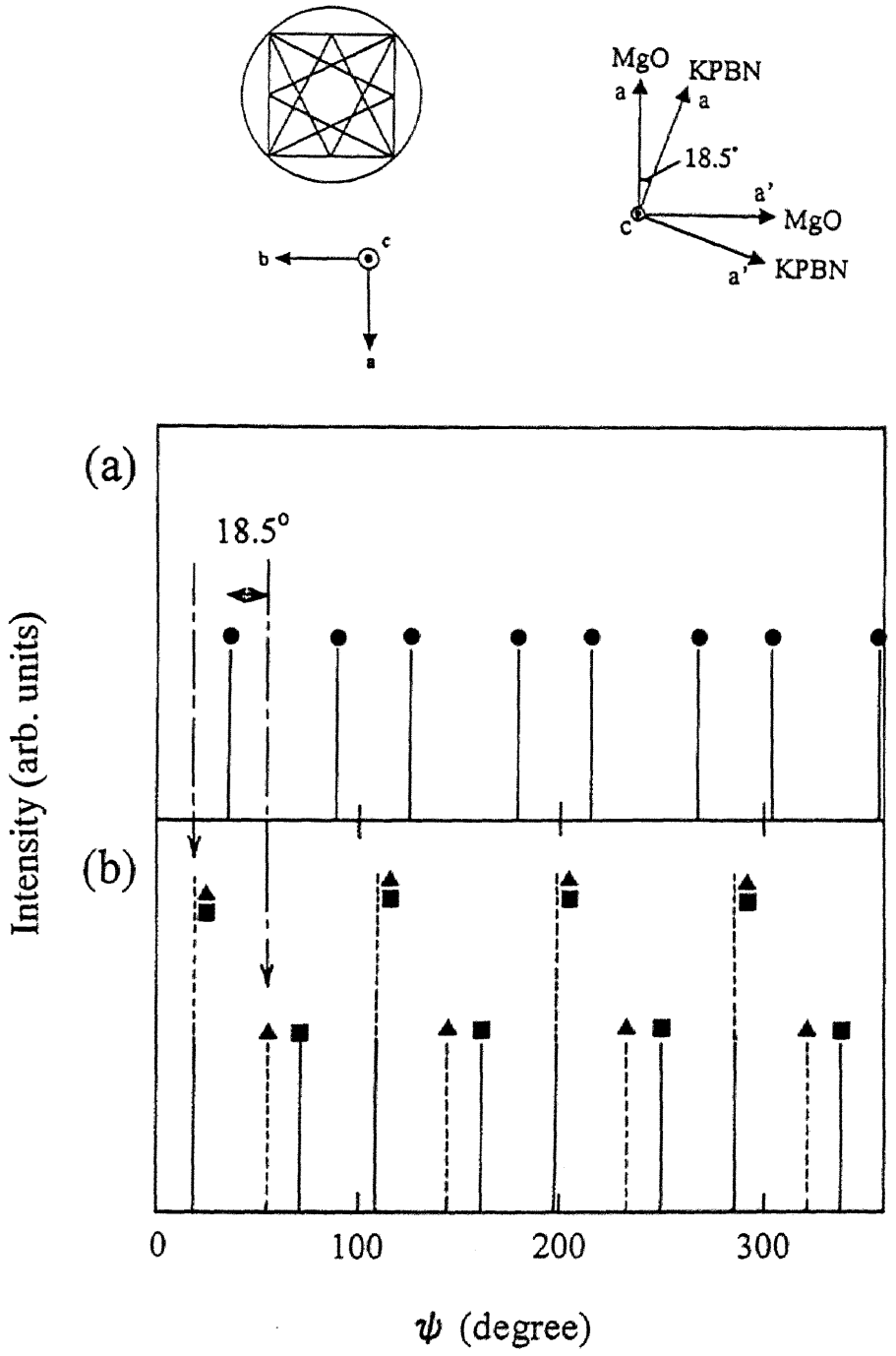


Fig.4-3-15 Calculated $\psi$ scans of $K_{0.4}$PBN60 (a) pattern of $K_{0.4}$PBN60 single crystal constructed for tetragonal (211) and (b) pattern of $K_{0.4}$PBN60 film including two lattices intersected at 18.5° on MgO(100) or Pt(100)/MgO(100).

### 4.3.6 Ferroelectric behavior of synthesized KPBN films

In the case of PBN synthesis, it is quite difficult to prepare tungsten bronze PBN film on substrates, because the PBN thin film easily crystallizes to the low-temperature phase which does not show any ferroelectric properties. When the film was heat-treated at higher temperature at 900°C, the film quality was degraded due to the exaggerated grain growth as described in section 4.3.4. However, potassium substituted PBN (KPBN) has an advantage in crystallizing to the tungsten bronze phase on MgO(100) and Pt(100)/MgO(100) with c-axis preferred orientation at around 750°C. Figure 4-3-16 shows the edge-on profile of $K_{0.4}$PBN60 film on Pt(100)/MgO(100) substrate crystallized at 750°C. The crystallized film thickness is about 0.5 μm after 18 cycles dipping (included 2 cycles dipping for underlayer). The film appears crack-free, and has a uniform thickness and no voids. The quality of the film was found to be good enough to characterize dielectric properties.

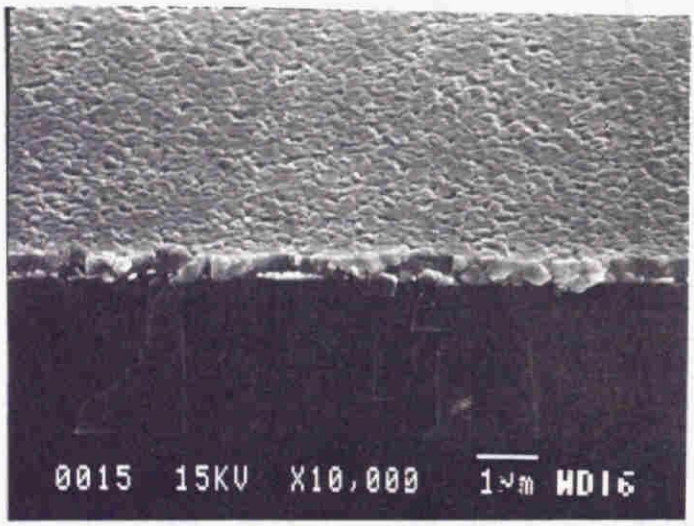


Fig.4-3-16 SEM photograph of $K_{0.4}$PBN60 thin film on a Pt(100)/MgO(100) substrate heat-treated at 750°C.

The effects of crystallization conditions on the electrical properties of the KPBN films were also studied. The measurement at low temperatures was also carried out for every sample, because the ferroelectric phase was considered to be stable enough to show nearly saturated P-E hysteresis loops. In order to investigate the ferroelectric properties of the KPBN films, P-E hysteresis loop was measured from –190°C to room temperature. Figure 4-3-17 shows a P-E hysteresis loop measured at –150°C and change in remnant polarization with temperature for $K_{0.4}$PBN60 thin film on a Pt(100)/MgO(100) substrate. The remnant polarization ($P_r$) is 20 $\mu C/cm^2$, and the coercive field ($E_c$) was 140 kV/cm at –150°C. The hysteresis loop at –150°C was highly saturated with a $P_r/P_s$ ($P_s$: spontaneous polarization) ratio of 0.85. The value of $P_r$ gradually decreases with raising the measurement temperature. The shape of hysteresis changed from typical large ferroelectric one to small one. In addition, the gradual change of P-E hysteresis loop is due to the relatively low crystallinity compared with PBN single crystals, and to the random distribution of $K^+$, $Pb^{2+}$ and $Ba^{2+}$ ions in the A1 and A2 sites of the tungsten bronze structure. From Fig.4-3-16, the Curie temperature of $K_{0.4}$PBN60 film seems to shift to the low temperature region. The substitution with potassium is one of the reasons for the shift of the Curie point, because, in general, the Curie temperature of PBN does shift to lower temperature by alkali ion substitution as shown in $PbNb_2O_6$ (560°C) and $Pb_2KNb_5O_{15}$ (420°C).[7]

Figure 4-3-18 shows P-E hysteresis loops for the KPBN60 thin films on Pt(100)/MgO(100) substrates crystallized at 700°C and 750°C. The P-E hysteresis loops were measured at 20°C and −140°C. The values of remnant polarization ($P_r$), coercive field ($E_c$) and dielectric constant ($\varepsilon_r$) are summarized in Table 4-3-1. The ferroelectric properties of the KPBN60 films were strongly dependent on the crystallinity and grain size of the films. The grain sizes of the KPBN60 thin films were confirmed to be approximately 50-100 nm and 200 nm crystallized at 700°C and 750°C, respectively, as observed from atomic force microscope (AFM) images. The KPBN60 film crystallized at 750°C showed higher values of $\varepsilon_r$ at 20°C and $P_r/P_s$ ratio ($P_s$; spontaneous polarization) in the low-temperature region, at which

the ferroelectric phase was considered to be more stable. This result indicates that the KPBN60 film crystallized at 700°C has relatively low crystallinity and small grain size compared with the KPBN60 film crystallized at 750°C. Also, the polarization of the KPBN60 thin films showed a lower value than that of PBN60 single crystal ($P_s$=70 μC/cm$^2$, after poling).[7] The value of dielectric constant ($\varepsilon_r$=650 at 20°C at 10 kHz) was lower than that of PBN60 bulk ceramics.[7] The substitution of potassium, small grain size and mechanical stress from substrates are considered to be responsible not only for the lower $P_r$ and $\varepsilon_r$ value but also for the higher $E_c$ compared with single crystals.

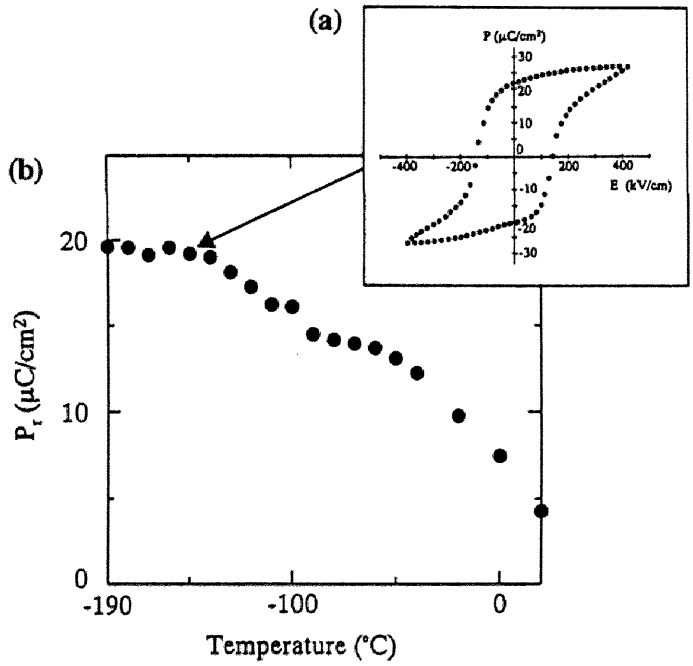


Fig.4-3-17 (a) P-E hysteresis loop measured at –150°C and
(b) temperature dependence of remnant polarization change for $K_{0.4}$PBN60 thin film on a Pt(100)/MgO(100) substrate heat-treated at 750°C.

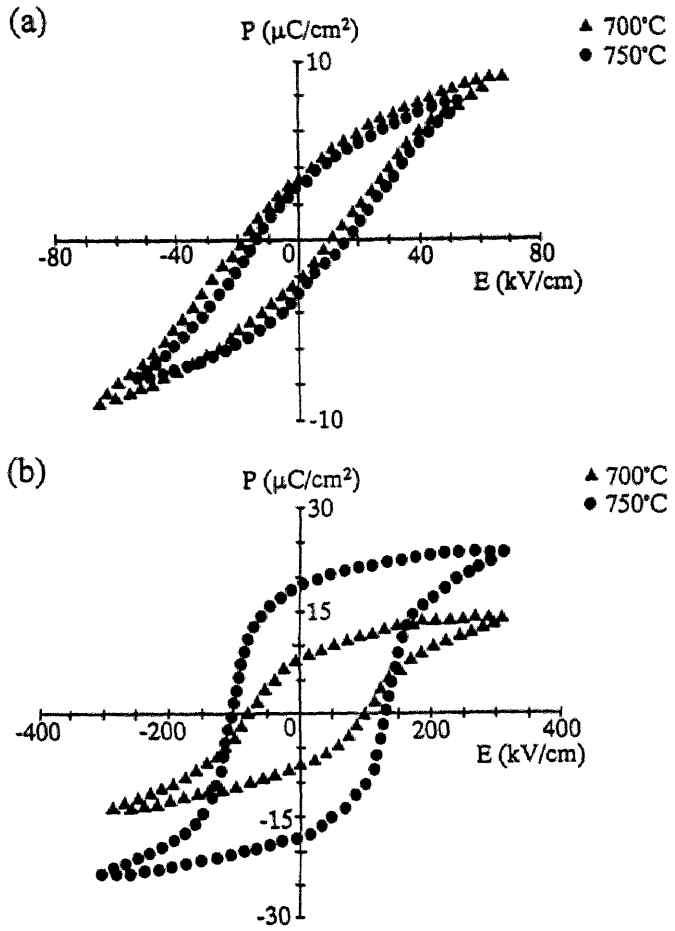


Fig.4-3-18 P-E hysteresis loops of $K_{0.4}$PBN60 thin films on a Pt(100)/MgO(100) substrates crystallized at 700°C and 750°C, (a) measured at 20°C and (b) measured at −140°C.

Table 4-3-1 Electrical properties of $K_{0.4}$PBN60 thin films prepared on Pt(100)/MgO(100) substrates

| Crystallization temperature | $P_r$ (μC/cm²) 20°C ($P_r/P_s$) | -140°C ($P_r/P_s$) | $E_c$ (kV/cm) 20°C | -140°C | $\varepsilon_r$ at 1kHz (20°C) |
|---|---|---|---|---|---|
| 700°C | 3.4 (0.38) | 8.3 (0.57) | 13.5 | 88 | 760 |
| 750°C | 3.0 (0.39) | 19.1 (0.80) | 14.9 | 119 | 830 |

### 4.3.7 Preparation and properties of La doped KPBN thin films

*(1) Effect of La doping on the crystallization of tungsten bronze KPBN*

KPBLN powder sample was prepared from the KPBLN precursor solution. Figure 4-3-19 shows the XRD profiles of $K_{0.45}(Pb_{0.6}Ba_{0.4})_{0.7}La_{0.05}Nb_2O_6$ (KPBLN60/5) powders heat-treated at various temperatures. The KPBLN60/5 powder was X-ray-amorphous below 450°C and crystallized in the pyrochlore phase at 500°C (Fig. 4-3-19(b)), then transformed completely to the tungsten bronze phase at 650°C (Fig. 4-3-19(d)). When $K_{0.4}(Pb_{0.6}Ba_{0.4})_{0.8}Nb_2O_6$ ($K_{0.4}$PBN60) was synthesized by the same process, the KPBN60 powder crystallized to the tungsten bronze phase at 700°C (section 4.3.3). Fig.4-3-19 indicates that La doping is effective for crystallization to the tungsten bronze phase at lower temperatures.

Doping of La ions into the KPBN structure facilitates the formation of the tungsten bronze phase as described above. KPBLN is considered to be the solid solution between $K_{0.8}La_{0.4}Nb_2O_6$ and

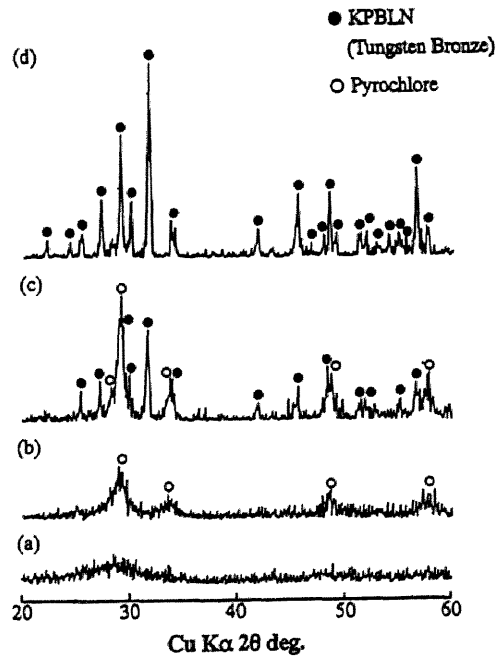


Fig.4-3-19 XRD profiles of $K_{0.45}(Pb_{0.6}Ba_{0.4})_{0.7}La_{0.05}Nb_2O_6$ (KPBN60/5) precursor powders heat-treated at (a) 400°C, (b) 500°C, (c) 600°C and (d) 650°C.

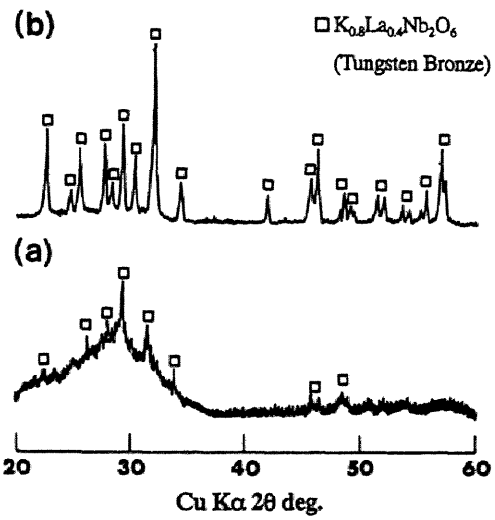


Fig.4-3-20 XRD profiles of $K_{0.8}La_{0.4}Nb_2O_6$ precursor powders heat-treated at (a) 550°C and (b) 650°C.

$K_{0.4}(Pb_{0.6}Ba_{0.4})_{0.8}Nb_2O_6$. In particular, alkali rare earth niobates, such as $K_{0.8}La_{0.4}Nb_2O_6$, are known to have a filled-tungsten bronze structure.[16] $K_{0.8}La_{0.4}Nb_2O_6$ precursor powder synthesized by a similar chemical process directly crystallized in the tungsten bronze phase at 650°C as shown in Fig.4-3-19. Based on the XRD data in Fig.4-3-20, the $K_{0.8}La_{0.4}Nb_2O_6$ precursor is observed to crystallize easily to the tungsten bronze phase without the formation of the low temperature phase. According to the direct crystallization of $K_{0.8}La_{0.4}Nb_2O_6$ to the tungsten bronze phase (Fig.4-3-20), $La^{3+}$ and $K^+$ ions must occupy all of the 15-fold or 12-fold coordinated sites, leading to enhancement of the structural stability of the tungsten bronze phase. Hence, the KPBLN precursor also crystallizes to the tungsten bronze phase more easily compared to the KPBN precursor.

***(2) Synthesis and characterization of KPBLN films on fused silica***

Thin films were synthesized using the KPBLN precursor solution on fused silica substrates, since fused silica has high transparency over a wide wavelength region. Figure 4-3-21 shows the XRD profile of $K_{0.45}(Pb_{0.6}Ba_{0.4})_{0.7}La_{0.05}Nb_2O_6$ (KPBLN60/5) thin film on a fused silica substrate. This film was prepared by the rapid heating and cooling process to suppress the formation of the pyrochlore phase.

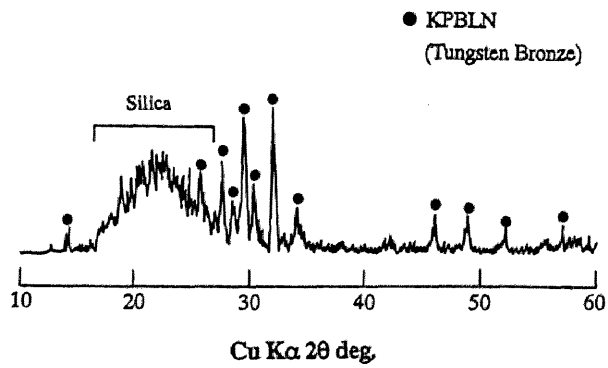


Fig.4-3-21 XRD profile of KPBLN60/5 thin film on a fused silica substrate crystallized at 700°C.

It was quite difficult to prepare thin films of single-phase tungsten bronze on the silica substrate, because the pyrochlore phase crystallized easily before the crystallization of the tungsten bronze phase, as in the case of the lead magnesium niobate (PMN) system.[22] The rapid heating process was known to effectively suppress the formation of low-temperature phases, such as the pyrochlore phase.

The use of fused silica substrates is meaningful on judging the effect of La doping, because the single phase of tungsten bronze $K_{0.4}$PBN60 thin films without La cannot be prepared on fused silica substrates even if rapid heating is performed. This result supports that the effect of La-doping was also confirmed to be remarkable similar to the case for the powder sample described in 4.3.7(1).

In order to investigate the qualities of the KPBLN films for application in optical waveguide devices, the propagation modes in the films were measured using the prism coupling method. Lead based ferroelectric tungsten bronze niobate crystals are known to have a high refractive index (above 2.30) compared to $SiO_2$ glass (1.46). Figure 4-3-22 shows the transmittance of a KPBLN60/5 thin film prepared on a fused silica substrate. It was observed that the KPBLN60/5 thin film had high transparency over a wide wavelength region and the absorption edge of the film was found to be about 340 nm. The interference fringes are derived from the uniform thickness of the film. Since the optical propagation loss depends upon the transmittance of the film, the KPBLN film is required to be highly transparent. La doping was also found to suppress the nonuniform grain growth, which usually gives cloudy films. Figure 4-3-23 shows the TE and TM modes via the prism coupling method for the KPBLN60/5 thin films prepared on fused silica substrates. Three modes, numbers (m) 0, 1 and 2, appear in both the TE and TM modes. The calculated refractive index and film thickness from the three mode angles in the TE mode were about 2.1 and 0.8 μm, respectively. This value of refractive index is lower than that of the tungsten bronze lead barium niobate single crystals, for example, PBN61.5 (2.37)[5]. The lower value of refractive index

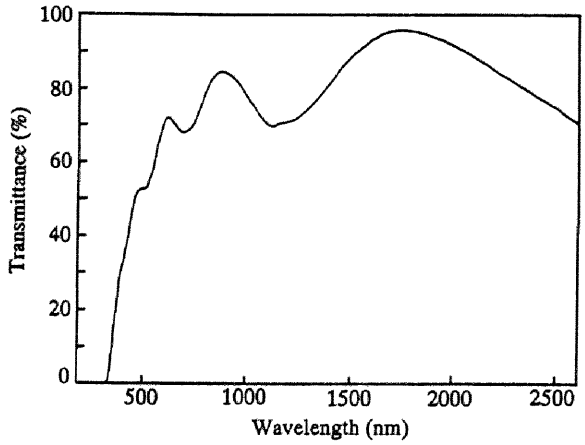


Fig.4-3-22 Optical transmittance of KPBN60/5 thin film on a fused silica substrate crystallized at 700°C.

may be due to the lower density of the KPBLN film compared to that of single crystals. Figure 4-3-24 shows the SEM and FE-SEM photographs of KPBLN60/5 thin films prepared on fused silica substrates after 20 cycles of dipping. The grain size of the film ranged from 50 to 100 nm and a slightly porous microstructure was observed on the FE-SEM surface image shown in Fig.4-3-24(b). The improvement in density of the film results in a higher refractive index, because, in general, the refractive index of the film depends upon its density. The film was dense enough to show a high refractive index and was found to be suitable for potential application to optical wave-guides in combination with the micro-patterning process.

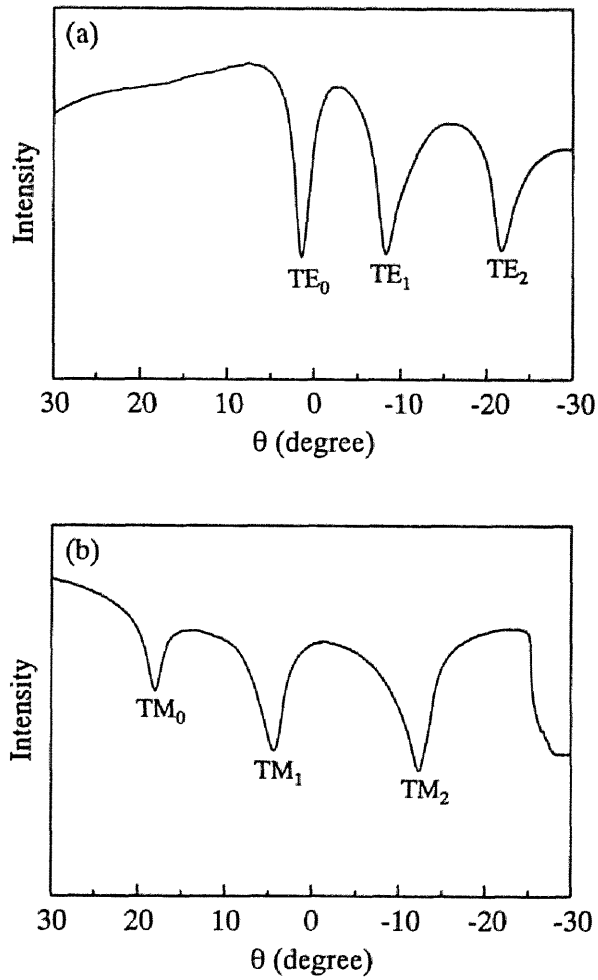


Fig.4-3-23 Optical-propagation of KPBLN60/5 thin film on a fused silica substrate crystallized at 700°C,
(a) TE-mode observation and (b) TM-mode observation.

(a)

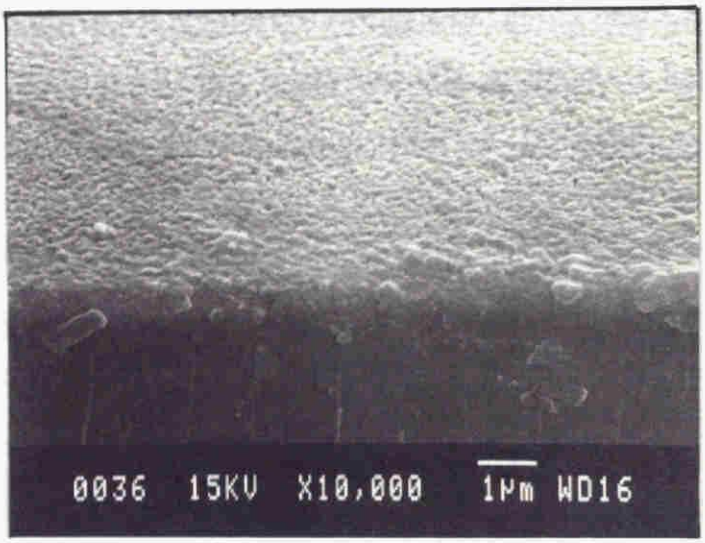


(b)

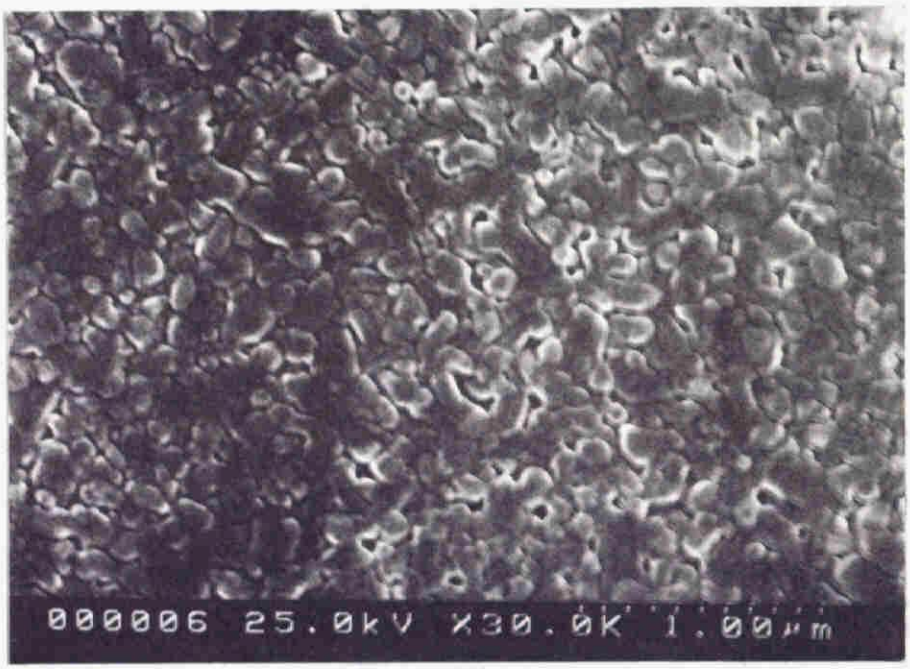


Fig.4-3-24 SEM and FE-SEM photograph of a KPBN60/5 thin film on a fused silica substrate crystallized at 700°C, (a) edge-on profile and (b) surface image.

### *(3) Synthesis and characterization of KPBLN films on MgO(100) and Pt/MgO(100)*

In order to prepare highly oriented KPBLN thin films along the c-axis (direction of polarization), MgO(100) and Pt(100)/MgO(100) substrates were selected, as for the case of KPBN60 synthesis in section 4.3.4. Figure 4-3-25 shows the XRD profiles of the KPBLN60/5 thin films on MgO(100) and Pt(100)/MgO(100) substrates crystallized at 700°C. These films were deposited using a 0.1 mol/l precursor solution and crystallized by the gradual heating and cooling process. Thin films with no preferred orientation are prepared using a solution with a higher concentration or by the rapid heating and cooling process. Not only the optimum concentration of the precursor solution but also the gradual heating process was found to play an important role for the synthesis of highly oriented films. Fig.4-3-25 reveals that the KPBLN60/5 films on both MgO(100) and Pt(100)/MgO(100) substrates have only 001 and 002 reflections with high intensities, although the KPBN60 film on a Pt(100)/MgO(100) substrate crystallized at 700°C included a small amount of the pyrochlore phase as shown in Fig.4-3-11. The formation of low-temperature phases, such as the pyrochlore phase, should be suppressed to obtain the desired properties. This result indicates that the KPBLN60/5 thin films on MgO(100) and Pt(100)/MgO(100) substrates crystallize to the tungsten bronze KPBLN single phase with a c-axis (direction of polarization)-preferred orientation. No reflections

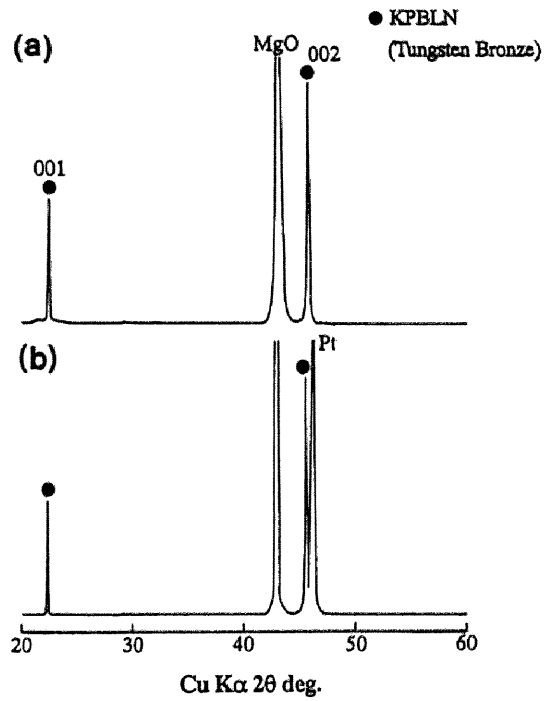


Fig.4-3-25 XRD profiles of KPBN60/5 thin films on (a) MgO(100) and (b) Pt(100)/MgO(100) substrates crystallized at 700°C.

of the pyrochlore phase shown in Fig.4-3-11(c) are observed in either Fig.4-3-25(a) or 4-3-25(b). The KPBLN thin films on MgO(100) substrates were also examined further by Raman microprobe spectroscopy as for the case of the SBN and KSBN films in Chap.2. The Raman scattering profile was consistent with that of the tungsten bronze KPBLN60/5 powder. The KPBLN60/5 thin films crystallized on MgO(100) substrates were thus confirmed to consist of a single-phase tungsten bronze. The three dimensional relation between film and substrate was found to be consistent with that of KPBN film.

La doping was found to be an effective method for the crystallization to the tungsten bronze phase as well as for the improvement of the surface morphology. Figure 4-3-26 shows the SEM photographs of the $K_{0.4}$PBN60 and KPBLN60/5 thin films on Pt(100)/MgO(100) substrates crystallized at 700°C. The film thickness is about 0.5 μm after 20 cycles of dipping (including 2 cycles of dipping for the underlayer). The surface smoothness of the KPBLN60/5 film (Fig.4-3-26(b)) was superior to that of the $K_{0.4}$PBN60 film crystallized at 700°C (Fig.4-3-26(a)). In addition, these films have a uniform thickness, with no voids and cracks, which enables characterization of dielectric and ferroelectric properties.

Figure 4-3-27 shows the temperature dependence of the dielectric constant ($\varepsilon_r$) and the loss tangent for the KPBLN60/5 thin film crystallized at 700°C on a Pt(100)/MgO(100) substrate, measured at 10 kHz. The film had an $\varepsilon_r$ of 740 at room temperature and the dielectric maximum at around 280°C. The peak of $\varepsilon_r$-T curve is broadened compared with that of the PBN single crystals.[3,4] This behavior reflects the diffuse phase transition of the KPBLN60/5 thin film on Pt(100)/MgO(100) substrates. The Curie temperature ($T_c$) of the KPBLN60/5 thin film was lower than that of the $K_{0.4}$PBN60 thin films on Pt(100)/MgO(100), because the dielectric maximum of $K_{0.4}$PBN60 could not be observed from 30°C to 300°C. The $\varepsilon_r$ of $K_{0.4}$PBN60 increased monotonously with an increase of temperature. La doping is the main reason for the shift of $T_c$, because the Curie temperature of $K_{0.8}La_{0.4}Nb_2O_6$ is reported to be about −100°C[16] and KPBLN60/5 is a solid solution between $K_{0.4}$PBN60 and $K_{0.8}La_{0.4}Nb_2O_6$. In addition, the Curie

temperature of PBN generally shifts towards lower temperatures following substitution with lanthanum ions.[9]

**(a)**

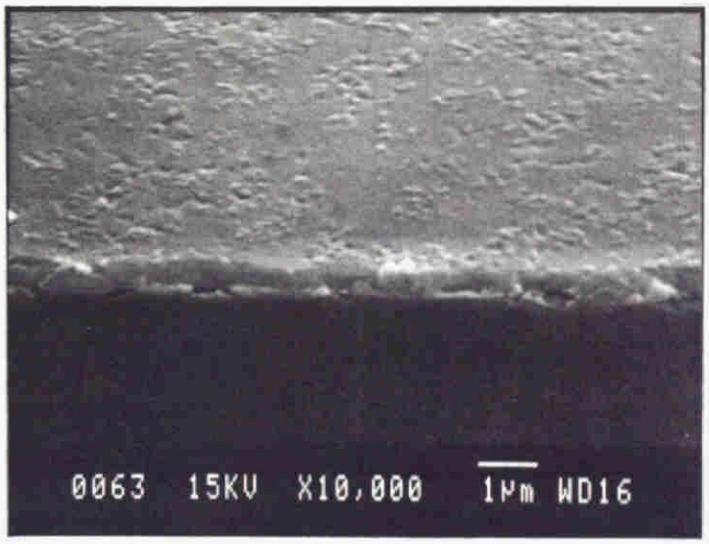


**(b)**

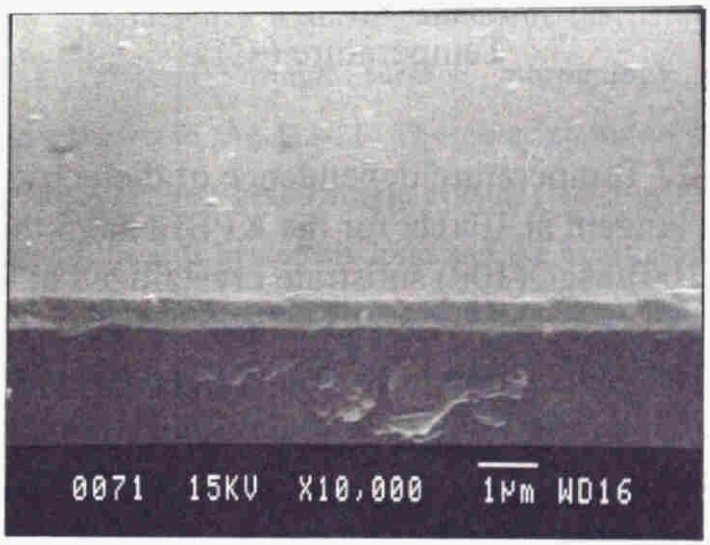


Fig.4-3-26 SEM photographs of (a) $K_{0.4}$PBNb60 and (b) KPBLN60/5 thin films on Pt(100)/MgO(100) substrates crystallized at 700°C.

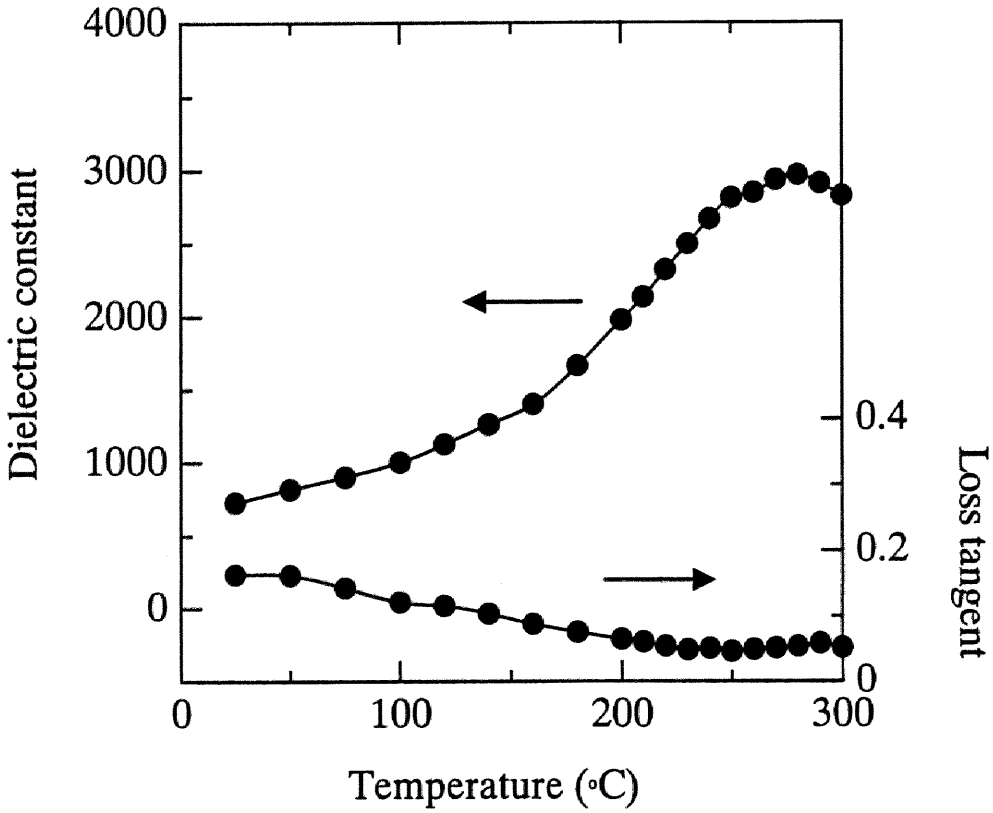


Fig.4-3-27 Temperature dependence of dielectric constant and loss tangent at 10kHz for the KPBLN60/5 thin film on a Pt(100)/MgO(100) substrate crystallized at 700°C.

The P-E hysteresis loop was measured so as to study the ferroelectric behavior of the KPBLN films. $K_{0.4}$PBN60 thin films on Pt(100)/MgO(100) were also characterized by a similar method. In this case, the measurement was carried out at low temperatures as described in section 4.3.6. Figure 4-3-28 shows the P-E hysteresis loops measured at −140°C and the temperature dependence of the remnant polarization for the $K_{0.4}$PBN60 and KPBLN60/5 thin films on Pt(100)/MgO(100) substrates crystallized at 700°C. The typical ferroelectric P-E hysteresis loops were also observed at 20°C. The value of remnant polarization ($P_r$) gradually decreases with an increase in measurement temperature. This behavior was observed for both the KPBN and KPBLN films on Pt(100)/MgO(100) substrates. The grain sizes of the $K_{0.4}$PBN60 and KPBLN60/5 thin films were confirmed to be approximately 50-100 nm by FE-SEM. KPBLN60/5 films crystallized at 700°C showed higher values of $\varepsilon_r$ at 20°C (840, at 1 kHz), $P_r/P_s$ ratio ($P_s$: spontaneous polarization) and a slightly lower coercive field ($E_c$) compared with KPBN60 films in Table 4-3-2. Since the $K_{0.4}$PBN60 film crystallized at 700°C it included a small amount of the pyrochlore phase as in Fig.4-3-11 with a relatively rough surface morphology compared to the KPBLN60/5 film as shown in Fig.4-3-26. The polarization of these films showed lower values than those of the PBN60 single crystal ($P_s$=70 μC/cm$^2$, after poling).[7] The gradual change of the P-E hysteresis loop and the broadening of the $\varepsilon_r$-T curve peak are attributed to the small grain size and the random distribution of element ions in the 15-fold and 12-fold sites of the tungsten bronze structure. Additional factors, such as the mechanical stresses imposed on the films by the substrates might be responsible for the observed dielectric and ferroelectric properties around and below the Curie temperature.

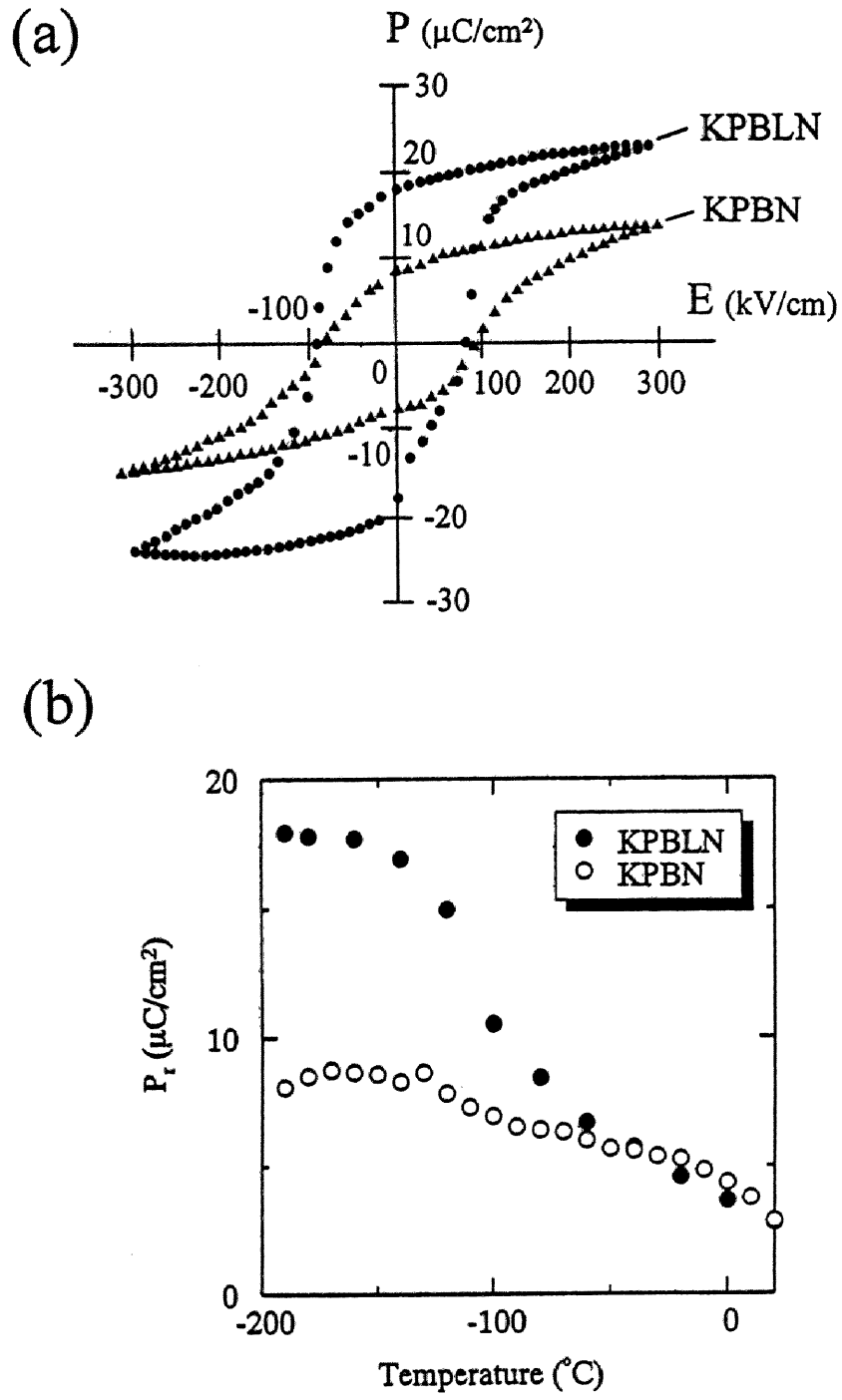


Fig.4-3-28 P-E hysteresis loops for (a) $K_{0.4}$PBN60 and KPBLN60/5 thin films on Pt(100)/MgO(100) substrates crystallized at 700°C, measured at –140°C and (b) temperature dependence of remanent polarization.

## 4.4 Conclusions

Crack-free PBN60 ($Pb_{0.6}Ba_{0.4}Nb_2O_6$), $K_{0.4}$PBN60 ($K_{0.4}(Pb_{0.6}Ba_{0.4})_{0.8}Nb_2O_6$) and KPBLN60/5 ($K_{0.45}(Pb_{0.6}Ba_{0.4})_{0.7}La_{0.05}Nb_2O_6$) films of tungsten bronze structure were successfully synthesized with preferred orientation on MgO(100) and Pt(100)/MgO(100) substrates from metallo-organics. The results are summarized as follows :

1. Homogeneous and stable PBN, KPBN and KPBLN precursor solutions were prepared from anhydrous lead acetate, barium metal, potassium ethoxide, lanthanum isopropoxide and niobium ethoxide in 2-methoxyethanol. The substitution of organic ligands was investigated by $^{1}H$ and $^{13}C$ NMR and the formation of stoichiometric precursor was confirmed by $^{93}Nb$ NMR.
2. By using the chemical solution process with the metallo-organic precursor, the PBN powder was found to be crystallized at 600°C as a hexagonal low temperature phase, which was completely transformed to the orthorhombic tungsten bronze phase at 1250°C.
3. The structure of the low temperature phase of PBN was confirmed to be the hexagonal $PbNb_2O_6$ like structure. The incorporation of $K^+$ for $Pb^{2+}$ or $Ba^{2+}$ site in the PBN structure was found to play an important role in lowering the crystallization temperature of the tungsten bronze phase.
4. KPBN films on MgO(100) and Pt(100)/MgO(100) substrates crystallized to the tungsten bronze phase below 750°C, which was much lower than that of PBN films without potassium substitution, and showed a prominent c-axis preferred orientation. Two crystal lattice planes of KPBN were intergrown at an orientation of 18.5° on MgO(100) and Pt(100)/MgO(100) substrates.
5. Ferroelectric hysteresis loops were observed for the $K_{0.4}$PBN60 thin films on Pt(100)/MgO(100). The value of remnant polarization of the film gradually decreased with increasing temperature from –190°C to room temperature.
6. Lanthanum doping was found to be a key for the improvement of the surface morphology of the synthesized films, as well as for the crystallization to the tungsten bronze phase at lower temperatures. This result is due to the

formation of a solid solution with $K_{0.8}La_{0.4}Nb_2O_6$, which exhibits high stability of the tungsten bronze structure.

7. The tungsten bronze KPBLN60/5 thin films on fused silica substrates showed high transparency over a wide wavelength region and were found to propagate the laser light in the film. The Curie temperature of the KPBLN60/5 films on Pt(100)/MgO(100) substrates was about 280°C. The ferroelectric KPBLN phase was sufficiently stable around room temperature and underwent a gradual phase transition with increasing temperature.

## References


1. M.H.Francombe, "The Relation between Structure and Ferroelectricity in Lead Barium and Barium Strontium Niobates", *Acta Cryst.*, **13** 131-140 (1960).

2. B.Jaffe, W.R.Cook Jr and H.Jaffe, "Chapter 9 Non-Perovskite oxide piezoelectrics and ferroelectrics", pp. 213-235 in Piezoelectric ceramics, Academic Press Limited, New York (1971).

3. R.Guo, A.S.Bhalla, C.A.Randall, Z.P.Chang and L.E.Cross, "Properties of Morphotropic Phase Boundary Lead Barium Niobate (PBN) Compositions", *Ferroelectrics*, **93** 193-201 (1989).

4. R.Guo, A.S.Bhalla, C.A.Randall, Z.P.Chang and L.E.Cross, "Polarization Mechanisms of Morphotropic Phase Boundary Lead Barium Niobate (PBN) Compositions", *J. Appl. Phys*, **67** [3] 1453-1460 (1990).

5. G.Burns, F.H.Dacol, R.Guo and A.S.Bhalla, "Ferroelectric $(Pb,Ba)Nb_2O_6$ near the Morphotropic Phase Boundary", *Appl. Phys. Lett.*, **57** [6] 543-544 (1990).

6. R.Guo, A.S.Bhalla, C.A.Randall and L.E.Cross, "Dielectric and Pyroelectric Properties of the Morphotropic Phase Boundary Lead Barium Niobate (PBN) Single Crystals at Low Temperature (10-300K)", *J. Appl. Phys.*, **67** [10] 6405-6410 (1990).

7. J.R.Oliver, R.R.Neurgaonkar and L.E.Cross, "Ferroelectric Properties of Tungsten Bronze Morphotropic Phase Boundary Systems", *J. Am. Ceram. Soc.*, **72** [2] 201-211 (1989).

8. E.A.Giess, B.A.Scott, G.Burns, D.F.O'kane and A.Segmuller, "Alkali Strontium-Barium-Lead Niobate Systems with a Tungsten Bronze Structure : Crystallographic Properties and Curie Points", *J. Am. Ceram. Soc.*, **52** [5] 276-281 (1969).

9. M.Yasuoka and M.Marutake, "Optical and Electrical Properties of La-Modified (Pb-Ba)$Nb_2O_6$ Ferroelectric Ceramics", *Jpn. J. Appl. Phys.*, **30** [9B] 2322-2325 (1991).

10. T.R.Shrout and L.E.Cross, "Ferroelectric Properties of Tungsten Bronze Lead Barium Niobate (PBN) Single Crystals", *Ferroelectrics Letters*, **44** 325-330 (1983).

11. M.H.Francombe, "Ferroelectric Films and Their Device Applications", *Thin Solid Films*, **13** 413-433 (1972).

12. L.M.Sheppard, "Advances in Processing of Ferroelectric Thin films", *Am. Ceram. Soc. Bull.*, **71** [1] 85-95 (1992).

13. M.Adachi and A.Kawabata, "Ferroelectric Thin Films of Tungsten-Bronzes", *Ceram. Trans.* **25** 303-313 (1991).

14. M.Adachi, A.Kawabata and F.Takeda, "Preparation of Tungsten-Bronze Thin Films", *Jpn. J. Appl. Phys.*, **30** [9B] 2208-2211 (1991).

15. K.Umakantham, S.N.Murty, K.S.Rao and A.Bhanumathi, "Effect of Rare-Earth Ions on the Properties of Modified (Sr,Ba)$Nb_2O_6$ Ceramics", *J. Mater. Sci. Lett.*, **6** 565-567 (1987).

16. B.A.Scott, E.A.Giess, G.Burns and D.F.O'Kane, "Alkali-Rare Earth Niobates with the Tungsten Bronze-Type Structure", *Mater. Res. Bull.*, **3** 831-842 (1968).

17. T.Yogo, K.Kikuta, Y.Ito and S.Hirano, "Synthesis of Highly Oriented KTN Film Using Metal Alkoxides.", *J. Am. Ceram. Soc.*, **78** [8] 2175-2179 (1995).

18. S.Govil, P.N.Kapoor and R.C.Mehrotra, "Double Isopropoxides of Niobium and Tantalum with Alkaline Earth Metals", *J. Inorg. Nucl. Chem.*, **38** [1] 172-173 (1976).

19. H.Brusset, H.Gillier-Pandraud and R.Mahe, "Structure de la solution solide $Pb_{0.7}Ba_{0.3}Nb_2O_6$", *Bull. Soc. Chim. France*, **3** 926-934 (1972).

20. Y.Repelin, E.Husson et H.Brusset, "Etude par spectroscopies d'absorption i.r. et de diffusion Raman des composes $A^{II}B_2{}^{V}O_6$ de structure de type "blocs 1×2" -I. Etude du niobate de baryum $BaNb_2O_6$", *Spectrochimica Acta*, **35A** 937-948 (1979).

21. S.S.Thony, K.E.Youden, J.S.Harris, Jr., and L.Hesselink, "Growth of Epitaxial Strontium Barium Niobate Thin Films by Pulsed Laser Deposition", *Appl. Phys. Lett.* **65** [16] 2018-2020 (1994).

22. S.Hirano, T.Yogo, K.Kikuta and W.Sakamoto, "Processing and Characterization of $Pb(Mg,Nb)O_3$-$PbTiO_3$ Thin Films from Metal Alkoxide Derived Gels", *J. Sol-Gel Sci. Tech.*, **2** [1-3] 329-334 (1994).

# Chapter 5

## Synthesis and Properties of Barium Sodium Niobate (BNN) Thin Films

## 5.1 Introduction

Barium sodium niobate ($Ba_2NaNb_5O_{15}$, BNN) is one of the ferroelectric niobate crystals with the tungsten bronze structure, especially filled tungsten bronze structure, in which all 15-fold- and 12-fold-coordinated sites are occupied by Ba and Na ions. BNN has large nonlinear optical coefficients and excellent electro-optic properties.[1] Therefore, BNN has been receiving great deal of attentions for applications in several electrooptic devices, such as second harmonic generation and laser oscillation.[2,3] BNN has a prominent nonlinear optical coefficient[4] and a higher SHG efficiency[5] than the well-known lithium niobate ($LiNbO_3$).

BNN single crystals have been grown mainly by the Czochralski method similar to other niobate crystals.[3,6] However, the growth of single crystal is usually difficult because crack formation occurs at the phase transition temperature (around 560°C) because of a large thermal expansion of the c-axis. Also, the Curie temperature varies depending upon the Ba/Na ratio reflecting composition fluctuation. Thin films of functional materials have been receiving increased attention, because of their application in integrated devices. BNN thin films were fabricated by several methods, such as sputtering[7] and laser ablation[8,9]. Usually, the control of composition is difficult in deposition methods under vacuum. Since the ferroelectric properties including the Curie temperature change with Ba/Na ratio, the precise control of composition is required for the synthesis of high optical quality BNN thin films. Boulton et al. reported the synthesis of polycrystalline BNN films via the sol-gel method.[10] However, thus far the structure of BNN precursor, crystallization process and several properties of film sample have not been clarified.

This chapter focuses on the synthesis and characterization of highly oriented tungsten bronze BNN thin films using metal alkoxides. The structure of BNN precursors in solution was analyzed by NMR spectroscopy. The crystallization behavior of alkoxy-derived powders and thin films was investigated. The dielectric and optical properties of tungsten bronze BNN thin films were also

studied.

## 5.2 Experimental

*(1) Synthesis of BNN precursor solutions, powders and thin films*

Ba metal [Furu-uchi Chemical, Japan], $NaOCH_2CH_3$ (sodium ethoxide, NaOEt) [Ko-jundo Chemical, Japan] and $Nb(OCH_2CH_3)_5$ ($Nb(OEt)_5$) [Trichemical and Ko-jundo Chemical, Japan] were commercially available. Ethanol was dried over magnesium ethoxide and distilled prior to use. Figure 5-2-1 shows an experimental procedure for fabrication of BNN powders and thin films. Since starting materials are extremely sensitive to moisture, therefore, all procedures were conducted in a dry $N_2$ gas atmosphere. At first, Ba metal was dissolved in absolute ethanol and refluxed for 1 h, and then NaOEt was added to the solution corresponding to $Ba_2NaNb_5O_{15}$ composition. After the solution was refluxed for 18 h, $Nb(OEt)_5$ solution was mixed with the solution. The mixed solution was reacted again at a reflux temperature for 18 h. Then, the solution was condensed to about 0.2 mol/l by removal of solvent under vacuum.

Powders were prepared from the precursor solution to study the crystallization behavior. The hydrolyzed powder and the non-hydrolyzed powder were prepared. The BNN solution was hydrolyzed using deionized water diluted with absolute ethanol. The precipitate was dried at 100°C yielding a white solid as the hydrolyzed powder. On the other hand, the non-hydrolyzed powder was prepared by vacuum evaporation of solvent from the BNN precursor solution. The powder was calcined at 300°C in $O_2$ atmosphere at a rate of 2°C/min, and then heat-treated at temperatures between 500°C and 750°C at 10°C/min in an oxygen flow for 1 h.

Films were fabricated using the precursor solution by dip-coating on fused silica, MgO(100) and Pt(100)/MgO(100) substrates. The Pt(100) layer was fabricated on MgO(100) by RF-magnetron sputtering as described in Chapter 2. The withdrawal rate of substrate from the precursor solution ranged from 0.6 to 1.5 mm/s. Prior to dip-coating, fused silica and MgO(100) substrates were cleaned

with absolute ethanol via ultrasonication. The substrates were soaked in absolute ethanol at 60°C to clean the surface. The deposited films were dried in flowing dry $N_2$.

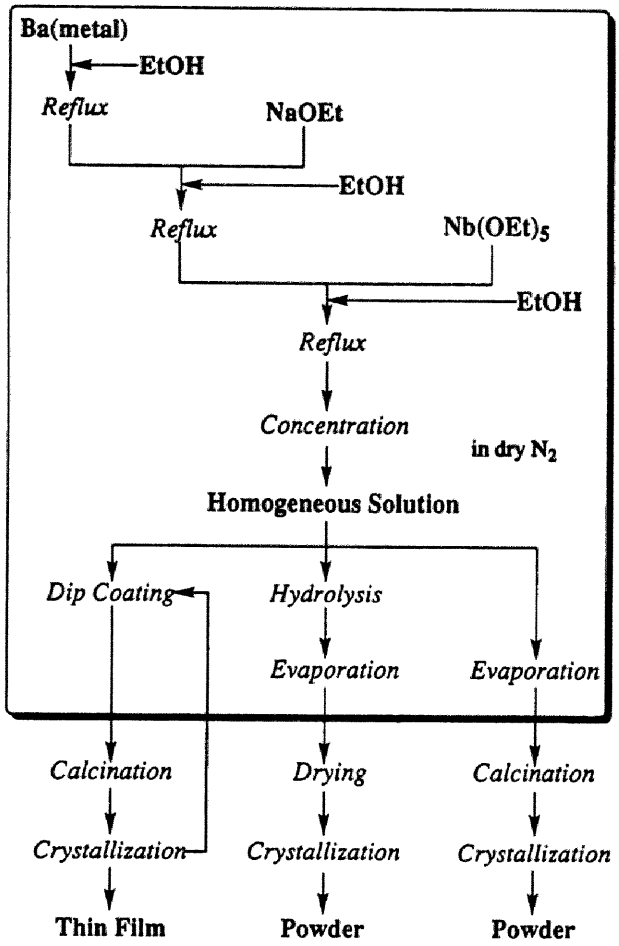


Fig.5-2-1 Processing scheme for alkoxy-derived $Ba_2NaNb_5O_{15}$ (BNN) powders and thin films.

The film on substrate was calcined at 300°C for 1 h, and then heated to a crystallization temperature for 1 h or 30 min, and finally cooled in an $O_2$ flow at 5°C/min or 10°C/min. On the other hand, crystallized films on substrates were prepared by a 2 cycle-dip coating method. Initially, a substrate was dipped into 0.01 mol/l solution and calcined at 500°C for 1 h in $O_2$. The calcined film was crystallized at 800°C for 1 h. This procedure was repeated twice in order to form

an underlayer film. The substrate with formed underlayer film was dipped into 0.2 mol/l solution and calcined at 500°C for 1 h. The calcined film was introduced to a furnace preheated at 700°C, and kept at 700°C for 30 min (rapid heating). The coating-crystallization process was repeated several times to increase the thickness of the film. The crystallized film thickness per dip coating was 0.05 μm, when the precursor film was withdrawn at 1.5 mm/s.

*(2) Characterization of BNN precursor solutions, powders and thin films*

$^{1}H$ and $^{13}C$ NMR spectra were recorded by a Gemini 200 spectrometer [Varian] in $CDCl_3$ or $CD_3SOCD_3$ solution using tetramethylsilane (TMS) as the internal standard. $^{23}Na$ and $^{93}Nb$ NMR spectra of the precursors were recorded at frequencies of 66.17 MHz and 61.14 MHz, respectively [Bruker Instruments, AC250] in ethanol solutions. Sodium chloride NaCl in $D_2O$ and tetramethylammonium hexachloroniobate $(CH_3)_4N[NbCl_6]$ in $CD_3CN$ were used as the standard for chemical shifts of the $^{23}Na$ and $^{93}Nb$ spectra, respectively.

The crystallographic phases and the microstructures of prepared powders and films, the transmittance of the films on transparent substrates were characterized by the same process described in Chap.2.

The electrical properties of films were measured using Au on the BNN films as a top electrode and sputtered Pt(100) layer on MgO(100) as a bottom electrode. The dielectric constants of the films were measured using an LCR meter [Hewlett-Packard, 4194A] in air from room temperature to 873K in a tube furnace. The P-E hysteresis loops of films were evaluated as in Chap.2.

The prepared films on fused silica substrates were exposed using 1064 nm light from $Nd^{3+}$:YAG laser with a pulse duration of ~ 8 ns to investigate the SHG effect. The second-harmonic (SH) light from the film specimen was analyzed by a monochromater equipped with a photomultiplier and boxcar integrator. The measurement system is shown in Fig.5-2-2. The maximum peak power of laser light that was irradiated on the films was ~ 130 kW. The SHG from Y-cut quartz (1.0 mm thick) was measured under the same conditions as the reference.

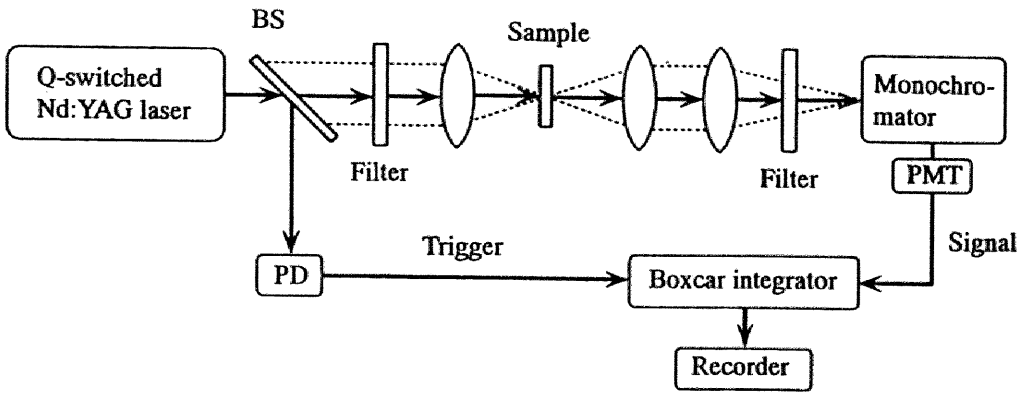


Fig.5-2-2 Outline of SHG measurement for $Ba_2NaNb_5O_{15}$ (BNN) thin films.

## 5.3 Results and discussion

### 5.3.1 Synthesis of precursor solutions

BNN precursor solutions were prepared from Ba, NaOEt and $Nb(OEt)_5$ in ethanol. In order to investigate the structure of the BNN precursor in solution, the complex alkoxide formed by the reaction of starting alkoxides was analyzed by $^{1}H$, $^{13}C$, $^{23}Na$ and $^{93}Nb$ NMR spectroscopy.

Figure 5-3-1 shows $^{1}H$ NMR spectra of BN ($BaNb_2O_6$), NN ($NaNbO_3$) and BNN ($Ba_2NaNb_5O_{15}$) precursor. The signals of ethoxy groups ($CH_3CH_2O$) of the BN precursor are observed at 1.11 ppm (methyl) and 4.15 ppm (methylene) in Fig.5-3-1(a). The NN precursor shows the signals of ethoxy group at 1.19 ppm (methyl) and 4.23 ppm (methylene) (Fig.5-3-1(b)). Figure 5-3-1(c) shows $^{1}H$ NMR spectrum of the BNN precursor, which comprises two kinds of ethoxy groups ($CH_3CH_2O$). The one appears at 1.23 and 4.25 ppm, the other at 1.31 and 4.38 ppm. The integration ratio of the former to the latter is 2, which is in good agreement with the composition of BN ($BaNb_2O_6$) to NN ($NaNbO_3$). Therefore, the former assigned to the BN precursor, while the latter to the NN precursor. The slight changes in chemical shift indicate the formation of the BNN precursor through the

reaction of starting alkoxides.

Figure 5-3-2 shows the $^{13}C$ NMR spectra of the BN, NN and BNN precursor. The spectrum of the NN precursor is composed of a signal of methylene carbon ($O\underline{C}H_2CH_3$) at 66.5 ppm, and that of methyl carbon ($OCH_2\underline{C}H_3$) at 19.7 ppm. The BN precursor shows signals at 64.5 ppm ($O\underline{C}H_2CH_3$) and 19.1 ppm ($OCH_2\underline{C}H_3$). After three alkoxides were reacted at 80°C in ethanol, the BNN precursor showed two kinds of ethoxy groups of methylene (66.2 and 66.3 ppm) and methyl carbon (19.3 and 19.5 ppm) as shown in Fig.5-3-2. The integrations of the pair at 66.2 and 19.5 ppm are larger than those at 66.3 and 19.3 ppm. Thus, the former is due to the $OCH_2CH_3$ of $Ba[Nb(OEt)_6]_2$, the latter those of $Na[Nb(OEt)_6]$. In other words, two kinds of chemically equivalent ethoxy groups are formed in the BNN precursor solution. This result was consistent with that of $^1H$ NMR spectra described above. The formation of $Ba[Nb(OEt)_6]_2$ and $Na[Nb(OEt)_6]$ are reported on the basis of elemental analysis and titration method.[11,12]

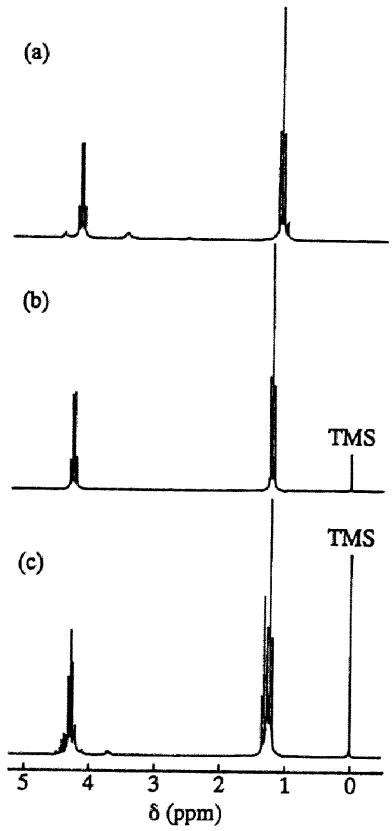


Fig.5-3-1 $^1H$ NMR spectra of (a) $BaNb_2O_6$ (BN) precursor, (b) $NaNbO_3$ (NN) precursor and (c) $Ba_2NaNb_5O_{15}$ (BNN) precursor.

Figure 5-3-3 shows $^{23}Na$ NMR spectra of NaOEt, the NN precursor and the BN precursor in ethanol solution. The NN precursor has a $^{23}Na$ resonance at –1.1 ppm with a half-value width of 900 Hz, which is different from that of NaOEt at 0.5 ppm ( a half-value width of 100 Hz) as shown in Fig.5-3-3. The shift corresponds to the change in chemical bond from NaOEt to the NN precursor. The $^{23}Na$ resonance of the BNN precursor also shows a similar single signal at –0.4

ppm as shown in Fig.5-3-3. The signal increases in half-value width to 1170 Hz compared with that of NN precursor (900 Hz). The increase in signal width indicates the interaction between the Na site of $Na[Nb(OEt)_6]$ and the $[Nb(OEt)_6]$ unit of $Ba[Nb(OEt)_6]_2$ in ethanol solution. Since $^{23}Na$ nucleus has a quadrupole moment (I=3/2), the broadening of signal suggests the decrease in molecular symmetry and increase in molecular weight.[13] The BNN precursor is, therefore, considered to consist of molecularly associated $NaNb(OEt)_6$ and $Ba[Nb(OEt)_6]_2$ in solution.

Figure 5-3-4 illustrates the $^{93}Nb$ NMR spectra of the BN ($BaNb_2O_6$), the NN ($NaNbO_3$) and the BNN precursor in ethanol. Starting niobium ethoxide exhibits two or three broad signals[14] due to the association and the ligand exchange. The BN and NN precursors show a signal at −1182 ppm (Fig. 5-3-4(a)) and at −1155 ppm (Fig. 5-3-4(b)), respectively. A single signal in these spectra corresponds to the presence of

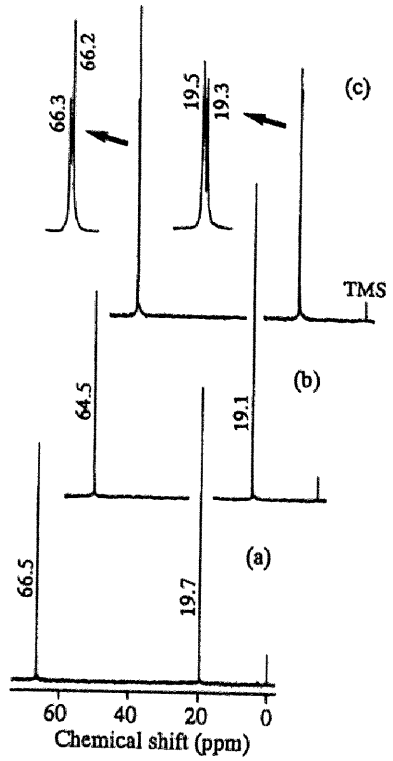


Fig.5-3-2 $^{13}C$ NMR spectra of (a) NN precursor, (b) BN precursor and (c) BNN precursor.

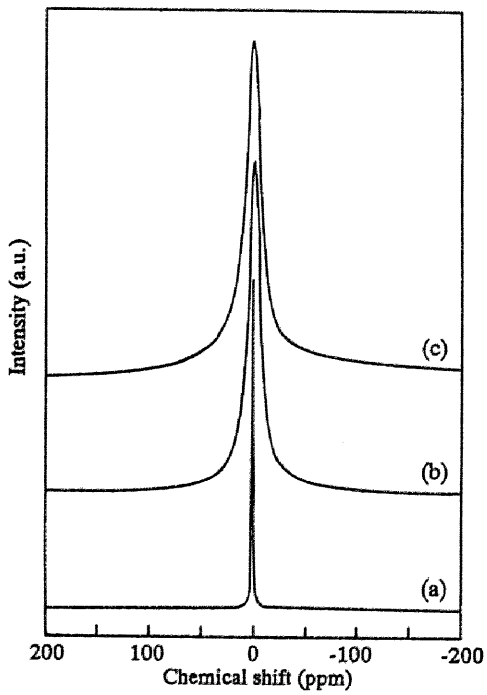


Fig.5-3-3 $^{23}Na$ NMR spectra of (a) NaOEt, (b) NN precursor and (c) BNN precursor in ethanol solutions.

niobium-ethoxy octahedra, $[Nb(OEt)_6]$, as reported for $Na[Nb(OEt)_6]$[11] and $Ba[Nb(O^iPr)_6]_2$[12]. The spectrum of the BNN precursor is composed of a single signal at a different chemical shift of $-1180$ ppm. The BNN precursor also contains $[Nb(OEt)_6]$ units. Two kinds of ethoxy groups of the BNN precursor observed in $^1H$ and $^{13}C$ NMR correspond to two kinds of $[Nb(OEt)_6]$ in the BNN precursor. However, in $^{93}Nb$ spectra, the difference appears as only a chemical shift of the BNN precursor.

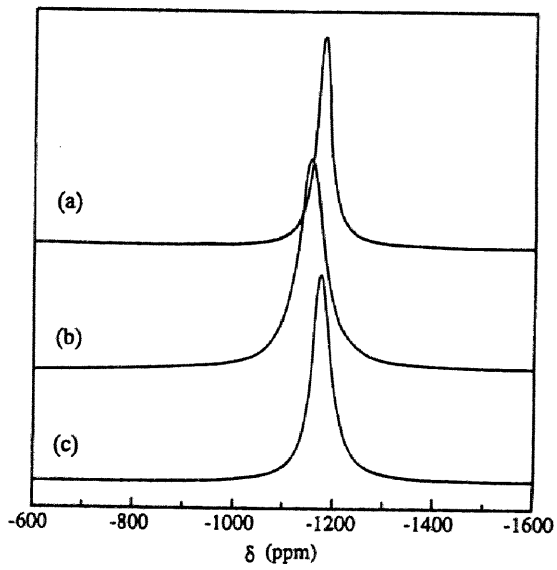


Fig.5-3-4 $^{93}Nb$ NMR spectra of (a) BN precursor, (b) NN precursor and (c) BNN precursor in ethanol solutions.

This is due to the broad signal of $^{93}Nb$ nucleus, which results from that $^{93}Nb$ is one of the quadrupolar nuclei (I=9/2).[15]

Based upon the spectroscopic data, the BNN precursor is considered to consist of a uniform mixture of $NaNb(OEt)_6$ and $Ba[Nb(OEt)_6]_2$ in 2:1 ratio with interaction at a molecular level similar to the SKN (in Chap.3) precursor.

### 5.3.2 Preparation of tungsten bronze BNN thin films

#### *(1) Crystallization behavior of BNN precursor powders*

BNN precursor powders were prepared from the precursor solution. First, the BNN precursor was hydrolyzed with excess water, and then heat-treated in air at various temperatures between 600°C and 1000°C for 1 h. The as-prepared powder was in a X-ray amorphous state up to 550°C, and crystallized to a mixture of $BaNb_2O_6$(BN) and $NaNbO_3$(NN) at 600°C. The BN phase was reacted with NN yielding orthorhombic BNN (tungsten bronze phase) at 1000°C. The result shows that the BNN precursor solution undergoes the phase segregation by hydrolysis.

The phase segregation was caused by difference in the rate of hydrolysis between each metal alkoxides. Water attacks sodium or barium ion of the BNN precursor, breaking the interaction between $NaNb(OEt)_6$ and $Ba[Nb(OEt)_6]_2$. Therefore, no hydrolysis was employed in the present BNN synthesis.

Figure 5-3-5 shows the XRD profiles of the unhydrolyzed powders heat-treated at temperatures from 500 to 750°C for 1 h. The product begins to crystallize at 500°C for 1 h as shown in Fig.5-3-5(d). However, the structure is not orthorhombic tungsten bronze BNN. The low-temperature phase is transformed to orthorhombic tungsten bronze BNN at 550°C for 1 h (Fig.5-3-5(c)). As shown in Fig.5-3-5(b), single-phase BNN of orthorhombic symmetry is formed after heat treatment at 600°C for 1 h. The as-prepared powder prepared from the BNN precursor solution releases organics during heating, and changes from molecular metal-organics to a noncrystalline solid including $(M\text{-}O)_n$ bonds.

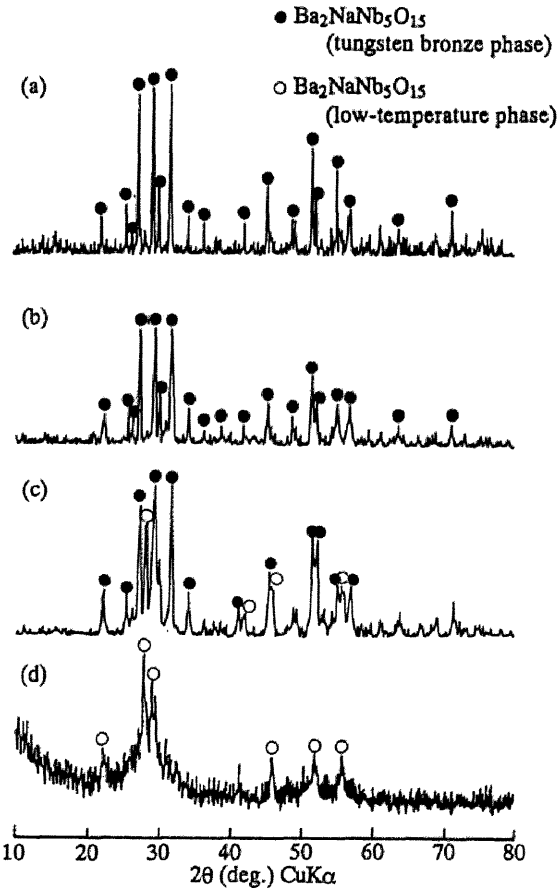


Fig.5-3-5 XRD profiles of unhydrolyzed BNN powders heat-treated at various temperatures, (a) 750°C, (b) 600°C, (c) 550°C and (d) 500°C.

Since the low-temperature phase of BNN is formed from the noncrystalline solid, this phase is considered to be a kinetically favored product under the burn-out condition in the alkoxy-derived system.

*(2) Synthesis of BNN films on fused silica*

Figure 5-3-6 shows XRD profiles of BNN films on fused silica substrates crystallized at various temperatures. Fused silica was used as substrates because fused silica substrate has high transparency over a wide wavelength region. The BNN low-temperature phase was formed at 600°C and 700°C as shown in Figs.5-3-6(b) and 5-3-6(c). Polycrystalline orthorhombic BNN (tungsten bronze structure) was obtained at 800°C on fused silica substrates (Fig.5-3-6(a)). Since the optical properties of BNN film, especially SHG depends upon the transmittance of film, the BNN film is required to be highly transparent.

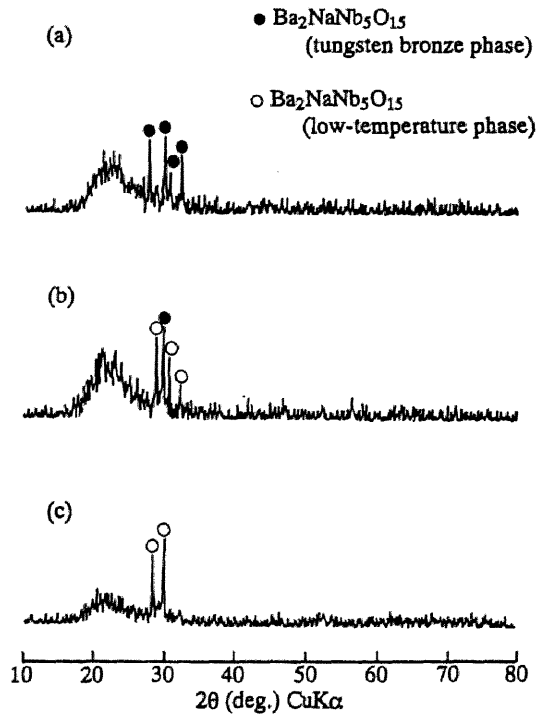


Fig.5-3-6 XRD profiles of BNN films on fused silica substrates prepared at various temperatures without the under-layer process, (a) 800°C, (b) 700°C and (c) 600°C.

However, the BNN films crystallized on fused silica substrates at 800°C were cloudy, and had the coarse grains of about 300 nm. The crystallization temperature, therefore, was lowered by using the underlayer method in order to suppress the nonuniform grain growth. Figure 5-3-7 shows the XRD pattern and Raman spectrum of the BNN films crystallized at 700°C on fused silica substrates. Both patterns are in good agreement with those of tungsten bronze BNN.[16] Transparent tungsten bronze BNN films were crystallized on fused silica substrates using the underlayer at 700°C. The grains of BNN were quite uniform, and had the uniform size of 150 nm via atomic force microscopy (AFM). In Fig.5-3-7, the BNN films crystallized on fused silica show more intense 002 and 004 diffractions than other

ones, which revealed a preferred orientation. The reason for the preferred orientation is the same for KSBN thin films on fused silica substrates as described in Chap.2.

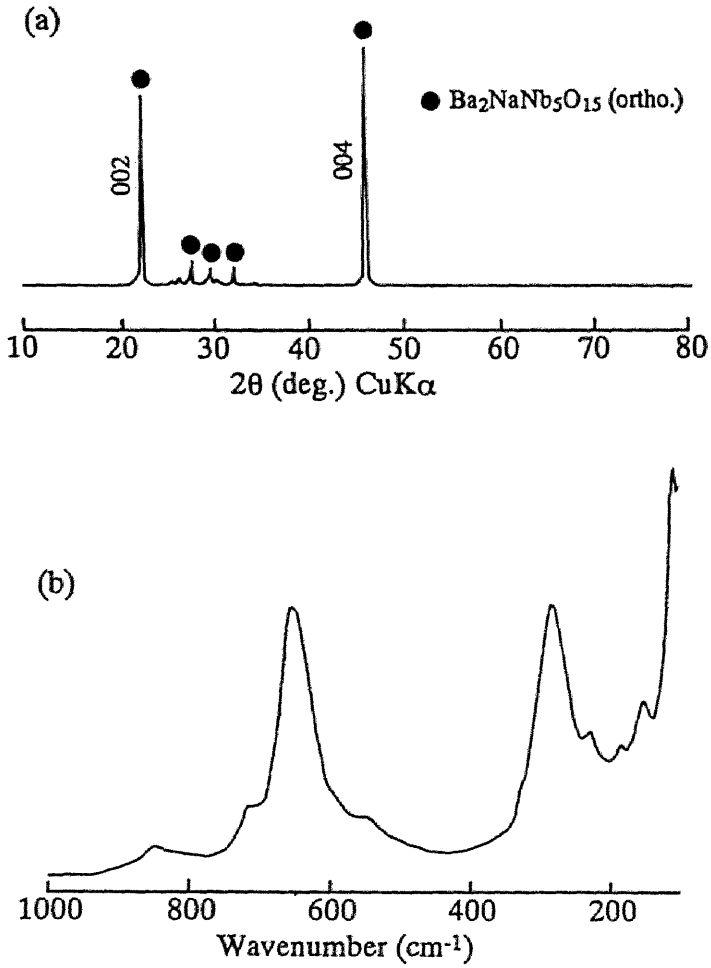


Fig.5-3-7 (a) X-ray diffraction pattern and (b) Raman spectrum of BNN films crystallized on fused silica substrates at 700°C using the under-layer process.

[ortho.: orthorhombic tungsten bronze phase]

*(3) Synthesis of BNN films on MgO(100) and Pt/MgO(100)*

MgO(100) and Pt(100)/MgO(100) substrates are used similarly to the SBN or PBN thin film fabrication to prepare highly oriented films. Alkoxy derived BNN films on MgO(100) substrates show strong 002 and 004 reflections as shown in Fig.5-3-8. However, the identification of the phase only by XRD is not sufficient, because the (002) oriented films show only 002 and 004 reflections, which have almost the same d-values for the low-temperature phase and tungsten bronze phase. Figure 5-3-9 shows Raman spectra of BNN films on MgO(100) substrates crystallized at various temperatures. The Raman scattering shown in Fig.5-3-9(b) exhibits clearly that the film at 700°C consists of the low-temperature phase and orthorhombic tungsten bronze phase[16], although the XRD was almost the same to each other for the oriented films. The spectrum pattern of BNN films crystallized at 800°C (Fig.5-3-9(a)) is the same as that of orthorhombic tungsten bronze BNN powder (Fig.5-3-9(d)).[16] The peak at around 720 $cm^{-1}$ in Figs.5-3-9(b) and 5-3-9(c) is assigned to the edge-shared $NbO_6$ octahedron.[17] The XRD pattern shown in Fig. 5-3-5(d) is quite similar to that of hexagonal $MNb_2O_6$ [M: $Ba^{2+}$, $Pb^{2+}$, etc.]. The hexagonal forms of niobate, such as $PbNb_2O_6$ and $BaNb_2O_6$, are composed of edge-shared niobium-oxygen octahedra, whereas apex-shared niobium-oxygen octahedra constitute the tungsten bronze. Although the precise structure of the low

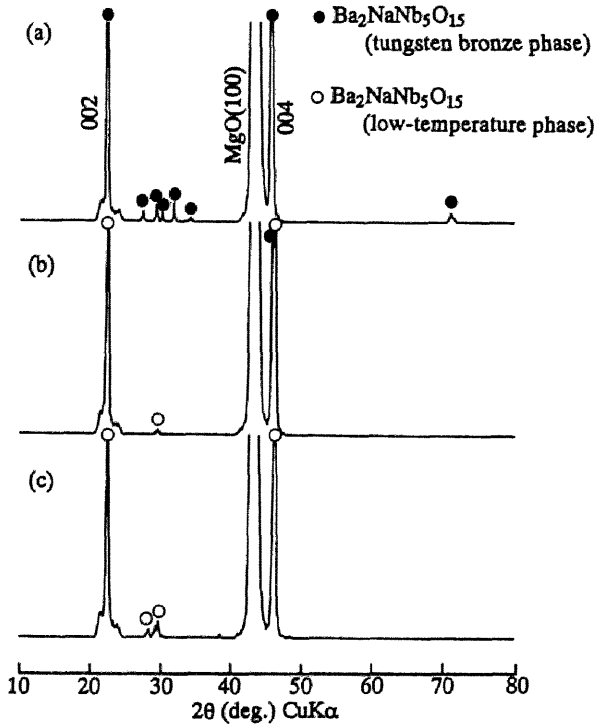


Fig.5-3-8 XRD profiles of BNN films on MgO(100) substrates prepared at various temperatures without the under-layer process, (a) 800°C, (b) 700°C and (c) 600°C.

temperature phase is now under investigation, the BNN low-temperature phase is considered to comprise the structure of edge-shared $NbO_6$ octahedron.

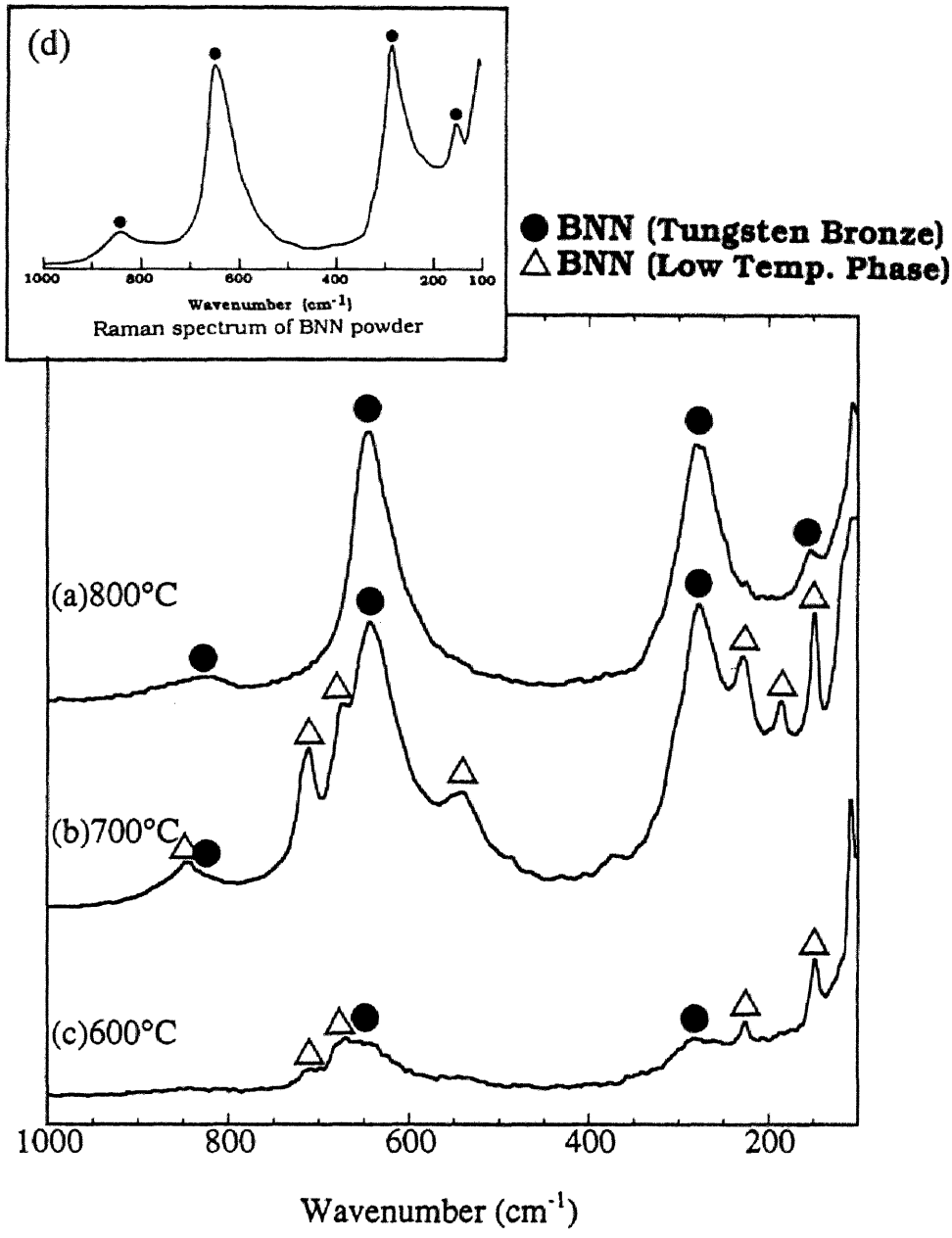


Fig.5-3-9 Raman spectra of BNN films on MgO(100) substrates crystallized at (a) 800°C, (b) 700°C, (c) 600°C and (d) tungsten bronze BNN powder.

Although BNN films crystallized at 800°C were found to be orthorhombic tungsten bronze, the films were cloudy as in the case of BNN film on fused silica (in previous section). SEM observation revealed that the films consisted of ununiform coarse grains due to grain growth. In order to synthesize the BNN films at low temperatures to avoid the grain growth, a thin BNN underlayer (<0.01 μm) was precrystallized on MgO(100) substrates at 800°C using a dilute precursor solution. On the underlayer, BNN films were synthesized at 700°C by rapid heating process.

Figure 5-3-10 shows the XRD profile of BNN films crystallized on MgO(100) substrates at 700°C. Since no small reflections except 002 and 004 are observed, the degree of preferred orientation of the film is much improved compared with that crystallized at 800°C without underlayer (Fig.5-3-8(a)). The BNN film thus formed at 700°C showed the same Raman spectrum as that in Fig.5-3-9(a), and was confirmed to be orthorhombic tungsten bronze. The precrystallized under-layer act as nucleation sites for the promotion of crystallizing the orthorhombic tungsten bronze BNN phase. When the concentration of precursor solution is low, the precursor film per dipping decrease in thickness. The crystallization of thin film depends much more upon the atomic alignment of substrates than that of thick films. Thus, the better orientation is considered to be obtained by using the underlayer. Similar effects of the underlying layer were also observed for the synthesis of oriented $K(Ta_{1-x}Nb_x)O_3$ films on MgO(100)[14] and other tungsten bronze niobate thin films as described in Chaps.2, 3 and 4. The (002) plane orientation of the BNN films on MgO(100) substrates is attributed to the lattice matching of oxygen atoms between orthorhombic BNN and MgO(100) substrates. The lattice mismatch of atomic

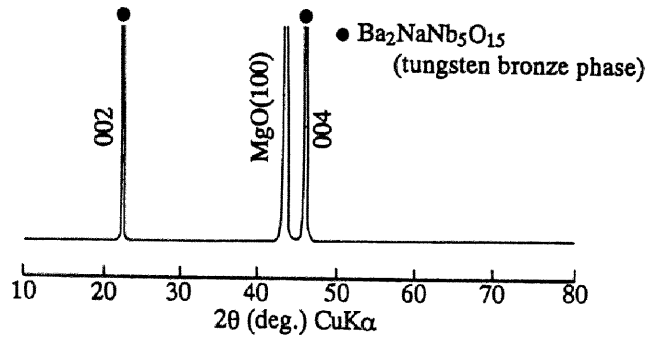


Fig.5-3-10 XRD profile of BNN film on a MgO(100) substrate crystallized at 700°C using the under-layer process.

alignment between orthorhombic BNN(002) and MgO(100) is estimated to be about 8%.

Figure 5-3-11 shows the edge-on profile of the orthorhombic tungsten bronze BNN film on an MgO(100) substrate crystallized using the underlayer. The film has a smooth surface with no cracks and voids. The grain size of the film is found to be less than 0.1 μm. The thickness of the crystallized film was about 1.4 μm after several cycles of dipping. Figure 5-3-12 shows the transmittance of the orthorhombic BNN film on an MgO(100) substrate. These films were transparent over a wide range of wavelength. The interference fringe reveals the uniform thickness of the film. The absorption edge was 370 nm, which was in good agreement with that reported for single-crystal.[2]

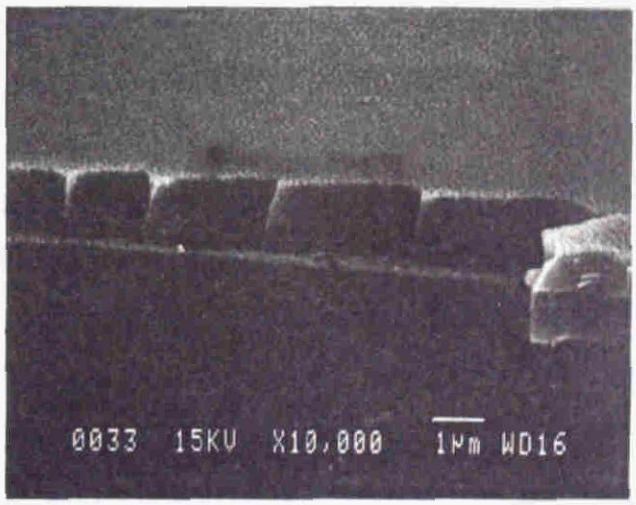


Fig.5-3-11 Edge-on SEM photomicrograph of a fractured BNN film crystallized at 700°C on a MgO(100) substrate using the under-layer process.

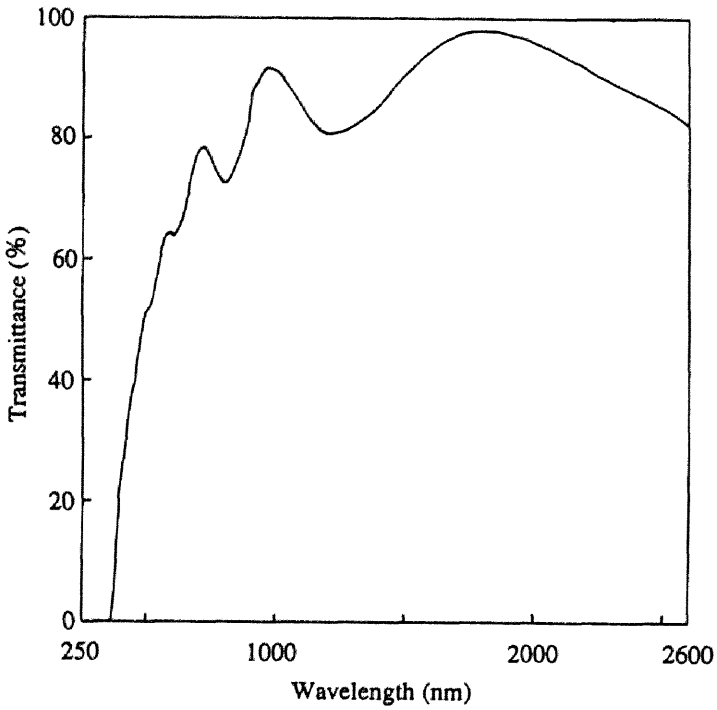


Fig.5-3-12 Transmittance of BNN film crystallized at 700°C on a MgO(100) substrate using the under-layer process.

Tungsten bronze BNN films on Pt(100)/MgO(100) with (002) preferred orientation were similarly prepared using the underlayer method. Figure 5-3-13 shows the XRD profile of BNN films crystallized on Pt(100)/MgO(100) substrates. The BNN films on Pt(100)/MgO(100) substrates also have (002) orientation, since the films shows only 002 and 004 reflections. The lattice matching of atoms between orthorhombic BNN and Pt(100) plane is responsible for the (002) plane orientation of BNN films on Pt(100).

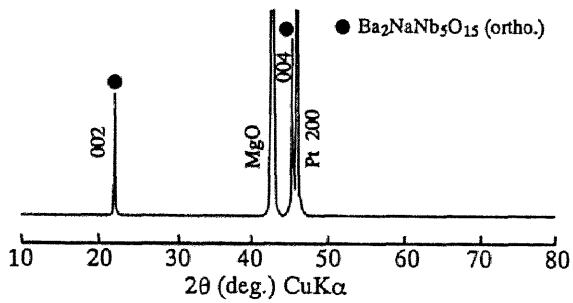


Fig.5-3-13 XRD profile of BNN film on a Pt(100)/MgO(100) substrate crystallized at 700°C using the under-layer process. [ortho.: orthorhombic tungsten bronze phase]

### 5.3.3 Three dimensional relation between oriented BNN thin film and substrate

Since the BNN films on MgO(100) and Pt(100)/MgO(100) were found to have (002) preferred orientation, three dimensional regularity of grains was investigated by X-ray pole figure measurement. The pole figure of the BNN film on Pt(100)/MgO(100) for {132} shows 12 spots at $\alpha=55^\circ$ as shown in Fig.5-3-14. $\beta$ is the rotation axis perpendicular to the film plane, and $\alpha$ is the rotation axis perpendicular to $\beta$ and $\theta$. The spots are classified into two groups with different intensities to each other. The intensity ratio is almost 2. The calculated pattern of BNN single crystals for {132} is shown in Fig.5-3-15. Since the lattice constants of a- and b-axis are 1.759 and 1.762 nm, respectively, the calculated pattern was constructed under the condition of a=b. When the pattern is rotated by $\pm 26.5^\circ$, the resulting pattern is produced as shown in Fig.5-3-15. The superimposed spots (marked with ○ and △ in Fig.5-3-15) have twice intensity than the unsuperimposed ones (○ or △). The constructed pattern shown in Fig.5-3-15 is in good agreement with that obtained for the BNN film.

The a-axis of Pt(100) is the same as that of MgO(100), because Pt(100) plane was confirmed to grow epitaxially on MgO(100) by X-ray pole figure method. One of a-axis plane of BNN intersected that of Pt at $26.5^\circ$ as shown in Fig.5-3-15. Therefore, the film consists of two lattices of BNN intergrown at an orientation of $26.5^\circ$ on Pt(100) substrates.

BNN films crystallized on MgO(100) were found to show similar pole figures to those on Pt(100)/MgO(100). Hence, the relation between BNN grains and MgO(100) is the same as that between BNN and Pt(100). This is due to the similar lattice constant of MgO(100) (0.4213 nm) to that of Pt(100) (0.399 nm). Similar intergrowth of two lattice planes is reported for tungsten bronze $Sr_xBa_{1-x}Nb_2O_6$ thin films on MgO(100) substrates by chemical solution process (in Chap.2) and pulsed laser deposition.[18]

On the other hand, the BNN thin films on fused silica substrates did not show any clear spots, but diffuse rings by X-ray pole figure measurement, and

were confirmed to have no three dimensional regularity perpendicular to substrates.

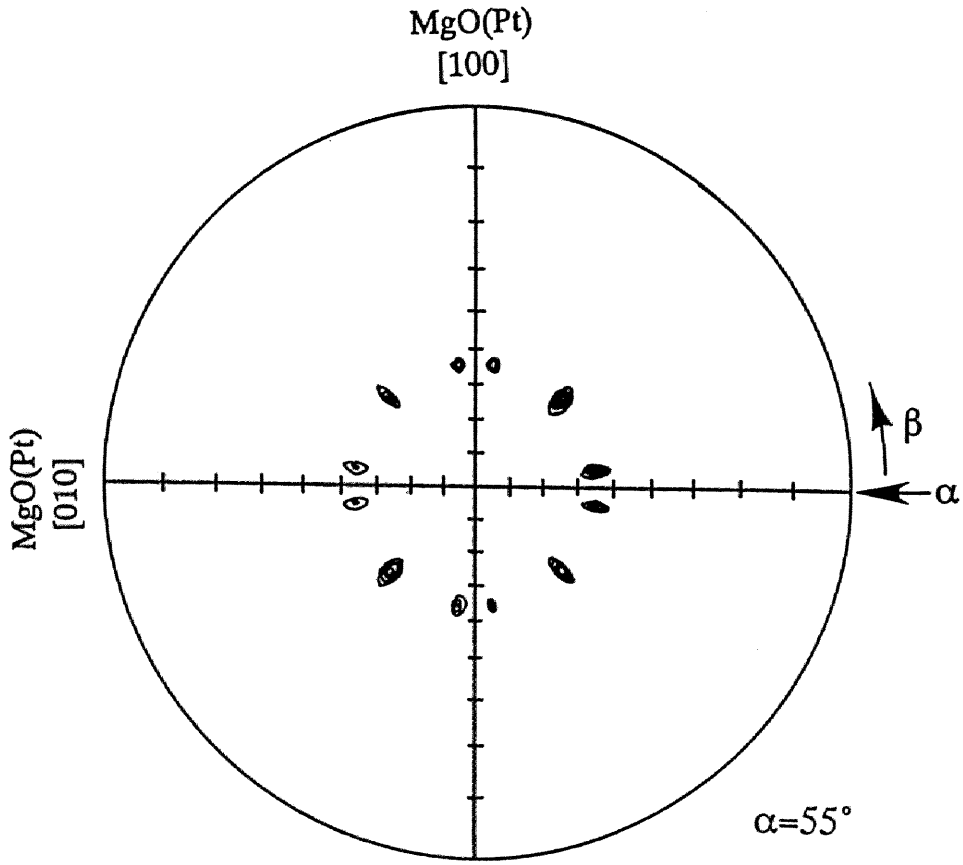


Fig.5-3-14 X-ray pole figure of BNN film on a Pt(100)/MgO(100) substrate for the {132} planes crystallized at 700°C.

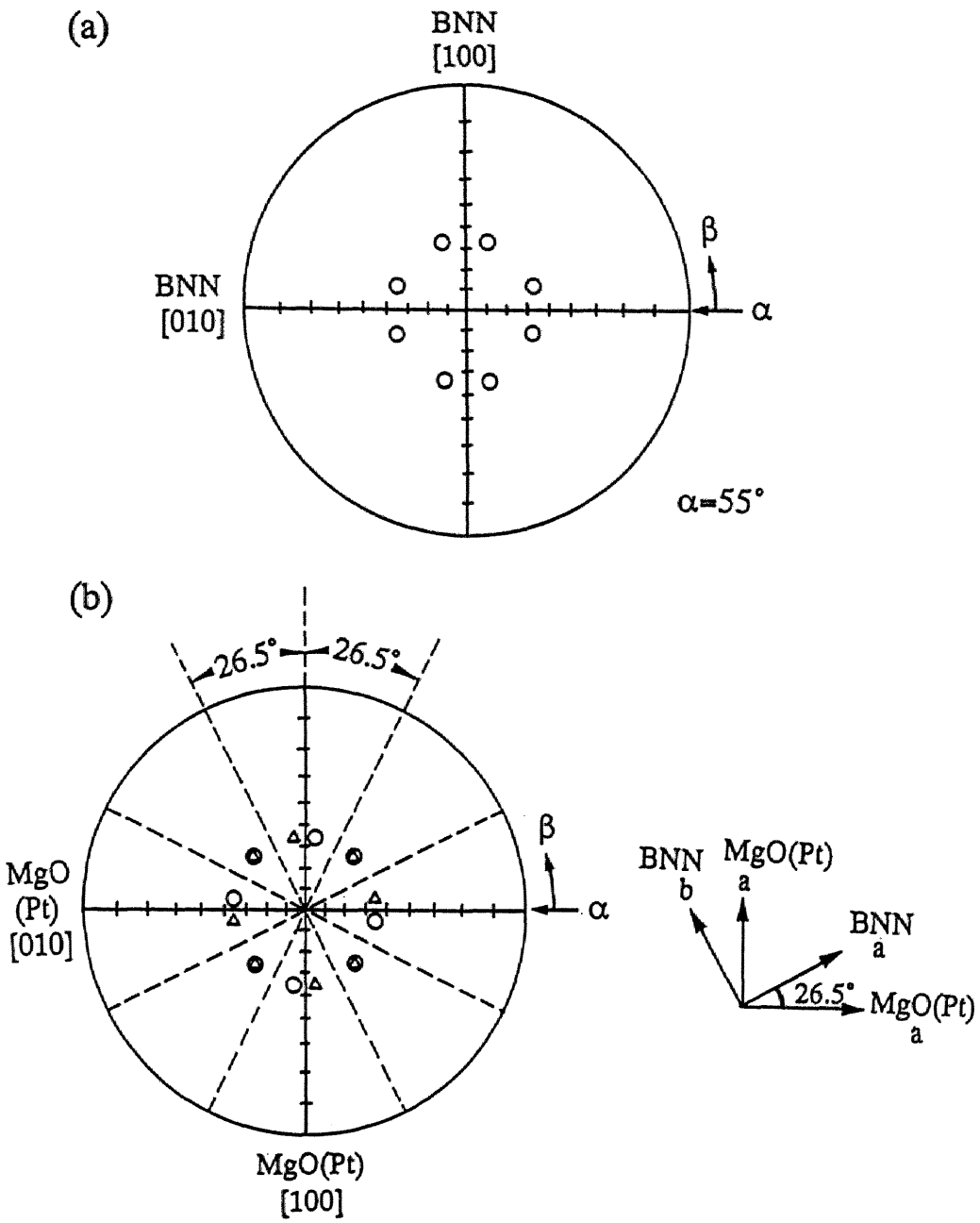


Fig.5-3-15 Calculated X-ray pole figures of BNN (a) calculated pattern of BNN for the {132} planes and (b) rotated pattern at an angle of $\pm 26.5^{\circ}$.

The two BNN lattices are indicated by "○" and "△".

### 5.3.4 Electrical properties of BNN films

In order to investigate the dielectric behavior of synthesized BNN films, the dielectric properties of the BNN films crystallized at 700°C on Pt(100)/MgO(100) substrates were measured. Figure 5-3-16 shows the change of dielectric constant ($\varepsilon_r$) of the BNN film with temperature. The $\varepsilon_r$ value of the film at room temperature was 280 at 10 kHz, which is comparable with that reported for single-crystal BNN.[19] The temperature dependence of $\varepsilon_r$ is similar to that reported previously.[19] The $\varepsilon_r$ value of single crystal BNN at $T_c$ is $4.8\times10^4$.[19] The film reveals a maximum $\varepsilon_r$ value of $4.9\times10^4$ at around 540°C. The typical hysteresis loops were also observed for the tungsten bronze BNN film on a Pt(100)/MgO(100) substrates from low temperature region to room temperature similar to the KSBN thin films described in Chap.2.

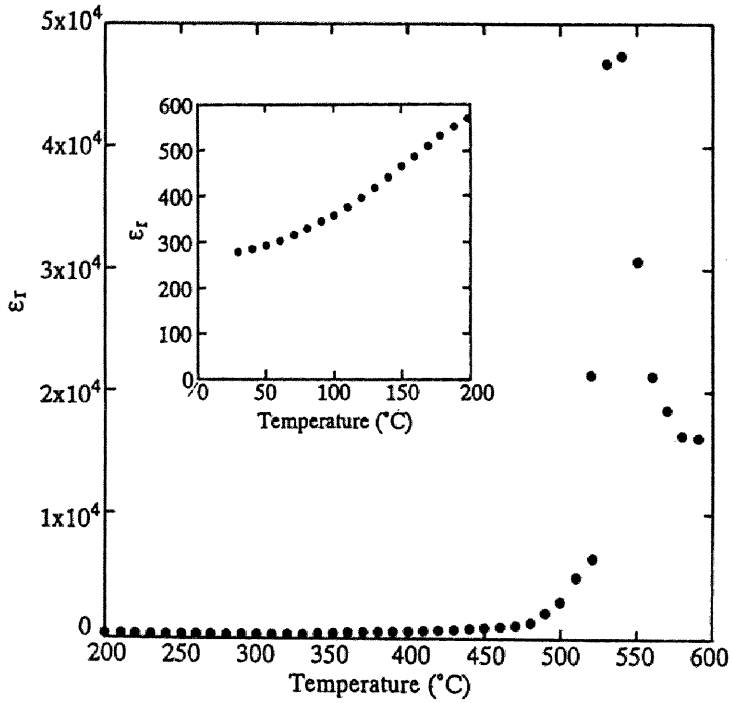


Fig.5-3-16 Change of dielectric constant ($\varepsilon_r$) with temperature for the BNN film crystallized at 700°C on a Pt(100)/MgO(100) substrate.

### 5.3.5 Optical properties of BNN films

In order to evaluate SHG of the films by the transmission method, tungsten bronze BNN films were synthesized on fused silica substrates as described in 5.3.2(2). Figure 5-3-17 shows the UV-visible spectrum of the BNN film crystallized at 700°C on a fused silica substrate. The BNN film has a high transparency from 500 to 2600 nm. The interference fringes are derived from the uniform thickness of the film. The absorption edge of the film was 370 nm, which is the same as that of single crystal.[2]

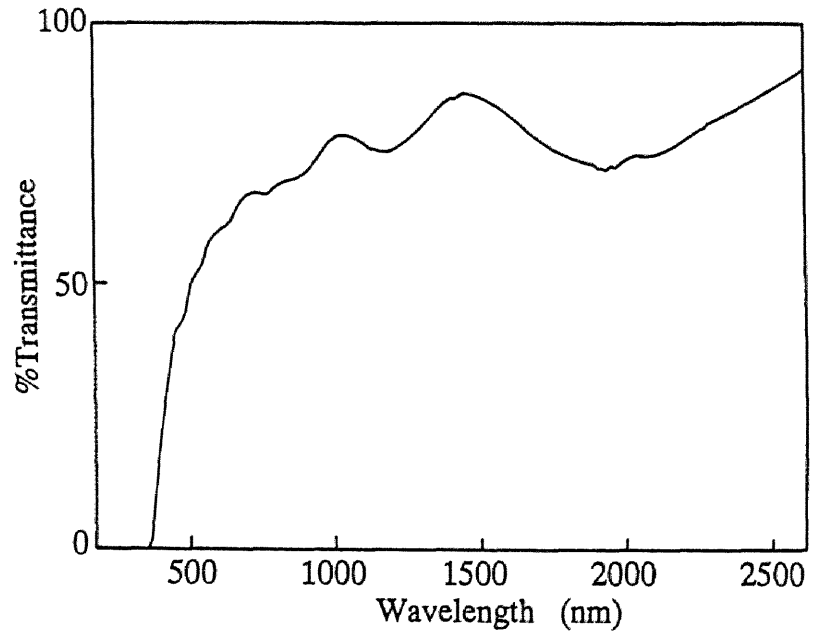


Fig.5-3-17 Transmittance of BNN film crystallized at 700°C on a fused silica substrate using the under-layer process.

The SHG effect was analyzed for the BNN thin films crystallized on fused silica substrates. The fundamental light (wavelength of 1064 nm) was irradiated onto the films. The polarization of the incident light was parallel to the BNN film. The transmitted light from the BNN film included 532 nm light. The SH power was then measured based upon 532 nm light from the BNN film on a fused silica substrate. Figure 5-3-18 shows the relation of incident-light power to that of

transmitted light (SH wave) from the BNN films on fused silica substrates. The film thickness was 1.0 μm. The BNN film on a fused silica substrate exhibited a straight line with a slope of 2.16, which satisfies the square-law proportionality according to the theory ($P_{2\omega} \propto P^2_{\omega}$) between the fundamental power ($P_{\omega}$) and the harmonic power ($P_{2\omega}$). The d-values were evaluated based upon the SH intensity of the Y-cut quartz according to the literature.[20,21] The $d_{eff}/d_{quartz}$ ratio of the BNN film was estimated to be 16 (1.0 for $d_{quartz}$). This value is about 35% of that reported for single-crystals BNN.[2]

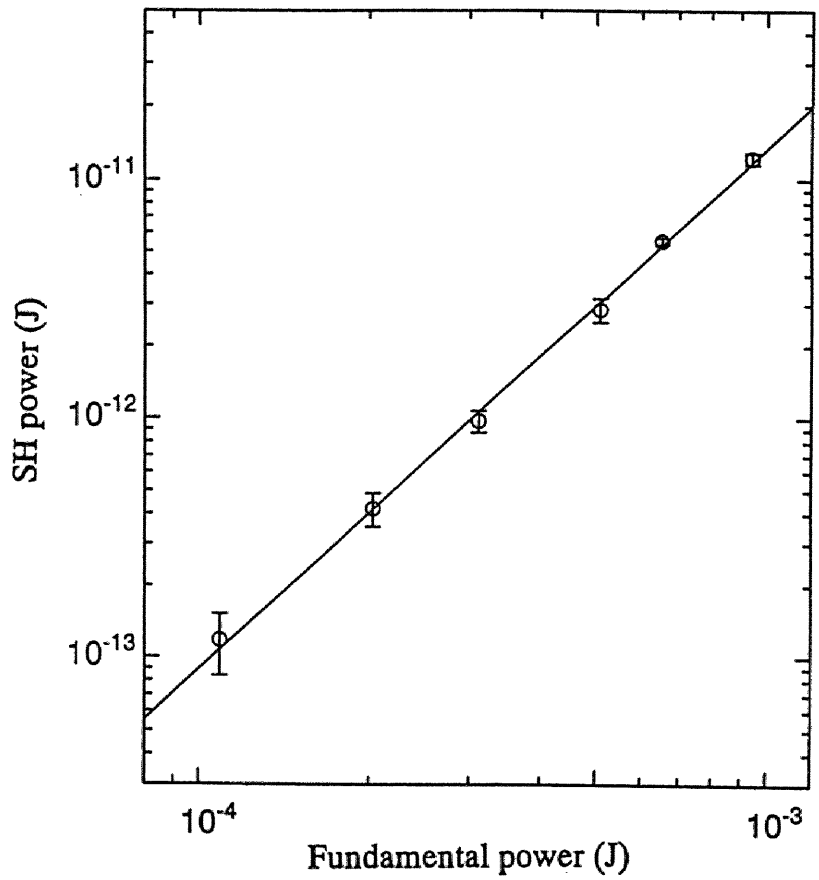


Fig. 5-3-18 Power relationship of power between fundamental light (1064 nm) and second harmonic light (532 nm) for BNN thin film on a fused silica substrate crystallized at 700°C.

## 5.4 Conclusions

Crack-free BNN films with highly preferred orientation were successfully synthesized on fused silica, MgO(100) and Pt(100)/MgO(100) substrates from the complex metal alkoxide precursor. A homogeneous BNN precursor solution was prepared from barium metal, sodium ethoxide and niobium ethoxide in ethanol. The BNN precursor was composed of a molecular mixture of $Ba[Nb(OEt)_6]_2$ and $NaNb(OEt)_6$. Unhydrolyzed BNN powder crystallized to tungsten bronze phase at lower temperatures compared with hydrolyzed powders. Tungsten bronze BNN film with (002) preferred orientation was crystallized by using an underlayer of BNN on MgO(100) substrates at 700°C. The formation of the underlying layer with desired structure was found to be a key for the crystallization of tungsten bronze phase at low temperatures on substrates and the improvement of degree of orientation. Two crystal lattice planes of orthorhombic BNN were intergrown at an orientation of 26.5 ° on MgO(100) and Pt(100)/MgO(100) substrate. The Curie temperature of the BNN film was found to be about 560°C. A typical ferroelectric hysteresis was observed for the BNN films crystallized at 700°C. The tungsten bronze BNN films on fused silica substrates were highly transparent and were confirmed to generate second harmonic wave.

## References

1. J.E.Geusic, H.L.Levinstein, J.J.Rubin, S.Singh and L.G.Van Uitert, "The Non-Linear Optical Properties of $Ba_2NaNb_5O_{15}$," *Appl. Phys. Lett.*, **11** [9] 269-271 (1967).

2. S.Singh, D.A.Draegert and J.E.Geusic, "Optical and Ferroelectric Properties of Barium Sodium Niobate", *Phys. Rev. B*, **2** [7] 2709-2724 (1970).

3. L.G.Van Uitert, J.J.Rubin and W.A.Bonner, "Growth of $Ba_2NaNb_5O_{15}$ Single Crystals for Optical Applications, *IEEE J. Quantum Electronics*, **4** [10] 622-667 (1968).

4. D.F.Eaton, "Nonlinear Optical Materials", *Science*, **253** [5017] 281-287 (1991).

5. S.K.Kurz and T.T.Perry, "A Powder Technique for the Evaluation of Nonlinear Optical Materials", *J. Appl. Plys.*, **39** [8] 3798-3813 (1968).

6. A.A.Ballman, J.R.Carruthers and H.M.O'bryan, Jr.,"Growth of Uncracked Barium-Sodium Niobate Crystals", *J. Cryst. Growth*, **6** [2] 184-186 (1970).

7. M.Tsukioka, T.Mashio, M.Shimazu and T.Nakamura, "Preferable Orientation of Crystalline Thin Film of Modified BNN System", *Modern Phys. Lett.*, **B 3** [6] 465-470 (1989).

8. J.M.Liu, F.Zhang, Z.G.Liu, S.N.Zhu, L.J.Shi, Z.C.Wu and N.B.Ming, "Epitaxial Growth of Optical $Ba_2NaNb_5O_{15}$ Waveguide Film by Pulsed Laser Deposition", *Appl. Phys. Lett.* **65** [16] 1995-1997(1994).

9. S.N.Zhu, Y.Y.Zhu, J.M.Liu, Z.Y.Zhang, H.Shu, J.F.Hong, C.Z.Ge and Z.S.Lin, "Epitaxial $Ba_2NaNb_5O_{15}$ Thin Film by Pulsed Laser Deposition and its Waveguide Properties", *Optics Lett.*, **20** [3] 291-293 (1995).

10. J.M.Boulton, G.Teowee, W.M.Bommersbach and D.R.Uhlmann, "Sol-Gel Derived Sodium Barium Niobate and Bismuth Titanate Films", pp.303-308, in Ferroelectric Thin Films II (Mater. Res. Soc. Proc. 243. Edited by A.I.Kingon, E.R.Myers and B.Tuttle), Mater. Res. Soc., Pittsburgh, 1992.

11. R.C.Mehrotra, M.M.Agrawal and P.N.Kapoor, "Alkali-metal Hexa-alkoxides of Niobium and Tantalum", *J. Chem. Soc.* (A) 2673-2676 (1968).

12. S.Govil, P.N.Kapoor and R.C.Mehrotra, "Double Isopropoxides of Niobium and Tantalum with Alkaline Earth Metals", *J. Inorg. Nucl. Chem.*, 38 [1] 172-173 (1976).

13. P.Laszlo, "Sodium-23 Nuclear Magnetic Resonance Spectroscopy", *Angew. Chem. Int. Ed. Engl.*, **17** [4] 254-266 (1978).

14. T.Yogo, K.Kikuta, Y.Ito and S.Hirano, "Synthesis of Highly Oriented KTN Film Using Metal Alkoxides.", *J. Am. Ceram. Soc.*, **78** [8] 2175-2179 (1995).

15. D.Rehder, "Early Transition Metals, Lanthanides and Actinides"; pp. 479-519 in Multinuclear NMR. Edited by J. Mason. Plenum Press, New York, 1987.

16. L.C.Bobb, I.Lefkowitz and L.Muldawer, "Raman Spectra of $Ba_2NaNb_5O_{15}$", *Ferroelectrics*, **2** [3] 217-223 (1971).

17. Y.Repelin, E.Husson et H.Brusset, "Etude par spectroscopies d'absorption i.r. et de diffusion Raman des composes $A^{II}B_2{}^{V}O_6$ de structure de type "blocs 1×2" -I. Etude du niobate de baryum $BaNb_2O_6$", *Spectrachim. Acta*, **35A**[8], 937-948 (1979).

18. S.S.Thony, K.E.Youden, J.S.Harris, Jr. and L.H.Hasselink, "Growth of Eptaxial Strontium Barium Niobate Thin Films by Pulsed Laser Deposition", *Appl. Phys. Lett.*, **65** [16] 2018-2020 (1994).

19. T.Yamada, H.Iwasaki and N.Niizeki, "Elastic Anomaly of $Ba_2NaNb_5O_{15}$", *J. Appl. Phys.* **41** [10] 4141-4147 (1970).

20. H.A.Lu, L.A.Wills, B.W.Wessels, W.P.Lin, T.G.Zhang, G.K.Wong, D.A.Neumayer and T.J.Marks, "Second-Harmonic Generation of Poled $BaTiO_3$ Thin Films", *Appl. Phys .Lett.*, **62** [12] 1314-1316 (1993).

21. B.Bihari, J.Kumar, G.T.Stauf, P.C.Van Buskirk and C.S.Hwang, "Investigation of Barium Titanate Thin Films on MgO Substrates by Second-Harmonic Generation", *J. Appl. Phys.*, **76** [2] 1169-1174 (1994).

# Chapter 6

## Summary

## 6.1 Summary

The chemical solution process is one of the most appropriate processes to synthesize electronic ceramics in the emerging area. The advantages of this processing have been extended to multi-component ceramics, such as ferroelectric tungsten bronze niobate. The feasible composition control is the significant factor for obtaining the desired properties of resultant films. In addition, the crystallization of ferroelectric thin films at lower temperatures is indispensable for the fabrication of high-quality films. Metallo-organic precursor-derived ferroelectric thin films are recognized to be the fabrication method characterized by the precise control of stoichiometry and preferred orientation on substrates at low temperature region compared with conventional bulk materials.

In this study, ferroelectric tungsten bronze niobate thin films with preferred orientation were successfully synthesized using the chemical solution deposition process. Key findings of this study are as follows;

1. Homogeneous and stable precursor solutions for coating were prepared by optimizing starting materials and solvents including stabilizing agent, and controlling the reaction of metallo-organic compounds in solution. The structure of synthesized precursors were molecularly designed and confirmed by applying the spectroscopic analyses. The precise control of stoichometry was achieved by controlling the intermediate coordination states of metals in precursor solutions. The synthesized precursors in solution were found to consist of a molecularly interacted mixture of complex alkoxides including highly symmetric niobium-oxygen octahedron.
2. In the case of alkaline-free tungsten bronze niobate of unfilled-tungsten bronze structure, such as SBN or PBN, the crystallization of ferroelectric tungsten bronze phase on substrates results in the problem of the formation of the low temperature phase, which showed poor dielectric properties. The low temperature phases were found to be the meta-stable phases and were completely transformed to the tungsten bronze phase at higher temperatures.

The incorporation of alkali ion, such as potassium and sodium, was found to be effective for the direct crystallization of niobate precursor powders and thin films in the tungsten bronze phase without intermediate formation of the low-temperature phase. Pre-coating and crystallization of underlayer (including seed layer) with desired structure was also found to have the pronounced effect not only on the low temperature synthesis and crystallinity of tungsten bronze, but also on the degree of orientation for tungsten bronze film.

3. The tungsten bronze niobate films showed a prominent c-axis preferred orientation which was a direction of polarization for tetragonal niobate. The orientation of ferroelectric tungsten bronze niobate thin film was attributed to both the closest packed atomic alignment of c-plane and atomic alignment of selected substrate.
4. The oriented tungsten bronze niobate thin film exhibited a typical ferroelectric P-E hysteresis loop. The value of remnant polarization of the prepared film gradually decreased with increasing temperature from low to high temperature. Tungsten bronze niobate thin films with c-axis preferred orientation showed diffuse phase transition as a relaxor, of which behavior is the characteristic property of tungsten bronze niobate single crystals along c-axis.
5. The tungsten bronze niobate films with high transparency and refractive index were found to propagate the laser beam and generate the second harmonic wave.

Synthesized Ferroelectric tungsten bronze niobate thin films with preferred orientation along polar axis can satisfy several requirements for various applications in piezoelectric or elecroacoustic transducers, high-frequency surface-acoustic-wave (SAW) devices, pyroelectric infrared detectors, ferroelectric memory cells, ferroelectric photoconductive displays, two dimensional special light modulators or optical waveguide devices, etc. The chemical solution processing will receive the increasing attentions for tailoring and integrating functionalities, especially in electric ceramics.

The concept described in this dissertation can be applied for the processing of functional ceramics films with controlled characters and orientations at relatively low temperatures. The crystallization of films can be promoted by controlling the reaction of designed complex metallo-organics in intermediate state and then the heat treatment of alkoxy-derived films. The chemical processing does demonstrate a promising route to synthesize functional ceramic films, which leads to the integration of functionalities.

## 6.2 Further Strategy

Further strategy of this study is summarized as follows :

1. Investigation of the relation between the structure of metallo-organic precursor and crystallization process in more detail.
2. The study of the effect of substitution by a wide variety of ions on the crystallographic phase and the properties of synthesized films.
3. Characterization of pyroelectric, piezoelectric, electro-optic properties of synthesized films to examine the applications in various electro and electrooptic devices.

# List of Publications

## Papers

1. W. Sakamoto, T. Yogo, K. Kikuta, T. Arimoto and S. Hirano, "Synthesis of Lead Barium Niobate Powders and Thin Films by the Sol-Gel Method", *J. Am. Ceram. Soc.*, **79** [4] 889-894 (1996).

2. W. Sakamoto, T. Yogo, K. Kikuta, K. Ogiso, A. Kawase and S. Hirano, "Synthesis of Strontium Barium Niobate Thin Films through Metal Alkoxides", *J. Am. Ceram. Soc.*, **79** [9] 2283-2288 (1996).

3. T. Yogo, W. Sakamoto, T. Isaji, K. Kikuta and S. Hirano, "Synthesis of $Ba_2NaNb_5O_{15}$ Powders and Thin Films Using Metal Alkoxides", *J. Am. Ceram. Soc.*, **80** [7] 1767-1772 (1997).

4. W. Sakamoto, A. Kawase, T. Yogo and S. Hirano, "Preparation and Properties of $K(Sr_{0.75}Ba_{0.25})_2Nb_5O_{15}$ Thin Films by Chemical Solution Deposition Method", *Jpn. J. Appl. Phys.*, **36** Part 1 [9B] 5930-5934 (1997).

5. W. Sakamoto, A. Kawase, T. Yogo and S. Hirano, "Preparation of Tungsten Bronze $(Sr_{0.5}Ba_{0.5})Nb_2O_6$ Thin Films Using a $K_{0.4}(Sr_{0.75}Ba_{0.25})_{0.8}Nb_2O_6$ Seed Layer", *Ceram. Trans.*, **88** 469-477 (1998).

6. W. Sakamoto, A. Kawase, K. Ogiso, K. Kikuta, T. Yogo and S. Hirano, "Preparation and Characterization of $K(Sr_{0.5}Ba_{0.5})_2Nb_5O_{15}$ Thin Films by Sol-Gel Method", *Integrated Ferroelectrics*, **20** 117-128 (1998).

7. W. Sakamoto, K. Kosugi, T. Yogo and S. Hirano, "Synthesis of Highly Oriented Tungsten Bronze $K(Pb_{0.6}Ba_{0.4})_2Nb_5O_{15}$ Thin Films by Chemical Solution Deposition Method", *Jpn. J. Appl. Phys.*, **37** Part 1 [9B] 5215-5219 (1998).

8. W. Sakamoto, A. Kawase, T. Yogo and S. Hirano, "Chemical Processing of Potassium Substituted Strontium Barium Niobate Thin Films through Metallo-organics", *J. Am. Ceram. Soc.*, **81** [10] 2692-2698 (1998).

9. W. Sakamoto, T. Yogo, T. Kuroyanagi and S. Hirano, "Synthesis of $Sr_2KNb_5O_{15}$ Thin Films by Chemical Solution Deposition Method", *J. Mater. Res.*, **14** [4] 1495-1502 (1999).

10. W. Sakamoto, K. Kosugi, T. Arimoto, T. Yogo and S. Hirano, "Chemical Processing of Potassium Substituted $(Pb_{0.6}Ba_{0.4})Nb_2O_6$ Powders and Thin Films through Metallo-Organics", *J. Sol-Gel Sci. and Tech.*, in print (accepted 1998).

11. T. Yogo, W. Sakamoto, T. Isaji, M. Ichida, A. Nakamura and S. Hirano, "Synthesis of Oriented $Ba_2NaNb_5O_{15}$ (BNN) Thin Films from an Alkoxy-Derived Precursor", *J. Am. Ceram. Soc.*, **82** [10] 2672-2676 (1999).

12. W. Sakamoto, K. Kosugi, T. Yogo and S. Hirano, "Chemical Solution Processing and Characterization of La Doped Tungsten Bronze $K_{0.4}(Pb_{0.6}Ba_{0.4})_{0.8}Nb_2O_6$ Thin Films", *Jpn. J. Appl. Phys.*, **38** Part 1 [9B] 5442-5447 (1999).

# Other papers

1. K. Kikuta, W. Sakamoto, and S. Hirano, "Sol-Gel Processing of $Pb(Mg,Nb)O_3$ Dielectrics", *Ceram. Trans.*, **12** 717-724 (1990.)

2. S. Hirano, T. Yogo, K. Kikuta, K. Kato, W. Sakamoto and S. Ogasawara, "Sol-Gel Processing and Characterization of Ferroelectric Films", *Ceram. Trans.*, **25** 19-32 (1992).

3. S. Hirano, T. Yogo, K. Kikuta, and W. Sakamoto, "Processing and Characterization of $Pb(Mg,Nb)O_3$-$PbTiO_3$ Thin Films from Metal Alkoxide-Derived Gels", *J. Sol-Gel Sci. and Tech.*, **2** 329-334 (1994)

4. W. Sakamoto, S. Yada, T. Kohigashi, K. Kikuta, T. Yogo and S. Hirano, "Synthesis of Highly Oriented $(Pb_{0.85}La_{0.1})TiO_3$ Thin Films by Chemical Solution Deposition Method", *Ceram. Trans.*, **83** 331-337 (1998).

# Review papers

1. S. Hirano, T. Yogo and W. Sakamoto, "Synthesis and Characterization of PZT Thin Films by Sol-Gel Method", *T. IEE Japan*, **117-E**, [10] 488-491 (1997).

2. W. Sakamoto, T. Yogo and S. Hirano, "Synthesis and Characterization of Ferroelectric Thin Films with Tungsten Bronze Structure by Chemical Solution Deposition Method", *NEW CERAMICS*, **11** [6] 37-44 (1998).